UNIVERSITY OF SOUTHAMPTON

Faculty of Engineering and Physical Sciences
Department of Physics & Astronomy

Dark Matter Models: Signals and Backgrounds at the LHC and Future Colliders

by

Arran Charles Freegard

MPhys

ORCiD: 0000-0003-4482-3001

A thesis for the degree of
Doctor of Philosophy

January 2023

University of Southampton

Abstract

Faculty of Engineering and Physical Sciences
Department of Physics & Astronomy

Doctor of Philosophy

Dark Matter Models: Signals and Backgrounds at the LHC and Future Colliders

by Arran Charles Freegard

We explore the phenomenological signals and potential backgrounds of various Minimal Consistent Dark Matter (MCDM) models in the context of the Large Hadron Collider (LHC), non-LHC and future collider experiment searches.
We study two key background processes to Dark Matter (DM), and indeed more general beyond the Standard Model (BSM) physics, at the LHC as part of the ATLAS collaboration. For the production of Z boson in association with high p_T jets, we present results for data-driven $t\bar{t}$ modelling and multi-jet background derivation. We also investigate non-perturbative corrections, and comparisons of our Monte Carlo generator results from the analysis' Rivet routine. For the production of Z boson in association with heavy flavour quarks (i.e. b and c quarks) we present a novel approach to jet flavour discrimination through a fitting algorithm.
We explore the full parameter space and provide new LHC limits for both inert 2-Higgs Doublet Model (i2HDM) scalar DM and Minimal Fermionic DM (MFDM) at 13 TeV through a multilepton+missing E_T analysis. We parametrise in terms of mass splits, providing a more intuitive picture of the underlying physics in addition to a no-lose theorem in MFDM. We find significant contributions to sensitivity from 3-lepton final states. These limits and efficiencies we provide can then be extrapolated and applied in a model-independent way.
We additionally study non-LHC constraints from relic density requirements, direct and indirect detection, including Cosmic Microwave Background (CMB) and future Cherenkov Telescope Array (CTA) projections. These are combined for a comprehensive picture of the MFDM model, in addition to a summary of the i2HDM limits.
We utilise a model independent method for discriminating DM mass at future e^+e^- colliders, by analysing the energy distributions of charged DM decay products in $D^\pm \to W^\pm D_1$ cascades. We apply this to the i2HDM and MFDM models with two example benchmark points that provide correct observed DM density and comply with direct detection experimental bounds. We additionally present a method for discriminating DM spin by observing angular distributions of $W^\pm$ from reconstructed dijets.

Contents

List of Figures

List of Tables

Acknowledgements

I wish many thanks to my supervisors Alexander Belyaev, Ulla Blumenschein and Stefano Moretti for their constant support and guidance along my academic journey.

I would also like to thank my many collaborators, including Dipan Sengupta, Ilya F. Ginzburg, Daniel Locke, Alexander Pukhov. I would also like to thank my ATLAS collaborators, Alain Bellerive, Benedetto Giacobbe, Matthew Gignac, Alexandre Laurier, Josh McFayden, Arantxa Ruiz Martinez, Manuella Vincter and Camilla Vittori on the Z+collinear jets analysis team.

Further thanks to ATLAS collaborators Pierre-Hugues Beauchemin, Emanuele Bisceglie, Jonathan Bossio, Vincent Alexander Croft, Alec Swenson Drobac, Evelin Meoni, Jake Oliver, Luis Pinto Cabrera, Federico Sforza, Semen Turchikhin, Camilla Vittori, Yusheng Wu and Yi Yu on the Z+heavy flavours analysis team.

Lastly, I thank my partner, my family and my dear friends, without whom I would have surely perished on this perilous journey.

El. Psy. Kongroo.

Chapter 1

Introduction

The anatomy of Dark Matter (DM) has become one of the greatest puzzles of modern particle physics and cosmology, while its signal is one of the most sought-after at the Large Hadron Collider (LHC) [1], non-LHC experiments [2–4] and planned searches for future colliders [5].

Its existence has been all but confirmed by the multitude of independent cosmological observations [6–8]. These consist of galactic rotation curves [9], Cosmic Microwave Background (CMB) fits of the WMAP [10] and PLANCK [11] data, gravitational lensing [12,13], the large scale structure of the Universe [14–16], and interacting galaxy clusters such as the Bullet Cluster [17,18]. While this plethora of evidence points towards existence of a cold non-baryonic particle DM, most of its properties remain a mystery. Beyond gravitational, we have no evidence for its other interactions, let alone its mass, spin, symmetry for its stability, number of associated states or possible Standard Model (SM) mediating particle.

Despite the enduring success of the SM throughout the last century, such as predicting the scalar Higgs Boson, with mass $m_H = 125$ GeV found at the LHC in 2012 [19,20], the SM is still an incomplete description. In addition to lacking a quantum description of gravity, an origin for neutrino masses and explanation for the hierarchy problem, there is also no SM particle that would account for the galactic observations previously described, requiring an extension to beyond the SM (BSM) physics.

With the rising popularity of DM research within the high energy physics (HEP) community, many papers explore a vast variety of models and aim to disentangle their experimental signals and distinguish from one another. The key DM models currently under study include supersymmetry (SUSY) [21–23], sterile neutrinos [24], general minimal Weakly Interacting Massive Particle (WIMP) models [25], Axions [26], Kaluza-Klein DM [27], Universal Extra Dimensions [28] and extended Higgs sectors [29–31]. In addition, the ability to determine properties of DM such as

its mass [32,33] and spin [34–36] are vital for cataloguing the true nature of DM and further building upon the SM.

DM can potentially be directly produced and detected at colliders when DM is light enough and interacts with the SM either directly or via the exchange of mediators. However, depending on the signature, difficulty arises when considering the strong background at the LHC, including large QCD jet contributions. Sufficient information on the nature and precision measurement of relevant backgrounds is therefore required in order to distinguish it from a potential BSM signal. Processes such as Z+Jets production provide an important background to BSM searches [37–39], especially in the case of mono-X DM searches. In the cases where the Z boson is produced in association with jets originating from b and c quarks, these processes contribute greatly to the backgrounds of BSM signatures containing leptons and b-jets in the final state [40].

One can consider introducing DM candidates by constructing minimal, fully renormalisable and calculable extensions to the SM in the form of Minimal Consistent Dark Matter (MCDM) models [41]. With these models, one can analyse the interplay between collider and cosmological constraints while allowing them to be embedded into more complex SUSY-like BSM models.

In this thesis, I discuss two potential BSM models with DM candidates of spin=0 and 1/2. I explore a method to potentially discriminate DM spin with a key angular variable, in addition to up-to-date collider and non-collider constraints. I study in detail, potential backgrounds from the LHC, including high-p_T Z+jets production and Z+ heavy flavour quark production.

The thesis is structured as follows. In section 2 the SM theory and relevant collider phenomenology are described. In section 3 the BSM models under study in this work are outlined. In section 4 the hardware components of the LHC and its various detectors are detailed. In section 5 the ATLAS analysis concerning the relevant background from high p_T Z+jets is discussed, followed by the ATLAS analysis for Z+heavy flavour quarks backgrounds in section 6. Section 7 then presents the current collider constraints for multilepton plus missing energy signals on the BSM models. Section 8 breaks down the current non-LHC limits on the MFDM model, in addition to a final, comprehensive picture of the LHC plus non-LHC constraints on MFDM and i2HDM, including future projections. In section 9 a method for DM mass and spin discrimination at future e^+e^- colliders is considered and applied to the two models under study. Conclusions are then drawn in section 10.

1.1 Attribution and Organisation

Before proceeding, I would like to clarify the attributions of the various works within this thesis. While the vast majority of the sections of analyses presented here is original, important contributions have been made by my collaborators as detailed below.

Chapter 5 is based on work with the ATLAS collaboration, for the publication *Cross-section measurements for the production of a Z boson in association with high-transverse-momentum jets in pp collisions at* $\sqrt{s} = 13$ *TeV with the ATLAS detector*. The analysis members include Alain Bellerive (Carleton), Ulla Blumenschein (London QMUL), Benedetto Giacobbe (Bologna), Matthew Gignac (Santa Cruz UC), Alexandre Laurier (Carleton), Josh McFayden (Sussex), Arantxa Ruiz Martinez (Valencia), Manuella Vincter (Carleton), Camilla Vittori (Bologna). The corresponding paper is published at [42]. My unique contributions include the Theory predictions and non-perturbative correction, generator comparisons, Rivet routine, data-driven $t\bar{t}$ background modelling and data-driven multijet background modelling, which are then used throughout the final analysis results.

Chapter 6 is based on my contributions to the ATLAS analysis with the ATLAS collaboration for $Z+$ heavy flavors at 13 TeV. The analysis members include Pierre-Hugues Beauchemin (Tufts), Emanuele Bisceglie (Cosenza), Ulla Blumenschein (London QMUL), Jonathan Bossio (CERN), Vincent Alexander Croft (Tufts), Alec Swenson Drobac (Tufts), Evelin Meoni (Cosenza), Jake Oliver (London QMUL), Luis Pinto Cabrera, (McGill), Federico Sforza, (Genova), Semen Turchikhin, (JINR Dubna), Camilla Vittori (Bologna), Yusheng Wu, (Hefei), Yi Yu (Hefei). The internal note can be found at [43]. The final paper is planned to be published in the near future. My unique contributions include the novel flavour fit approach and implementation, Rivet analysis and generator comparisons.

Chapter 7 covers my major publication *Multilepton Signatures from Dark Matter at the LHC*, with co-authors Alexander Belyaev, Ulla Blumenschein, Stefano Moretti, Dipan Sengupta. The respective paper is published at [44]. My contributions include the full analysis, diagrams and distributions.

Chapter 8 covers my contributions to the non-LHC studies for the MFDM model, with co-authors Alexander Belyaev, Stephen Bone, Naseem Bouchhar, Colm Sam and Alistair Brewin. My contributions include all diagrams and distributions. The corresponding paper is intended to be published soon.

Chapter 9 covers my contributions to the publication *Decoding dark matter at future* e^+e^- *colliders* with co-authors Alexander Belyaev, Ilya F. Ginzburg, Daniel Locke, Alexander Pukhov. The respective paper is published at [45]. My contributions include energy distributions, mass peak/kink fitting and derivations.

Chapter 2

Theory

2.1 The Standard Model (SM) Lagrangian

The Lagrangian density is used to define a local quantum field theory (QFT) [46]. It is related to the action by

$$S = i \int \mathcal{L} d^4x \tag{2.1}$$

which is minimised to yield the field's Euler-Lagrange (EL) equations of motion

$$\partial_\mu \frac{\partial \mathcal{L}}{\partial(\partial_\mu A_\nu)} - \frac{\partial \mathcal{L}}{\partial A_\nu} = 0. \tag{2.2}$$

Here it is a function of the interacting fields, and space-time derivatives of these fields. It is a local function used to describe the energy properties of a system, including the kinetics and interactions of fields.

In order for the Lagrangian to describe a real physical system, it must be renormalisable, that is any divergences caused by infinities must be absorbed, separated or cancelled out in the final, physical Lagrangian. This is ensured by modifying the Lagrangian parameters in all orders such that its perturbation expansion is finite.

In order for the theory to obey relativity and transform the same, irrespective of the chosen frame of reference, the Lagrangian must also be invariant under global gauge transformations of the Poincare group, which include translations generated by P^μ, Lorentz rotations and Lorentz boosts generated by $M^{\mu\nu}$. Its algebra is then given by the commutation relations:

$$[P_\mu P_\nu] = 0 \tag{2.3}$$

$$-i[M_{\mu\nu}, P_\rho] = \eta_{\mu\rho} P_\nu - \eta_{\nu\rho} P_\mu \tag{2.4}$$

$$-i[M_{\mu\nu}, M_{\rho\sigma}] = \eta_{\mu\rho} M_{\nu\sigma} - \eta_{\mu\sigma} M_{\nu\rho} - \eta_{\nu\rho} M_{\mu\sigma} + \eta_{\nu\sigma} M_{\mu\rho}. \tag{2.5}$$

The particles, or representations, of the Poincare group then have mass from the eigenvalue of Casimir operator P^2 and spin from that of $W^2 = (\epsilon MP)^2$.

Symmetry conditions corresponding to a different transformation group are applied to a Lagrangian to further restrict the forms of its constituent terms. The members of these groups must then leave the action unchanged. Such symmetries lead to conserved currents and charges, J_μ, Q respectively. These are then the generators of the group and define its Lie algebra.

Dirac fermions ψ (and anti-fermions $\overline{\psi}$), represented as chiral Weyl spinors:

$$\psi = \begin{pmatrix} \psi_L \\ \psi_R \end{pmatrix} \tag{2.6}$$

consist of left-handed and right-handed components ψ_L, ψ_R respectively. The Dirac Lagrangian describing a free-field, 1/2 spin fermion, of mass m, is then

$$\mathcal{L}_\psi = \overline{\psi}(i\gamma^\mu \partial_\mu - m)\psi. \tag{2.7}$$

It can be shown in general that, for a $SU(N)$ local symmetry transformation, via $U = e^{i\alpha(x)T^a_{ij}}$, with generators T^a, and some scalar function $\alpha(x)$, this Lagrangian is not invariant:

$$\psi_i'(x) = U_{ij}\psi_j, \quad \overline{\psi}_i'(x) = \overline{\psi}_j U^{-1}_{ij}, \tag{2.8}$$

$$\begin{aligned} \mathcal{L}'_\psi &= \overline{\psi}_j U^{-1}_{ij}(i\gamma^\mu \partial_\mu - m)U_{ik}\psi_k = \overline{\psi}_j U^{-1}_{ij}(i\gamma^\mu \partial_\mu (U_{ik}\psi_k)) - \overline{\psi}_j U^{-1}_{ij} m U_{ik}\psi_k \\ &= \overline{\psi}_j U^{-1}_{ij}\psi_k i\gamma^\mu \partial_\mu (U_{ik}) + \overline{\psi}_j i\gamma^\mu \partial_\mu(\psi_k) - \overline{\psi}_j m\psi_k \neq \mathcal{L}_\psi. \end{aligned} \tag{2.9}$$

As a consequence of this, a massless gauge field (and thus gauge bosons) must be introduced for each generator, to preserve local gauge symmetry. It is required to cancel the first term in Eq. 2.9. This is given by $A^a_\mu(x)$, the vector gauge field defined for the given gauge group.

After defining a coupling strength g, and replacing its standard derivative ∂_μ with the corresponding "transformed" covariant derivative,

$$D_\mu = \partial_\mu - igA^a_\mu T^a \tag{2.10}$$

the new combined Lagrangian is:

$$\mathcal{L}_\psi = \overline{\psi}(i\gamma^\mu D_\mu - m)\psi. \tag{2.11}$$

This $A^a_\mu(x)$ then transforms the covariant derivative the following way:

$$\begin{aligned} D'_\mu &= \partial_\mu - ig\left(U(x)A^a_\mu(x)T^aU^{-1}(x) - \frac{i}{g}U^{-1}(x)\partial_\mu(U(x))\right) \\ &= \partial_\mu - igU(x)A^a_\mu(x)T^aU^{-1}(x) - U^{-1}(x)\partial_\mu(U(x)). \end{aligned} \tag{2.12}$$

This then gives a Lagrangian that transforms invariantly:

$$\mathcal{L}'_\psi = \overline{\psi}_j U^{-1}_{ij}(x)(i\gamma^\mu D'_\mu - m)U_{ik}(x)\psi_k \tag{2.13}$$

$$= \overline{\psi}(i\gamma^\mu(\partial_\mu - igAT) - m)\psi = \mathcal{L}. \tag{2.14}$$

To prohibit the EL equations of motion for A to give $\overline{\psi}\psi = 0$, the gauge fields A^a_μ then have kinetic terms such that

$$-\frac{1}{4}A^{\mu\nu}_a A^a_{\mu\nu} \tag{2.15}$$

leading to the field strength tensors

$$A^{\mu\nu,a} = \partial^\mu A^{\nu,a} - \partial^\nu A^{\mu,a} - gf^{abc}A^\mu_b A^\nu_c. \tag{2.16}$$

The structure functions f^{abc} of a non-Abelian $SU(N)$ gauge group, theories where the generators do not commute, means $f^{abc} \neq 0$. They are then defined by the commutation relations

$$[T^a, T^b] = if^{abc}T^c \tag{2.17}$$

and normalization requirements lead to

$$Tr\{T^aT^b\} = \frac{1}{2}\delta^{ab}. \tag{2.18}$$

These are the commutators of the generators, and being non-zero means the theory contains self-interactions of its gauge bosons.

As seen in Quantum Electrodynamics (QED), the simplest Abelian $U(1)_{EM}$ theory where the generators commute, $f^{abc} = 0$ and the photons do not self-interact.

There are three internal local symmetries that help define the SM Lagrangian. The weak hypercharge Y generates the local, Abelian $U(1)_Y$ symmetry. Three weak isospin operators T_i, with eigenvalues of weak isospin $I^2_W = T_iT_j$, generate local $SU(2)_L$ symmetry, and have the algebra $[T_i, T_j] = i\epsilon_{ijk}$. From the Gell-Mann Nishijima formula, the electromagnetic (EM) charge Q is related to weak isospin I_W and hypercharge Y by $Q = I_W + Y/2$ [48]. The eight colour charged operators then generate the local $SU(3)_C$ symmetry, and have the algebra $[t^a, t^b] = if^{abc}t^c$, with non-zero structure functions f^{abc}.

	Spin	Fields	Hypercharge Y	Isospin I_W
Quarks		$\begin{pmatrix} u \\ d' \end{pmatrix}_L, \begin{pmatrix} c \\ s' \end{pmatrix}_L, \begin{pmatrix} t \\ b' \end{pmatrix}_L$	$\frac{1}{3}$	$\frac{1}{2}$
Up(u) Charm(c) Top(t) 2.4 MeV 1.28 GeV 172.44 GeV	$\frac{1}{2}$	u_R, c_R, t_R	$\frac{4}{3}$	0
Down(d) Strange(s) Bottom(b) 4.8 MeV 95 MeV 4.18 GeV		d'_R, s'_R, b'_R	$-\frac{2}{3}$	0
Leptons		$\begin{pmatrix} \nu_e \\ e^- \end{pmatrix}_L, \begin{pmatrix} \nu_\mu \\ \mu^- \end{pmatrix}_L, \begin{pmatrix} \nu_\tau \\ \tau^- \end{pmatrix}_L$	-1	$\frac{1}{2}$
Electron(e^-) Muon(μ^-) Tau(τ^-) 0.5 MeV 105.7MeV 1.78GeV	$\frac{1}{2}$	e_R, μ_R, τ_R	-2	0
Neutrinos (ν_e, ν_μ, ν_τ) ~ 0				
Bosons				
$U(1)$	1	B	0	
$SU(2)$ Z $W^\pm$ 91 GeV 80.39 GeV	1	W^1,W^2,W^3	0	0
$SU(3)$	1	g^1,g^2,g^3,g^4,g^5,g^6,g^7,g^8	2	0
Higgs (H) 125.09 GeV	0	$\Phi = \begin{pmatrix} \phi_1 + i\phi_2 \\ \phi_3 + i\phi_4 \end{pmatrix}$	1	$\frac{1}{2}$

TABLE 2.1: A table summarising SM fields, with fundamental representation fermions, spin-1/2 particles separated into quarks and leptons [47].

Table 2.1 shows the fundamental quarks, leptons and bosons, with corresponding spin, fields, hypercharge and isospin. The SM is then an $SU(3)_C \times SU(2)_L \times U(1)_Y$ local gauge theory, spontaneously broken through the Higgs mechanism to $U(1)_{EM}$. These spin-1/2 fermions form representations of the gauge groups. The resulting fundamental interactions in the SM, being quantum chromodynamics (QCD) and electroweak (EW) will then be discussed in the following sections.

2.2 Quantum Chromodynamics (QCD)

QCD describes the strong interactions between the six families of spin-1/2 quarks, each with 3 possible colours, and the 8 spin-1 massless gluon gauge bosons. It acts under $SU(3)_C$ gauge symmetry, and requires no symmetry breaking to occur. The quark mass terms are instead being generated via Higgs coupling in the EW sector and can be neglected for this section.

Quarks are fermions, which are a fundamental 3 colour representation, while antiquarks are complex conjugate $\overline{3}$ colour representation:

$$\psi = \begin{pmatrix} \psi_f^{red} \\ \psi_f^{green} \\ \psi_f^{blue} \end{pmatrix}, \quad \overline{\psi} = \begin{pmatrix} \overline{\psi}_f^{red*} \\ \overline{\psi}_f^{green*} \\ \overline{\psi}_f^{blue*} \end{pmatrix}. \tag{2.19}$$

The gluon field strength tensor is

$$G^a_{\mu\nu} = \partial_\mu G^a_\nu - \partial_\nu G^a_\mu + g_s f^{abc} G^b_\mu G^c_\nu \tag{2.20}$$

in terms of gluon fields G^a_μ, the strong coupling constant g_s and structure functions f^{abc}. These structure functions are the commutators of the generators of $SU(3)_C$, following the algebra

$$[t^a, t^b] = i f^{abc} t^c \tag{2.21}$$

and normalisation requirements lead to

$$Tr\{t^a t^b\} = \frac{1}{2}\delta^{ab}. \tag{2.22}$$

The t^a colour matrices here are the $N^2 - 1 = 8$ colour symmetry group generators of $SU(3)_C$ in quark fundamental representation.

The quark covariant derivative, requiring summation over the quark flavours i, j and gluon colour indices a, is

$$D^\mu_{ij} = \partial^\mu + i g_s t^a_{ij} G^{a\mu}. \tag{2.23}$$

such that the Lagrangian for QCD interactions (using slashed notation) is given by

$$\mathcal{L}_{QCD} = -\frac{1}{4} G^{a\mu\nu} G^a_{\mu\nu} + \overline{\psi}_i (i \not{D}^\mu_{ij}) \psi_j. \tag{2.24}$$

The Lagrangian for QCD is invariant under the following infinitesimal gauge transformations

$$\phi_i(x) \to (\delta_{ij} - i g_s \theta^a(x) t^a_{ij}) \phi(x) \tag{2.25}$$

$$G^a_\mu(x) \to G^a_\mu(x) + D^{ab}_\mu \theta^b(x). \tag{2.26}$$

To ensure gauge invariance under $SU(3)_C$ in quark colour space, this forces the introduction of the gluon field G^a_μ, with the addition of the fermion-gluon interaction term in the Lagrangian. This is in contrast to the EM field strength tensor $F^{\mu\nu} = \partial^\mu A^\nu - \partial^\nu A^\mu$ which has no such additional term. These would contain the commutators f^{abc} of the generators of the gauge group, present in Eq.2.20, but such commutators for the photon are zero (it is an Abelian theory), hence the term vanishes in EM.

Another aspect of the theory different from QED, due to the presence of the non-zero commutation relations in QCD, is that it causes issues when quantising the theory. The gluon field's gauge freedom property means adding these relations by hand would violate this. Fadeev-Popov Ghost fields must be introduced, in order to cancel the additional, unphysical degrees of freedom that arise from summing over all polarisations, including non-physical gluon longitudinal polarisations that would otherwise produce singularities. These new scalar fields would transform under $SU(3)$, as gluons would, while never appearing as physical final state objects. The Faddeev-Popov Lagrangian is

$$\mathcal{L}_{ghost} = \bar{c}^a(-\partial^2\delta^{ac} - g\partial^\mu f^{abc}A^b_\mu)c^c \tag{2.27}$$

with the addition of the gauge fixing term

$$\mathcal{L}_{gaugefix} = -\frac{1}{2\xi}(\partial_\mu G^\mu_a)^2. \tag{2.28}$$

QCD calculations of transition amplitudes between initial and final states are then carried out in the perturbative regime, valid for $\alpha_s \ll 1$. These are in the form of expansions of the S-matrix [49], which would then lead to computation of cross sections via Fermi's golden rule [50,51]. The remaining components of the SM, being EW interactions and the Higgs mechanism, will first be described in the next section.

2.3 Electroweak (EW) Sector

EW theory, governed by local $SU(2)_L \otimes U(1)_Y$ gauge symmetry, describes the interactions between fermion multiplets, quarks and leptons, arranged by weak isospin $SU(2)_L$ doublets

$$\ell_L = \begin{pmatrix}\nu_i \\ \ell_i^-\end{pmatrix}_L = \begin{pmatrix}\nu_e \\ e^-\end{pmatrix}_L, \begin{pmatrix}\nu_\mu \\ \mu^-\end{pmatrix}_L, \begin{pmatrix}\nu_\tau \\ \tau^-\end{pmatrix}_L \quad I_W = \frac{1}{2} \quad Y_W = -1 \tag{2.29}$$

$$q_L = \begin{pmatrix}u_i \\ d_i\end{pmatrix}_L = \begin{pmatrix}u \\ d\end{pmatrix}_L, \begin{pmatrix}c \\ s\end{pmatrix}_L, \begin{pmatrix}t \\ b\end{pmatrix}_L \quad I_W = \frac{1}{2} \quad Y_W = \frac{1}{3} \tag{2.30}$$

for weak hypercharge Y_W and isospin I_W. L indicates their left-handedness. The $SU(2)$ isoscalar singlets, right-handed fermions, (excluding neutrinos as these have intrinsic chirality) are then:

$$u_R = u_R, c_R, t_R, \;\; Y_W(u_R) = \frac{4}{3}, \qquad d_R = d_R, s_R, b_R, \;\; Y_W(d_R) = -\frac{2}{3} \tag{2.31}$$

$$\ell_R = e_R, \mu_R, \tau_R, \quad Y_W(\ell_R) = -2. \tag{2.32}$$

Left-handed and right-handed fermion fields are defined in terms of the projection operators $P_L = \frac{1}{2}(1-\gamma^5)$, $P_R = \frac{1}{2}(1+\gamma^5)$ respectively, such that

$$\psi_{i,L} = P_L\psi_i, \quad \psi_{i,R} = P_R\psi_i. \tag{2.33}$$

Here parity violation is present, due to left-handed and right-handed components possessing different quantum numbers [52].

The Lagrangian for the massless fermions is then

$$\mathcal{L}_{fermions} = \overline{q}_L \not{D} q_L + \overline{u}_R \not{D} u_R + \overline{d}_R \not{D} d_R + \overline{\ell}_L \not{D} \ell_L + \overline{\ell}_R \not{D} \ell_R \tag{2.34}$$

summing over the three fermion generations. The coupling constant g_1 is associated to the $U(1)_Y$ B_μ field, while g_2 associates to the $SU(2)_L$ W^i_μ field. Its covariant derivative is then given by

$$\not{D} = \gamma^\mu \left(\partial_\mu + ig_1 \frac{Y_W}{2} B_\mu + ig_2 I_W \begin{pmatrix} W^3_\mu & W^1_\mu - iW^2_\mu \\ W^1_\mu + iW^2_\mu & -W^3_\mu \end{pmatrix} \right). \tag{2.35}$$

The fermion mass terms, which take the form

$$m\overline{\psi}\psi = m \begin{pmatrix} \psi^\dagger_L & \psi^\dagger_R \end{pmatrix} \begin{pmatrix} 0 & 1 \\ 1 & 0 \end{pmatrix} \begin{pmatrix} \psi_L \\ \psi_R \end{pmatrix} \tag{2.36}$$

break gauge invariance under $SU(2)_L$, due to the asymmetry of left-handed and right-handed spinor field components. Mass terms must be instead generated via the Higgs mechanism of electroweak symmetry breaking (EWSB).

Before EWSB, the gauge bosons then have Lagrangian

$$\mathcal{L}_{Gauge,KE} = -\frac{1}{4} W^{\mu\nu} W_{\mu\nu} - \frac{1}{4} B^{\mu\nu} B_{\mu\nu} \tag{2.37}$$

with $SU(2)_L$ field strength tensor

$$W_{\mu\nu} = \partial_\mu W_\nu - \partial_\nu W_\mu - g_2 W_\mu W_\nu \tag{2.38}$$

and $U(1)_Y$ field strength tensor

$$B_{\mu\nu} = \partial_\mu B_\nu - \partial_\nu B_\mu. \tag{2.39}$$

The $W_{\mu\nu}$ field strength tensor $SU(2)_L$ is similar to $G_{\mu\nu}$ in QCD, where the structure function f^{abc} is replaced with ϵ^{ijk}, while for the Abelian $U(1)_Y$ tensor, $B_{\mu\nu}$, this vanishes.

Here there is no gauge invariant mass term, but this is needed to generate the experimentally observed massive EW gauge bosons. At the moment, this is an

unbroken $SU(2) \otimes U(1)$ gauge symmetry, containing 4 massless gauge bosons. It is required to have spontaneous symmetry breaking via the Higgs mechanism, in order to generate the massive vector bosons needed to mediate current interactions. This must also leave $U(1)_{EM}$ unbroken.

2.3.1 The Higgs Mechanism

The SM Higgs is then given by the doublet of scalar fields

$$\Phi = \frac{1}{\sqrt{2}} \begin{pmatrix} \phi_1 + i\phi_2 \\ \phi_3 + i\phi_4 \end{pmatrix} \tag{2.40}$$

in unitary gauge, with four degrees of freedom, ϕ_1,ϕ_2,ϕ_3 and ϕ_4. This complex $SU(2)_L$ doublet has weak isospin $\frac{1}{2}$ and unit hypercharge. Given the Higgs potential term

$$V(\Phi) = \mu^2 \Phi^\dagger \Phi - \frac{\lambda^2}{2} (\Phi^\dagger \Phi)^2 \tag{2.41}$$

for Higgs parameters μ and λ, the Lagrangian of the Higgs, with covariant derivative D, is

$$\mathcal{L}_{Higgs} = (D^\mu \Phi)^\dagger (D_\mu \Phi) - V(\Phi(x)). \tag{2.42}$$

Taking the minimum for the Higgs potential, $\frac{\partial V(\Phi)}{\partial \Phi} = 0$, it is useful to consider the case for $\mu^2 < 0$, leading to

$$\frac{\partial V(\Phi)}{\partial \Phi} = \mu^2 \frac{\partial}{\partial \Phi}(\Phi^2) - \frac{\lambda^2}{2} \frac{\partial}{\partial \Phi}(\Phi^4) = 2\Phi(\mu^2 - \lambda^2 \Phi^2) = 0 \tag{2.43}$$

and for $|\Phi^\dagger \Phi|_{min} = \mu^2/\lambda^2 = v^2/2$,

$$\frac{v}{\sqrt{2}} = \frac{\mu}{\lambda}, \tag{2.44}$$

$$V(\Phi) = \frac{\mu^4}{2\lambda^2}. \tag{2.45}$$

This is assuming that the potential is bound from below (taking the minimum as a global minimum), in order to keep the vacuum from collapsing, leading to $\lambda < 0$. As visualised in Fig.2.1, the potential forms the "Mexican-hat" distribution in the (ϕ_1,ϕ_2) plane.

This form of the Higgs potential then gives rise to the spontaneous symmetry breaking of $SU(2)_L \otimes U(1)_Y \rightarrow U(1)_{EM}$:

$$\Phi = \frac{1}{\sqrt{2}} \begin{pmatrix} \phi_1 + i\phi_2 \\ \phi_3 + i\phi_4 \end{pmatrix} \rightarrow \frac{1}{\sqrt{2}} \begin{pmatrix} 0 \\ v + h \end{pmatrix}. \tag{2.46}$$

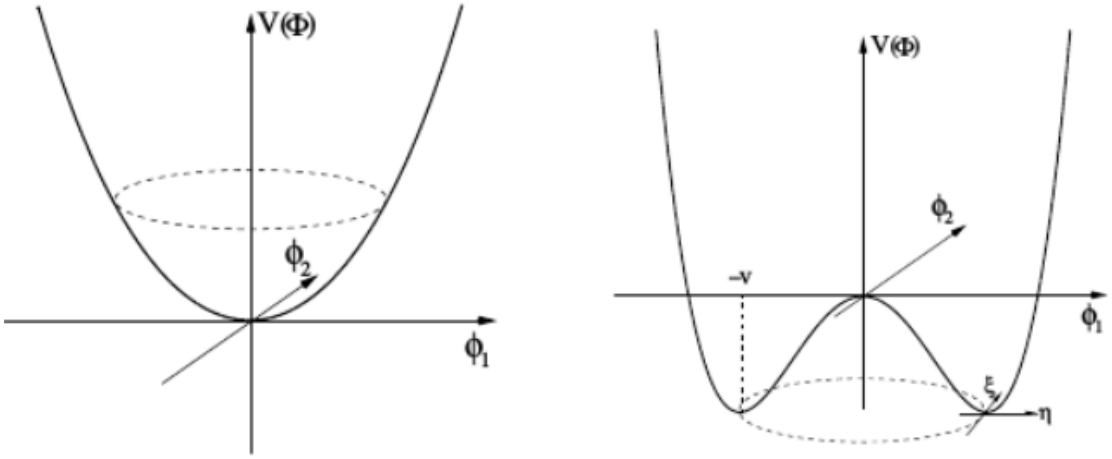

FIGURE 2.1: The Higgs potential for a single complex scalar Φ before (left) and after (right) EWSB. It has a set of degenerate energy states along the dotted line, at $\langle\Phi\rangle = 0$ (left) and $\langle\Phi\rangle \neq 0$ [53].

The missing degrees of freedom in Eq. 2.46 have been absorbed by the W and Z bosons such that these massive gauge bosons obtain the required longitudinal components. The direction in $SU(2)$ space for symmetry breaking is what inevitably defines the direction of the photon and W vectors. This Higgs doublet Φ then takes a vacuum expectation value (VEV) v in the ground (vacuum) state, preserving $U(1)_{EM}$ gauge invariance as only the real component is taken to be non-zero. The vacuum does not change under $U(1)_{EM}$. In total, this leaves the photon massless for example, and gives three massive vector bosons, as will be demonstrated below.

Considering a small perturbation, h, transforming into the unitary gauge leads to Eq. 2.46 such that, for EM charge operator Q:

$$Q\Phi_0 = (I_3 + Y_W)\Phi_0 = (\frac{1}{2}\tau_3 + \frac{1}{2}I)\Phi_0 = \begin{pmatrix} 1 & 0 \\ 0 & 0 \end{pmatrix}\Phi_0 = 0. \tag{2.47}$$

This then allows for computing the covariant derivative acting on scalars

$$D_\mu\Phi = \frac{1}{\sqrt{2}}\begin{pmatrix} ig_2 I_W(v+h)(W_\mu^1 - iW_\mu^2) \\ \partial_\mu(v+h) + ig_1\frac{Y_W}{2}B_\mu(v+h) - ig_2 I_W W_\mu^3(v+h) \end{pmatrix}. \tag{2.48}$$

As required by Eq.2.42, applying this twice leads to:

$$|D_\mu\Phi|^2 = \frac{1}{2}|(\partial_\mu + ig_1\frac{Y_W}{2}B_\mu + ig_2 I_W\begin{pmatrix} W_\mu^3 & W_\mu^1 - iW_\mu^2 \\ W_\mu^1 + iW_\mu^2 & -W_\mu^3 \end{pmatrix})\begin{pmatrix} 0 \\ v+h \end{pmatrix}|^2$$

$$= \frac{1}{2}g_2^2 I_W^2 (v+h)^2 (W_\mu^1 + iW_\mu^2)(W_\mu^1 - iW_\mu^2) + \frac{1}{2}(\partial(v+h))^2 + \frac{1}{2}(g_2 I_W W_\mu^3 - g_1 \frac{Y_W}{2} B_\mu)^2. \tag{2.49}$$

Diagonalisation of the mass matrix then leads to the mass terms for the massive gauge bosons. With the substitution of

$$W_\mu^\pm = \frac{1}{\sqrt{2}}(W_\mu^1 \mp iW_\mu^2), \;\; m_W = \frac{1}{2}g_2 v, \tag{2.50}$$

where the mass matrix is given by

$$M = \begin{pmatrix} g_1^2 & -g_1 g_2 \\ -g_1 g_2 & g_2^2 \end{pmatrix} \tag{2.51}$$

with non-zero eigenvalue of $g_1^2 + g_2^2$, the mixing matrix of B and W to A and Z^0 via the sin of the Weinberg mixing angle θ_W is

$$\begin{pmatrix} A \\ Z^0 \end{pmatrix} = \begin{pmatrix} cos\theta_W & sin\theta_W \\ -sin\theta_W & cos\theta_W \end{pmatrix} \begin{pmatrix} B \\ W_3 \end{pmatrix}. \tag{2.52}$$

This gives the relation between the massive EW boson masses

$$Z_\mu = \frac{1}{\sqrt{g_1^2 + g_2^2}}(g_1 W_\mu^3 - g_2 B_\mu^0), \;\; m_Z = \frac{1}{2}\sqrt{g_1^2 + g_2^2 v} \tag{2.53}$$

$$m_Z = \frac{m_W}{cos\theta_W}. \tag{2.54}$$

Meanwhile mixing between weak and mass eigenstates, with the eigenvalue of 0 from the mass matrix, leaves the photon massless as

$$A_\mu = \frac{1}{\sqrt{g_1^2 + g_2^2}}(g_2 W_\mu^3 + g_1 B_\mu), \;\; m_A = 0 \tag{2.55}$$

and gives relations between the couplings

$$sin\theta_W = \frac{g_1}{\sqrt{g_1^2 + g_2^2}}, \;\; e = \frac{g_1 g_2}{\sqrt{g_1^2 + g_2^2}}. \tag{2.56}$$

This result of one massless and three massive gauge bosons is an example of Goldstone's theorem in action, for which it is expected to gain an additional degree of freedom per generator of a broken symmetry [54].

After spontaneous symmetry breaking of $SU(2)_L \otimes U(1)_Y$ to $U(1)_{EM}$, the charge Q of the fermion field for $U(1)_{EM}$ is then given by

$$Q = \tau^3 + Y_W \tag{2.57}$$

where τ^3 is the isospin I_W parallel to W_μ^3, the gauge field for which only left-handed $SU(2)_L$ doublets can couple.

In terms of currents and physical gauge boson fields, the EW Lagrangian is

$$\mathcal{L}_{EW} = g_w(W_\mu^+ J_{W+}^\mu + W_\mu^- J_{W-}^\mu + Z_\mu^0 J_Z^\mu) + eA_\mu J_{EM}^\mu \tag{2.58}$$

and these EW currents are given by

$$J_{W+}^\mu = \frac{1}{\sqrt{2}}(\overline{\nu}_L \gamma^\mu e_L + \overline{u}_L \gamma^\mu d_L), \tag{2.59}$$

$$J_{W-}^\mu = \frac{1}{\sqrt{2}}(\overline{e}_L \gamma^\mu \nu_L + \overline{d}_L \gamma^\mu u_L), \tag{2.60}$$

$$\begin{aligned} J_Z^\mu = \frac{1}{\cos\theta_w}\Big(& \overline{\nu}_L \gamma^\mu I_{W_\nu} \nu_L \\ & + \overline{e}_L \gamma^\mu (-Q_e \sin^2\theta_w + I_{W_e}) e_L + \overline{e}_R \gamma^\mu (-Q_e \sin^2\theta_w) e_R \\ & + \overline{u}_L \gamma^\mu (-Q_u \sin^2\theta_w + I_{W_u}) u_L + \overline{u}_R \gamma^\mu (-Q_u \sin^2\theta_w) u_R \\ & + \overline{d}_L \gamma^\mu (-Q_d \sin^2\theta_w + I_{W_d}) d_L + \overline{d}_R \gamma^\mu (-Q_d \sin^2\theta_w) d_R \Big), \end{aligned} \tag{2.61}$$

$$J_{EM}^\mu = \overline{e}\gamma^\mu Q_e e + \overline{u}\gamma^\mu (Q_u) u + \overline{d}\gamma^\mu (Q_d) d. \tag{2.62}$$

After symmetry breaking, the full fermion Lagrangian, complete with mass terms is then

$$\begin{aligned} \mathcal{L}_{Fermions} = \overline{\psi}(i\partial\!\!\!/ - m_f - \frac{m_f H}{v})\psi - \frac{g}{2\sqrt{2}}\overline{\Psi}\gamma^\mu(1-\gamma^5)(T^+ W_\mu^+ + T^- W_\mu^-)\Psi \\ -eQ\overline{\psi}\gamma^\mu\psi A_\mu - \frac{g}{2cos\theta_W}\overline{\psi}\gamma^\mu(g_V - g_A\gamma^5)\psi Z_\mu \end{aligned} \tag{2.63}$$

where the gauge invariant mass terms, generated via Yukawa interaction with the Higgs field, leads to the Lagrangian

$$\mathcal{L}_{Yukawa} = -\frac{1}{\sqrt{2}} v(Y_u u_L(x) u_R(x) + Y_d d_L(x) d_R(x) + Y_\ell \ell_L \ell_R) \tag{2.64}$$

with the Yukawa coupling Y_f which relates to the mass as

$$m_f = \frac{1}{\sqrt{2}} Y_f v. \tag{2.65}$$

This gives a direct correlation between the Higgs-fermion coupling strength and the fermion's mass. The Higgs itself has a mass M_h, brought on by self-interactions,

$$\mathcal{L}_{Higgs} = -\frac{1}{2v}M_h^2 h^3 - \frac{1}{8v^2}M_h^2 h^4 \tag{2.66}$$

giving mass term

$$M_h = v\sqrt{2\lambda}. \tag{2.67}$$

The Higgs boson was then experimentally observed in 2012, with mass ~ 125 GeV, by ATLAS [55] and CMS [56].

2.3.2 CKM Matrix

Quark mass terms are generated via Higgs field Yukawa interactions in Eq. 2.64, as the Higgs acquires a VEV. Instead of mass eigenstates in the Yukawa term, the quarks will form weak eigensates when coupling to the W boson. This allows for mixing to occur between the quark generations via diagonalisation of their mass matrices, incorporating the unitary CKM matrix V_{CKM}, given by

$$V_{CKM} = V_L^u V_L^{d\dagger} = \begin{pmatrix} V_{ud} & V_{us} & V_{ub} \\ V_{cd} & V_{cs} & V_{cb} \\ V_{td} & V_{ts} & V_{tb} \end{pmatrix} \tag{2.68}$$

which, in terms of cos, c_{ij} and sin, s_{ij} of the three mixing angles θ_{ij}, is

$$\begin{pmatrix} c_{12}c_{13} & s_{12}s_{13} & s_{13}e^{-i\delta} \\ -s_{12}c_{23} - c_{12}s_{23}s_{13}e^{i\delta} & c_{12}c_{23} - s_{12}s_{23}s_{13}e^{i\delta} & s_{23}c_{13} \\ s_{12}s_{23} - c_{12}c_{23}s_{13}e^{i\delta} & -c_{12}s_{23} - s_{12}c_{23}s_{13}e^{i\delta} & c_{23}c_{13} \end{pmatrix}. \tag{2.69}$$

Here the δ is the CP-violating phase, for which CP-violation gives this phase difference in the CP conjugate of a given process. Only weak interactions do not conserve flavour of quark, parity (P) and charge conjugation (C). Conservation of CP is obeyed by strong, electromagnetic and almost weak interactions.

Different generations of the quarks can then mix via the rotation matrix, with couplings

$$\frac{-g_2}{\sqrt{2}}\bar{q}_L\gamma^\mu W_\mu V_{CKM} q'_L = \frac{-g_2}{\sqrt{2}}\begin{pmatrix}\bar{u}_L & \bar{s}_L & \bar{t}_L\end{pmatrix}\gamma^\mu W_\mu V_{CKM}\begin{pmatrix} d'_L \\ s'_L \\ b'_L \end{pmatrix}. \tag{2.70}$$

CP violation is measured in the quark sector, which is then encoded in CKM matrix. The complex phase δ from the CKM matrix provides some CP violation, as they cannot be eliminated by a phase rotation of quarks. Significant CP violation is

required in the SM, since the amount of particles and antiparticles in the universe is evidently not equal and we have indeed not been annihilated by their interaction [57]. This asymmetry is defined as the ratio of baryon-antibaryon asymmetry, in terms of their cosmic background number densities n_B and $n_{\overline{B}}$ respectively, to the photon cosmic background number density n_γ, as:

$$\eta = \frac{n_B - n_{\overline{B}}}{n_\gamma}. \tag{2.71}$$

The measured value of η is $\simeq 6 \times 10^{-10}$. However, the degree of CP-violation provided by the CKM matrix is not sufficient to account for observations. This is tested experimentally via semileptonic asymmetry calculations [58] defined by the ratio of decays to particle and decay to antiparticle. Astrophysical evidence [59] also suggests this, from the lack of observations of photons coming from the boundaries between known regions of matter and antimatter. One would expect these to be produced in balanced mater-antimatter annihilations, but this is not observed [60].

Having defined the SM, the relevant collider observables will be described in the following section. These underpin the calculations that will yield numerical results produced by these interactions, for which one can test the accuracy of model theory predictions to data.

2.4 Kinematics, Luminosity and Cross Section

In particle physics, the incoming and outgoing momentum four-vectors, given by $p = (E, \vec{p})$ where E is the rest energy of the particle and $\vec{p}$ is its three-vector momentum, can be parametrised by the Mandelstam variables. These are given by

$$s = (p + k)^2 = (p' + k')^2 \tag{2.72}$$

$$t = (p' - p)^2 = (k' - k)^2 \tag{2.73}$$

$$u = (k' - p)^2 = (p' - k)^2 \tag{2.74}$$

where p' indicates the outgoing particle momentum, while k, k' represent an additional particle's incoming and outgoing momenta respectively. These s-,t- and u-channel diagrams are represented pictorially in Fig. 2.2.

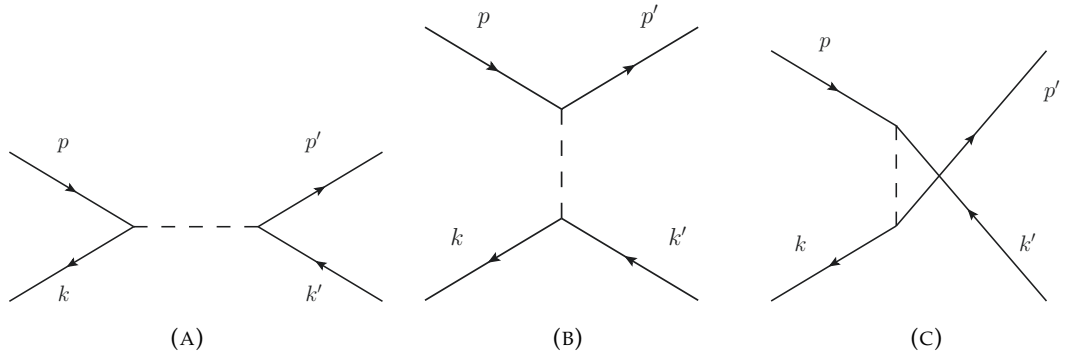

FIGURE 2.2: Feynman diagrams for the s- (a), t- (b) and u-channel (c) processes, for incoming p, k and outgoing p', k' particles.

2.4.1 Perturbation Expansion of S-matrix

The unitary scattering operator, or S-matrix, relates incoming eigenstates $|p_i\rangle$ with outgoing eigenstates $\langle p_f|$, before and after the scattering process as

$$\langle p_f| S |p_i\rangle \tag{2.75}$$

where S, in terms of the time-evolution operator $U = exp\{-Ht\}$ defining the dynamics of the system as a function of the Hamiltonian $H = H_0 + V = p^2/(2m) + V$, is

$$S = \lim_{t_{f,i}\to\pm\infty} U(t_f, t_i) = \lim_{t_{f,i}\to\pm\infty} e^{iH_0 t_f} e^{-i(H_0+V)(t_f-t_i)} e^{-iH_0 t_i}, \tag{2.76}$$

The Hamiltonian is required to be "time-ordered", to ensure causality of the theory. This time ordering requires placing operators for the most recent time t_n to the left, and initial time t_1 to the right, leading to a scattering operator:

$$S = 1 + \sum_{n=1}^{\infty} (-i)^n \int_{-\infty}^{\infty} dt_n ... \int_{-\infty}^{t_3} dt_2 \int_{-\infty}^{dt_2} dt_1 H(t_n)...H(t_2)H(t_1) \tag{2.77}$$

known as the LSZ reduction formula [61]. The S-matrix can be expressed in terms of the n-point Green's functions $G_n(x_1, ...x_n) = \langle 0| T\{\phi(x_1)...\phi(x_n)\} |0\rangle$, the VEVs of Heisenberg fields, such that

$$G_n(x_1, ...x_n) = \frac{\langle 0| T\{\phi_i(x_1)...\phi_i(x_n)S\} |0\rangle}{\langle 0| S |0\rangle}. \tag{2.78}$$

Next, perturbation theory is performed, that is expanding the Green's function [62] in powers of the coupling. Wick's theorem [63] allows for expressing the VEVs of the numerous fields to VEVs of only two fields. To obtain the Feynman propagator [64], one can look at

$$G_2(x, y) = \langle 0| T\{\phi_i(x)\phi_i(y)S\} |0\rangle . \tag{2.79}$$

So the Feynman propagator is

$$G_F(x-y) = \langle 0| T\{\phi(x)\phi(y)\} |0\rangle = i\int \frac{d^4p}{(2\pi)^4}\frac{e^{-ip\cdot(x-y)}}{p^2-m^2+i\varepsilon}. \tag{2.80}$$

Feynman rules coming from the Lagrangian are derived from the functional integrals over the different fields. For the fermions, the fermion propagator can be written as

$$\langle \psi_{i\alpha}(x)\bar{\psi}_{j\beta}(y)\rangle = \int \frac{d^4k}{(2\pi)^4}\left(\frac{i}{\not{k}-m}\right)_{\alpha\beta}\delta_{ij}e^{-ik\cdot(x-y)}. \tag{2.81}$$

The gauge field propagator is given by

$$\langle G^a_\mu(x)G^b_\nu(y)\rangle = \int \frac{d^4k}{(2\pi)^4}\frac{-i}{k^2+i\epsilon}\left(g_{\mu\nu}-(1-\zeta)\frac{k_\mu k_\nu}{k^2}\right)\delta^{ab}e^{-ik\cdot(x-y)} \tag{2.82}$$

for which, setting $\zeta = 1$ is the Feynman-'t Hooft gauge

$$\langle G^a_\mu(x)G^b_\nu(y)\rangle = \int \frac{d^4k}{(2\pi)^4}\frac{-i}{k^2+i\epsilon}\left(g_{\mu\nu}\right)\delta^{ab}e^{-ik\cdot(x-y)}. \tag{2.83}$$

The Feynman rules are then derived from these calculations of the Green's functions in position or momentum space. Richard Feynman's diagrams and set of rules for computing various aspects of subatomic interactions formulated in the late 1940's [65] were revolutionary for the field, while proving invaluable for obtaining numerical results in QFT and processes such as Compton scattering [66]. In order to quantify the probability of a given scattering process occurring, the calculation of the differential cross section is required. To obtain this, knowledge of the fundamental interactions' matrix element is needed, which also necessitates understanding of the formal theory with regards to the interaction's Feynman diagrams with the possibility of multiple contributing parts. Each diagram is a term of the perturbation expansion of the S-matrix.

Fermi's golden rule [51] then gives the transition probability, or decay rate, from state $|p_i\rangle$ to $\langle p_f|$,

$$\Gamma = \frac{2\pi}{\hbar}|\langle p_f| H_{fi} |p_i\rangle|^2\rho(E_F). \tag{2.84}$$

The scattering amplitude $\mathcal{M}$ is then related to the S-matrix by

$$\langle p_f| S |p_i\rangle = \langle p_f|p_i\rangle + 2\pi\delta(E_F-E_I)\mathcal{M} \tag{2.85}$$

which leads to the production cross-section, relating the rate of transition over the flux of the particles, requiring an integral over the momentum phase-space. This is

retrieved as:

$$\sigma = \frac{1}{\mathcal{F}}\left[\prod_{f=1}^{n_f}\int \frac{d^3p_f}{(2\pi)^3(2E_f)}\overline{|\mathcal{M}|}^2(2\pi)^4\delta^4(\sum_{f=1}^{n_f}p_f - p_1 - p_2)\right] \tag{2.86}$$

where $\mathcal{F} = 4E_aE_b|v_a^z - v_b^z|$ is the flux factor, a function of the incoming particles energies E_a, E_b and velocities v_a, v_b in the z beam direction.

2.4.2 Luminosity

The rate at which events occur for a given process R is defined in terms of the number of events N per unit time t, as

$$R = \frac{dN}{dt}, \quad R = \sigma\mathcal{L} \tag{2.87}$$

where σ is the production cross section (in barns) of that particular interaction at a given energy [57]. The luminosity (in inverse barns) of a collider, $\mathcal{L}$, relates to the number of particles crossing a collision region per unit area per unit time. This luminosity for two beams containing n_1 and n_2 particles respectively, at frequency f across a collision's effective area A is

$$\mathcal{L} = f\frac{n_1n_2}{A} = f\frac{n_1n_2}{4\pi\cdot dx\cdot dy} \tag{2.88}$$

The total number of events is then expressed in terms of the integrated luminosity:

$$N = \sigma\int Ldt. \tag{2.89}$$

2.4.3 Rapidity and Pseudo-rapidity

Rapidity, y, is defined as

$$y = \frac{1}{2}\ln\left(\frac{E + p_zc}{E - p_zc}\right), \tag{2.90}$$

which is related to the angle between the xy plane and the direction of the product of a collision. Rapidity falls to zero when the particle is close to transverse to the beam axis, and tends towards ∞ when the particle trajectory is close to the beam axis. This variable is essential for the highly relativistic regime, since it is invariant with respect to a Lorentz boost along the z–axis [67]. However, for highly energetic particles, it is difficult to measure both the energy and the total momentum to high precision.

We can write rapidity as

$$y = \frac{1}{2}ln\left(\frac{(p^2c^2 + m^2c^4)^{1/2} + p_zc}{(p^2c^2 + m^2c^4)^{1/2} - p_zc}\right) \tag{2.91}$$

and for highly relativistic particle, $pc \gg mc^2$. Therefore, pc terms can be factored out, and using binomial expansion along with assuming that the trajectory angle relative to the beam pipe is small ($p_z/p = cos\theta$), we obtain the much easier to measure pseudo-rapidity, which is defined as

$$\eta = -\ln\left(\tan\left(\frac{\theta}{2}\right)\right), \tag{2.92}$$

which gives the angle of a particle relative to the beam axis. From this, one can see that for highly relativistic particles $y \simeq \eta$, making this observable a good approximation to rapidity. The observable ΔR for angular separation between two particles is related to this by

$$\Delta R = \sqrt{(\Delta\eta)^2 + (\Delta\phi)^2}. \tag{2.93}$$

2.5 Collider Phenomenology and Hadron Physics

Here it is required to make the connection between the hard partonic level of interactions, to the soft, hadronic physics. The previously defined perturbative QCD framework, while it still holds for leptons and non colour-charged gauge bosons, is only valid in short-distance interactions of quarks and gluons. Once a large enough distance is considered, the QCD running coupling diverges, and the strong force between partons becomes large, meaning perturbation theory is no longer valid in this regime. This is known as the confinement regime [68], due to quarks never appearing as isolated objects, instead staying confined with one another. We can define quarks in the fundamental representation, 3 of flavor $SU(3)$, and antiquarks in the complex conjugate representation $\overline{3}$. Quarks are only observed as bound, net-colourless states called hadrons: $3 \otimes \overline{3}$ (decomposed to singlet and octet $1 \oplus 8$), named mesons or $3 \otimes 3 \otimes 3$ (decomposed to $1 \oplus 8 \oplus 8 \oplus 10$), named baryons.

Hadronisation then defines the process where the coloured partons cluster into jets of hadrons, photons or leptons, with no colour charges present in the final stage. The process of hadronisation is thus essential for colliders, as partons assemble together to form observable hadrons in the detectors, for which colour is no longer a factor. Examples of various hadrons and their properties are given in Table 2.2. Linear confinement gives rise to the string model [70], used to interpret the process of hadronisation, or fragmentation, as discussed later.

Baryon	Quark Content	Spin	Isospin	I_3	Mass (MeV/c^2)
p	uud	1/2	1/2	+1/2	938
n	udd	1/2	1/2	−1/2	940
Δ^{++}	uuu	3/2	3/2	+3/2	1232
Δ^{+}	uud	3/2	3/2	+1/2	1232
Δ^{0}	udd	3/2	3/2	−1/2	1232
Δ^{-}	ddd	3/2	3/2	−3/2	1232
Σ^{+}	uus	1/2	1	+1	1189
Σ^{0}	uds	1/2	1	0	1193
Σ^{-}	dds	1/2	1	−1	1197
Meson	Quark Content	Spin	Isospin	I_3	Mass (MeV/c^2)
π^{+}	$u\bar{d}$	0	1	+1	140
π^{0}	$\frac{1}{\sqrt{2}}(u\bar{u}-d\bar{d})$	0	1	0	135
π^{-}	$d\bar{u}$	0	1	−1	140
ρ^{+}	$u\bar{d}$	1	1	+1	775
ρ^{0}	$\frac{1}{\sqrt{2}}(u\bar{u}-d\bar{d})$	1	1	0	775
ρ^{-}	$d\bar{u}$	1	1	−1	775
ω	$\frac{1}{\sqrt{2}}(u\bar{u}+d\bar{d})$	1	0	0	782
K^{+}	$u\bar{s}$	0	1/2	+1/2	494
K^{0}	$d\bar{s}$	0	1/2	−1/2	498
$\overline{K^{0}}$	$s\bar{d}$	0	1/2	−1/2	494
K^{-}	$s\bar{u}$	0	1/2	−1/2	495

TABLE 2.2: Examples of baryons and mesons with constituent u, d, s quarks and $\overline{u}$, $\overline{d}$ and $\bar{s}$ antiquarks [69].

2.5.1 Parton Distribution Functions (PDF)

PDFs aim to parametrise the hadrons' non-perturbative interactions via the perturbative, partonic cross section. Within high energy proton collisions, the partonic interactions considers the protons constituent valence quarks, sea quarks and gluons, which requires an analytical connection to the hadronic level interaction. The equation that links the hard scattering parton level's squared centre of mass energy $\hat{s}$ with the hadronic squared centre of mass energy s, by parton energy fractions x_1,x_2 is given by

$$\hat{s} = x_1 x_2 s. \tag{2.94}$$

To describe the probability distribution of a certain parton a, with energy fraction x, residing within the hadron beam particle A, the PDF $f_a^A(x, Q^2)$ is used. It is also dependent on Q^2, the momentum transfer for the hard (high energy) scattering process. This functional dependence as energy scales reach the bare values is understood as follows: while low energy Q parton interactions are done mostly by the parton and cloud quarks or gluons surrounding them, with some fraction of the total available momentum, higher energy Q interactions have the bare partons themselves possess this momentum.

PDFs are key for simulating interactions that occur in colliders, and many groups have made available functions for modeling these distributions, based on existing data. Fig.2.3 shows the NNPDF3.0 PDF used in MadGraph [71], its valence quark, sea quark and gluon content varying in probability distributions for two energy scales. Sea quarks such as charm and strange quarks posses a smaller fraction of the total

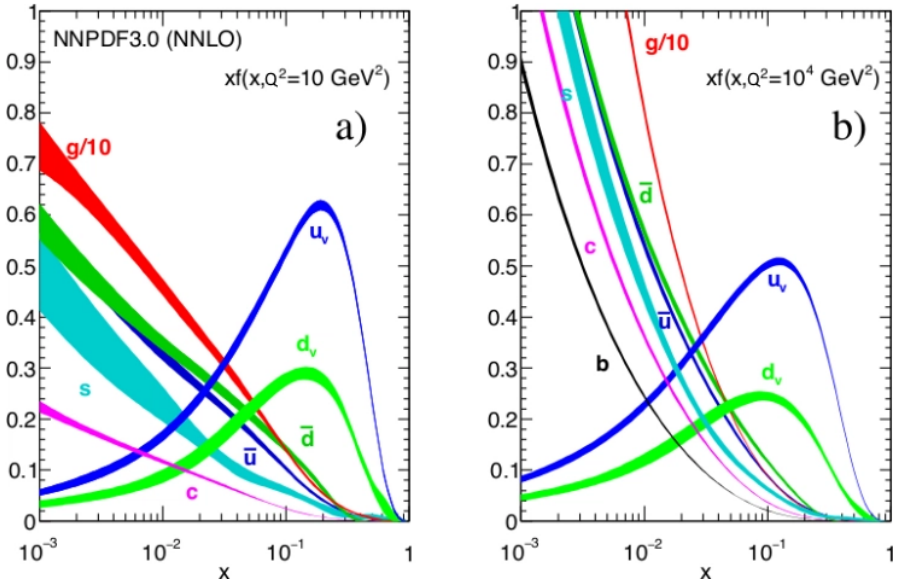

FIGURE 2.3: PDF analysis plots for NNPDF3.0 from the 2016 PDG review. [69]

proton's energy than the valence up or down quarks. The gluons usually take up the lower half of the protons overall momentum.

Even fundamental particles such as the electron have PDF descriptions, useful for studying aspects of e^+e- collisions. These give the probability that the electron interacting in the hard process will keep the energy fraction x of the original process. The rest of this fraction would then contribute to some initial state photon radiation. In this sense, the electron can contain a photon.

2.5.2 Hadronic Cross section

It is required to integrate over the PDFs of each incoming beam and the final state momentum of the process,

$$\sigma(A,B \to C) = \sum_{a,b} \int \hat{\sigma}(a,b \to C) f_{a/A}(x_1, Q^2) f_{b/B}(x_2, Q^2) dx_1 dx_2 \tag{2.95}$$

for two hadrons, A, B to final state C, where $f_{a/A}$ and $f_{b/B}$ are the PDFs (probabilities of emitting a from A and b from B), integrated over the partons 1 and 2. This is the QCD factorisation theorem [72] allowing for the cross section to be calculated from contributing parton sub-processes, interacting via QCD.

Taking the Drell-Yan example of a $q, \overline{q} \to \ell, \ell$ scattering process, the leading order differential cross section, for quark and antiquark PDFs $f_q(x_i, Q^2)$ and $f_{\overline{q}}(x_j, Q^2)$ respectively, for this process is

$$\frac{d\sigma(p, p \to \ell, \ell)}{dQ^2} = \sum_{q,\overline{q}} \int \int f_q(x_1, Q^2) f_{\overline{q}}(x_2, Q^2) + f_{\overline{q}}(x_1, Q^2) f_q(x_2, Q^2) dx_1 dx_2 \frac{d\hat{\sigma}(q, \overline{q} \to \ell\ell)}{dQ^2}. \tag{2.96}$$

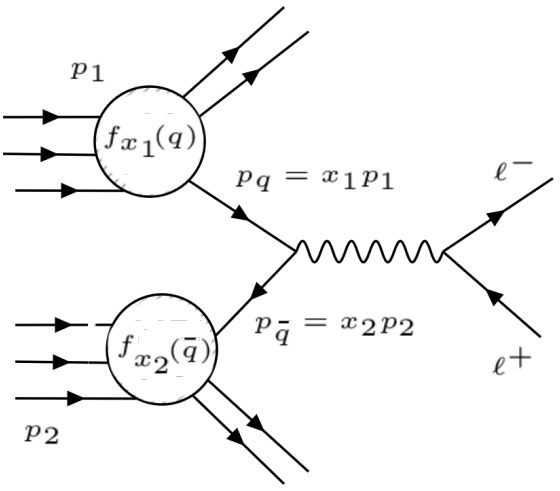

FIGURE 2.4: The schematic diagram of the simple Drell-Yan process $p, p \to \ell, \ell$, and partonic subprocess $q, \overline{q} \to \ell, \ell$
[73]

A diagram for such a process is depicted in Fig.2.4. The parton-level cross-section, given by $\hat{\sigma}$ for the Drell-Yan production of two leptons via a virtual mediating photon is a well known result which can be calculated from Eq. 2.94 to give

$$\hat{\sigma} = \frac{4\pi\alpha^2}{9\hat{s}} e_q^2 \tag{2.97}$$

where the factor of $\frac{1}{9}$ accounts for the possibility of different colour combination of quarks involved in the process. By taking the derivative with respect to the energy scale Q^2, this leads to the differential cross section

$$\frac{d\hat{\sigma}}{dQ^2} = \frac{4\pi\alpha^2}{9Q^2} e_q^2 \delta(Q^2 - \hat{s}). \tag{2.98}$$

Looking back at the cross-section equation, now in terms of PDFs as a function of the previously defined factorisation scale, μ_F, gives

$$\sigma(p_A, p_B \to C) = \sum_{a,b} \int \hat{\sigma}(a, b \to C) f_{a/A}(x_1, \mu_F) f_{b/B}(x_2, \mu_F) dx_1 dx_2. \tag{2.99}$$

Additional divergences can be introduced when initial state radiations are taken into account as discussed later. These can originate either from the PDF or an additional hard scattering process and, when aligned collinearly with the initial state, will cause divergences similarly to those seen above. This can be partially solved by absorbing certain terms that give these infinities into a corresponding PDF. Some Infrared radiation (IR) singularities can then be cancelled by this PDF renormalisation, though this does not apply in all cases. [74]

2.5.3 Multiple-Parton Interactions (MPI)

When considering hadron–hadron collisions, it may not be sufficient to only consider the presence of a single hard interaction per event. This is because, unlike e^+e^- collisions, the incoming protons do not consist of only one parton, and one must account for the possibility of multiple interactions between these beams, consisting of multiple constituent partons [75]. This factor would result, not only in additional scattering processes between two separate partons per beam, but also individual partons scattering against multiple different partons originating from the one opposite beam.

There is a limit that must be applied when considering these additional QCD scattering processes, as they become divergent as $p_T \to 0$. Gluons exchanged in this low p_T phase space cannot resolve the specific colour charge of the colliding hadrons, due to its large transverse wave function, and will instead couple to the average of the colour charge. However, this vanishes for $p_T \to 0$, causing this divergence. This is an example of a colour coherence effect, and to combat it, this divergent phase-space region should be cut, by introducing some $p_{T_{min}}$ on the final state.

As the cross section for QCD $2 \to 2$ scattering falls drastically with increasing p_T, MPIs [75] are usually dominant in the low p_T region. The impact of the MPI is rather large for low-p_T jets, contributing a higher fraction of events, while impact is negligible for higher p_T jets. This is because these additional collisions result in jets losing energy, and so not many high p_T jets come from MPIs. There is still a small probability of MPIs in high p_T events, near the $p_{T_{min}}$ cut-off scale, however. Below this scale, one assumes these contributions are damped to negligible effects.

MPIs are still not comprehensibly understood and Monte Carlo (MC) generators rely on models to approximate these complex mechanics and their effects. For example, the correlation between subsequent scatterings momenta, colour charges and quark flavour are yet to be absolutely defined. Nor have the MPI probability differences between events that do or do not contain hard interactions been defined [76].

2.5.4 Initial-State Radiation (ISR) and Final-State Radiation (FSR)

The colour and charge of particles in both in initial and final state of a scattering process will contribute to some higher-order effects, requiring significant corrections to account for the increased number of final-state topologies and the resulting cross section [77]. The largest factor comes from the addition of gluon and photon radiation, which will increase the overall energy of the process, and ultimately increase the number of particles in the final state. As opposed to being performed explicitly, the perturbative corrections must be modelled, traditionally carried out via two methods [76] detailed below.

2.5.5 Modelling via Matrix elements

When modelling using matrix elements [78], leading order (LO) calculation of the Feynman diagrams, derived from the perturbative expansion of the S-matrix, to give the QCD amplitudes and phases for a given order of α_s. However, as one reaches higher orders of α_s, calculations become particularly difficult and computationally expensive, as more loop diagrams are introduced. As a result, only a few orders above the leading have currently been calculated, leaving certain soft phase-spaces excluded in event generation of this kind.

2.5.6 Modelling via Parton showers

Modelling via partonic showers [79] takes a probabilistic approach to branchings of the partons to its daughter partons, each receiving a fraction of the original energy from its mother. This is parameterised by the Altarelli-Parisi splitting functions $P(z)$, for which one daughter receives fraction z or the original energy, while the other receives $1 - z$. Each daughter could then further split and branch off, given enough energy in their respective fraction.

While the total effects of the showers can be incorporated into the parton distribution functions inclusively, one still requires a method for reconstruction of individual showers to include their exclusive effects. This is done by tracing backwards from the hard scattering process.

From the hard interaction energy scale Q^2, FSR and ISR are time-evolved forwards and backwards respectively. The partons of final-state showers have $m^2 = E^2 - p^2 \geq 0$ and are thus considered time-like. Meanwhile, the initial-state showers are space-like, with $m^2 = E^2 - p^2 \leq 0$. However, there is the possibility for branchings from these showers to be on the mass shell or virtual and thus treated as time-like. This

showering process then accounts for the higher order effects, resumming the leading-log divergences coming from the perturbative expansion.

This is an adequate approximation for radiation from collinear and soft partons, however, for sufficiently high p_T, this showering method can not fully construct the original kinematics of the hard process. This is because the effects of ISR and FSR inherently displace the original kinematics for the original process, leading to disagreements with the initially chosen variables. The original picture of two head on, high p_T beams is replaced with a more complex topology. For the same reason, this is a bad approximation for resolving particularly wide-angled partons in the final state [80].

2.5.7 Beam Remnants and The Underlying Event

For individual parton-parton interactions, beam remnants [81] would come from the remaining beam energy, the fraction which is not accounted for by the ISR algorithm to reconstruct the shower. This is to say that the hard interacting parton and its ISR does not account for the entire energy of the original hadron, instead leaving a hadron remnant. The remnant of the beam possesses a colour-connection to the original hard process. For example, an up quark from a proton-proton collision would result in a remnant in the form of a up-down quark pair, with antitriplet colour charge. A more complex example would be the gluon, with a remnant of an up-up-down quark system, that is, a proton of eight colour charge state. As a results, non-trivial additional degrees of freedom are obtained: the relative transverse momentum between pairs of remnant objects and the division of energy across them. In fact, even e^+e^- collisions produce these beam remnants, due to photon interactions. These can lead to quark pair production, with resulting e^+ and e^- beam remnants. Additionally, when considering PDF's for electrons, energy that is not utilised by the hard process and is left over would be taken as part of the initial-state photon radiation photon, which is then considered a beam remnant.

A primordial transverse momentum k_T is defined for the initiator partons of these beam remnants, to account for quark movement within the original hadronic particle, which would then effect the transverse momentum distributions of its decay products. The hadron remnant is also assumed to take in the recoil of this. Fragmentation of these remnants would also give additional decay products in the final state.

This then leads to contributions in the form of the underlying event [82], defined as the combination of these beam remnants and ISR, identified via soft final state products. As these decay products are usually produced close to the beam axis, it is easily missed by the detectors, making it difficult to use for reconstruction. This is why instead, transverse properties of the final state are used for analysis, such as p_T [76].

2.5.8 String Fragmentation

The fundamental concept behind the Lund string model [70] concerns the mathematical construction of a one-dimensional string to describe the confining colour field acting between colour-charged partons. One defines this colour flux tube connecting two partons coming from the same production vertex such that, as the quark and anti-quark pair begin to separate, this string stretches. This stretching causes the colour dipole field connecting the pair to linearly increase in energy, proportional to their separation distance. After enough potential energy has built up, the string can snap, breaking to produce two new quark-antiquark pairs via quantum tunnelling. Indeed, additional fragmentations will proceed, given a sufficiently heavy invariant mass of a quark-antiquark pair has been already produced, and will continue to do so until only hadrons remain in the final state. This is one of the defining characteristics of the Lund string model. Kinks can also form on the connecting string, due to the production of gluons in the parton showering. The Lund string model process is depicted pictorially in Fig. 2.5.

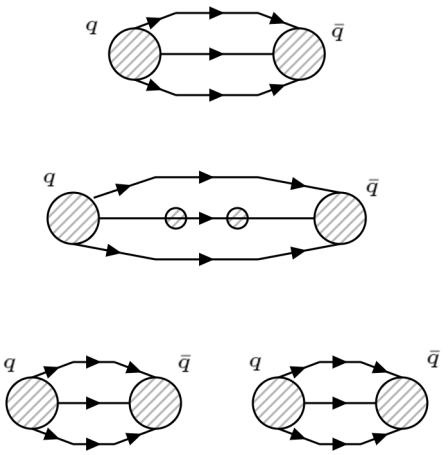

FIGURE 2.5: Evolution of a quark-antiquark pair in the Lund string model, as it splits to form a second pair of quark-antiquark. [83]

2.5.9 Independent Fragmentation

An alternative model is Independent Fragmentation. As a quark is produced in a hard interaction, this quark jet then splits into two collinear objects: a hadron of quark-antiquark pair and a remainder quark jet. This is an iterative process, as with String Fragmentation, leading to continuously produced successive hadrons. This then justifies clustering on quark antiquark pairs and then decaying these clusters into further hadrons.

2.5.10 Cluster fragmentation

This model, as used by HERWIG [84], does not produce showers from gluons, only from quark-antiquark pairs. It is found that the energy scale of the original hard scattering process does not have an effect on the colour-connected parton's invariant mass distributions after showering. A key difference, as seen in Fig.2.6, is the gluon behaviour which, after showering, now undergo non-perturbative splitting into colour-singlet quark-antiquark pairs before being clustered. Models of this type have also implemented colour recombination, where quark antiquark pairs which are not colour connected can still form colour-singlet states. However, this addition to the model has yet to improve agreement with existing data [85]. In addition, the model encounters difficulty when trying to decay particularly heavy clusters, leading to massive hadrons and quarks being overproduced.

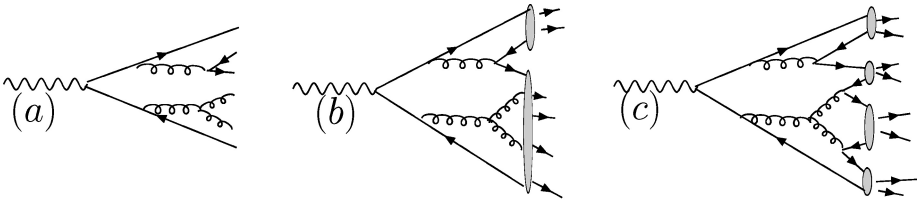

Mangano ML, Stelzer TJ. 2005.
Annu. Rev. Nucl. Part. Sci. 55:555–88

FIGURE 2.6: Illustration of the different fragmentation models on the radiation pattern (a) in the string fragmentation case (b) and cluster hadronisation case (c) [85].

2.5.11 Jet Algorithms

The term jet is ascribed to the cone of particles, final state objects resulting from the hadronisation of an individual quark, which must then be traced back to determine the properties of mother particles to understand the underlying process [86]. Given the vast number of collisions and hadrons in the final states at colliders, it would be impossible to treat each observable separately. It would be more sensible to analyse the cluster of hadrons found in the detector, as collimated jets. These leave deposits of energy in the hadronic calorimeter (HCAL), which is then used to classify the number of jets in a given process. An increasing number of hard partons are produced as higher orders of perturbation theory are achieved, in turn leading to more showers. For every hard parton produced in the scattering interaction, with well defined directions, the subsequent showering and soft or collinear radiation emissions will affect the final state observed. The additional hadronisation corrections also leads to smearing out of the parton's directional component. This gives a jet from the radiation with some smearing effects applied.

Various jet algorithms are used to reconstruct these emissions by reversing the partonic fragmentation that occurs, and will be discussed. The substructure of these jets consists of complex QCD constituents, requiring sophisticated algorithms to fully approximate and cluster hadrons from the final state into jets. Jets can contain multiple particles, and so the mapping between final state hadrons and jets 4-momenta is not necessarily one-to-one.

Cluster algorithms [87] work by implementing an iterative pair-wise clustering on the fundamental objects, in order to build these up to the compound final state objects. The observable used must be IR safe, unchanged by additional components of soft or collinear particles. This is to compare theory predictions with experimental data, and must be defined equally in both cases. A successful example includes using the variables d_{ij} for the distance between two particles i,j and $d_{i,z}$ for the distance between i and the beam axis z. The general algorithm procedure is then the following: the first step is to obtain a measurement for d_{ij} and d_{iz} per particle pair. Then calculate the minimum of this set of variables. If the smaller of the two is $d_{i,z}$, then i is sufficiently unique from j, and i is defined as a final state jet. If d_{ij} is smaller instead, i and j are merged to form a single jet. This process is repeated until all particles have been accounted for in this way. The anti-k_T algorithm for example uses the variables $d_{i,z} = (p_{Ti}^2)^n$, $d_{i,j} = min[(p_{Ti}^2)^n, (p_{Ti}^2)^n]\frac{\Delta R_{ij}}{R}$, where $\Delta R_{i,j}$ is the jet radius, defined as the rapidity-ϕ (y, ϕ) plane distance between i, j, and $n = -1$. For the k_T algorithm, $n = 1$ is used. The performance of these algorithms is illustrated by Fig 2.7.

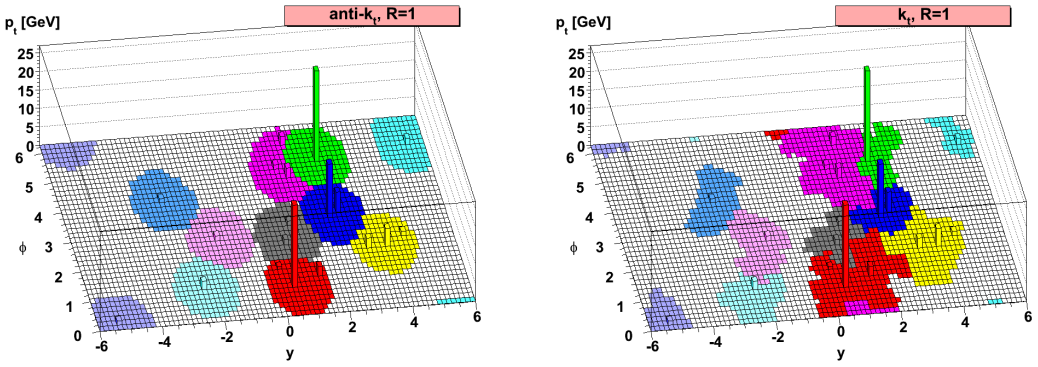

FIGURE 2.7: anti-k_T(left) and k_T(right) jet algorithms [88].

2.5.12 Unfolding and The Response Matrix

The process of unfolding is crucial in correcting for experimental distortion effects. The goal is to estimate the truth-level observables as they would be measured by an ideal detector. The most basic method for unfolding in ATLAS is applying bin-by-bin corrections factors, derived from comparison between MC truth-level and reconstructed events.

For a given observable (p_T, for example) we define D_i as the observed number of detector events in bin i. D_i follows a Poisson distribution, with mean R_i. The correction factor C_i for bin i is then related to this by

$$C_i = \frac{T_i}{R_i} \tag{2.100}$$

where T_i is the expected number of events at truth-level from MC and R_i is the is the expected number of events after selection of events that pass triggers, jet reconstruction, primary vertex requirements, jet quality criteria and so on [89]. After bin-by-bin correction on the truth level distribution, the result for bin i is U_i such that

$$U_i = C_i \cdot D_i \tag{2.101}$$

for an estimator of T_i [89]. This procedure allows for results which are independent from detector and reconstruction effects. This also then facilitates better tuning of MC generators, as it helps its developers to closer study a more pure representation of a specific sample without dependence on detector effects [90].

The response matrix can be defined when observing continuous variables. If we define $f_t(x_t)$ as the distribution of true values, $f_m(x_m)$ as distribution of measured values and $f_b(x_m)$ as the distribution of background, we define the response function

as the probability to observe x_m given a particular x_t such that

$$\mathcal{R}(x_m|x_t) = r(x_m|x_t) \times \varepsilon(x_t) \tag{2.102}$$

where $r(x_m|x_t)$ accounts for the smearing effects and $\epsilon(x_t)$ describes the efficiency. The response matrix then shows the correlation between detector-level and particle-level events for a given observable. An element of the matrix is defined such that

$$\mathcal{R}_{ij} = Prob(observed\ in\ bin\ i|true\ in\ bin\ j). \tag{2.103}$$

The unfolding procedure can also be performed by inverting the response matrix, where the covariant matrix is given by

$$U = \mathcal{R}^{-1}V(\mathcal{R}^{-1})^T \tag{2.104}$$

for $V_{i,j} = cov[n_i, n_j]$ where $\overline{n}$ is the observed sample data histogram $\overline{n} = (n_1, ..., n_N)$. However, this method is prone to create large correlation between bins, in addition to smearing out fine structure and applying additional unwanted structure [91].

Bayesian Unfolding is another method, applied in an iterative way. This is initiated by choosing a prior distribution, such that the response matrix is given by

$$\mathcal{R}_{ji} = P(E_j|C_i, I) \tag{2.105}$$

where I defines the prior knowledge about probabilities of the causes C_i. Using Bayes' theorem, we have

$$P(C_i|E_j, I) = \frac{P(E_j|C_i, I) \cdot (P(C_i|I))}{\sum_{k=1}^{M} P(E_j|C_k, I) \cdot P(C_k|I)} \tag{2.106}$$

which can be written as

$$P(C_i|E_j, I) = \frac{R_{ji} \cdot P(C_i|I)}{\sum_{k=1}^{M} R_{jk} \cdot P(C_k|I)}. \tag{2.107}$$

The estimator for the number of true events in bin i, given that we measure n_j events in bin j is given by

$$\mu_i|_{n_j} = \frac{P(C_i|E_j, I) \cdot n_j}{\varepsilon_i} \tag{2.108}$$

and by summing over all observed bins, we have

$$\mu_i|_{\overline{n}} = \frac{1}{\varepsilon_i} \sum_{j=1}^{N} P(C_i|E_j, I) \cdot n_j \tag{2.109}$$

and therefore the efficiency is defined as

$$\varepsilon_i = \sum_{j=1}^{N} P(E_j|C_i, I) = \sum_{j=1}^{N} R_{ji} \tag{2.110}$$

where the matrix is derived from MC simulations. In the iterative process, the prior is then updated according to the measured values and iterated upon [91]. This is done by apply correction to each bin of the initial MC-generated distribution, tuned to data such that it can be considered a reasonable starting point. New correction factors are then generated from the corrected spectrum of the previous iteration. This is updated on each iteration, improving the measurement by scaling it closer to the truth-level distribution. A convergence criterion χ^2 is defined to determine the suitable number of iterations, as

$$\frac{\chi^2}{N_{bins}} < 1 \tag{2.111}$$

where

$$\chi^2 = \sum_{i=1}^{N_{bins}} \left(\frac{n^{i,current} - n^{i,previous}}{\sqrt{n^{i,previous}}} \right)^2 \tag{2.112}$$

such that the iteration is stopped when the current unfolded distribution $n^{i,current}$ is statistically consistent with the previous unfolded distribution $n^{i,previous}$ [89].

2.6 Running Coupling and Higher-Order Corrections

The running couplings, α_i, of the SM fields corresponding to the three fundamental interactions are shown in Fig.2.8, demonstrating their dependence on the energy scale at which the interaction takes place [92]. The general formula for running coupling α_i can be written as

$$\alpha_i = \frac{g_i^2}{4\pi} \tag{2.113}$$

where coupling g_i corresponds to e for EM coupling, g_W for weak coupling or g_S for strong coupling[1]. A crucial difference between QCD and QED is the self-interaction term for the gluon, brought on by the non-vanishing structure functions for a non-Abelian gauge theory. This is then the source of the running of the strong coupling [93], in the opposite direction to QED.

Of particular interest is the Callan–Symanzik β function, which describes the rate of change of the running coupling as a function of the renormalisation scale [94], demonstrating the running coupling feature present in QFT. The function itself was formulated in the 1970's by both Curtis Callan and Kurt Symanzik on separate occasions [95] and takes different forms in QCD as a consequence of the contributions

[1]The α_B as seen in Fig. 2.8 refers to $U(1)_Y$ hypercharge coupling associated with B boson, which mixes with W^i after EWSB to give the photon, $W^{\pm}$ and Z bosons (see section 2.52).

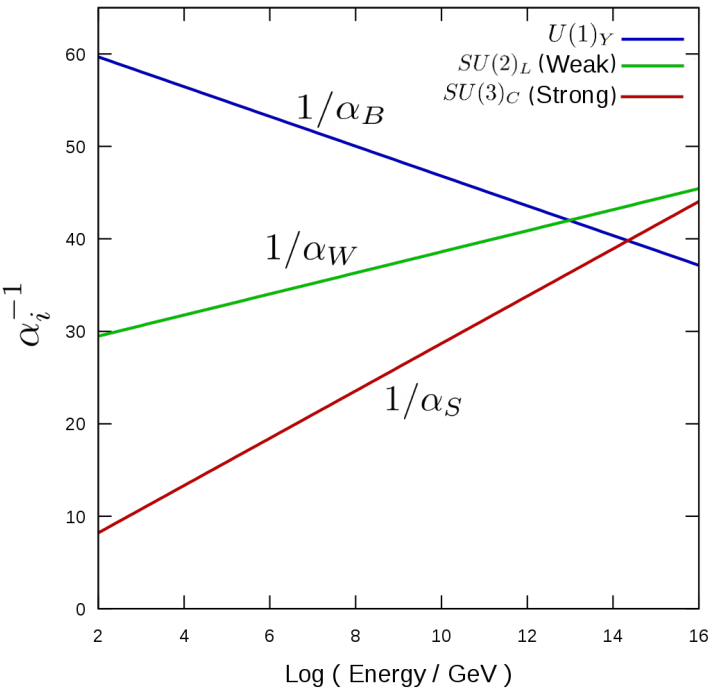

FIGURE 2.8: Dependence of the (inverse) running coupling with energy scale [92].

from fermions and scalars, due to how the counter-terms cancel one another in computation.

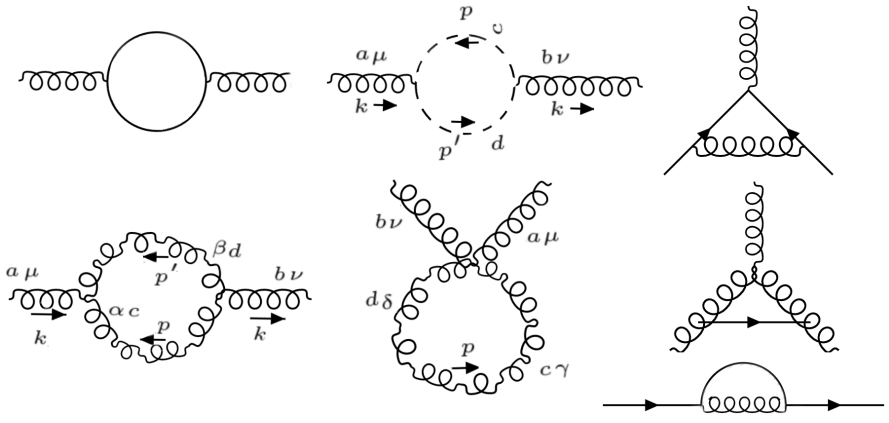

FIGURE 2.9: QCD self-energy gluon one-loop corrections.

Diagrams in Fig.2.9 show the one-loop level corrections to the gluon propagator. These self-interactions will then result in this running feature. The β-function comes from the renormalisation group equation defined as

$$\beta(\alpha) = \mu^2 \frac{\partial \alpha}{\partial \mu^2} \tag{2.114}$$

$$= -(b_0\alpha^2 + b_1\alpha^3 + b_2\alpha^4 + \dots). \tag{2.115}$$

The negative aspect of this function is a demonstration of asymptotic freedom present in strong interactions, where the coupling is weaker for larger transfer momentum involved in the process. The concept of confinement of the quarks and gluons is then also observed at low energy scales, as the strong coupling between them increases. Because of this, at high enough energy, perturbative QCD calculations can then be performed, as the partons act as quasi-free particles.

One of the forms of the β-function for n_f quark flavours, at 1-loop, can be given in terms of the renormalisation functions Z by the computation

$$\beta = g\mu\frac{\partial}{\partial\mu}(Z_\psi - Z_{g\psi} + \frac{1}{2}Z_A) \tag{2.116}$$

or, in terms of the counter-terms δ,

$$\beta = 2g(\frac{\partial}{\partial(log(\mu^2))}(\delta_\psi - \delta_{g\psi} + \frac{1}{2}Z_A). \tag{2.117}$$

The function coefficients refer to the loop number, the 1-loop β-function coefficient for example is given by

$$b_0 = \frac{11C_A - 4n_f T_R}{12\pi} \tag{2.118}$$

where $C_A = 3$, and the 2-loop β-function coefficient is found to be

$$b_1 = \frac{17C_A^2 - n_f T_R 10(C_A + 6C_F)}{24\pi^2} \tag{2.119}$$

where $C_F = \frac{4}{3}$.

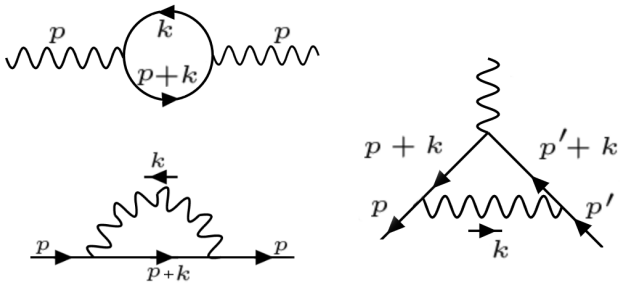

FIGURE 2.10: QED one-loop corrections.

QED provides the first coefficient of the β-function from loop corrections to the propagator as in Fig. 2.10, leading to

$$b_0 = -2Z_g = -\frac{1}{3\pi}, \tag{2.120}$$

$$\beta_{QED}(\alpha) = \frac{1}{3\pi}\alpha^2. \tag{2.121}$$

In contrast to QCD, this gives the property of stronger coupling as energy increases. Looking at all the contributions, the general $SU(N)$ non-Abelian gauge theory β function, including scalar and fermionic contributions, should be given by

$$\beta(g) = -\frac{g^3}{16\pi^2}(\frac{11}{3}n_c C_2(G) - \frac{4}{3}n_f C(r_f) - \frac{1}{3}n_s C(r_s)) \tag{2.122}$$

whereas the result for QCD was found to specifically take the form, for n_f flavours and n_s coloured scalar bosons,

$$\beta(g) = -\frac{g^3}{16\pi^2}(11 - \frac{2}{3}n_f - \frac{n_s}{3}). \tag{2.123}$$

It is clear that gluon loop corrections dominate over the quark loop ones. By looking at the general form of the β function Eq. 2.123, so long as there exists up to 6 flavours, this function will then remain negative and results in quark confinement at low energies. Considering just the b_0 term, and for a constant number of flavours, the solution to the β-function is found to decrease, with the form

$$\alpha(Q^2) = (b_0 \ln\left(\frac{Q^2}{\Lambda^2}\right)^{-1} \tag{2.124}$$

in terms of the energy scale Q and a non-perturbative 'divergence-scale parameter' Λ. A consequence of this running coupling is that the renormalised scale is dependent on the chosen energy scale of measurement. As demonstrated in Fig.2.11, this gives a coupling that is not constant, but in fact evolves as the energy changes.

As the energy scale is decreased, the coupling then becomes large, and so the assumption of perturbation theory is no longer valid. This is also seen in the plot for coupling as a function of energy scale. As energy increases, the quarks coupling is feeble and they become asymptotically free, where perturbation theory does apply. For very low energy, confinement of the quarks occurs and computation must be done non-perturbatively.

2.6.1 Divergences and Renormalisation

The existence of loops in Feynman diagrams introduced beyond LO, due to the presence of virtual particles, requires integration over all possible unconstrained loop momenta, and momentum conservation alone is no longer sufficient.

The example one-loop correction to the photon from the diagram in Fig.2.12 is given by

$$(ie)^2 \int \frac{d^4k}{(2\pi)^4} \frac{Tr[\gamma_\mu(\not{k} + \not{p} + m)\gamma_\nu(\not{k} + m)]}{(k^2 - m^2)((k+p)^2 - m^2)}. \tag{2.125}$$

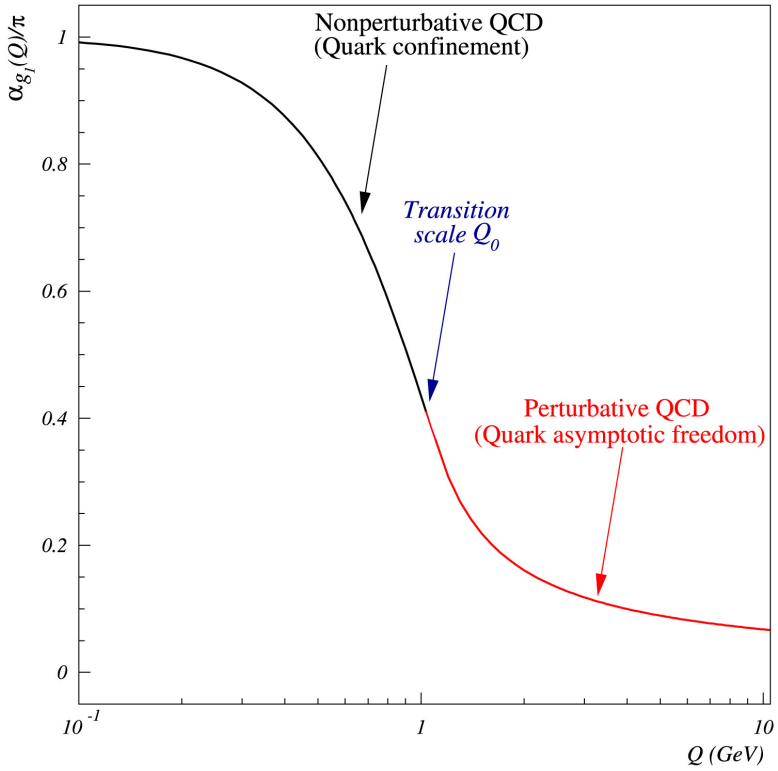

FIGURE 2.11: The strong coupling strength as a function of Q scale [93].

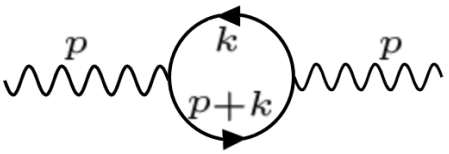

FIGURE 2.12: One-loop photon Feynman diagram.

As a result, integrals can diverge, for which powers in the numerator cause it to inflate faster than the denominator. The process of power counting is used to determine the degrees of divergence, D, by taking the general integral form

$$\int \frac{d^d k}{(2\pi)^4} \frac{N(k^i)}{M(k^j)}, \tag{2.126}$$

such that D is defined as

$$D = d + (i) - (j). \tag{2.127}$$

While logarithmic divergences occur for $D = 0$, loop momentum explodes when Ultra-Violet (UV) divergences occur for $D \geq 0$. These UV divergences occur as poles in the form of $1/\epsilon$ and need to be cancelled out by the renormalisation functions. The process of renormalisation to counter divergences from higher-loop corrections is achieved by a redefinition of terms in the Lagrangian, to absorb the unwanted infinities. Fields and couplings are rescaled by renormalisation constants Z, to give

bare quantities such as

$$\phi_0 = Z_\phi \phi_R \tag{2.128}$$

in terms of a renormalised quantity, ϕ_R field in this case. The QCD couplings and fields are rescaled as

$$\psi_0 = Z_2^{\frac{1}{2}} \psi \tag{2.129}$$

$$G_0^\mu = Z_3^{\frac{1}{2}} G^\mu \tag{2.130}$$

$$\eta_0 = Z_\eta^{\frac{1}{2}} \eta \tag{2.131}$$

$$g_{s,0}^2 = Z_g g_s^2. \tag{2.132}$$

The bare Lagrangian, neglecting the mass terms, can then be separated into two parts: the finite renormalised part and the counter terms. By only considering $\mathcal{L}_R$, the UV divergences are ignored in $\mathcal{L}_{counter}$ as follows:

$$\mathcal{L}_0 = \mathcal{L}_R + \mathcal{L}_{counter} \tag{2.133}$$

$$= \left(-\frac{1}{4} G^{a\mu\nu} G^a_{\mu\nu} + \overline{\psi}_i i \not{D}_{ij} \psi_j \right) \tag{2.134}$$

$$+ \Bigg((Z_2 - 1) \overline{\psi}_i i \not{\partial} \psi_i + g (Z_g Z_2 Z_3^{\frac{1}{2}} - 1) \overline{\psi}_i \not{G}^a T^a \psi_i$$

$$- \frac{1}{4} (Z_3 - 1)(\partial_\mu G^a_\nu - \partial_\nu G^a_\mu)^2 - g (Z_g Z_3^{\frac{1}{2}} - 1) \partial_\mu G^a_\nu \varepsilon^{abc} G_{\mu,b} G_{\nu,c}$$

$$+ \frac{1}{4} g^2 (Z_g^2 Z_3^2 - 1)(\varepsilon^{abc} G_{\mu,b} G_{\nu,c})^2 \Bigg).$$

This requires a choice of renormalisation scheme to define how the Lagrangian is split. An example is the Minimal Subtraction (MS) scheme, for which $\mathcal{L}_{counter}$ is purely divergent, while all the finite terms are instead included in $\mathcal{L}_R$. To prevent reaching momenta of large energy, a cut-off parameter can be introduced, and parametrise the divergence. Dimensional regularisation takes $d = 4 - 2\varepsilon$, leading to the requirement of an unphysical renormalisation energy scale μ_R to maintain dimensionality d of the bare coupling. This gives a dimensionless coupling of the form

$$\mu^{\frac{4-d}{2}} g_R(\mu_R) = \mu^\varepsilon g_R(\mu_R). \tag{2.135}$$

The renormalised coupling in QCD, as a function of the renormalisation scale μ_R^2, is $\alpha(\mu_R^2)$.

2.6.2 IR Soft and Collinear Limits

The infrared (IR) singularities refer to low energy divergences, which can occur in real emissions for two cases. One case is the soft gluon limit where external gluon energy

tends to zero. The second case is the collinear limit, for which massless quarks emit collinear with each other, thus indistinguishable as an emission. Both cases will cause the propagator to diverge, as seen for a typical gluon emission diagram in Fig.2.13. This can be is written as

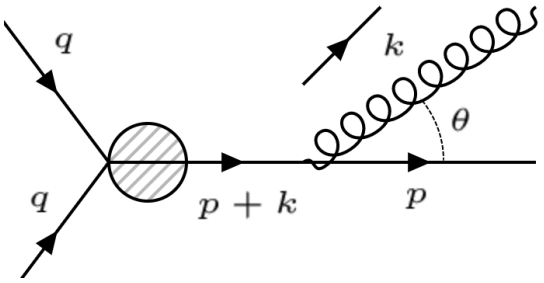

FIGURE 2.13: Feynman diagram for gluon emission, demonstrating where IR divergences can occur.

$$\frac{\not{p} + \not{k}}{(p^\mu + k^\mu)^2 + i0} = \frac{\not{p} + \not{k}}{p^\mu p_\mu + k^\mu k_\mu + p \cdot k + k \cdot p} \sim \frac{\not{p} + \not{k}}{2|p||k|(1 - \cos(\theta))}. \tag{2.136}$$

The denominator in Eq.2.136 causes divergences when it tends to zero, either in the soft gluon limit for $|k|$ tending to zero, or in the collinear limit where the angle θ between the quark and gluon tends to zero. IR divergences also arise from loop diagrams with infinitesimal internal momentum. Combining these with divergences from real emissions, the resultant contributing infinities must cancel in order to obtain a real result for a physical, 'IR-safe' observable.

The factorisation scale μ_F is the energy scale at which the perturbative hard scattering process is split from the soft hadronisation physics, as previously described.

2.6.3 Cross-sections at Higher Orders: NLO, NNLO

Processes beyond LO in coupling constant, that is, next-to-leading order (NLO) and next-to-next-to-leading order (NNLO) and so on, introduce new interaction diagrams with more degrees of freedom, as loops in the diagrams that must be integrated over in different ways. This depends on whether they pertain to real emissions, for which the phase space integral absorbs these increase in degrees of freedom as dimensions increase, or virtual loops, where all possible loop momenta need to be integrated over. For perturbative calculations, the partonic cross section is then expanded in the coupling constant

$$d\sigma = \sum \left(\frac{\alpha_s}{2\pi}\right)^n d\sigma^n = d\sigma_{LO} + \frac{\alpha_s}{2\pi} d\sigma_{NLO} + \left(\frac{\alpha_s}{2\pi}\right)^2 d\sigma_{NNLO} + ... \tag{2.137}$$

The NLO contributions for a QCD Drell-Yan process, for example are represented by

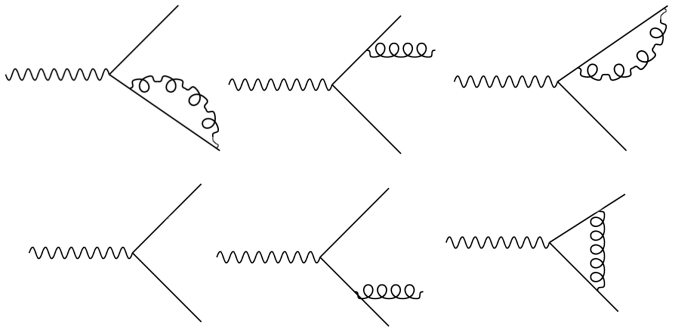

FIGURE 2.14: NLO contributions for a QCD Drell-Yan process [96–98].

Feynman diagrams in Fig.2.14. In terms of real and virtual contributions for NLO corrections, the perturbation cross section is given by

$$\sigma = \alpha_s^n(\sigma_{LO} + \alpha_s(\sigma^{real} + \sigma^{virt}) + O(\alpha_s^2)) \tag{2.138}$$

for Born matrix element $\mathcal{M}_{LO}$. The bremsstrahlung real radiation comes from particles with colour charge, contributing the matrix element $\mathcal{M}^{real}$ (containing IR divergences). In addition, the one-loop virtual matrix element contributes $\mathcal{M}^{virt}$ (containing both virtual IR and UV divergences). One can obtain the respective contributing cross sections by performing phase space integrals of these matrix elements, convoluted with the PDFs

$$\sigma_{LO} = \int_N d\sigma_{LO} = \int d\Phi_N \sum |\mathcal{M}_{LO}(k_1, k_2, p_1, ..., p_N)|^2 \times J_q^N(k_1, k_2, p_1, ..., p_N) \tag{2.139}$$

$$\sigma^{virt} = \int_N d\sigma^{virt} = \int d\Phi_N \sum 2\,\mathrm{Re}(\mathcal{M}_{LO}(k_1, k_2, p_1, ..., p_N) \times \mathcal{M}^{virt*}(k_1, k_2, p_1, ..., p_N) J_q^N(k_1, k_2, p_1, ..., p_N) \tag{2.140}$$

$$\sigma^{real} = \int_{N+1} d\sigma^{real} = \int d\Phi_{N+1} \sum |\mathcal{M}^{real}(k_1, k_2, p_1, ..., p_{N+1})|^2 \times J_q^{N+1}(k_1, k_2, p_1, ..., p_{N+1}) \tag{2.141}$$

for jet functions J_q which satisfy the IR safety conditions

$$\lim_{p_i \to 0} J_q^{N+1}(k_1, k_2, p_1, ...p_i, ..., p_{N+1}) = J_q^N(k_1, k_2, p_1, ..., p_{N+1}) \tag{2.142}$$

$$\lim_{p_i p_j} J_q^{N+1}(k_1, k_2, p_1, ..., p_j, ..., p_i, ..., p_N + 1) = J_q^N(k_1, k_2, p_1, ..., p_j + p_i, ..., p_{N+1}) \tag{2.143}$$

$$\lim_{p_i \to (1-x)k_1} J_q^{N+1}(k_1, k_2, p_1, ...p_i, ..., p_{N+1}) = J_q^N(xk_1, k_2, p_1, ..., p_{N+1}) \tag{2.144}$$

$$\lim_{p_i \to (1-x)k_2} J_q^{N+1}(k_1, k_2, p_1, ...p_i, ..., p_{N+1}) = J_q^N(k_1, xk_2, p_1, ..., p_{N+1}) \tag{2.145}$$

$$\lim_{p_i \cdot p_j \to 0} J_q^{N+1}(k_1, k_2, p_1, ..., p_j, ..., p_i, ..., p_{N+1}) = 0 \tag{2.146}$$

$$\lim_{k_{1,2} \cdot p_j \to 0} J_q^{N+1}(k_1, k_2, p_1, ..., p_j, ..., p_i, ..., p_{N+1}) = 0. \tag{2.147}$$

This property of IR safety means the previously stated effects of the soft and collinear limits that give IR divergences should not impact the observable quantities of the jets. These quantities are then considered IR safe, such as k_T and anti-k_T.

The phase space integral here includes summing over all possible final state momentum configurations and all possible helicities,

$$\int d\Phi_N = \sum \int dx_1 dx_2 f_{a/A}(x_1, \mu_F) f_{b/B}(x_2, \mu_F) \frac{1}{4|k_2^0 k_1^z - k_1^0 k_2^z|} \tag{2.148}$$

$$\times \prod_{i=1}^{N} \int \frac{d^4 p_i}{(2\pi)^4} \theta(E_i) \delta(p_i^2 - m_i^2) (2\pi)^4 \delta^4 (\sum_{i=1}^{N} p_i - k_1 - k_2). \tag{2.149}$$

However, to proceed with the full integrations, the cancellations required must be made using complex methods, such as slicing or subtraction. These methods are briefly described below.

2.6.4 Slicing

This is a non-local singularity cancellation method, performed by implementing a cut O_{CUT} to an observable O to prevent the integrand from approaching a singularity. Such observables could include $N_{jettiness}$[2], or transfer momentum Q_T. It is usually valid for the high-p_T region, applied as the following

$$\sigma^{NLO} = \int_{\Phi_{n+1}} d\sigma^{real} \Theta(O - O_{CUT}) + \int_{\Phi_n} dF + \int_{\Phi_n} d\sigma^V |_{O=O_0}. \tag{2.150}$$

This equation then partitions off singular regions from non-singular regions. In the region where $O > O_0$, the higher-order computation requires information about the cross-section at the first order below itself [100, 101].

2.6.5 Subtracting

A subtraction method (Antenna subtraction for example [102, 103]) requires introducing a counter term with the same divergent structure as the integrand into the

[2] $N_{jettiness}$ provides an inclusive measure of how N-jet-like the event with at least N energetic jets, looks like. For $N_{jettiness} \to 0$ the event contains exactly N infinitely narrow jets. For $N_{jettiness} \sim 1$ the event has hard radiation between the N signal jets. For $N_{jettiness} << 1$, the radiation outside the signal and beam jets is constrained, providing an inclusive way to veto additional central jets [99].

real emission calculation. These counterterms must be integrable over a certain number of additional degrees of freedom in the unresolved phase space. The integrals give $\frac{1}{\epsilon}$ poles, and can then be added to the lower multiplicity phase space to cancel the poles that came from the virtual contributions at lower order. Due to this cancellation, the total cross-section is unchanged. Subtraction counter terms have some flexibility in their divergent structure and as a result can be constructed in many ways, leading to the existence of numerous subtraction schemes. These methods are most suitable for the low-p_T region. By introducing the counterterm $d\sigma^{counter}$, this gives

$$\sigma^{real} + \sigma^{virt} = \int_{N+1} d\sigma^{real} - d\sigma^{counter} + \int_{N} d\sigma^{virt} + \int_{div} d\sigma^{counter}, \tag{2.151}$$

integrating over the divergent subspace $\int_{div}$ to counter the $d\sigma^{virt}$ contribution. In order to obtain a suitable $d\sigma^{counter}$ term, the "dipole formalism" can be used to express the soft and collinear region amplitudes in terms of sub-amplitudes and dipoles [104].

2.6.6 Colour Ordering

To tackle the colour dependence of the loop level matrix elements, one should introduce colour factors $F(T, f)$, functions of the $SU(3)$ generator matrices T and structure functions f^{abc}. Also introduced are colour-ordered partial amplitudes $|\mathcal{M}^i\rangle$, a kinetic term that then allows for the decomposition of the squared matrix element such that

$$|\mathcal{M}|^2 = \sum_{i,j} F_i^\dagger(T, f) F_j(T, f) \langle \mathcal{M}^i | \mathcal{M}^j \rangle. \tag{2.152}$$

The linear combinations of colour factors multiplied by the colour-ordered partial amplitudes provides information on the colour dependence of desired QCD amplitudes. The Fierz identity gives:

$$T^a_{ij} T^a_{kl} = \frac{1}{2}(\delta_{il}\delta_{jk} - \frac{1}{N}\delta_{ij}\delta_{kl}) \tag{2.153}$$

and using the previously defined commutation relations

$$[T^b, T^c] = i f^{abc} T_a \tag{2.154}$$

this gives

$$(T^a_{ij} T^b_{jk} T^c_{ki} - T^a_{ij} T^c_{jk} T^b_{ki}) = i\frac{1}{2} f^{abc}. \tag{2.155}$$

For example, the leading case where $i = j$ gives:

$$|\mathcal{M}|^2_{leading} = \sum_i F_i^\dagger(T, f) F_i(T, f) \langle \mathcal{M}^i | \mathcal{M}^i \rangle = \sum_i |F_i(T, f)|^2 |\mathcal{M}^i|^2. \tag{2.156}$$

2.6.7 *K*-factor

The *K*-factor is then defined as the ratio of NLO to LO cross section for a given process, $K_{NLO} = \frac{\sigma_{NLO}}{\sigma_{LO}}$, and thus quantifies the impact of higher-order contributions. *K*-factor can also describe further orders, such as NNLO, $K_{NNLO} = \frac{\sigma_{NNLO}}{\sigma_{LO}}$. dependent on several variables, including the PDF of the process, the *K*-factor is then different for each process and can even vary for different kinematic regions of the same process. In addition, the *K*-factor changes depending on the final state being a fixed parton state or parton shower.

Following this, we extend the SM to BSM physics by detailing the motivation behind DM, our current understanding of its properties, and methods for its detection.

2.7 Dark Matter

The convincing evidence for the existence of DM has been well established ever since the observation of rotation curves of stellar objects within neighbouring galaxies in 1932 [9]. The velocity distribution of these stellar objects as a function of their distance from the centre of its galaxy remains constant, and does not show the expected Keplerian fall-off. This implies the presence of large halos of undetectable mass about the galaxy. In addition, gravitational lensing observations of numerous Massive Compact Halo Objects (MACHOs) [12, 13] confirm that these objects could not account for the missing mass we observe.

Big Bang nucleosynthesis (BBN) measurements set rigid limits on the mass of thermal DM to be above few MeV, by constraining the number of additional degrees of freedom to the SM in the thermal bath, below a temperature of $\sim$ 10 MeV. Meanwhile, COBE [105], WMAP [10] and PLANCK [6, 11] surveys of the CMB measure the baryonic content of the universe from anisotropies, leaving 84% of the matter unaccounted for, thereby setting very tight constraints on the amount of non-baryonic DM. Recent observations of the Bullet Cluster (1E0657-558), in which two galaxy clusters passed through one another, also point towards non-baryonic DM. After measuring the baryonic components distributed across the Bullet Cluster, a spatial offset of the center of mass from the baryonic mass peaks was observed [17, 18, 106]. The classification of hot or cold DM is determined by its average velocity to mass ratio; hot (cold) for a large (small) velocity/mass. If DM is hot, it cannot allow for the formation of the large scale structures we observe, as the non-uniform "seeds" of gravitational potential would be washed out by this relativistic DM. Conversely, if DM velocity is too low, it would collapse in a singularity. Large scale structure simulations imply existence of cold (mass>keV) DM [14–16]. Given the lack of DM candidate in the SM, it is required to look beyond and theorise new particles. Many

models have been suggested and studied that provide particle non-baryonic cold DM candidates which also provide rich phenomenology in collider and non-collider searches. These include SUSY [21–23], sterile neutrinos [24], Axions [26], Kaluza-Klein DM [27] and extended Higgs sectors [29–31].

In addition to the cosmological deductions, the combined results from collider, indirect and direct detection experiments is crucial in probing the nature of DM. With these multiple avenues we can narrow down its various properties such as spin, mass, mediators, couplings to SM and symmetries. The mechanisms are illustrated in Fig.2.15, where DM production in colliders (Fig.2.15→), direct detection via scattering of DM against SM particles (Fig.2.15 ↑, ↓) and DM annihilation to SM (Fig.2.15 ←) can all constrain DM properties for different regions of the model parameter space. The next few sections will detail the various sources of DM observations or constraints.

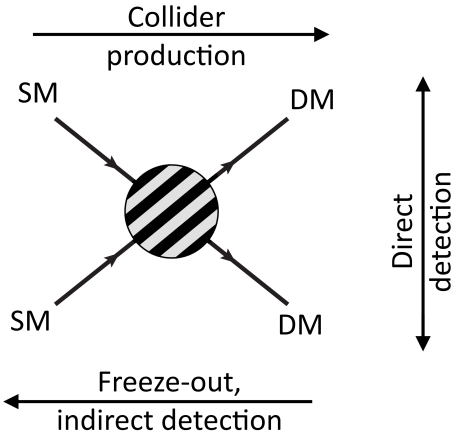

FIGURE 2.15: Diagram for the possible DM-SM interactions and resulting detection mechanisms.

2.7.1 Relic Density, Freeze-out and Freeze-in

In the early universe before BBN, it is assumed that matter and radiation were produced thermally, their entropy conserved and they eventually decoupled in the radiation-dominated epoch. Through $DM\ DM \rightarrow SM\ SM$ annihilation processes, thermal DM particles sustain thermal equilibrium with SM particles after the reheating process. The conventional freeze-out mechanism assumes that, in the early universe, DM initially has very large thermal density. As the temperature of the hot plasma within the early universe falls below the DM mass, DM thermal density is diluted, reducing the number of DM annihilation processes until this rate falls below the Hubble expansion rate of the universe when

$$\Gamma(T_{dec}) = H(T_{dec}) = \sigma_{DM\ DM} v n_{DM} \tag{2.157}$$

and for a radiation dominated universe, the Friedmann equation gives

$$H(T_{dec}) = \frac{\pi}{3\sqrt{10}M_{Pl}}\sqrt{g_{eff}(T_{dec})}T_{dec}^2. \tag{2.158}$$

Assuming a weakly interacting DM and a Majorana or complex scalar DM, we have $g = 2$, giving an annihilation cross section

$$\sigma_{DM\ DM} = \frac{\pi\alpha^2 m_{DM}^2}{s_W^4 m_W^4} \tag{2.159}$$

leading to decoupling at $X_{dec} = m_{DM}/T_{dec} \approx 28$. The number density then falls proportional a^{-3}, until reaching

$$\Omega_{DM}h^2 \approx 0.11\left(\frac{100\text{GeV}}{m_{DM}}\right). \tag{2.160}$$

This is known as the "WIMP miracle", whereby DM would give a density around the Planck measurement for DM density of $\Omega_\chi h^2 = 0.11$. At this point, DM freezes out with this fixed number density.

As the number of interactions between SM and DM particles increases, the relic abundance generated by freeze-out decreases. This is because a larger annihilation cross section keeps the abundance closeer to thermal equilibrium at lower temperatures, resulting in a reduced abundance [107].

However, an alternate mechanism, freeze-in, instead leads to an increase in relic abundance after interactions between DM and SM particles increases. This is because here the couplings are assumed to be much weaker than in the freeze-out case and the abundance, which is assumed to be initially vanishing, is assumed to always be below the thermal abundance. Both freeze-in and freeze-out are represented in Fig. 2.16 where increasing coupling strength reduces relic density for freeze-out scenario, and increases relic density for freeze-in scenario.

In addition to DM annihilation, relic density is also dependent on the amount of DM co-annihilation with non-DM candidate dark sector particles (additional particles introduced from the doublets of DM models, such as the heavier non-stable D_2 particle or charged D^+ particle) to SM particles and annihilation with additional DM candidates that also contribute to the total relic density. In this case, both the DM candidate and associated dark sector particle number densities fall in the co-annihilation process.

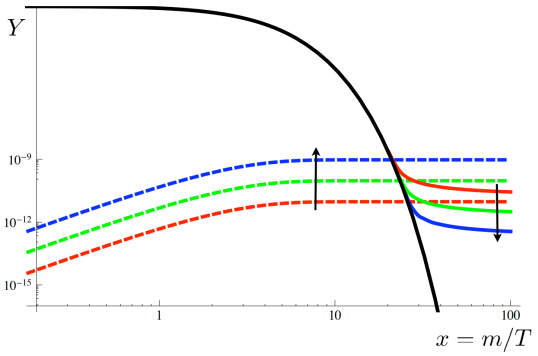

FIGURE 2.16: The evolutions of DM relic density freeze-out (solid coloured) and freeze-in (dashed coloured). The arrow indicated the change with increasing coupling strengths for both process
[107].

2.7.2 Direct Detection

Direct detection (DD) is a powerful addition to the many methods DM can be probed. DD experiments search for DM-SM scattering events, leading to SM and DM particles in the final state, such as in Eq.2.161,

$$SM\ DM \rightarrow SM\ DM. \tag{2.161}$$

The most recent limits come from the Xenon1T experiment [3] and LUX-ZEPLIN (LZ) experiment [108]. The previous limits are given in Fig.2.17, while the most recent limits from LZ are given in Fig.2.18.

Measurements use the standard Halo Model which assumes DM has an isotropic and isothermal spherical distribution. This implies it has velocity distributions

$$f(v < v_{esc}) = \frac{1}{N} \exp\left\{-\frac{v^2}{v_c^2(R)}\right\}, \tag{2.162}$$

$$f(v \geq v_{esc}) = 0, \tag{2.163}$$

where v_c is the average velocity around the galactic centre, and v_{esc} is the velocity required for DM to escape the gravitational pull of the galaxy. The $1/R^2$ density dependence of DM recreates the flat galactic rotation curves that we observe. We expect a circular velocity of $v_c(R_0) \approx 220\ \text{kms}^{-1}$.

DD experiments require low energy scale (sub-MeV) DM-SM particle recoil detection, and so models must be mapped to non-relativistic interactions as measured by the experiment. Using form factors which describe the quark content of nucleons, the DM-nucleon amplitude can then be extrapolated from the DM-quark amplitudes, computed in the $v \rightarrow 0$ limit, for a particular model [109].

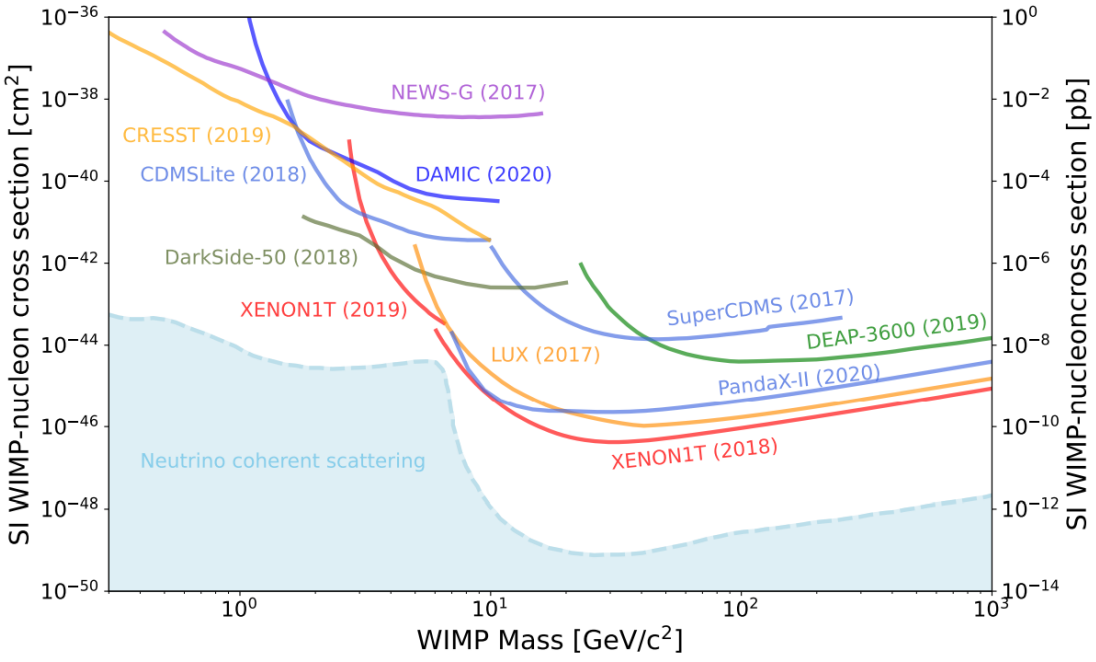

FIGURE 2.17: The combination of current DD experiment results for WIMP-nucleon spin-independent cross section limits [110].

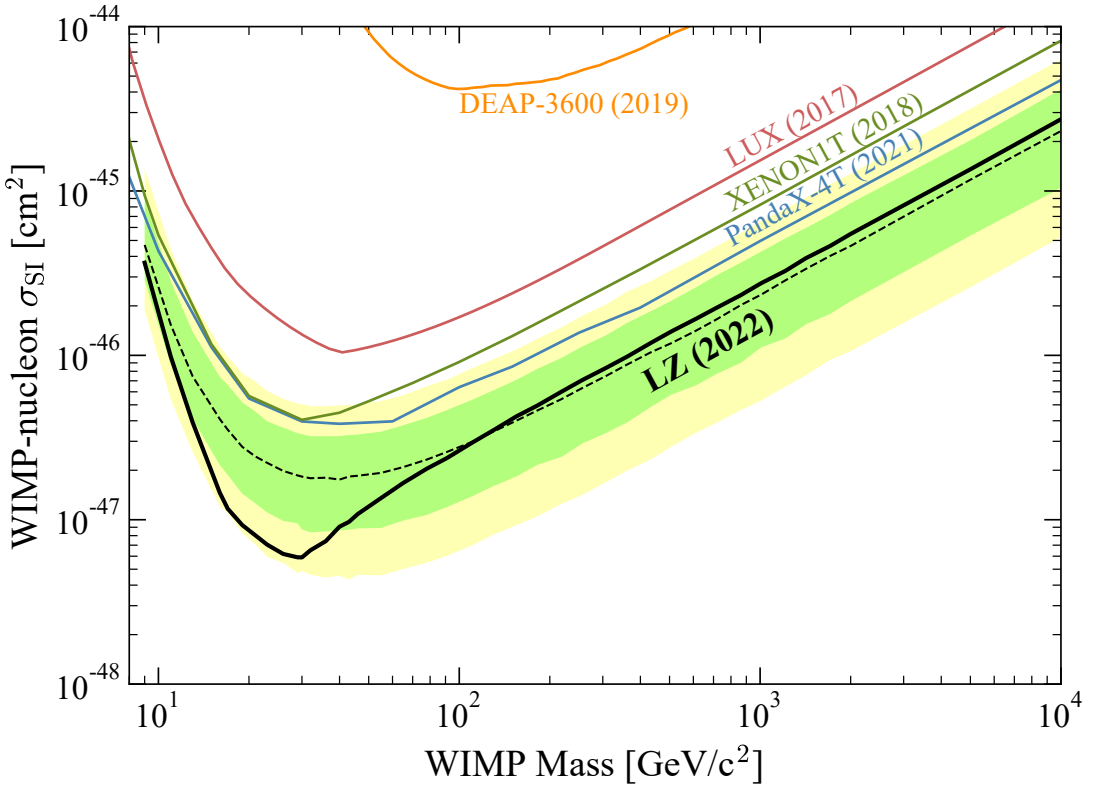

FIGURE 2.18: The limit (black line) on the WIMP - nucleon cross section vs. WIMP mass to 90% C.L., with green and yellow bands for the 1σ and 2σ uncertainty respectively. The dotted line represents the median of the projected uncertainty [108].

2.7.3 Indirect Detection

Indirect detection (ID) stems from self-interactions of DM or with other dark sector particles through annihilation into observable SM particles. The generic process is given in Eq.2.164,

$$DM\,DM \rightarrow SM\,SM. \tag{2.164}$$

The final state observable particles are detected in satellites, both by Earth bound satellites and those within Earth's orbit. These annihilation processes are concentrated in dense areas of DM, such as in stars or the centre of galaxies, where DM annihilation is sufficient enough to produce observable photons, or particle-antiparticle pairs such as electron-positron pairs.

These kind of processes have large SM background, although can be distinguished by the abundance of antiparticles produced in the DM signal. Under the assumption that DM has a relatively small velocity compared to astronomical objects, the energy dependence of the proton-antiproton ratio near the DM mass can be used to distinguish DM ID signal from SM background.

2.7.4 Collider Detection

DM can be produced at colliders, given that it interacts strongly enough with the SM and has mass below achievable collider energies. The DM produced would pass through the detector as an invisible object but will leave hits through cascades from co-production with heavier dark sector particles. The stable DM candidate would result in missing energy in the reconstructed final state but difficulty would still arise in identifying its origin as being from a DM source and not SM background such as neutrinos. Colliders such as the LHC would search for SM objects including energetic jets, H, W or Z bosons, in addition to DM in the form of a significant amount of missing transverse momentum E_T^{miss}. The general DM process considered is given by

$$SM\,SM \rightarrow DM\,DM\,+\,X \tag{2.165}$$

where X can be a SM observable emission such as decaying bosons, photons or hadronic jets.

Signs of dark sector mediators between SM and DM can also be probed by searching for dijet or dilepton products. Additionally, DM models with connection to the Higgs sector, Higgs portal models, use the $H \rightarrow$ invisible as a key constraining observable.

There are typically two types of model approaches to interpret the possible results from collider searches. The complete models, such as MSSM, are targeted searches that can heavily constrain specific models. This is useful for classifying the likelihood

of various DM observables for a given model, but only apply to the chosen model in question. A second approach considers effective field theories (EFTs) which can provide a wide range of signatures and benchmark points at a given energy scale. The problem arises when trying to validate an EFT for a given energy scale of DM observables, which narrows its usefulness. An alternative approach is to construct simplified models which address this issue, while supplementary dark sector partners or mediators may still reduce their application for a model-independent search. As it stands today, despite the strong limits on many possible DM signatures from collider searches, no significant deviation from SM has been found so far [111].

With the underlying theory of high energy particle physics established and the proposal for DM well-motivated, We now describe the BSM models with DM candidates, under study in the thesis.

Chapter 3

BSM Models

3.1 Inert Two Higgs Doublet Model (I2HDM)

The I2HDM [112, 113] is a minimal extension to the SM that introduces a second spin-0 scalar doublet Φ_2 to the Higgs sector. The new doublet possesses the same quantum numbers to the pre-existing SM Higgs doublet Φ_1, but without the direct coupling to fermions, hence it being 'inert'.

The discrete Z_2 symmetry leads to Φ_2 being odd, while all other fields are even. The Lagrangian is imposed to be invariant under this symmetry, by parity transformation $\Phi_2 \to -\Phi_2$, which prevents the existence of Yukawa couplings between fermions and the inert doublet. The Lagrangian for the scalar sector of the model is given by

$$\mathcal{L}_\Phi = |D_\mu \Phi_1|^2 + |D_\mu \Phi_2|^2 - V(\Phi_1 \Phi_2) \tag{3.1}$$

where the new potential,

$$\begin{aligned} V(\Phi_1, \Phi_2) = -m_1^2(\Phi_1^\dagger \Phi_1) - m_2^2(\Phi_2^\dagger \Phi_2) + \lambda_1(\Phi_1^\dagger \Phi_1)^2 + \lambda_2(\Phi_2^\dagger \Phi_2)^2 + \lambda_3(\Phi_1^\dagger \Phi_1)(\Phi_2^\dagger \Phi_2) \\ +\lambda_4(\Phi_2^\dagger \Phi_1)(\Phi_1^\dagger \Phi_2) + \frac{\lambda_5}{2}[(\Phi_1^\dagger \Phi_2)^2 + (\Phi_2^\dagger \Phi_1)^2], \end{aligned} \tag{3.2}$$

contains all of the scalar interactions allowed by Z_2 symmetry. $m_{1,2}$ are the non-physical mass parameters corresponding to Φ_1,Φ_2 , which are later related to the physicsal DM particle masses, and λ_{1-5} are free couplings. All masses and λs are defined as positive and real, which prevents CP violation in the scalar sector.

For a significant portion of the parameter space, the second doublet does not acquire a VEV, and only the original SM Higgs doublet does. This 'inert minimum', for $\langle \Phi_i^0 \rangle = \frac{v_i}{\sqrt{2}}$, corresponds to $v_1 = v$ and $v_2 = 0$. The doublets then expand about this

minimum as

$$\Phi_1 = \frac{1}{\sqrt{2}}\begin{pmatrix} 0 \\ v+H \end{pmatrix}, \Phi_2 = \frac{1}{\sqrt{2}}\begin{pmatrix} \sqrt{2}D^+ \\ D_1 + iD_2 \end{pmatrix} \tag{3.3}$$

The Z_2 symmetry is still conserved by this vacuum state, meaning that coupling between the singlet inert fields and SM field is forbidden, thus stabilising the lightest inert boson from decaying into SM particles. Meanwhile, pair-wise interactions between the inert scalars and SM gauge bosons is still permitted.

The model contains one inert charged D^+ with mass m_{D^+}, and two inert neutral scalars, D_1 and D_2 with masses m_{D_1} and m_{D_2} respectively. While D_1 and D_2 have opposite CP parties, the model has two CP-symmetries, $D_1 \to D_1$, $D_2 \to -D_2$ and $D_1 \to -D_1$, $D_2 \to D_2$ upon change of basis $\Phi_2 \to i\Phi_2$, such that it is impossible to determine which of $D_1$and D_2 are CP even or CP odd.

The physical masses are then given by

$$m_H^2 = -2m_1^2 = 4\lambda_1 v^2, \tag{3.4}$$

$$m_{D_1}^2 = \frac{1}{2}(\lambda_3 + \lambda_4 - \lambda_5)v^2 - m_2^2, \tag{3.5}$$

$$m_{D_2}^2 = \frac{1}{2}(\lambda_3 + \lambda_4 + \lambda_5)v^2 - m_2^2, \tag{3.6}$$

$$m_{D^+}^2 = \frac{1}{2}\lambda_3 v^2 - m_2^2, \tag{3.7}$$

where we define

$$\lambda_{345} = \lambda_3 + \lambda_4 + \lambda_5, \tag{3.8}$$

such that the parameter space is described in total by

$$m_{D_1},\ m_{D_2},\ m_{D^\pm},\ \lambda_{345},\ \lambda_2. \tag{3.9}$$

The constraints for vacuum stability and a global minimum give the condition from [31] as

$$m_{D_1}^2 \geqslant (\lambda_{345}/2 - \sqrt{\lambda_1\lambda_2})v^2. \tag{3.10}$$

The choice of $m_{D_1} < m_{D_2}$ is made such that D_1 is the DM candidate, without specifying which is scalar and which is pseudo scalar. For certain analyses in this work, we reduce the number of parameters by noting that λ_2 does not affect certain LHC phenomenology under study, since it only controls DM the self-interactions.

Additionally, we can exclude λ_{345} from certain analyses for the following reason. The relevant coupling for the $gg \to H^* \to D^+D^-$ and $gg \to H^* \to D_2D_2$ processes are λ_3 and $\lambda_3 + \lambda_4 - \lambda_5$, respectively, which are limited by EW precision tests plus perturbativity [31,114] and related to the mass splitting between D^+ and D_2. We have checked that, even if we maximise the cross section of either of the two processes by

increasing the respective coupling up to the maximal allowed value, the respective cross section[1] will still be below the signal production cross section via the weak coupling. Moreover, the value of the λ_{345} coupling is also strongly limited by DM direct detection constraints as well as by limits on the invisible Higgs boson decay branching ratio in the case when $m_H > 2m_{D_1}$ (see, e.g., [31,115]). Therefore, in order to establish a conservative and generic limit on the i2HDM parameter space, we exclude λ_{345} from certain studies presented in this work and set its value to zero. The remaining parameters can then be easily visualised in 2D planes, while fixing one parameter. We use the

$$\left\{m_{D_1},\ \Delta m^+,\ \Delta m^0\right\}_{\text{i2HDM}} \tag{3.11}$$

parametrisation, where

$$\Delta m^0 = m_{D_2} - m_{D^\pm},\ \ \Delta m^+ = m_{D^\pm} - m_{D_1}\ , \tag{3.12}$$

which allows an even better visualisation and interpretation of the model parameter space. We note one important caveat for some of our analyses here: we deliberately choose the mass hierarchy $m_{D_2} > m_{D^\pm} > m_{D_1}$, such that D_1 is the lightest state. This choice is motivated by phenomenological reasons in order to bring out the intricacies of the collider constraints set by 2- and 3-lepton searches. The other hierarchy $m_{D^\pm} > m_{D_2} > m_{D_1}$ is entirely feasible and will lead to constraints comparable to the ones described in this paper. We leave this possibility for a future work.

3.2 Minimal Fermionic Dark Matter Model (MFDM)

The Lagrangian for the MFDM model, which introduces the EW fermion DM doublet of χ_1^0,χ_2^0,χ^+ and Majorana singlet fermion χ_s^0, is

$$\mathcal{L}_{MFDM} = \mathcal{L}_{SM} + \overline{\psi}(i\not{D} - m_\psi)\psi + \frac{1}{2}\overline{\chi}_s^0(i\not{\partial} - m_s)\chi_s^0 - (Y_{DM}(\overline{\psi}\Phi\chi_s^0) + h.c.) \tag{3.13}$$

where the fermion $SU(2)$ doublet is

$$\psi = \begin{pmatrix} \chi^+ \\ \frac{1}{\sqrt{2}}(\chi_1^0 + i\chi_2^0) \end{pmatrix}. \tag{3.14}$$

Note that Majorana fermions χ_1^0 and χ_s^0 mix via the Yukawa coupling, meanwhile χ_2^0 and $\chi^+$are mass degenerate, since the mass and gauge eigenstate of χ_2^0 coincide. The physical masses are then obtained by diagonalisation of the mass matrix from

[1] Both cross sections cannot be simultaneously made large since either D^+ or D_2 should be heavier than the other, which would make one of the cross sections much smaller than the other.

$(\chi_1^0, \chi_s^0, \chi_2^0)$ basis to the (D_1, D_2, D') mass basis as,

$$M = \frac{1}{2}\begin{pmatrix} m_\psi & Y_{DM}v & 0 \\ Y_{DM}v & m_s & 0 \\ 0 & 0 & m_\psi \end{pmatrix} \tag{3.15}$$

diagonalised via rotation angle θ such that

$$\tan 2\theta = \frac{2Y_{DM}v}{m_\psi - m_s}, \tag{3.16}$$

$$\sin 2\theta = -\frac{2Y_{DM}v}{m_{D_2} - m_{D_1}} \tag{3.17}$$

which give the eigenstate relations

$$\chi_s^0 = D_1 \sin\theta + D_2 \cos\theta \tag{3.18}$$

$$\chi_1^0 = D_1 \cos\theta + D_2 \sin\theta. \tag{3.19}$$

This leads to five new dark sector particles: the lightest and DM candidate D_1, the two second-lightest charged components $D^\pm$ mass degenerate with the neutral D', and the heaviest neutral particle D_2. These physical mass parameters are then related back to the Lagrangian parameters as

$$m_s = m_{D1} + m_{D_2} - m_{D+}, \tag{3.20}$$

$$m_\psi = m_{D^+} = m_{D'}, \tag{3.21}$$

so the physical parameters of the model are given by

$$\{m_{D_1},\ m_{D'} = m_{D^\pm},\ m_{D_2}\}_{MFDM}, \tag{3.22}$$

where a real Yukawa coupling requires that $m_{D_2} > m_{D\pm} = m_{D'} > m_{D_1}$. In Fig. 3.1 we present the Y_{DM} dependent $D_1 D_2 H$ coupling and cos^2 of the $\chi_1^0 - \chi_s^0$ mixing angle θ as functions of mass split Δm^+. Looking in terms of the coupling relations between the mass splittings, we have

$$\Delta m^0 = m_{D_2} - m_{D+},\ \ \Delta m^+ = m_{D^+} - m_{D1} \tag{3.23}$$

where the Yukawa coupling is given by

$$Y_{DM} = \frac{\sqrt{(m_{D_2} - m_{D^+})(m_{D^+} - m_{D1})}}{v} = \frac{\sqrt{\Delta m^0 \Delta m^+}}{v}. \tag{3.24}$$

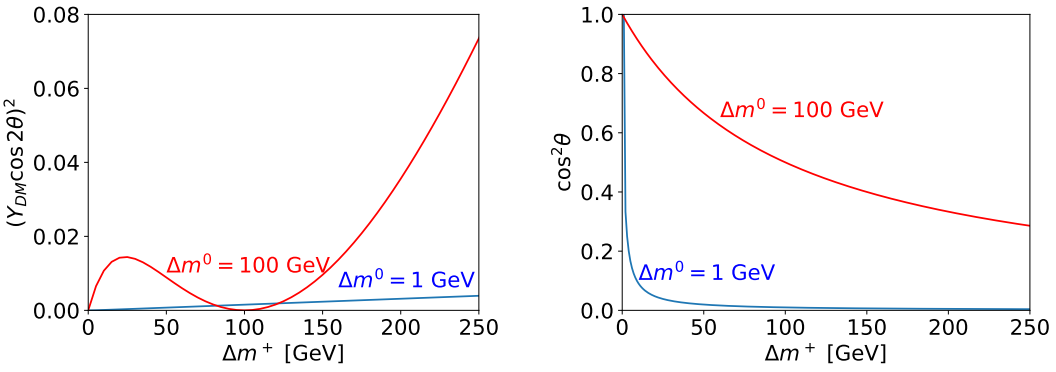

(A) (B)

FIGURE 3.1: The square of the $D_1 D_2 H$ coupling(a) and $cos^2\theta$ of the $\chi_1^0 - \chi_s^0$ mixing angle(b) as a functions of Δm^+.

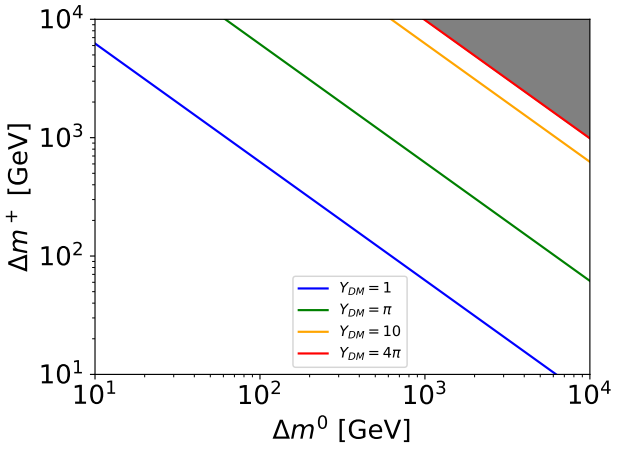

FIGURE 3.2: Contours for the Yukawa Y_{DM} in the $\Delta m^+ - \Delta m^0$ plane. The limit of $Y_{DM} > 4\pi$ excludes these points.

As with the i2HDM, the change of parameters is made to better visualise the physics, with constant interactions in the $\Delta m^+ - m_{D1}$ plane,

$$\{m_{D_1},\ \Delta m^+,\ \Delta m^0\}_{MFDM}\,. \tag{3.25}$$

The model is also subject to various theoretical constraints, like perturbativity and radiative stability. The perturbative limit on the Yukawa is represented in Fig.3.2, in the $\Delta m^+ - \Delta m^0$ plane, where the contour above $Y_{DM} > 4\pi$ is excluded.

Contributions to electroweak radiative corrections from BSM physics apply additional constraints on any BSM models, parametrised by the S, T, and U observables [116]. T is proportional to the difference between W and Z boson self energies at $Q^2 = 0$, while S is related to the difference between Z self-energy at $Q^2 = M_Z^2$ scale and $Q^2 = 0$.

Additionally, $(S+U)$ is related to the difference between W self-energy at $Q^2 = M_W^2$ scale [110].

While for the i2HDM, S and T parameters have been computed in [117,118] (where contributions to U parameter for I2HDM can be neglected), for MFDM, the S and T parameters have been previously derived in [45], where it is found that T and U parameters are explicitly zero. The S parameter is given by

$$S = \frac{1}{\pi}\left[\cos^2\theta\Pi'_V(M_{D'},M_D) + \sin^2\theta\Pi'_V(M_{D'},M_{D_2}) - \Pi'_V(M_+,M_+)\right], \quad (3.26)$$

where $\Pi_V^{(\prime)} = \Pi_{V+A}^{(\prime)} + \Pi_{V-A}^{(\prime)}$, given by

$$\Pi'_{V+A} = \left(\frac{1}{3}div + \frac{1}{3}L\right) + \frac{m_1^4 - 8m_1^2m_2^2 + m_2^4}{9\left(m_1^2 - m_2^2\right)^2} + \frac{\left(m_1^2+m_2^2\right)\left(m_1^4 - 4m_1^2m_2^2 + m_2^4\right)}{6\left(m_1^2 - m_2^2\right)^3}\ln\left(\frac{m_2^2}{m_1^2}\right), \quad (3.27)$$

$$\Pi'_{V-A} = m_1m_2\left(\frac{\left(m_1^2+m_2^2\right)}{2\left(m_1^2 - m_2^2\right)^2} + \frac{m_1^2m_2^2}{\left(m_1^2 - m_2^2\right)^3}\ln\left(\frac{m_2^2}{m_1^2}\right)\right) \quad (3.28)$$

and θ is the χ^0-χ_s^0 mixing angle defined by Eq. 3.16.

The limits on these parameters are given by [110]

$$S = -0.02 \pm 0.10 \quad (3.29)$$

$$T = 0.03 \pm 0.12 \quad (3.30)$$

$$U = 0.01 \pm 0.11 \quad (3.31)$$

and so $T, U = 0$ already satisfy the latter two conditions. For the S parameter, this gives the maximal bounds at 1σ level of $-0.12 < S < 0.08$ as used in Fig.3.3. As the Yukawa coupling must be $< 4\pi$ as plotted in Fig.3.2, this limit is also overlaid in Fig.3.3 to show where the points are excluded due to perturbativity constraints. From the contour of the S-parameter in Fig. 3.3 we show that the model is always consistent with the EWPT.

For DM constraints, we first assess direct detection constraints. Since there is no tree-level Z-boson interaction with the DM candidate, the spin-independent direct detection constraint only arises from DM-nucleon scattering controlled by the Higgs coupling to DM. By controlling the mass splitting, this coupling can be made small, leaving a viable parameter space. In order to obtain the correct (not over-abundant)

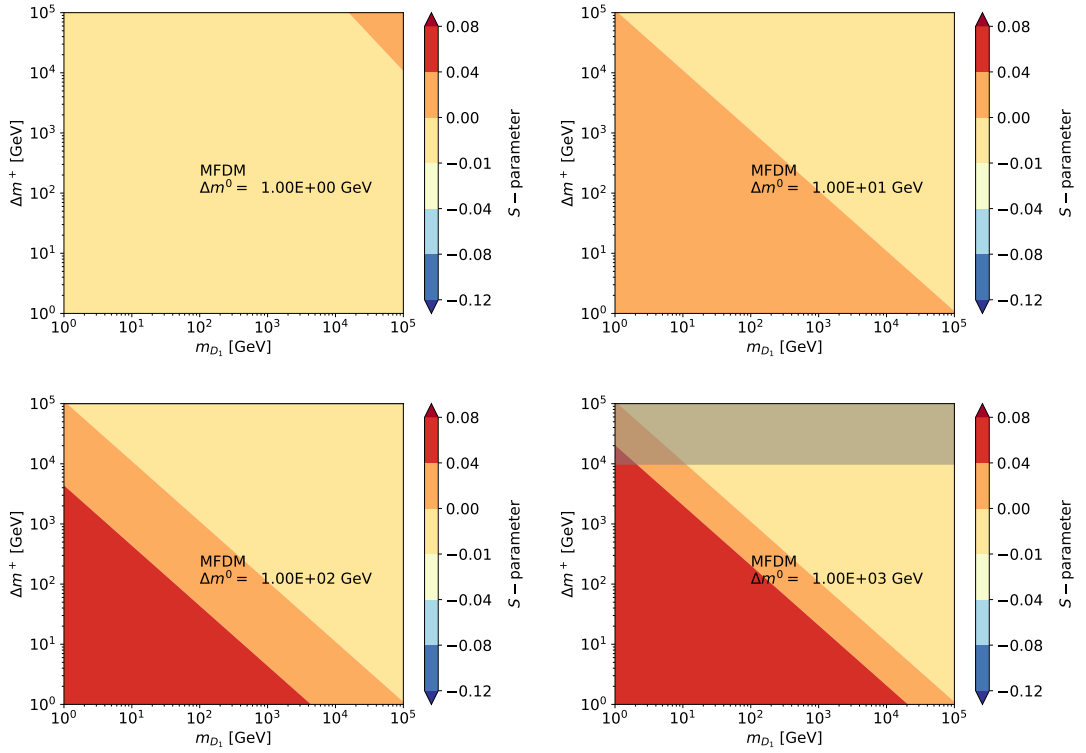

FIGURE 3.3: Contour of limit on S parameter for various Δm^0, where $S < -0.12$, $S > 0.08$ are excluded to 1σ on the boundaries [110]. The grey region show the exclusion due to perturbativity constraints.

relic abundance, one needs an efficient annihilation mechanism via the Higgs funnel $m_{D_1} \simeq m_{h/2}$. These considerations were taken into account in Ref. [45].

In order to connect theoretical models to experimental signals, the layout and inner workings of the largest experimental collider, the LHC, is described in the following section.

Chapter 4

The Large Hadron Collider and The ATLAS Detector

The focus of the analyses in this thesis involves the collision of two particles, followed by the resultant production of showers of detectable (and undetectable) particles. To facilitate collisions of high enough energy required to induce such showers, high energy colliders are constructed to accelerate incoming particles to relativistic speeds, leading to hard head-on collisions. To then be able to detect the resultant showers made of many types of particles, complex particle detectors consisting of various sub-detectors are developed, built close to the collision point.

In the following sections, the Large Hadron Collider (LHC) [1] is first described, followed by the ATLAS detector [119] and its various sub-detectors

4.1 The Large Hadron Collider

The LHC [1], located 100 m underground near Geneva on the France–Switzerland border, is currently the largest particle accelerator, with a circumference of 27 km. The European organisation for nuclear research (CERN) [120] conducts proton-proton collisions up to 13.6 TeV (while potentially capable of up to 14 TeV) centre of mass energies. Each beam is initially given an injection energy of 450 GeV, which undergoes a ramp up from their numerous revolutions within the circular accelerator until reaching 6.5 TeV before colliding.

Dipole magnets within this synchrotron accelerator bend the path of accelerated charged particles through the circular beam pipe, where two counter-rotating proton beams require two sets of dipole magnets to facilitate this. Its path-bending magnets synchronise the increase in magnetic field with the increasing kinetic energy of the accelerated protons. The LHC contains 1232 copper-clad niobium-titanium

superconducting magnet coils [1] maintained by a liquid helium cryogenic system and has a critical temperature around 10 Kelvin.

2500 bunches of protons are accelerated through a vacuum in the LHC, increasing the likelihood of target collisions while minimising energy loss from air molecule interactions. The 16 radio-frequency cavities [1] with EM fields oscillating at 400 MHz provide the accelerating force, where the 25 ns (Run2) distance between accelerated bunches matches the frequency of the EM standing wave.

To further reduce beam loss from the accelerator, sets of 24 quadrupole magnets [1] correct any imperfections in the magnetic fields, by horizontally and vertically applying a force proportional to the distance of the beam from the beam-pipe axis, thus focusing the beam within the beam pipe.

Increasing the collisions per second at the LHC allows us to overcome the limited schedule of runs at the LHC, therefore increasing Luminosity, defined as

$$N = n_{bp} n_1 n_2 \nu_r \tag{4.1}$$

where n_{bp} is the number of colliding bunch pairs, $n_{1,2}$ are the proton number per beam and ν_r is the beam revolution frequency about the LHC. Higher luminosity increases the volume of collected data, thus can increase the sensitivity of a given analysis. The cumulative integrated luminosity over time by ATLAS is given in figure.4.1, reaching a total delivered integrated luminosity of 156 fb^{-1}. The future High-Lumi LHC

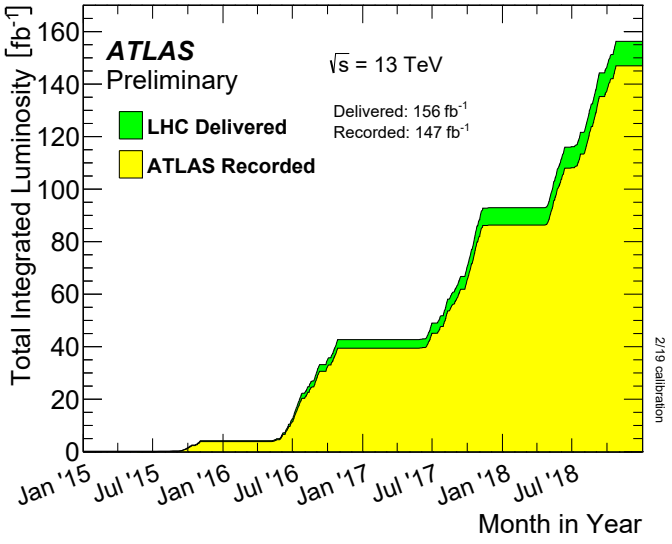

FIGURE 4.1: The cumulative integrated luminosity vs time by ATLAS for high energy $p-p$ collisions [121].

(HL-LHC) [122] aims to boost the maximum integrated luminosity after Run 3 from 300 fb^{-1} to 3000 fb^{-1}.

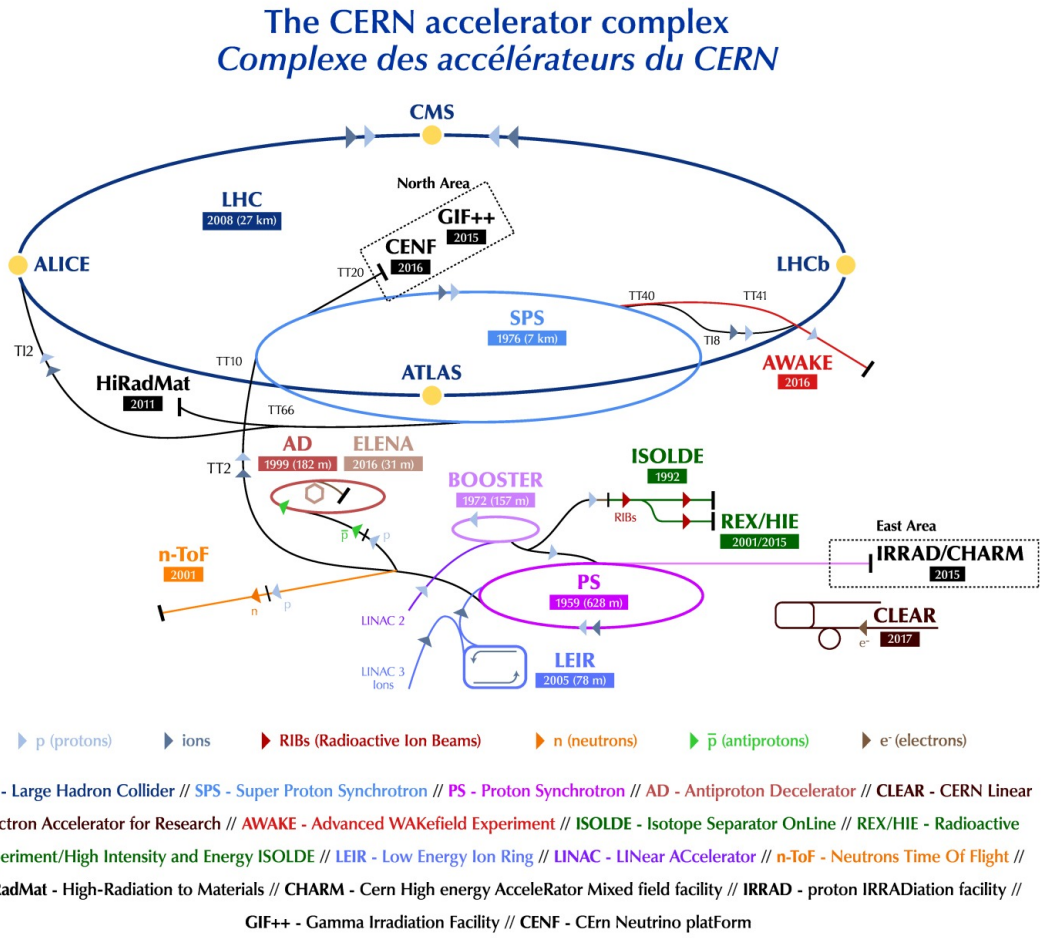

FIGURE 4.2: Layout of the CERN accelerator complex. [123]

The complete accelerator path, shown in Fig.4.2, starts from the LINAC linear accelerator to reduce the beam emittance effects (the total cross-sectional area that the beam occupies within the beam pipe) before entering the LHC's proton synchrotrons (PS). The beam path then connects to the super proton synchrotrons (SPS) before entering the central ring that connects the interaction points of the main experiments.

The seven experiments currently located at the LHC include: ATLAS [124], CMS [125], LHCb [126], ALICE [127], MoEDAL [128], TOTEM [129] and LHCf [130].

4.2 The ATLAS Detector

The ATLAS (A Toroidal LHC ApparatuS) detector [119], located 100m below ground at point 1 on the LHC ring, is a particle detector designed to probe many sectors of HEP including Higgs, top quark, SUSY, CP-violation and heavy ion physics. The 25 m wide, 44 m long cylinder weighs 7,000,000 kg, and consists of many sub-detectors to

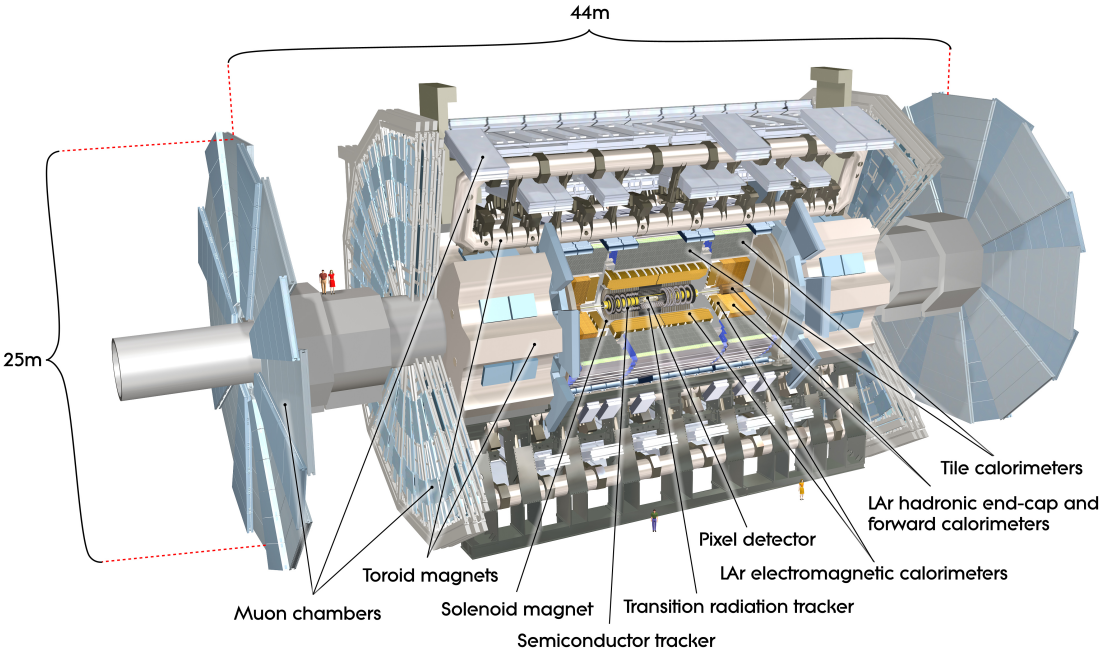

FIGURE 4.3: Computer generated image of the ATLAS detector. [131]

Parameter	Design	Run-1	Run-2	Run-3	HL-LHC
Energy [TeV]	14	7/8	13	14	14
Bunch spacing [ns]	25	50	25	25	25
Bunch Intensity [10^{11} ppb]	1.15	1.6	1.2	up to 1.8	2.2
Number of bunches	2800	1400	2500	2800	2800
Emittance [μm]	3.5	2.2	2.2	2.5	2.5
β^* [cm]	55	80	$30 \rightarrow 25$	$30 \rightarrow 25$	down to 15
Crossing angle [μrad]	285	-	$300 \rightarrow 260$	$300 \rightarrow 260$	TBD
Peak Luminosity [10^{34} cm^{-2}s^{-1}]	1.0	0.8	2.0	2.0	5.0
Peak pileup	25	45	60	55	150

TABLE 4.1: A table summarising the accelerator parameters for the LHC Run-1, Run-2, Run-3 and future HL-LHC [132]. More up-to-date numbers for Run-3 can be found in [133].

identify unique particles and their observables. The diagram in Fig.4.3 shows the dimensions and various components of the ATLAS detector.

As a pair of proton bunches cross, there is a high probability of successful scattering events which, due to the composite structure of the proton, leads to many possible decay cascades. In addition, the pile-up from collisions, defined as the average number of hard scattering events per bunch crossing, is increasingly large for higher luminosity runs. The accelerator parameters are given in Fig. 4.1. For Run-2, the average pile-up is 33 but peaks around 60, as seen in Fig.4.4. A more detailed, up-to-date view of the Run-3 parameters from [133] is given in Tables 4.2 and 4.3.

Parameters	2022	2023	2024
Bunch population ($[10^{11}]$ p/b)	1.40 → 1.80	1.80 → 2.10	2.10 → 2.30
Norm. transverse emittance ([μm])	1.30	1.30 → 1.55	1.55 → 1.70

TABLE 4.2: Additional beam parameter ranges at the start of stable beam in LHC Run-3. [133].

Calendar Year	2022	2023 / 2024
Number of bunches	2748	2748 → 2496
Number of collisions at IP1/5	2736	2736 → 2484
Number of collisions at IP2	2250	2250 → 1949
Number of collisions at IP8	2376	2376 → 2131
Bunch population ($[10^{11}]$ p/b)	1.40	1.80
Bunch length ([ns])	1.20	1.20 (→ 1.35)
Norm. transverse emittance ([μm])	1.80 → 2.50	

TABLE 4.3: A more detailed table including LHC Run-3 beam parameters per year [133].

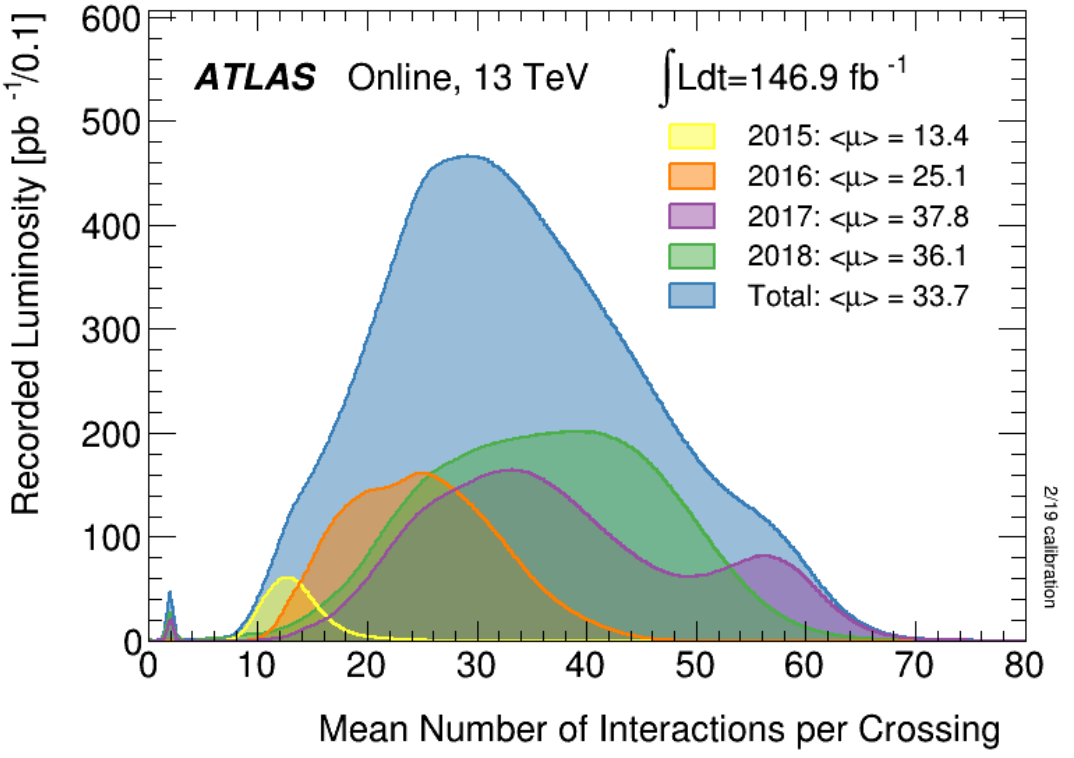

FIGURE 4.4: The pileup distribution for Run-2 [134].

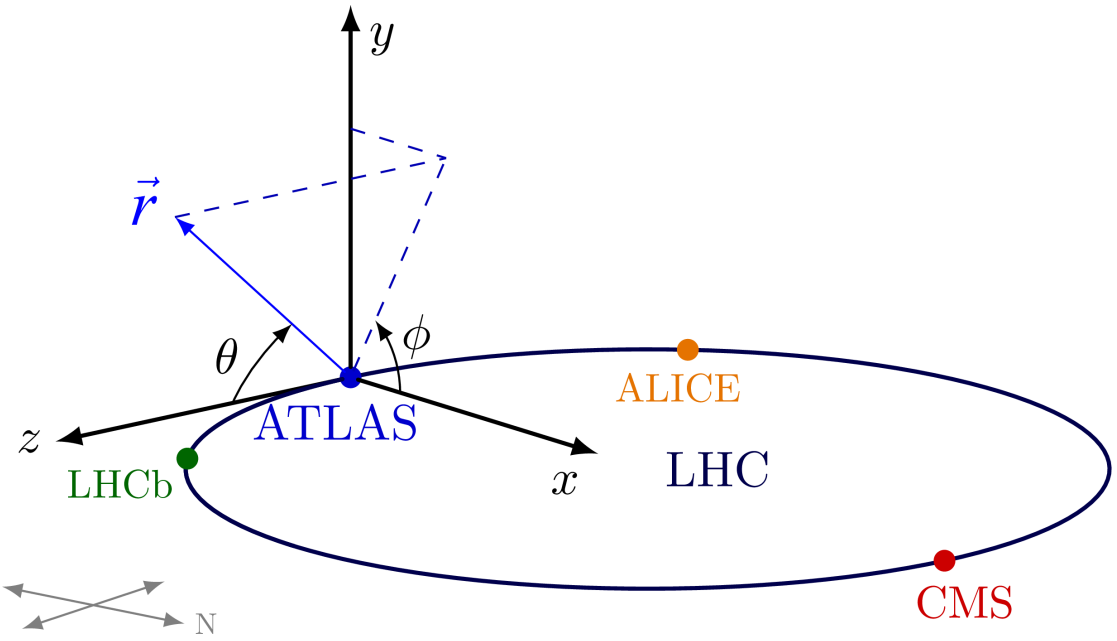

FIGURE 4.5: Diagram depicting the ATLAS coordinate system [135, 136].

Specialised sub-detectors are therefore necessary to both handle specific decay products differently, such as charged or neutral particles, and retain accuracy in large pile-up scenarios. These sub-detectors, located either in the detector barrel cylinders or their end-caps, have significantly different designs for the same operations to account for the varying amounts of radiation exposure, proportional to their relative distance form the beam pipe.

ATLAS uses (x, y, z) coordinates [135, 136] to describe the dimensions of the detector with origin at the point of interaction, where the x-axis points towards the centre of the LHC ring, the y-axis points vertically and the z-axis points along the beam axis. Additionally, cylindrical coordinates (r, ϕ, θ) define observables of the detector events, where r is the distance from the interaction point, θ is the zenith angle between r and the beam axis and ϕ is the azimuthal angle between r and the direction towards the LHC ring centre. This coordinate system is visualised in Fig.4.5.

To distinguish charged particles in the detectors, their trajectory is curved by strong magnetic fields while conserving their energy. The four ATLAS magnet systems [137] that produce these fields consist of a solenoid surrounding the inner detector, a barrel toroid around the muon chambers and two end-cap toroids, producing fields of 12×10^4 m^3 in volume and storing a combined 1.6 GJ of energy. Fig. 4.6 shows the heat map of the magnetic field configuration throughout the detector.

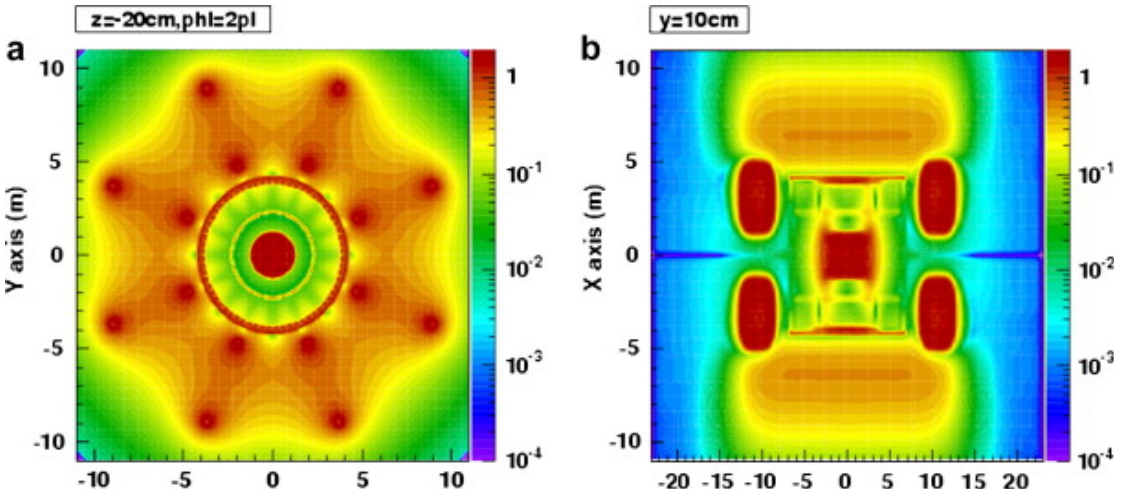

FIGURE 4.6: Heat map of the magnetic field configuration, in arbitrary units. The left figure shows the transverse cross section in the centre of the magnet system and the right figure shows the longitudinal section [137].

4.3 Physics and Performance Requirements

In order to maintain the ATLAS detector and its many sub-detectors in conditions of high radiation, a set of performance requirements must be achieved. Table 4.4 presents these required physics thresholds, such as energy resolution, momentum resolution and angular coverage in η for each sub-detector at ATLAS.

Detector component	**Required resolution**	**η coverage**	
		Measurement	Trigger
Tracking	$\sigma_{p_T}/p_T = 0.05\%\ p_T \oplus 1\%$	± 2.5	
EM calorimetry	$\sigma_E/E = 10\%/\sqrt{E} \oplus 0.7\%$	± 3.2	± 2.5
Hadronic calorimetry (jets)			
barrel and end-cap	$\sigma_E/E = 50\%/\sqrt{E} \oplus 3\%$	± 3.2	± 3.2
forward	$\sigma_E/E = 100\%/\sqrt{E} \oplus 10\%$	$3.1 < \lvert\eta\rvert < 4.9$	$3.1 < \lvert\eta\rvert < 4.9$
Muon spectrometer	σ_{p_T}/p_T=10% at p_T = 1 TeV	± 2.7	± 2.4

TABLE 4.4: A table of the physics requirements of the ATLAS experiment [119].

Each sub-detector must meet at least the minimum requirements in resolution and coverage, set out by Table 4.4. The following sections describe each of these sub-detectors in further detail.

4.4 Inner Detector

The Inner Detector (ID) [138] is designed to track and measure charged particles' direction, momentum, charge and resolve the primary and secondary vertices [139] by

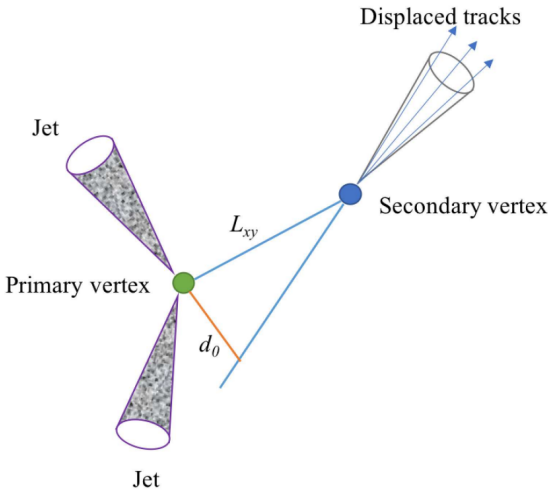

FIGURE 4.7: Diagram depicting the primary vertex and secondary vertex, where d_0 is the impact parameter for one of the displaced tracks [140].

detecting their trajectory hits through the detector volume and employing track-finding algorithms to distinguish them.

The three different tracking sub-systems are the pixel detector, the semiconductor tracker (SCT), which cover $|\eta| < 2.5$, and the transition radiation tracker (TRT) covering $|\eta| < 2.0$. The transverse momentum p_T of the particle can be derived by defining the sagitta

$$S = \frac{qL^2B}{8p_T} \tag{4.2}$$

where q is the particle's charge, L is the distance between first and last hits detected in the track and B is the solenoid system's magnetic field strength. The 5.8m long solenoid with inner and outer diameters of 2.46m and 2.56m respectively, produces a 2T field along the beam axis. By utilising multiple tracks, vertex reconstruction distinguishes response of the primary interaction vertex, the vertex of the highest energy collision, from the reconstructed softer secondary and pile-up interaction vertices.

The secondary and pile-up interaction vertices, along with short-lived b-quarks and τ-leptons, are then identified using impact parameters d_0 and z_0. As shown in Fig. 4.7, d_0 is defined as the shortest distance between the track and the beam axis, while z_0 is the distance in the $z-$axis between the primary vertex and the point on the track where d_0 is defined. These tracks are further used to measure the impact point in the calorimeter and to match detections in the outer regions to an interaction vertex. A list of the primary inner detector components and their dimensions are given in Table 4.5.

The pixel detector and SCT contain modules which both utilise silicon based detectors that act as a reverse bias diode. The incident charged particles then ionise the depletion layer, generating a charged signal from the resulting electrons and holes.

Item		Radial extension (mm)	Length (mm)
Pixel	Overall envelope	$45.5 < R < 242$	$0 < \|z\| < 3092$
3+1 cylindrical layers	Sensitive barrel	$50.5 < R < 122.5$	$0 < \|z\| < 400.5$
2×3 disks	Sensitive end-cap	$88.8 < R < 149.6$	$495 < \|z\| < 650$
SCT	Overall envelope	$255 < R < 549$ (barrel)	$0 < \|z\| < 805$
		$251 < R < 610$ (end-cap)	$810 < \|z\| < 2797$
4 cylindrical layers	Sensitive barrel	$299 < R < 514$	$0 < \|z\| < 749$
2×9 disks	Sensitive end-cap	$275 < R < 560$	$839 < \|z\| < 2735$
TRT	Overall envelope	$554 < R < 1082$ (barrel)	$0 < \|z\| < 780$
		$617 < R < 1106$ (end-cap)	$827 < \|z\| < 2744$
73 straw planes	Sensitive barrel	$563 < R < 1066$	$0 < \|z\| < 712$
160 straw planes	Sensitive end-cap	$644 < R < 1004$	$848 < \|z\| < 2710$

TABLE 4.5: Table of the main parameters of the inner detector [141].

The module's application-specific integrated circuits (ASIC) then convert the analogue signal to digital read-outs.

4.4.1 Pixel Detectors

The silicon pixel detectors [142], the closest component of the ID to the interaction point, consist of four layers of 250 μm thick 50x250 μm oxygen-doped n-type silicon crystal pixels. Given their rectangular shape, each of these four detectors resolve hits in two directions. Their small dimensions also allows for dense distribution of pixels per module, but each require individual conductors for readout. The Insertable B-layer (IBL) [143] is the closest layer to the beam pipe, added later in the timeline to compensate for the radiation damage during Run-1, and improves the precision of interaction vertex measurements. Performance algorithms require precise reconstructed of vertices for jet classification algorithms.

4.4.2 Semiconductor Tracker

The Semiconductor Tracker [144], the second-closest detector to the interaction point, consists of back-to-back wafers of long, flat strips of p-in-n type silicon diodes covered in a metallised layer. Separated by 80μm and parallel to the beam axis, each strip has a small angular offset to further increase their 4-layer coverage. These strips provide high resolution, but unlike the pixel detectors, it is only in one direction.

The outer section of the detector contains layers of long strips while the layer closest to the pixel detectors contain shorter strips, all with 1.25 MΩ [145] poly-silicon

resistors at the end of each strip to calibrate their response. A biasing voltage of 150 V is supplied, now boosted up to 300V to account for radiation exposure.

The modules are mounted on cylindrical supports such that they provide an 11° angle to the tangent of the coaxial cylinder for the inner barrels, and 11.25° for the outer barrels, increasing the overall volume passed through by the particles. The end-cap disks then contain up to three rings of modules with back-to-back sensors: two joint side-by-side sensors in the outer and middle rings, while only a single sensor per side of the inner ring.

4.4.3 Transition Radiation Tracker

The Transition Radiation Tracker [146] is the furthest detector from the interaction point in the ID. Supported by a carbon fibre structure, the TRT is a wire chamber consisting of 4mm diameter polymide drift tubes with a cathode potential of 1530 V and filled with a xenon gas mixture. It is designed to improve electron identification by measuring their transition radiation, the energy from charged ultra-relativistic particles that cross between two surfaces, emitting photons at small angles with respect to the parent's trajectory. This radiation signature, generated by scintillating fibres and foils between the tubes, distinguishes electron tracks from charged hadron tracks which otherwise leave similar signals in the calorimeter.

While the barrel section consists of tubes layered parallel to the beam axis and distributed in a rotational symmetry with linear geometry, the two end-caps have tubes running perpendicular to the beam axis, arranged in multiple loops with radial geometry.

4.5 Calorimeters

The various types of calorimeters [147] measure the energy of incoming particles, charged or neutral, passing through their hermetic volume, while also capturing their direction and used to determine the missing energy of an event. The particles must be stopped and fully absorbed to make a measurement of their properties and, without the presence of a magnetic field, they exclude muons from detection while also preventing unwanted particles passing through to the muon-specific spectrometers. ATLAS houses the Electromagnetic Calorimeter (ECAL) [148] for measuring electromagnetic showers of electrons and photons through EM interactions with a pseudorapidity coverage of $|\eta| < 3.2$, and the Hadronic calorimeter (HCAL) [149] for measuring hadronic showers through strong and EM interactions. The latter includes the hadronic barrel calorimeter, covering $|\eta| < 1.7$, the hadronic end-cap calorimeters, covering $1.5 < |\eta| < 3.2$ and the forward calorimeters, covering $3.1 < |\eta| < 4.9$.

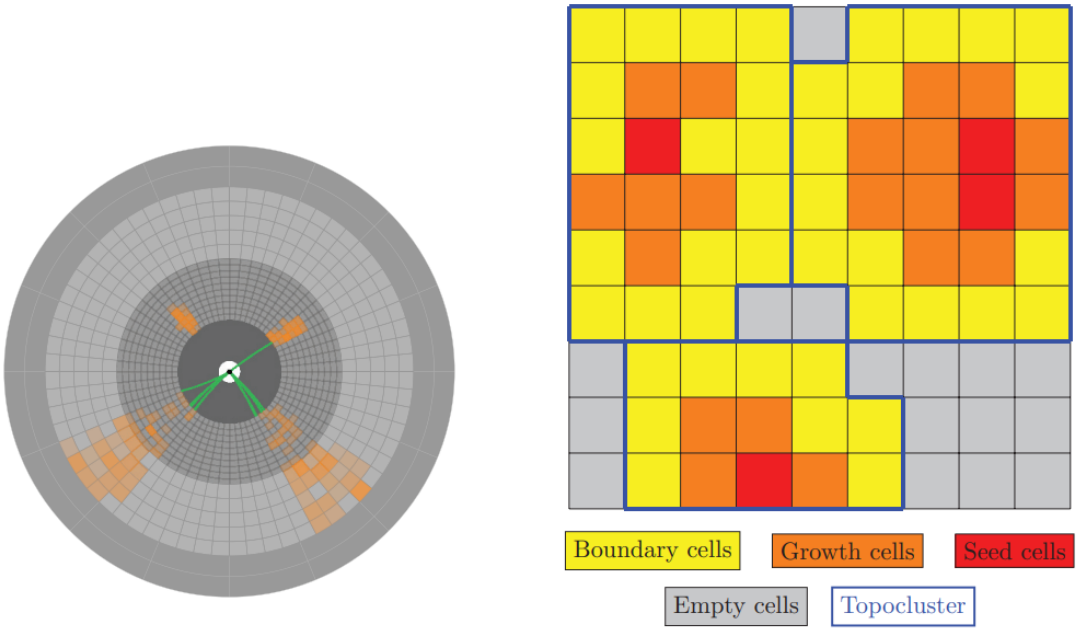

FIGURE 4.8: An example of a detector display showing energy deposits in the calorimeters (left) and cells combined in spatial dimensions to form clusters (right). Red seed cells have the most energy and intiate the process, while nearby cells have less energy further from the seed (orange followed by yellow. [150]

The various cells that comprise the calorimeters detect the final decay products' positions, and readings from both calorimeters are combined to trace back these assorted decay products to the shared parent particles. Each hadron in a jet makes their own hadronic shower, while each electron makes their own electromagnetic shower. Jets or charged leptons can then be identified by the properties of their hadronic or EM showers respectively. As the incident particle loses energy, the showers produced are propagated through the sampling calorimeters' alternating layers of passive absorber medium, where the showers cascade rapidly, and active detection medium to measure the final outcome of these showers. The pictoral view of a calorimeter cell and clusters are given in Fig.4.8. The general layout of the ATLAS calorimeter and its components is given in Fig. 4.9. Table 4.6 summarises the η coverage segmentation, granularity and sampling of the various ATLAS calorimeters.

4.5.1 Electromagnetic Calorimeters

The ECAL [148] is a lead, liquid-argon (LAr) detector that measures energy loss of electrons, positrons and photons from electromagnetic showers. These electromagnetic showers are then produced by the particles as they interact, and an electric field is applied such that the ions of the electromagnetic showers drift in the LAr gap. As an energetic particle passes by, this ionises the LAr and induces a signal from the Argon molecule's lost electrons which are measured, with signal

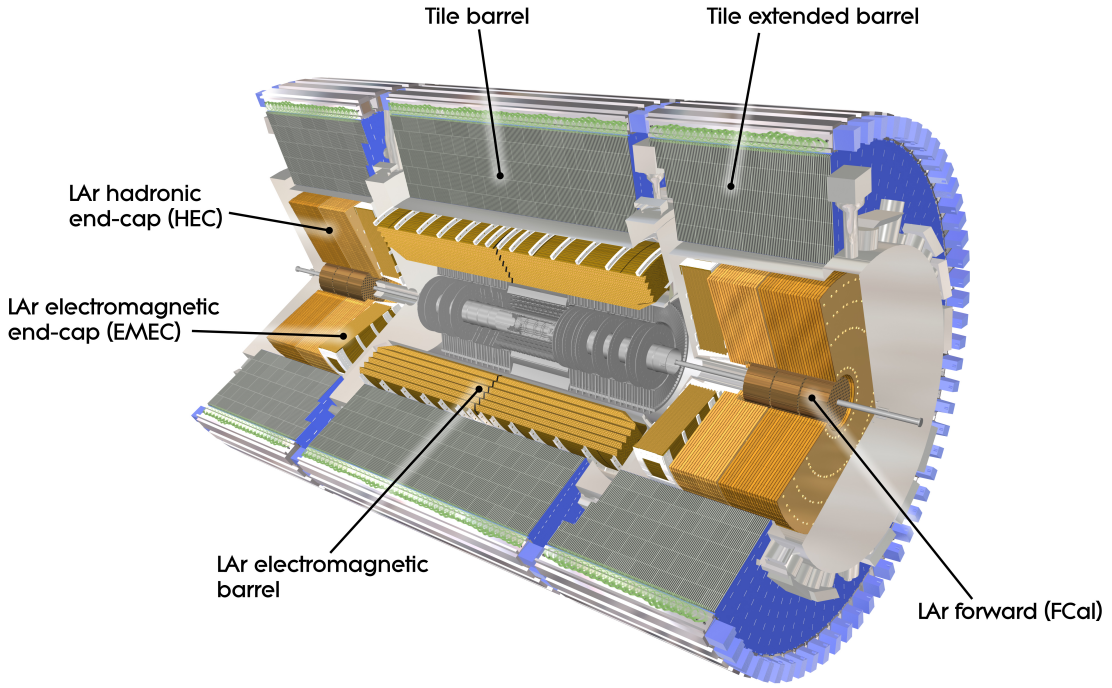

FIGURE 4.9: Computer generated image of the ATLAS calorimeter [151].

proportional to the energy deposit by the incident particle. In addition, the energy of the primary particle is proportional to the number of particles in the showers. The 'radiation length', X_0, of a shower through the absorbing medium over which an electron loses energy is then inversely proportional to number of absorber material nucleons squared. The EM calorimeter has a total thickness $> 24X_0$ in the barrel and $> 26X_0$ in the end-caps.

The detector has three LAr EM sampling calorimeters, with pseudorapidity covering $|\eta| < 1.475$ in the barrel, $1.375 < |\eta| < 3.2$ in the two end-caps and $|\eta| < 4.9$ in the forward calorimeters (FCAL). Each end-cap calorimeter is then split between two coaxial wheels: an outer wheel with $1.375 < |\eta| < 2.5$ coverage and an inner wheel with $2.5 < |\eta| < 3.2$ coverage. Both the barrel and end-cap calorimeters have "accordion-like" geometry, which provides complete ϕ symmetry. [119] Its alternating layers consist of an 2.1 mm thick gap of active LAr material and lead absorber material, both naturally resistant to radiation damage, necessary since the ECAL is situated closer to the interaction point than the HCAL.

The EM calorimeter is preceded by a presampler detector [152], to correct for any loss of energy throughout the material. Various 'preshower' detection, such as γ/π^0 or e/π separation enhances particle identification in the strip section of the EM calorimeter and allows for a precise η measurement [153].

EM CALORIMETER	**Barrel**	**End-cap**	
Coverage	$\|\eta\| < 1.475$	$1.375 < \|\eta\| < 3.2$	
Longitudinal segmentation	3 samplings	3 samplings	$1.5 < \|\eta\| < 2.5$
		2 samplings	$1.375 < \|\eta\| < 1.5$
			$2.5 < \|\eta\| < 3.2$
Granularity ($\Delta\eta \times \Delta\phi$)			
Sampling 1	0.003×0.1	0.025×0.1	$1.375 < \|\eta\| < 1.5$
		0.003×0.1	$1.5 < \|\eta\| < 1.8$
		0.004×0.1	$1.8 < \|\eta\| < 2.0$
		0.006×0.1	$2.0 < \|\eta\| < 2.5$
		0.1×0.1	$2.5 < \|\eta\| < 3.2$
Sampling 2	0.025×0.025	0.025×0.025	$1.375 < \|\eta\| < 2.5$
		0.1×0.1	$2.5 < \|\eta\| < 3.2$
Sampling 3	0.05×0.025	0.05×0.025	$1.5 < \|\eta\| < 2.5$
PRESAMPLER	**Barrel**	**End-cap**	
Coverage	$\|\eta\| < 1.52$	$1.5 < \|\eta\| < 1.8$	
Longitudinal segmentation	1 sampling	1 sampling	
Granularity ($\Delta\eta \times \Delta\phi$)	0.025×0.1	0.025×0.1	
HADRONIC TILE	**Barrel**	**Extended barrel**	
Coverage	$\|\eta\| < 1.0$	$0.8 < \|\eta\| < 1.7$	
Longitudinal segmentation	3 samplings	3 samplings	
Granularity ($\Delta\eta \times \Delta\phi$)			
Samplings 1 and 2	0.1×0.1	0.1×0.1	
Sampling 3	0.2×0.1	0.2×0.1	
HADRONIC LAr		**End-cap**	
Coverage		$1.5 < \|\eta\| < 3.2$	
Longitudinal segmentation		4 samplings	
Granularity ($\Delta\eta \times \Delta\phi$)		0.1×0.1	$1.5 < \|\eta\| < 2.5$
		0.2×0.2	$2.5 < \|\eta\| < 3.2$
FORWARD CALORIMETER		**Forward**	
Coverage		$3.1 < \|\eta\| < 4.9$	
Longitudinal segmentation		3 samplings	
Granularity ($\Delta\eta \times \Delta\phi$)		$\sim 0.2 \times 0.2$	

TABLE 4.6: A table summarising the various calorimeters, sampling unit and hadronic components their including η coverage [135].

4.5.2 Hadronic Calorimeter

The hadronic calorimeters (HCAL) [149], covering the pseudorapidity $|\eta| < 4.9$, consist of barrel and extended barrel tile calorimeters in the $|\eta| < 1.7$ range, the

end-cap calorimeter in the range $1.5 < |\eta| < 3.2$ and forward calorimeter in the range $3.1 < |\eta| < 4.9$. The HCAL measures the energy loss from the more complex hadron showers with many different particle components, through alternating layers of LAr active material and copper absorber material in the end-caps. The HCAL's 11 hadronic interaction-length (λ) thickness and additionally 1.5 λ from outer support allows the hadronic showers to be contained and reduce their punch-through into the muon chambers. In addition, with large η coverage this also provides a good missing transverse energy (see section 4.7) measurement, important for BSM searches including DM signatures [154].

The hadronic barrel calorimeter, consisting of one barrel and two extended barrels, is a sampling calorimeter made of iron absorber and scintillating tiles as its active material. The radiation-resistant LAr is used in the end-caps as they are more exposed to radiation than the barrel region due to their proximity to the beam pipe. Scintillation, where light is emitted by a sampling calorimeter as a charged particle passes through it, occurs in the barrel sections with their scintillating tiles as the active material and steel absorber material. Photo-multiplier tubes (PMTs) utilise the photo-electric effect to measure photon-scale light, proportional to the energy of the shower-initiating particle and convert this into digital signals. A series of dynodes, electrodes in a vacuum tube, then act as a multiplier for the generated current through secondary emission.

4.6 Muon Spectrometers

The muon spectrometers [155], designed to measure unique energy deposits from uninterrupted propagating muons, surround the calorimeters as the outermost layer of the detector. The muon spectrometers consist of many chambers: the thin-gap chambers for triggering and non-bending measurement, the cathode strip chambers for measuring coordinates at the end of the detector, and resistive plate chambers for triggering and coordinate measurements in the central region. In addition, monitored drift tubes are in place to measure the exact trajectory of the muons.

Toroid magnets in the barrel and end-caps generate a 4 T magnetic field to curve the muon trajectory. The full layout of the muon detector subsystems is given in Fig.4.10. Utilising the muon's small energy deposits (per distance travelled) left within the calorimeters, the muon tracks found in the ID can be matched to those in the muon spectrometer.

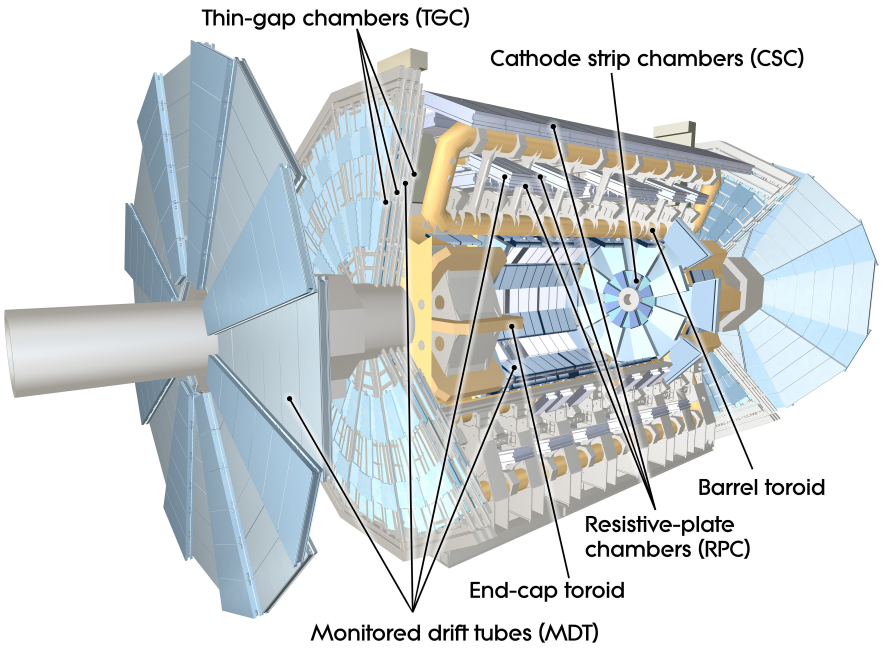

FIGURE 4.10: Computer generated image of the ATLAS muon detector subsystem [156].

4.7 Missing Transverse Momentum Resolution

Missing transverse momentum, or missing transverse energy E_T^{miss} is defined as the negative of vector sum of p_T of visible particles in the final state. Given that the initial, and therefore final, total transverse energy of collisions should equal zero, missing transverse energy, e.g. in the form of undetectable neutrinos, can be reconstructed from a non-zero sum of transverse energy in the final state. For the ATLAS detector, the performance of missing transverse momentum resolution therefore depends on the detector's general performance of transverse momentum resolution, in addition to information from each sub detector to aid in reconstruction. This is particularly important for background searches for BSM signatures involving invisible particles such as DM, which would show up in the detector as missing energy (plus associated SM decay products). The calculation for E_T includes the physics objects: electrons, photons, muons, τ-leptons and jets. The reconstructed momentum associated to soft terms is reconstructed with calorimeter energy deposits or tracks [157]. However, the main algorithm for Run-2, the Track Soft Term (TST), fully relies on tracks for reconstruction.

Pile-up is removed for good E_T resolution, with the jet-vertex-tagger (JVT) technique. This uses a track-to-vertex association method to extract pile-up jets. Fig. 4.11 shows the missing transverse momentum resolution for different pile-up suppression methods.

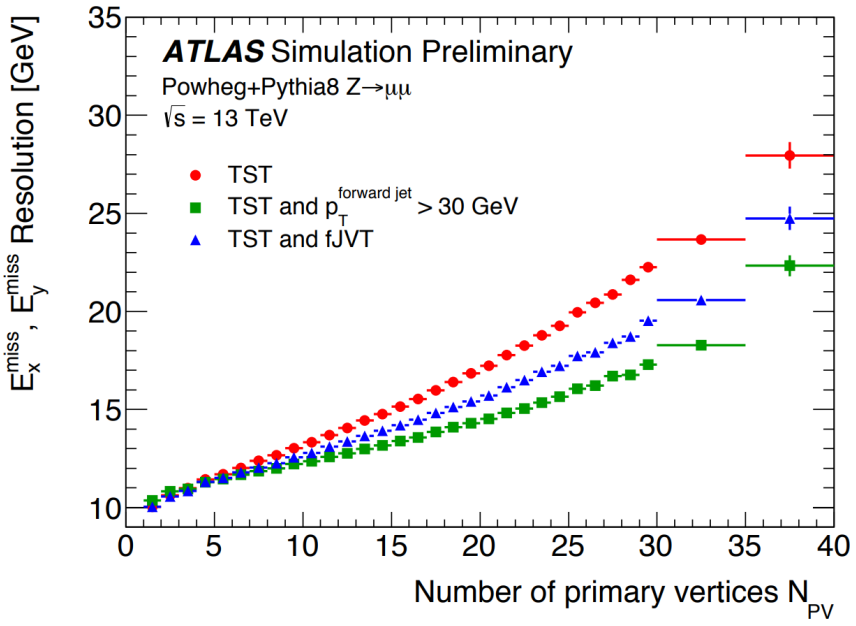

FIGURE 4.11: Missing transverse momentum resolution E_x^{miss}, E_y^{miss} as a function of the number of primary vertices N_{PV} measured in $Z \rightarrow \mu^+\mu^-$ simulation for three different pile-up suppression methods with TST [158].

4.8 Trigger Systems

The trigger systems [159] in ATLAS discriminate the large number of events being recorded by applying cuts, thus reducing unwanted background interactions that would be impossible to store in their entirety. There is finite data-processing speed, so sensitivity of the detection medium is prioritised for interesting physics processes. The trigger system consists of hardware components, including the L1 calorimeter L1Calo trigger searching for energy clusters in the calorimeters, L1Muon system corresponding to the muon systems, and L1 Topological (L1Topo) which takes combined data from the L1Calo and L1Muon, passing it through the central trigger processors. To account for the limitations of this hardware, the trigger system also consists of software, the High level trigger (HLT). Information from the L1 system is then read by high-speed software within a 2.5 μs time interval, to further accept or reject events based on passing an extensive set of cuts in the trigger algorithm. The L1 trigger makes decisions on limited information, operating at 40 MHz bunch crossing rate and accepts events below the rate of 100 kHz. The HLT then further reduces in order to record complete physics events to disk at about 1 kHz [160].

4.9 ATLAS Object Reconstruction

All physics objects necessary for any ATLAS analysis are initially reconstructed and identified using a combination of detector information. They aim to represent the particles that have travelled through the detector, originating from the initial proton-proton collision. Algorithms have been developed for reconstruction and identification of physics objects, initially to run on simulated MC samples, but have since been optimised for data. Reconstruction of particles within ATLAS have also been improved over the years, to better trace-back the final state objects found in the detector to their particle shower's origin and to keep up with changing energy and pile-up conditions. Reconstruction consists of two main stages.

Before these two stages and reconstruction proper is the initialisation stage. This stage involves obtaining the global coordinates of hits and cells from the GEANT or ATLAS geometry database (AMDB) routines. The map of the magnetic field is loaded, designed to be as realistic as possible throughout most of the detector. The main program itself is run by datacards allowing a wide variety of setting and parameters, such as package choice, noise levels, thresholds, efficiencies, and algorithm parameters. Following this, the first of the two stages to the reconstruction process is Stand-alone reconstruction. Signals from the detectors are reconstructed into objects in a stand-alone mode, where matrices in the calorimeter cells are filled, jets are built from algorithms and E_T^{miss} is calculated using the sum of the cell transverse energies.

The magnets surrounding the inner detector curve the paths of charged particles, such that their charge and momentum can be measured from the sign of their trajectory curvature and the bending radius respectively. Note that, for high p_T particles, their trajectory will typically curve less than lower p_T particles, resulting in more uncertainty in measuring their momentum and possible charge mismeasurement. As charged particles pass through different layers of the tracking detectors, these being pixels and strips, their position in each layer is precisely recorded, and labeled as *hits*. These hits are then categorised into particle trajectories called tracks, using pattern-recognition track-fitting algorithms. Algorithms such as a Kalman Filter [161] use complete knowledge of the track parameters at each detector layer to acquire a compatible measurement in the following detector layer. The initial collision vertex can then be reconstructed by extrapolating each track back to its point of origin.

Electromagnetic clusters are reconstructed in the barrel and end-cap EM calorimeters, while electron/gamma identification is performed using shower-shape variables. Electrons are then reconstructed from a combination of their short, curved charged tracks leading to ECAL energy deposits with unique electromagnetic shower shape. Difficulty can arise when distinguishing electrons from misidentified jets/photons or those from non-prompt sources, such as photons producing electron-positron pairs (photon conversion), charged pion decays or semi-leptonic heavy-flavour decays.

Discriminating variables, including the shower width, number of hits, the fractions of energy deposits in each calorimeter layer, impact parameters, energy leakage into the hadronic calorimeter and the quality of the track fitting help uniquely identify electrons. The shower shape variables, for example, take advantage of the lateral and longitudinal segmentation of the calorimeters. Electrons can also only be detected within the tracker requirements of $|\eta| < 2.5$, and minimum p_T thresholds are used to obtain better selection efficiency and calibration [150].

Since photon are not charges, they are reconstructed using the combination of energy deposits in the ECAL and the absence of a corresponding track. Misrecontruction of jets or electrons as photons, or non-promt photons from hadron decays can be discriminated from 'real' photon events using shower-shape variables. Converted photons can also be distinguished from unconverted photons as they typically have at least one track originating from a vertex, while unconverted photons do not. Photons also require to be detected within the $|\eta| < 2.5$ tracking volume, as their reconstruction requires the absence of a track.

Muons are much heavier than electrons, leaving only a small fraction of energy in the ECAL electromagnetic interactions and do not interact with the atomic nuclei of the calorimeter material. Therefore, they must be reconstruced with the use of the specialused muon chambers. Muons are reconstructed in terms of track segments, within the muon system using a combination of searches, single-station track segments and fits performed on the hits. Multiple scatterings in the apparatus material are taken into account by the use of a non-homogeneous magnetic field for tracking. A list of tracks and parameters tracing back to the interaction point are then given in the final analysis. The presence of low p_T muons can also be interpreted from the list of track segments in the inner stations, only achievable to high enough precision in combined reconstruction. Muons must also be detected within $|\eta| < 2.5$ and some minimum p_T thresholds. Particularly energetic pions may sometimes pass through the HCAL, and be stopped in the muon chamber, resulting in a fake muon.

Following the stand-alone reconstruction is when this combined reconstruction is performed, where the final objects, such as photons, leptons, jets, E_T^{miss}, primary vertex, etc. are reconstructed from the combined data gathered from every detector. Muon reconstruction is also further refined at this stage, where its muon system track is matched to an Inner Detector track for improved momentum resolution (especially for low p_T). High p_T electron identification requires a reconstructed track using transition-radiation hits from the Inner Detector's TRT, and requires the measured momentum to match a corresponding calorimeter energy deposit.

Charged and neutral hadrons, originating from quarks or gluons, travel further than electrons or photons due to them being heavier, and deposit energy in the HCAL. Charged hadrons also leave tracks. Jets are then reconstructed from collections of

collimated bunches of hadrons. Hadrons originating from ISR, FSR, MPI and pile-up also become part of jets. Jets need to be detected within the expanse of the calorimeter, and with some minimum p_T thresholds. Jets are reconstructed using clustered cells, with a default cone size of 0.4. Any clusters that are not associated with an isolated electron or photon have their energy smeared with the energy resolution [162]. Once a jet is formed, these are then use to characterise parts of events, instead of using their individual hadron components. In addition, $\tau-$leptons are identified from narrow jets with a small number of charged tracks.

Particle flow objects use charged particle track information to provide better angular resolution. Tracks are matched to energy clusters in the calorimeters and the calorimeter signals associated with the tracks are either fully removed (the whole cluster) or partially removed (some cells from the clusters). The charged, matched or unmatched tracks and the original, neutral particle flow objects are used as inputs for the jet forming algorithm [163].

When tagging jets containing B mesons, or originating from b-quarks, b-tagging techniques identify these by utilising the unique properties of these objects. B-hadrons have a longer lifetime compared to pions, and so travel further, while b-quarks are heavier than all other flavours, excluding the tau. The b-quark also has a 10% branching fraction to leptons. A secondary vertex can therefore be identified associated to B-hadron decay and, in combination to its other unique properties, a jet containing a B-hadron, or originating from a b-quark can be identified This is also assisted by requiring certain selection cuts. These include $p_T(j) > 5$ GeV, $\Delta R = 0.2$ around the reconstructed jet for jets with $|\eta| < 2.5$ [162].

With the LHC, ATLAS detector and its many sub-detectors now described in detail, the analyses and measurements of the collider background processes are presented, starting with measurements on the Z boson production in association with high transverse jets in the following section.

Chapter 5

Production of Z boson in association with high-transverse-momentum jets

The production of a Z boson in association with jets is not only a powerful test for perturbative QCD (pQCD), but also allows us to probe the complex interplay between QCD and higher-order EW processes, in the case of high-p_T jets. The leptonically decaying Z (to both $\ell^+\ell^-$ and $\nu\nu$) also produces a clean signal, that can be precisely measured and contributes a significant background to both Higgs physics and BSM searches (such as $Z \to \nu\nu$ process).

In the first case considered for this analysis, $Z + 1$-jet at leading order, the Z recoils against a quark or a gluon. In the case of NLO, real and virtual QCD and EW effects correspond to contributing topologies of dijet events where Z is emitted from an incoming or outgoing quark. Two example diagrams for these processes are given in Fig.5.1.

A key observable sensitive to collinear Z emissions includes the angular distance between Z and the closest jet, $\Delta R^{min}_{Z,j}$ The collinear region corresponds to $\Delta R^{min}_{Z,j} \leq 1.4$ where real Z emission is enhanced, while the back-to-back region corresponds to $\Delta R^{min}_{Z,j} \geq 2.0$ where the large EW corrections and recoiling jet are expected.

Another variable of interest includes the ratio of the Z boson p_T ($p_{T,\ell\ell}$) to the closest-jet p_T, defined as

$$r_{Z,j} = \frac{p_{T,\ell\ell}}{p_T(closestjet)}. \tag{5.1}$$

The collinear emission will have small $r_{Z,j}$ values, since it is dominated by events with soft Z production. Finally, the jet multiplicity, N_{jets}, aids in distinguishing

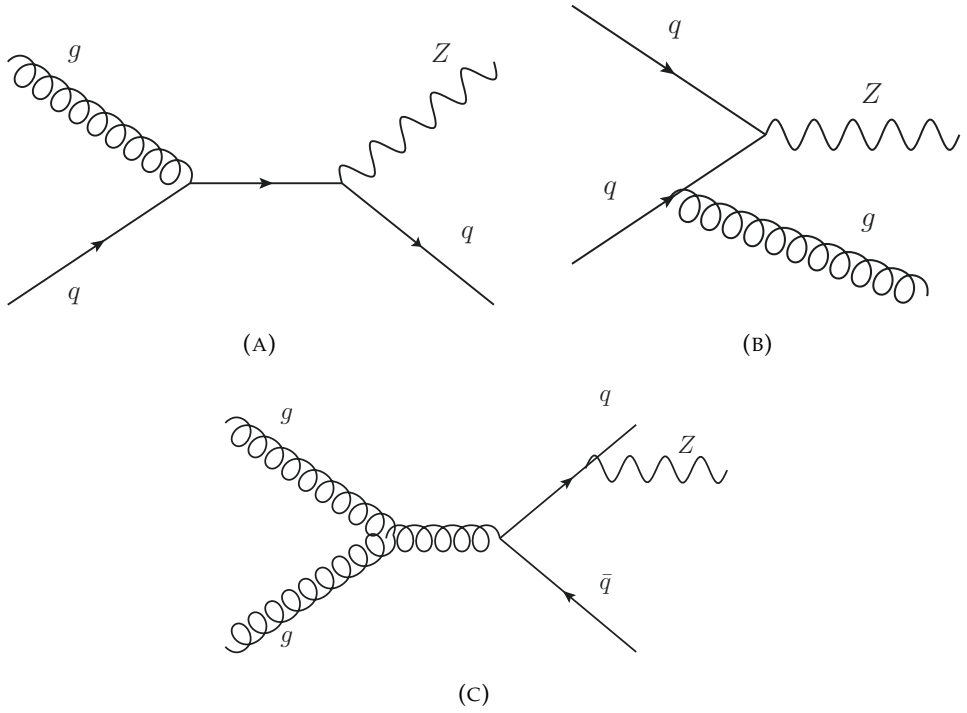

FIGURE 5.1: Examples of Feynman diagrams for LO $Z+1$-jet production (a), NLO Drell-Yan $Z+1$-jet (b) and NLO $Z+2$-jet contributing diagram (c). Diagram (a) represents the majority of the back-to-back region processes, with (b) at NLO, while diagram (c) makes up the diagrams in the collinear region, where the angular distance between the Z and closest jet, $\Delta R^{min}_{Z,j}$, is small

back-to-back and collinear events, where it is expected to observe $Z+1$-jet and $Z+2$-jet events respectively.

In summary, for the selection phase space requiring jets with $p_T(jet) > 100$ GeV, the observables we measure include $p_T(leading\ jet)$, $p_T(Z)$, jet H_T, exclusive and inclusive jet multiplicity. For the high p_T selection phase space of $p_T(leading\ jet) > 500$ GeV, we measure $\Delta R^{min}_{Z,j}$, high-p_T $p_T(Z)$, $p_T(Z)/p_T(jet)$ high-p_T exclusive and inclusive jet multiplicity..

5.1 Event Selection

Events are selected using triggers [164–166] shown in Table 5.1, requiring at least two electrons, two muons or a combination of one electron and one muon. The trigger efficiencies plateau for $p_T > 25$ GeV. Electrons must satisfy the 'PflowLoose' [167] isolation requirements and the 'Medium' likelihood-based identification criteria from [167]. Electrons are selected for the analysis if they satisfy $p_T \geq 25$ GeV and $|\eta| < 1.37$ or $1.52 < |\eta| < 2.47$. Muons must also satisfy the 'PflowLoose' isolation requirement, while needing to pass 'Medium' identification criteria [168, 169]. To

Electron channel	
2015	HLT_2e12_lhloose_L12EM10VH
2016	HLT_2e17_lhvloose_nod0
2017-2018	HLT_2e24_lhvloose_nod0
Muon channel	
2015	HLT_mu18_mu8noL1
2016	HLT_mu22_mu8noL1
2017-2018	HLT_mu22_mu8noL1
Top validation region	
2015	HLT_e17_lhloose_mu14
2016-2018	HLT_e17_lhloose_nod0_mu14

TABLE 5.1: Triggers used for the various channels and taking periods for the collinear Z+jets analysis [170].

improve muon p_T resolution, muons with $p_T \geq 300$ GeV require tighter identification criteria. Muons are therefore selected for the analysis if $p_T \geq 25$ GeV and $|\eta| < 2.4$.

Jets are reconstructed using a particle flow algorithm [163] and are clustered using the anti-k_t [88] algorithm within the FastJet package [171] with a radius parameter $R = 0.4$. For jet selection, we require at least one jet, with jets needing $p_T > 100$ GeV and $|y| < 2.5$.

Overlap removal procedures are applied to uniquely identify the independently reconstructed electrons, muons and jets. To preselect jets with a higher probability of being initiated by an electron or radiated photon, we consider softer jets ($p_T \geq 30$ GeV, $|y| < 2.5$) and remove all jets within $\Delta R < 0.2$ of a dressed[1] lepton. Following this, we remove leptons within $\Delta R < 0.4$ of any remaining jet. We apply a Z mass-window cut to select events with a Z boson reconstructed from e^+e^- or $\mu^+\mu^-$ pair, with 71 GeV$\leq m_{\ell\ell} \leq$ 111 GeV. Finally, in addition to the inclusive $Z+$ jets region, for the high-p_T region we select events with at least one $p_T \geq 500$ GeV jet. We then split this region into a collinear region, where $\Delta R^{min}_{Z,j} \leq 1.4$ and a back-to-back region, requiring $\Delta R^{min}_{Z,j} \geq 2.0$ [42].

The following sections detail my unique contributions to the collinear Z+jet production analysis, including non-perturbative checks, data-driven background $t\bar{t}$ and multijet modelling. These are then followed by unfolded cross-section results of the analysis.

5.2 Theory Predictions and Non-perturbative Corrections

Four different generators are utilised for this particular analysis. Two of these, `Sherpa 2.2.1` [172–181] 0-2p (parton) NLO, 3-4p LO and MadGraph `MG+PY8` [182–185] 0–4p

[1]Dressed leptons are defined as four-vector combinations of prompt leptons, not originating from hadron decay, τ-leptons or photon conversions, and prompt photons within a $\Delta R < 0.1$ cone.

LO with CKKW-L [184] matching are fully simulated. The two new generators studied, `Sherpa 2.2.11` [173–181, 186–188] and MadGraph at NLO with FxFx matching, `MG+PY8 FxFx` [182, 186, 188–192], were then introduced at a later stage of the analysis. The purpose of using these different generators are threefold. The primary reason is to cross-validate the unfolding procedure. We unfold using `Sherpa 2.2.11` and therefore results from these generator studies should agree with our final unfolded cross sections. Secondly, it is to compare the performance of each generator, within the high-p_T region. This gives insight into which generator requires additional development to provide more precise predictions, especially for a phase space that is typically difficult to model precisely. Thirdly, they are used to calculate the non-perturbative corrections to be detailed in this section. In this analysis we unfold to the hadron level. However, since some fixed-order predictions are given at parton level, and many other analyses unfold to the parton level, we may require corrections to account for the differences between hadron and parton level measurements. For the theory predictions presented, non-perturbative corrections should be provided to communicate with theorists the appropriate scale factors to apply, when considering the differences between parton-level and hadron-level results. The corrections address multi-parton interactions (MPI) and hadronisation effects. I demonstrate in the following section that the MPI and hadronisation corrections are negligible for the high-p_T regions this analysis considers.

In the following sections, the MC generators and common settings used for the theory predictions and non-perturbative corrections are first detailed. The generator performances are then compared and commented on. Following this, the setup for computing non-perturbative corrections is described and correction plots are performed to show their negligible impact for the high p_T region.

5.2.1 MadGraph+Pythia 8 CKKW-L (LO) Generation

The leading order samples produced with MadGraph 5 [193], with JobOptions found at [194], use the following parton level settings. The dilepton invariant mass, M_{ll}, has a minimum threshold cut of $M_{ll} > 40$ GeV applied, with 5 maximum jet flavour (such that b-quarks are cut in the same way as other lighter jet flavours). To allow for up to 4 jets in the matrix element calculation, *nJetMax* is set to 4. The *ktdurham* variable describes the merging scale used by MadGraph for merging the produced LHE files, which is set to 30 GeV. The D parameter for these events, required by the longitudinally invariant k_T separation definition, is set to 0.4. Using the SM mode with no b-quark mass, the proton and jets are defined as including gluons, up, charm, down, strange, bottom quarks and antiquarks. The incoming protons are then simulated with the NN23LO1 PDF [192, 195] set. Minimum cuts on $p_T(j)$ and $p_T(b)$ are at > 20 GeV. Meanwhile $\eta(l)$ is cut at > 10, and $\eta(b)$ $\eta(j)$ are both cut at > 6. Then

for Pythia 8 [183], *CKKWL kTMerging* as described in section 5.2.3 is used for parton showers and jet matching.

For the H_T slicing procedure applied at the generator level, these are split into 8 ranges: $0 < H_T < 70$ GeV [196], $70 < H_T < 140$ GeV [197], $140 < H_T < 280$ GeV [198], $280 < H_T < 500$ GeV [199], $500 < H_T < 700$ GeV [200], $700 < H_T < 1000$ GeV [201], $1000 < H_T < 2000$ GeV [202] and $H_T > 2000$ GeV [203]. The default initial number of events generated for the respective H_T slicing are 200,000 events for low $HT < 140$ GeV, 50,000 events for low-mid $140 < H_T < 500$ GeV, 20,000 events for mid $500 < H_T < 1000$ GeV, and 8,000 events for high $H_T > 1000$ GeV. These are then further split into three classes: C-Vetoed and B-Vetoed (remove both c-hadron and b-hadron events) [196], C-Filtered and B-Vetoed (filter for c-hadron and remove b-hadron events) [204], and just B-Filtered (filter for b-hadron events) [205].

5.2.2 MadGraph+Pythia8 FxFx (NLO) Generation

There are two different sets of samples considered, for the inclusive generator comparison and for the high-p_T studies. The previous H_T sliced[2] samples suitable for high-p_T analysis are available up to 2 jets NLO, and 3 jets LO. These are split into the 4 ranges, $200 < H_T < 500$ GeV [206], $500 < H_T < 800$ GeV [207], $800 < H_T < 1500$ GeV [208] and $1500 < H_T < 13000$ GeV [209]. The current generation, used for the inclusive comparisons includes up to 3 jets NLO, and up to 4 jets at LO [210]. The $qCut = 30$ GeV is set for the merging scale. The CKKW merging for LO, with definition of longitudinally invariant k_T is used, and hyperbolic function of pseudorapidity of partons. In this case, a reweight scale is used, with parameters rw Rscale down $= 0.5$, rw Rscale up $= 2.0$, rw Fscale down $= 0.5$, rw Fscale up $= 2.0$, and reweight PDF applied. With the $M_{\ell,\ell} > 40$ GeV cut in place, a jet radius is set to 1.0, and cuts on $p_T(j)$,$\eta(j)$ of 10 GeV are also applied. This production then takes advantage of the new Pythia 8 FxFx merging for NLO, as detailed next in section 5.2.3.

5.2.3 Matching/Merging: CKKW-L and FxFx

When introducing higher orders to the base level Born, leading order process, the merging procedure combines two methods to achieve accurate results at multiple scales. Carrying out perturbative expansion for every order, adding more final state particles and intermediate loops is limited to only a few orders. One must neglect virtual and loop corrections for higher orders, and is prone to double counting, while being invalid for soft and collinear phase spaces. This is the matrix element generation, used for the hard production. Applying parton showers, which include

[2] H_T is defined as the scalar sum of final state jet transverse momenta p_T.

real and virtual emissions for higher orders, can describe the soft and collinear regions well. [79, 180]

With a tree-level matrix element generated process, and the same process with up to N additional partons, regularisation is applied via a cut on the jets. This is a merging scale t_{MS}, where a parton shower with emissions below this scale is added to the hard partons to model the soft and collinear emissions more accurately. Re-weighting is required to make the samples exclusive, since the matrix elements are currently inclusive with n additional partons above the t_{MS} scale. The probability of no emissions used by patron showers that would have produced the same partonic state are the Sudakov form factors [211] used for this re-weighting. These are calculated by reconstructing the history of the parton showers from the final state, from the matrix element generation. [212]

Different matching/merging methods are defined by which matrix elements are used, the methods for preventing double-counting, and the scale at which one shifts between the hard and soft scale, governing the switch between the matrix element method to the parton shower method.

The **CKKW-L** [185] method reconstructs all possible parton shower histories, and then, based on the probabilities from the splitting functions, applies the appropriate parton shower. The Sudakov form factor, giving the probability of no parton shower emissions from states S_{+i} between scales ρ_i and ρ_{i+1} is

$$\Delta_{S_{+i}}(\rho_i, \rho_{i+1}) = \exp\left[-\int_{\rho_{i+1}}^{\rho_i} d\rho \int dz \alpha_s(\rho) P_i(\rho, z)\right]. \tag{5.2}$$

Generating one parton shower emission from an intermediate state S_{+i} below the maximum scale ρ_i, the event is removed if the probability of emission is above $\rho_i + 1 = 1 - \Delta_{S_{+i}}$, which is an application of the re-weighting. When the merging scale is about to be reached, the final emission scale must be treated carefully if the parton shower ordering variable is not used as the matrix element cut-off. For $n < N$ the event is removed if the emission probability is above the matrix element cut-off. For $n = N$, no Sudakov re-weighting is applied, and the event is not removed.

When merging the matrix element and parton shower regions, the CKKW-L algorithm minimises the dependence on the scale at which this merging takes place. The combination of matrix element generated events and parton shower events must fill the entire phase space of interest to do this. This means, unless the hard process is particularly divergent, additional cuts on the parton level generation should be avoided, making the merging scale cut the most stringent cut out of any others applied to the partons involved.

The **FxFx** [189] method describes the NLO merging procedure used by MadGraph in aMC@NLO. This uses the subtraction method from the fixed-order generation at NLO

for removing excess parton showers. Once showered, this gives NLO accurate results for inclusive observables. The shower emission probabilities are needed in order to correctly extend the subtraction scheme from the NLO fixed order result. This results in a competitive NLO+parton shower (NLO+PS) matching scheme, for which Pythia can speed up shower subtractions, by generating emissions with a recoil scheme, a recoil of emission given globally for all final states.

5.2.4 Sherpa 2.2.1 Generation

The samples generated with `Sherpa 2.2.1` [172] follow the similar C,B filters, vetoes and H_T slicing to the MadGraph samples. Sherpa generation uses 0, 1 and 2 jets at NLO, in addition to 3,4 jets at LO. The OpenLoops [174] plugin is used for one-loop matrix elements. The squared factorisation, renormalisation and resummation scale factors $FSF = 1$, $RSF = 1$ and $QSF = 1$ are set for scale variation. The METS scale setter is used to set a threshold to cease clustering when either no combination of jets can be found that match the given parton shower branching, or two subsequent branchings are not ordered with respect to the parton shower evolution parameter. [172] Then, using the $METS$ scale setter, the scale at which the parton shower resummation in a matrix element + parton shower (ME+PS) merged sample is started, is $STRICT\ METS$, $FSF * \mu_{F^2}$, $RSF * \mu_{R^2}$, $QSF * \mu_{Q^2}$, where $STRICT\ METS$ clusters using the inverse of the parton shower [172].

While the multiplicity of the NLO sub-processes is set with *NJET=3*, the maximal number of extra jets is chosen with *LJET=2,3,4*, and the merging cut with $Q_{CUT} = 20$ GeV. The matrix element generation settings are for AMEGIC [213], while Comix [173] more efficiently handles the subtracted real-emission NLO matrix element part and loop generation is controlled by OpenLoops.

CKKW matching is used, with a separation cut of $\sqrt{Q_{CUT}/E_{CMS}}$. The max number of quarks is set to 4, while *Max Epsilon* which defines the epsilon used for maximum weight reduction is set to 0.01. *Integration Error* of 0.99 sets the target integration error for certain processes per final state multiplicity. A minimum cut of the final state leptons of $M_{\ell\ell} > 40$ GeV is then set. Fastjet is switched on, with standard antikt settings $p_T(j) > 20.0$ GeV, and $dR > 0.4$.

5.2.5 Sherpa 2.2.11 Generation

The newer version of Sherpa used for generation, `Sherpa 2.2.11` [214], includes many improvements over `Sherpa 2.2.1`, with the generation now including up to 5 jets leading order, in addition to the 2 jets NLO. The most notable of which is the LO and NLO EW corrections, with the associated contributions variation parameters. A

new EW input scheme is also introduced, to improve certain Z+jets angular variables. These are all applied on-the-fly, in addition to on-the-fly ME + PS scale variations [172] for which `Sherpa 2.2.1` only has ME variations.

The most impactful update between `Sherpa 2.2.1` and `Sherpa 2.2.11` for this particular analysis is the way unordered emissions are treated. The modifications to the scale variation settings gives an improved treatment of these unordered histories, to account for the compensating Sudakov factor. This is done by starting backwards from the born-level process and clustering partons backwards to give a parton shower history. These give nodal values which are then used for the Sudakov rejection factors [181], allowing the renormalisation scale to be deduced.

Other improvements include the NLO subtraction scheme, which has been tuned to improve low p_T^V (p_T of W/Z vector boson [215]) modelling [214]. Changes to the EW correction setup gives a factor 3 increase in speed, while changes to the negative weight fraction results in a factor 2 reduction in negative weights. The associated contributions option has been chosen such that NLO EW virtual corrections are now done in three different approaches. Changes to the enhancement function means there is also continuous enhancement in $\max(H_T, p_T^V)$ (the maximum of the scalar sum of all partonic jet transverse momenta H_T or transverse momentum of the lepton pair p_T^V [216]) [214].

The new version also allows for a mixed shower evolution scheme, where $g \to bb$ is treated massless and $b \to gb$ as massive. Although not used here, for heavy-flavour scenarios, the new 'fused' 4-flavour scheme (4FS) V+bb + 5-flavour scheme (5FS)[3] V+jets prediction is possible.

On the technical side, new statistical enhancement are applied, which replace the original slicing method that could cause problems in some variable distributions when merging.

5.2.6 Generator Comparisons

The purpose of this section is to compare the performances, i.e. the agreement to data, of the four available generators for Z+jets production. The goal is to not only cross validate the unfolding procedure and current generator results, but also to observe the potential improvements from new generators, which should be just as good at representing the data, if not better than the current standard. It is also useful to see how these different generators perform for the high-p_T phase space and selected variables.

[3] 4FS forbids the presence of a b-quark in the initial proton, while 5FS allows the presence of a b-quark in the initial proton. [217]

Using the Rivet [218] library, first the performance is compared against the validated 2017 Rivet analysis [219] for Z plus jets at 13 TeV, 3.16 fb^{-1} [220] integrated luminosity, with comparison to data. The analysis uses the FastJets algorithm with anti-k_T $R = 0.4$, and jet cuts $p_T > 30$ GeV, $|y| < 2.5$. Lepton cuts are $p_T > 25$ GeV, $|\eta| < 2.5$, requiring two charged leptons, in the mass window $71 < M_{ll} < 111$ GeV. There is also a fixed jet, lepton overlap removal with $dR = 0.4$.

The following comparison plots allow for testing the different generators accuracy and improvements in modelling the data, using a more inclusive, reduced kinematic view for a first impression of the full comparison. The representative inclusive observables are inclusive jet multiplicity, N_{jets}, inclusive p_T of the leading jet, p_T^{jet}(leading jet) and scalar sum of jet transverse momenta H_T. These give insight into the more generic generator performance for a wide range of energies. This is then followed by high-p_T observables from the high-p_T event selection, including leading $p_T(jet)$, $p_T(Z)$ and $p_T(Z)/p_T(jet)$. The latter two require leading $p_T(jet) \geq 500$ GeV. Here we can observe how generators perform for energies with a lower number of events, and therefore higher statistical uncertainty.

A "dressed" lepton is defined as the four-vector combination of a prompt lepton (that does not originate from the decay of a hadron, a τ-lepton or from a photon conversion) and all prompt photons within a cone of $\Delta R < 0.1$ to the bare lepton. The particle level also includes jets clustered using the anti-k_t algorithm with radius parameter $R = 0.4$ for final-state particles with decay length $c\tau > 10$ mm, excluding the dressed Z-boson decay products [170].

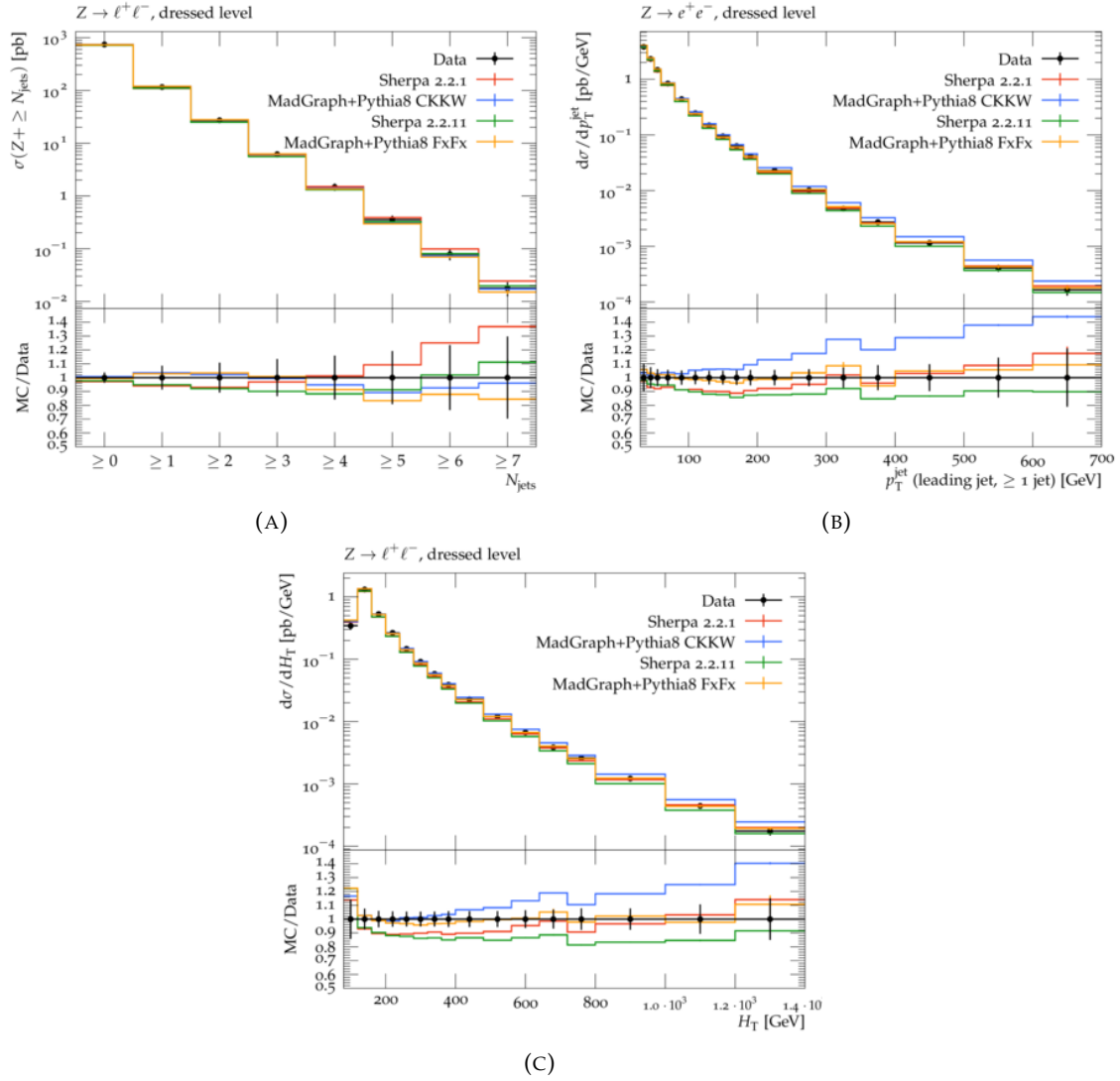

FIGURE 5.2: ATLAS 2017 [219] data and MC comparisons between `Sherpa 2.2.11`, `Sherpa 2.2.1`, `MG+PY8 FxFx` and `MG+PY8 CKKW`, for inclusive jet multiplicity (a), leading jet p_T (b) and H_T (c). The error bars represent statistical uncertainty.

Fig. 5.2 shows the comparisons of inclusive jet multiplicity (a), leading jet p_T (b) and H_T (c) for the four MC generators, these being `Sherpa 2.2.11`, `Sherpa 2.2.1`, `MG+PY8 FxFx` and `MG+PY8 CKKW`. The comparisons in Fig. 5.2(a) show an agreement in inclusive jet multiplicities up to 4 jets, beyond which Sherpa 2.2.1 overestimates data, while Sherpa 2.2.11 the MadGraph generators agree within data uncertainty. The leading jet p_T and H_T plots in Fig. 5.2(b) and (c) respectively show a distinct overestimation of `MG+PY8 CKKW` compared to data and all other generators, demonstrating a great improvement of `MG+PY8 FxFx` and NLO matrix element performance.

Following this, the generators are tested on the Rivet routine produced for this analysis, *collinear Z+ jets production in p − p collisions at 13 TeV*. This analysis uses the FastJets algorithm with anti-k_T $R = 0.4$, and requires jet cuts of $p_T > 100$ GeV, $|y| < 2.5$. Electron cuts are $p_T > 25$ GeV, $|\eta| < 2.47$, and muon cuts of $p_T > 25$ GeV,

$|\eta| < 2.4$, while requiring two charged leptons, in the mass window $71 < M_{ll} < 111$ GeV. There is also a fixed jet, lepton overlap removal with $dR = 0.4$. The following plots compare generator performance for the high-p_T variables relevant for this analysis, and to study differences in a new kinematic phase space. The observables presented in Fig.5.3 include $p_T(leading\ jet)$, $p_T(Z)$ with $p_T(leading\ jet) \geq 500$ GeV and $p_T(Z)/p_T(jet)$ for $p_T(leading\ jet) \geq 500$ GeV (NB: no high-p_T data is currently available for this particular analysis in Rivet).

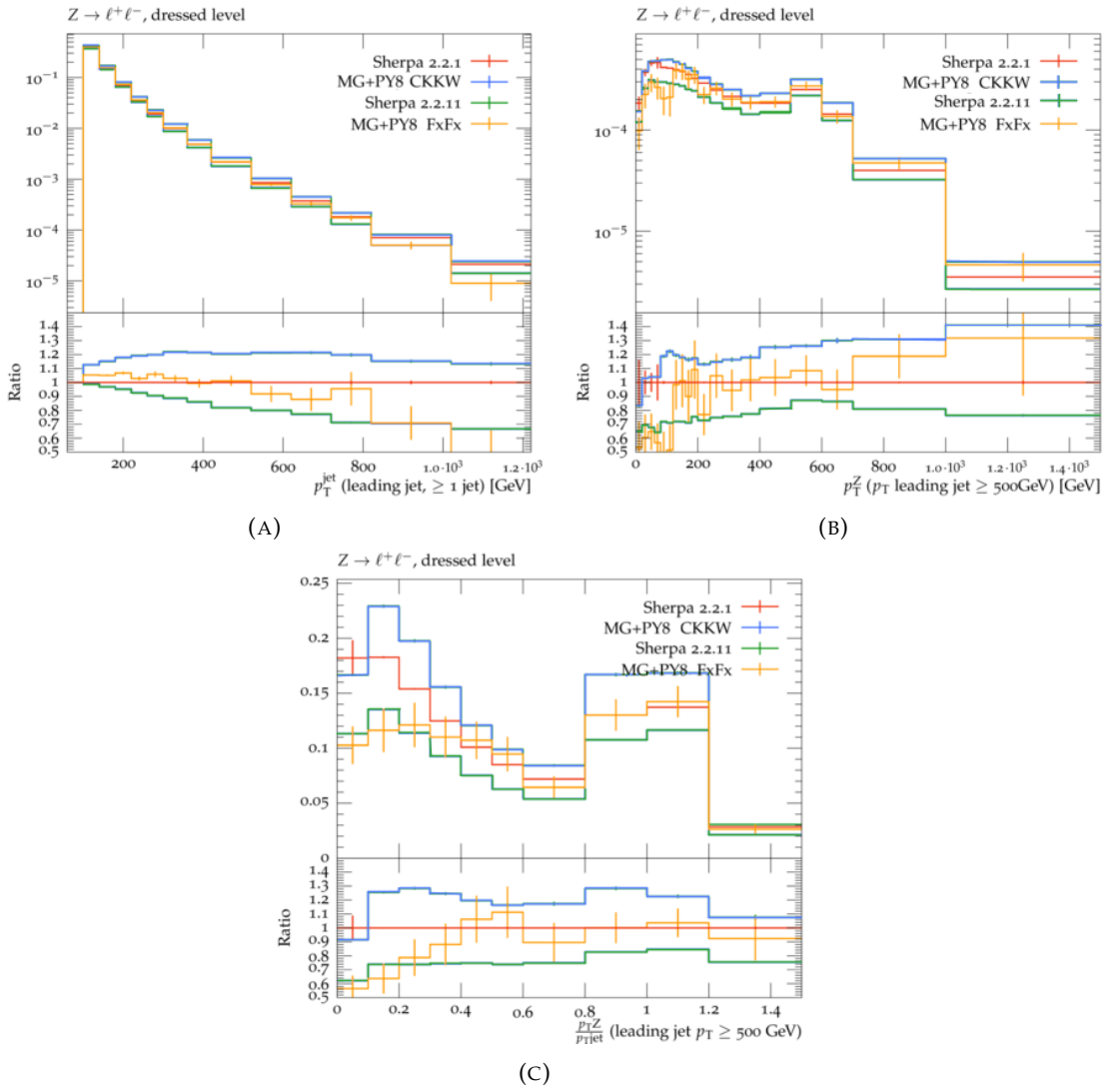

FIGURE 5.3: Comparisons between Sherpa 2.2.11, 2.2.1, Madgraph+Pythia 8 FxFx and CKKW for the high-pT phase space variables, leading jet $p_T \geq 100$ GeV (a), $p_T(Z)$ (b) and $p_T(Z)/p_T(jet)$ (c) for $p_T(leading\ jet) \geq 500$ GeV. The error bars represent statistical uncertainty.

The peak in p_TZ/P_Tjet around 1 comes from the presence of back-to-back events: Z and jet pairs produced with approximately equal p_T.

For the high-p_T selection plots in Fig. 5.3, `MG+PY8 CKKW` predicts a higher cross section in $p_T(jet)$ Fig. 5.3(a) and $p_T(Z)/p_T(jet)$ Fig. 5.3(c) compared to the other generators.

For the $p_T(Z)$ distributions in Fig. 5.3(b), both `MG+PY8 CKKW` and `MG+PY8 FxFx` generators give higher cross sections compared to `Sherpa 2.2.1` generator, while `Sherpa 2.2.11` predicts a lower cross section compared to the previous version in the high-p_T region. The significant error bars in the `MG+PY8 FxFx` distribution represent large statistical uncertainty, due to small number events especially for the high-p_T region.

It can be concluded here that `Sherpa 2.2.11` displays smaller cross sections to `Sherpa 2.2.1` in distributions such as $p_T(Z) > 600$ GeV and $p_T(Z)/p_T(jet) > 1$ for which the QCD and EW effects are non-negligible. Ths is especially true for the high-p_T cases where $p_T(leading\ jet) \geq 500$ GeV, such as in Fig. 5.3(b). Meanwhile, `MG+PY8 FxFx` presents a greater convergence to Sherpa generators for some distributions, over the `MG+PY8 CKKW` results.

Following these comparisons, the non-perturbative corrections are investigated by first detailing the underlying theory.

5.2.7 Multiple-Parton Interactions (MPI) & Hadronisation Effects

As stated in section 2.5.3, it is not sufficient to only consider a single hard interaction per event, but instead to acknowledge the presence of multiple interactions between hadrons, with numerous constituent partons. This leads to additional scattering processes between two separate partons per beam, and individual partons scattering against multiple different partons from the collision partner [221]. The primary effect at large energies occurs when an MPI jet overlaps with harder jets, thus increasing their energy (typically by a few GeV).

Another effect being assessed is hadronisation, which results in wider jets. This is because of processes such as gluon splitting, resulting in wider jets, with a larger angle with respect to the jet axis. It is easier to lose hadrons during the jet clustering if the jet is wider, and so the clustering results in smaller jet energies.

To summarise, there is an opposing effect from both MPI and hadronisation: MPI increases the overall jet energies while hadronisation decreases the jet energies.

5.2.8 Correction Results

To perform the non-perturbative corrections, the combination of MPI and hadronisation effects is assessed. These are handled in Pythia8 by applying the Pythia commands:

```
genSeq.Pythia8.Commands += ["partonlevel:mpi = off",
```

```
"HadronLevel:Hadronize = off"]
```

and for the Athena generate command, appending the option:

```
--postExec='del testSeq.TestHepMC'
```

to remove HepMC production due to the lack of hadronisation required to produce this file.

The hadronisation corrections are then accounted for by O_{parton}/O_{hadron}, where O_{parton} is the parton-level observable (MPI OFF+HAD OFF) used in perturbative calculations and O_{hadron} is the hadron-level observable (MPI ON+HAD ON), the value in calculations of both perturbative and non-perturbative contributions. The combined effect of MPI-off and hadronisation off is less pronounced than MPI-off alone, as the MPI-off effects are partially counteracted by the removal of hadronisation. The MPI-off effects are then suppressed for the higher H_T region.

The first set of plots in Fig. 5.4 utilise the generic $Z(\ell^+\ell^-)+$ jets production, MC_{ZJETS} [222] Rivet analysis for inclusive comparisons. It requires $|\eta| < 3.5$ and $p_T > 25$ GeV for its leptons. It imposes a Z mass window of $65 < m_{\ell\ell} < 115$ GeV and lepton separation ΔR of 0.2. Jets are clustered with anti-k_T with R=0.4 and the default Rivet $p_T(jet)$ cut of $p_T(jet) > 20$ GeV is applied. A fixed jet, lepton overlap removal is applied with $\Delta R = 0.2$ [222]. In the lower ratio pads of Fig.5.4, the blue line indicates the size of the parton/hadron corrections.

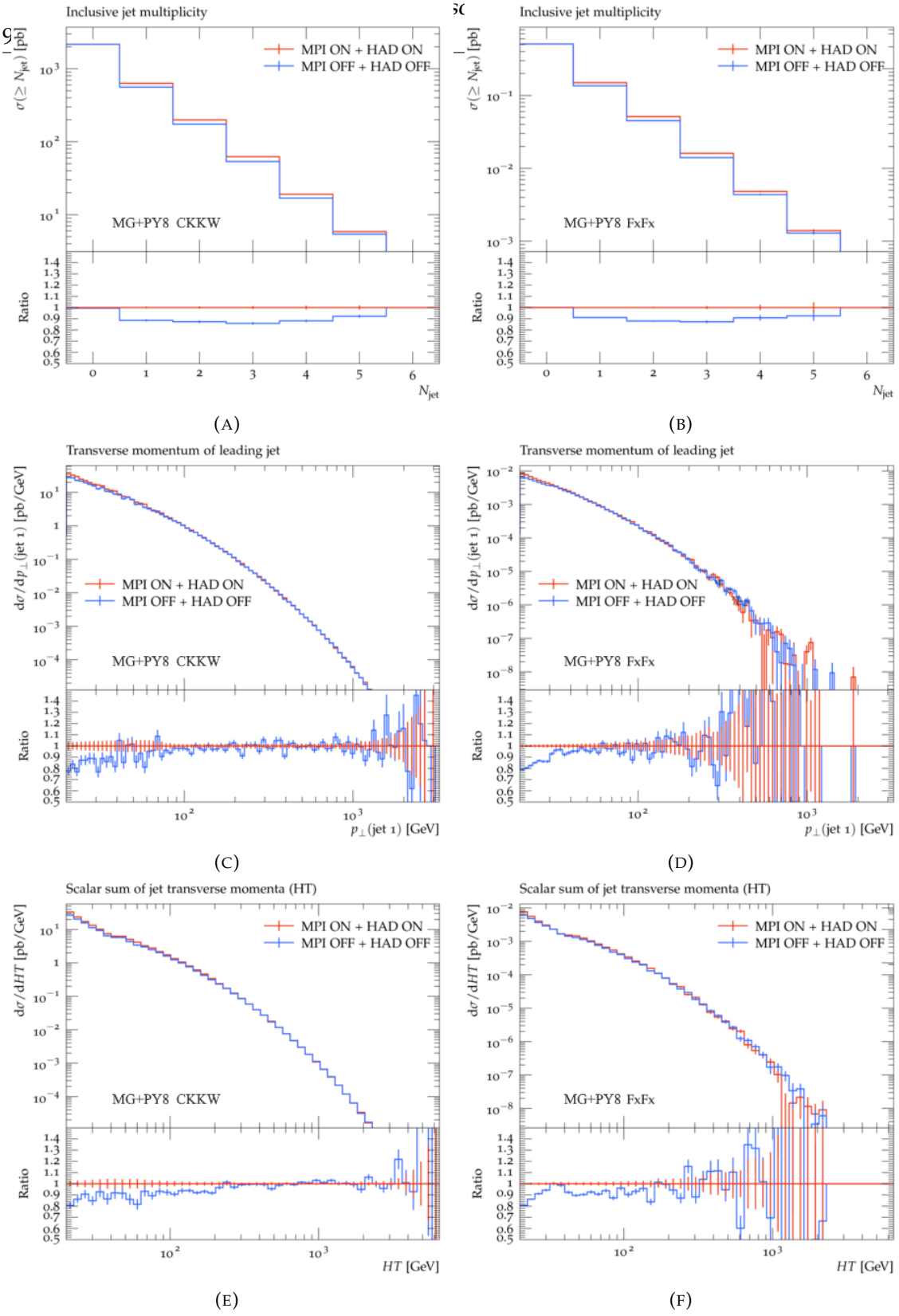

FIGURE 5.4: The MC_ZJETS [222] rivet analysis distributions of jet multiplicity, N_{jet} (a)-(b), p_T of the leading jet $p_\perp$(jet 1) (c)-(d) and H_T (e)-(f) for `MG+PY8 CKKW` samples (left) and `MG+PY8 FxFx` samples (right). The $p_T(jet) > 20$ GeV cut is applied. The red line indicates MPI and hadronisation (HAD) effects are switched on, while these are switched off in the case of the blue line. The blue line in the ratio pad give the parton/hadron correction factors.

$N_j(inclusive)$	O_{parton}/O_{hadron}
0	0.994±0.008
1	0.89±0.01
2	0.87±0.01
3	0.86±0.02
4	0.88±0.02
5	0.92±0.02

TABLE 5.2: For MG+PY8 LO, inclusive jet multiplicity corrections for leading jet $p_T >$ 20 GeV.

For the `MG+PY8 CKKW` samples shown in Figure 5.4, there is a $\sim$ 10% reduction from having MPI and hadronisation off in some jet multiplicity bins, also shown in Table 5.2. For the lower $p_T(jet)$ distribution, this discrepancy is at most 5%, and converges for higher $p_T(jet) > 100$ GeV. The exact numbers are given in appendix B Table B.1 for the inclusive $p_T(jet)$ and H_T distributions, demonstrating that corrections below $p_T(jet)$ of 85 GeV or H_T below 200 GeV are not accounted for by statistical error. Above these two thresholds, the corrections do indeed converge to 1 within statistical error, and are further investigated for the new kinematic phase space, instead of this looser selection. Similar results are seen for both `MG+PY8 CKKW` and `MG+PY8 FxFx` showing that these corrections are present regardless of the different matching/merging method.

The following distributions then look at $p_T(jet) > 100$ GeV, using the collinear $Z + jets$ [42] Rivet analysis [223] as detailed earlier, to further investigate the convergence of non-perturbative effects.

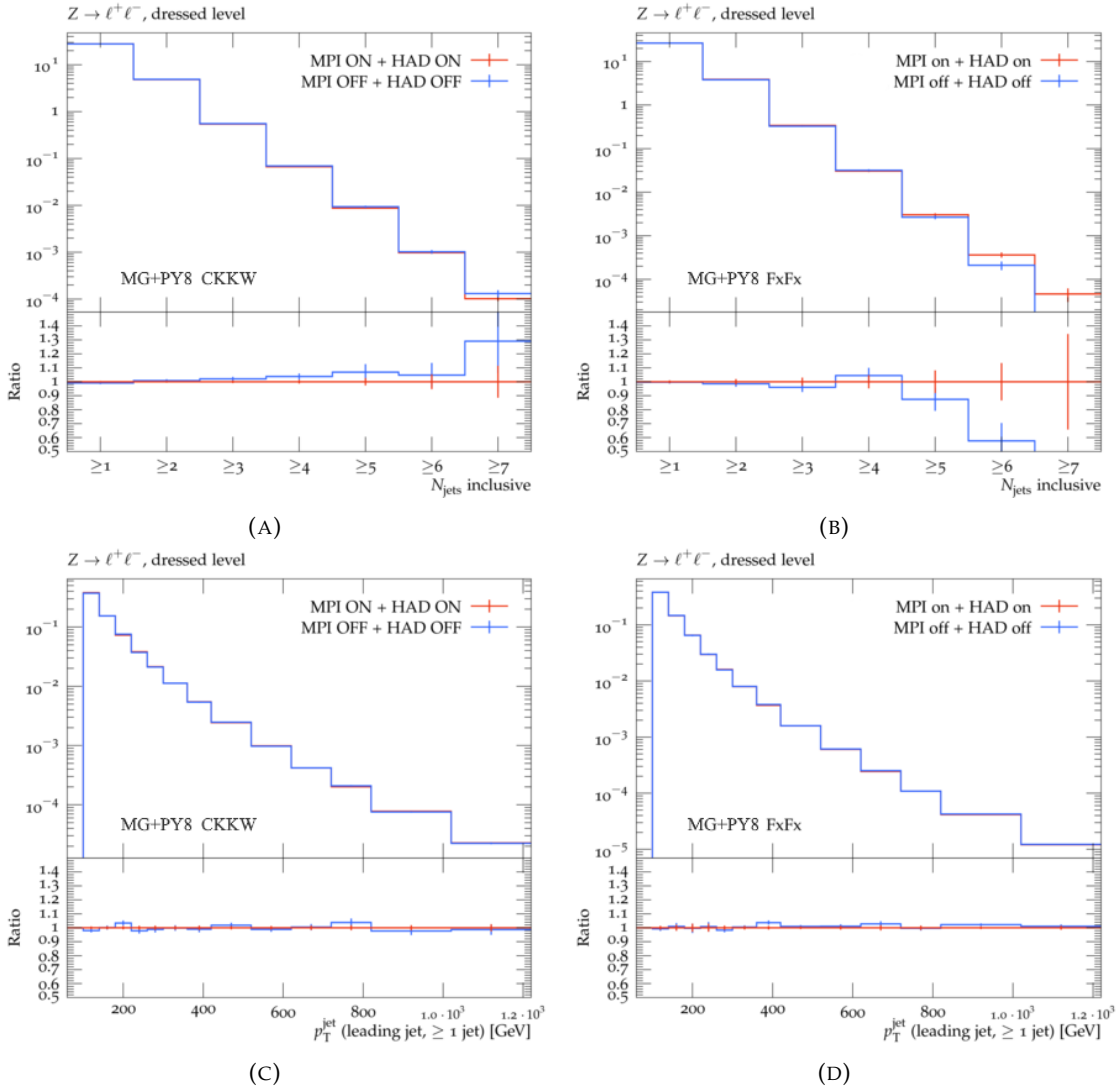

FIGURE 5.5: `MG+PY8 CKKW`(left) and `MG+PY8 FxFx` (right) Rivet plots for muon channel, inclusive high p_T jet multiplicity (a-b) and $p_T(jet)$ (c-d). The red line indicates MPI and hadronisation (HAD) effects are switched on, while these are switched off in the case of the blue line.

N_j	O_{parton}/O_{hadron}incl	O_{parton}/O_{hadron}excl
1	0.98±0.01	0.98±0.01
2	1.00±0.01	1.00±0.01
3	1.01±0.02	1.01±0.02
4	1.02±0.02	1.02±0.03
5	1.06±0.06	1.06±0.07
6	1.01±0.10	0.99±0.10
7	1.16±0.26	0.99±0.25

TABLE 5.3: MG+PY8 LO Inclusive and exclusive jet multiplicity corrections for jet $p_T > 100$ GeV.

$p_T(jet1)$(GeV)	O_{parton}/O_{hadron}
100-140	0.97±0.01
140-180	1.00±0.02
180-220	1.03±0.02
220-260	0.97±0.02
260-300	0.99±0.03
300-360	0.99±0.02
360-420	0.99±0.03
420-520	1.01±0.02
520-620	0.99±0.02
620-720	1.00±0.03
720-820	1.03±0.03
820-1020	0.97±0.03
1020-1220	0.99±0.04

TABLE 5.4: MG+PY8 LO leading jet p_T corrections, for jet $p_T > 100$ GeV.

The distributions in Fig. 5.5 only show $< 10\%$ differences in some bins in the $p_T(jet) > 100$ GeV selection, and all within uncertainty. Therefore these results are compatible with 1 and no non-perturbative corrections from underlying event effects are needed for these variables in this phase space.

Table 5.3 shows the hadronisation corrections needed for the inclusive and exclusive jet multiplicities, compatibility with 1 when accounting for uncertainties, with the exception of `MG+PY8 FxFx` $N_{jets} \geq 6$ which is not relevant for the analysis. This is then followed by Table 5.4 for the leading jet p_T bins, for which the same conclusion is drawn for the jet $p_T > 100$ GeV.

The following distributions in Fig 5.6 then also show more evidence for the convergence of these two scenarios at higher p_T, with all corrections compatible with 1 for this $p_T(jet) \geq 500$ GeV phase space.

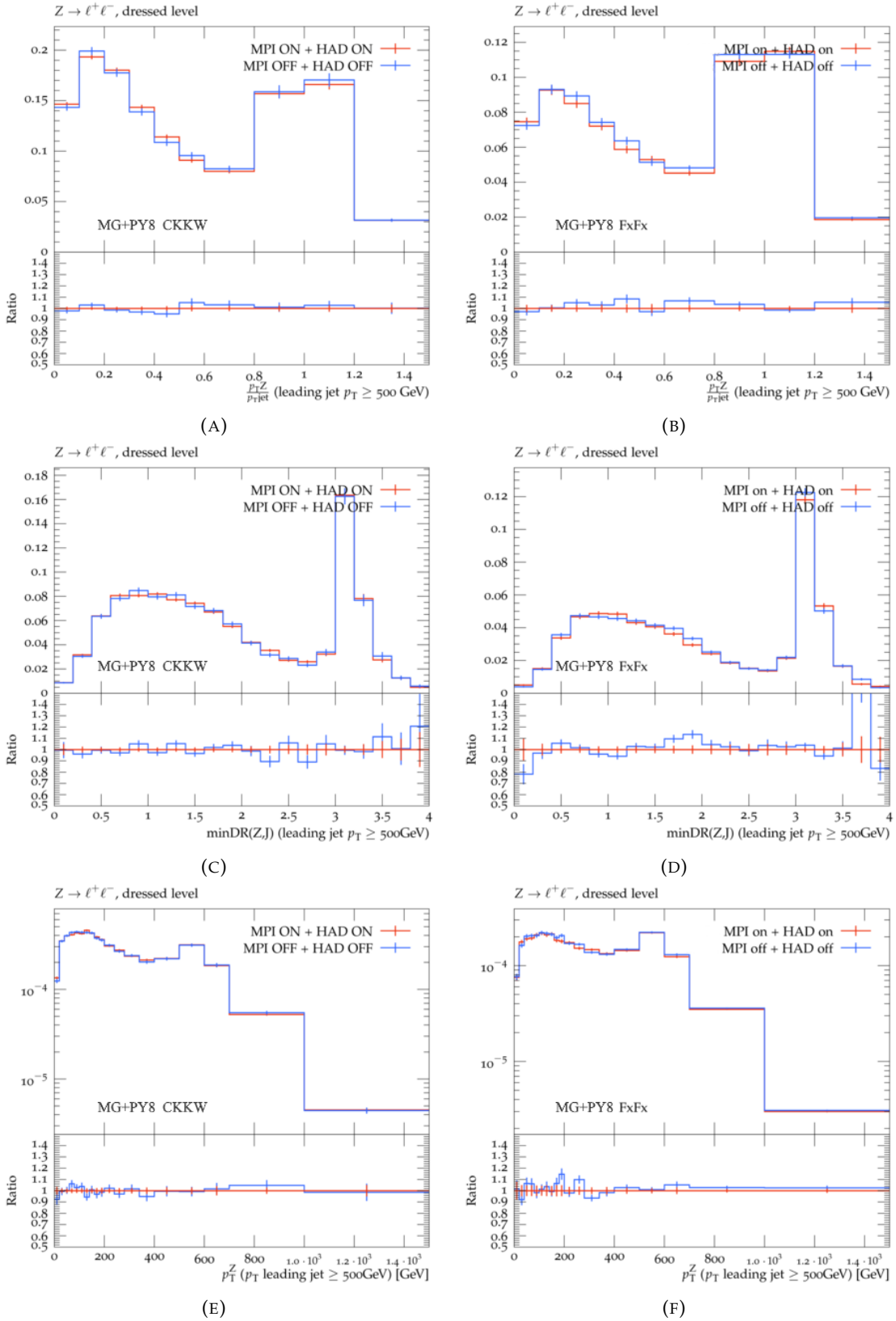

FIGURE 5.6: MadGraph+Pythia8 LO (left) and FxFx (right) Rivet plots for combined electron and muon channels, high p_T region for $p_T(Z)/p_T(j)$ (a-b), minimum $\Delta R(Z,j)$ (c-d) and $p_T(Z)$(e-f).

$pT(Z)/p_T(jet)$	O_{parton}/O_{hadron}
0.0-0.1	0.98±0.02
0.1-0.2	1.03±0.02
0.2-0.3	0.98±0.02
0.3-0.4	0.96±0.03
0.4-0.5	0.96±0.03
0.5-0.6	1.05±0.05
0.6-0.7	1.02±0.04
0.7-0.8	1.00±0.05
0.8-0.9	1.02±0.05
0.9-0.10	1.00±0.06

TABLE 5.5: MG+PY8 LO corrections for high-pT variable $pT(Z)/p_T(jet)$, with leading jet $p_T > 500$ GeV.

To conclude, it is observed that, while the non-perturbative corrections for the underlying event effects are present with a maximal 10% impact in certain variables where $p_T(jet) < 100$ GeV as seen in figure 5.4, these become compatible with 1 within uncertainty in our high-p_T regions of $p_T(jet) > 100$ GeV and $p_T(jet) > 500$ GeV. Therefore these corrections are not necessary for the rest of the analysis.

5.3 Systematic Uncertainties

The relative uncertainties on the measured integrated cross sections for different kinematic regions of Z+jets production are summarised in Table 5.6. The next sections describe the treatment of the various systematic uncertainties.

5.3.1 Detector Level Experimental Uncertainties

For the MC signal and background samples, every systematic effect is given distribution corresponding to $\pm 1\sigma$ variations. These are then propagated to the detector-level distributions and unfolding. Each experimental systematic variation is treated such that the full analysis is executed on the MC modified by the given systematic variation. This is to say that they are treated as being correlated across channels, different kinematic regions, signal and control regions, distributions of observables and over signal and background processes. However, lepton systematics are considered to be uncorrelated between channels.

Jet reconstruction systematics are split between jet energy scale (JES) and jet energy resolution (JER). Both JES and JER uncertainties are typically described by many nuisance parameters (NPs). However, we also impose various configurations from the Jet Performance Group [224] to reduce the total number of NPs. We use the category reduction scheme for the JES in this analysis, involving

- 5 NPs from modelling, non-closure and statistics η-intercalibration,
- 2 NPs from flavour composition and response,
- 1 NP from b-jet response,
- 4 NPs from pile-up,
- 1 NP for punch-through[4],
- 1 NP from high p_T single particle,
- 2 NPs for detector,
- 4 NPs from modelling,
- 6 NPs from statistics,
- 3 Mixed NPs.

[4]Effects caused by shower particles created inside the calorimeter with high enough energy such that they leave the dense calorimeter material and penetrate the surrounding sensitive detector parts [225].

We utilise the "full JER" reduction scheme [226, 227] for the JER systematics, involving 1 NP for data/MC discrepancies and 12 generic NPs. The electron systematics are given by the EGamma Performance Group [228]. The efficiency scale factors also have associated systematic uncertainties, for which there is a variation for the identification, isolation and reconstruction and the two triggers. Additional systematics are given for the electron energy and resolutions. Muon systematics are provided by the Muon Performance Group [168]. The uncertainties associated to the efficiency scale factors include muon reconstruction, isolation, Track-to-Vertex Association (TTVA) and trigger. Two additional variations are given for the systematic and statistical uncertainties, globally correlated in the full phase space. At low p_T, the muon reconstruction also has a separate set of variations. Additional muon systematics include the muon momentum scale, ID and MS resolution and sagitta-bias correction. Pileup reweighting also provides an uncertainty from the pileup reweighting SF efficiency. A luminosity uncertainty of 1.7% is also applied to the final normalisation of the samples [229].

5.3.2 Detector Level Modelling Uncertainties

The modelling and normalisation of the MC samples provide uncertainties, which are propagated through the reconstruction and unfolding level. The modelling uncertainties on the Z+jets account for QCD scale and PDF variations. The scale uncertainties are computed by varying the renormalisation and factorisation scales by a factor of two. The systematics on the PDF are computed by the standard variation of the 101 NNPDF 3.0 NLO replicas, using NNPDF 3.0 NLO PDFs with varied α_S [188] and by comparing with the nominal MMHT2014 NNLO and the CT14 NNLO PDF sets [230]. Sherpa 2.2.11 samples also include NLO virtual EW corrections, for which another systematic is required, derived from the envelope of all possible EW+QCD combination schemes. These uncertainties are propagated to the unfolded cross sections by performing the unfolding on data with the varied response matrices of the corresponding modelling uncertainties. Diboson modelling uncertainties include QCD scales and PDF variations, derived from the Z+jets samples. Electroweak Zjj modelling uncertainties include QCS scales, PDF variations and interference between QCD and EW Z+jets diagrams. Both diboson and electroweak uncertainties are propagated to the unfolded cross section when the background is subtracted from the data. Since a data-driven approach is taken for the $t\bar{t}$ background, this sample is not affected by MC modelling uncertainties on $t\bar{t}$. Any experimental uncertainties are only propagated through the background subtraction in the $e\mu$ control region and scale factors to the final data-driven $t\bar{t}$ samples. However, there is some non-negligible contribution from the electron/muon related experimental uncertainties on the scale factors, due to their asymmetric nature. Single-top uncertainties also include scale and

Relative uncertainty for $\sigma(Z(\rightarrow \ell^+\ell^- + \text{jets}))$ [%]					
Uncertainty source	*Inclusive*	*High-p_T*	*Collinear*	*Back-to-back*	*High-S_T*
Jet JER/JES	2.6	3.2	2.8	3.6	2.8
Muon	0.6	1.0	0.8	1.3	0.7
Electron	0.6	1.2	1.1	1.5	0.9
Luminosity	1.7	1.7	1.7	1.7	1.7
Pile-up	0.1	0.4	0.4	0.4	0.4
Unfolding	0.5	1.0	1.1	1.4	0.8
Background modelling	0.5	2.0	2.0	1.9	1.7
Signal modelling	0.5	1.2	1.1	1.1	1.1
Total syst. uncertainty	3.4	4.8	4.4	5.3	4.2
Stat. uncertainty	0.1	2.1	2.9	2.7	1.2
Total uncertainty	3.4	5.3	5.3	5.9	4.4

TABLE 5.6: Relative statistical and systematic uncertainty percentages in the measured integrated cross sections for Z+jets production in five different kinematic search regions, computed in the different jet multiplicity observables [42].

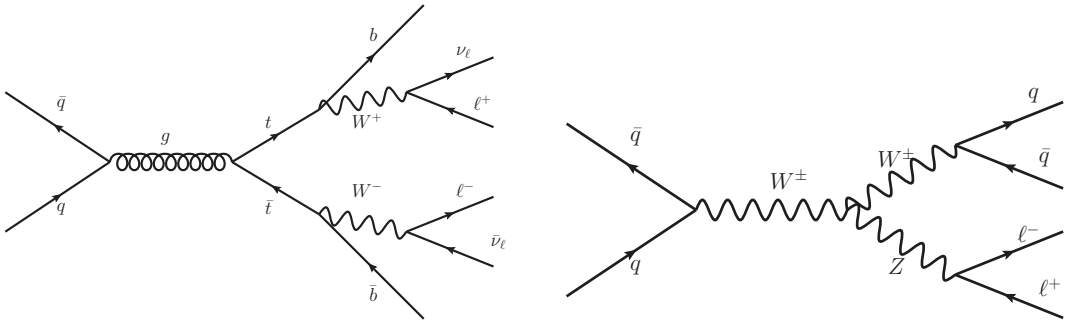

FIGURE 5.7: Examples of Feynman diagrams for the $t\bar{t}$ (a) and WZ diboson (b) background processes.

PDF uncertainties, which amount to normalisation uncertainties of 4% on these samples.

5.4 Background Estimation

Backgrounds come mainly from $t\bar{t}$ (3.4% in inclusive region) and diboson (1.5% in inclusive region) processes, examples of which are shown in Fig. 5.7, with small contributions from single-top (0.2%), $Z\tau\tau$ (0.03%) and $W + jets$ (0.01%). These background processes are simulated with MC generators. The modelling of diboson background is studied within theoretical uncertainties on the respective samples. The $t\bar{t}$ simulation is validated in a dedicated control region and extracted from data. The contributions from multi-jet events are evaluated using a data-driven method and are later shown to be negligible.

5.4.1 Diboson Background

Semi-leptonic and fully-leptonic decays of WW, WZ and ZZ processes are considered as potential source of background in the analysis. The dominant semi-leptonic processes are $W(\to qq)Z(\to \ell\ell)$ and $Z(\to qq)Z(\to \ell\ell)$, contributing with more than 50% to the total diboson events. The $W(\to \ell\nu)Z(\to qq)$, $W^+(\to \ell\nu)W^-(\to qq)$ and $W^+(\to qq)W^-(\to \ell\nu)$ productions are also considered and found to be negligible. The fully-leptonic processes $\ell\ell\nu\nu$, $\ell\ell\ell\nu$ and $\ell\ell\ell\ell$ represent the second largest contribution to the diboson background.
Diboson events are the second main source of contamination in the Z+$\geq$1 jet region and they become the dominant background contribution when requiring leading jet p_T $\geq$500 GeV. In the particular case of collinear events, the diboson and $t\bar{t}$ processes almost equally contribute (5.8% and 4.2% respectively) [42].
The semi-leptonic and fully-leptonic decays of WW, WZ and ZZ processes are well modelled by MC generators, as recently studied by ATLAS in [231–235], and disagreements with the central value of the data are covered by systematic uncertainties on the samples. The systematic uncertainties relative to the modelling of diboson samples involve PDF set variation, PDF choice, variation of α_s and QCD scale. Fig. 5.8 shows the breakdown of the modelling systematics on the diboson processes as a function of the exclusive jet multiplicity. The dominant source of systematic is due to the choice of the renormalisation and factorisastion scales, which increases with the number of jets in the signal region: from $\sim$15% in events with 0 jets up to $>$30% in events with $\geq$3 jets. The scale uncertainties and the systematics on the PDF are computed according to section 5.3. The other uncertainties contribute with few %. In Figure 5.9 the distribution of the modelling uncertainty is presented as a function of the minΔR(Z, J).

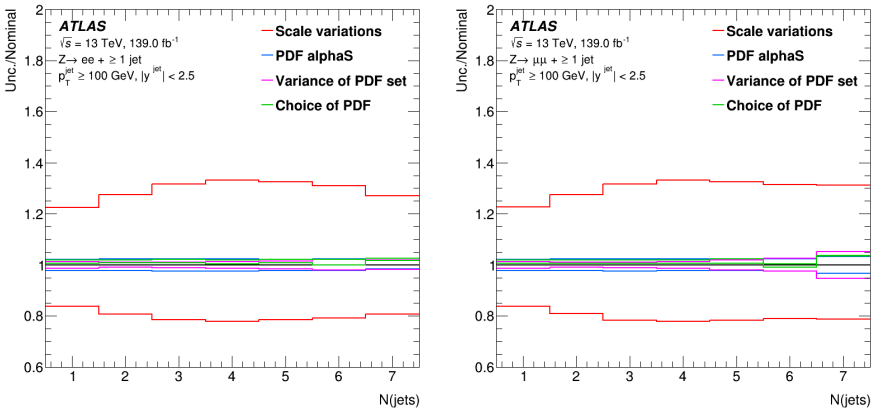

FIGURE 5.8: The contribution of the modelling uncertainties on the diboson background samples as a function of N_{jets}^{ex} distribution for the electron (left) and muon (right) decay channels [42].

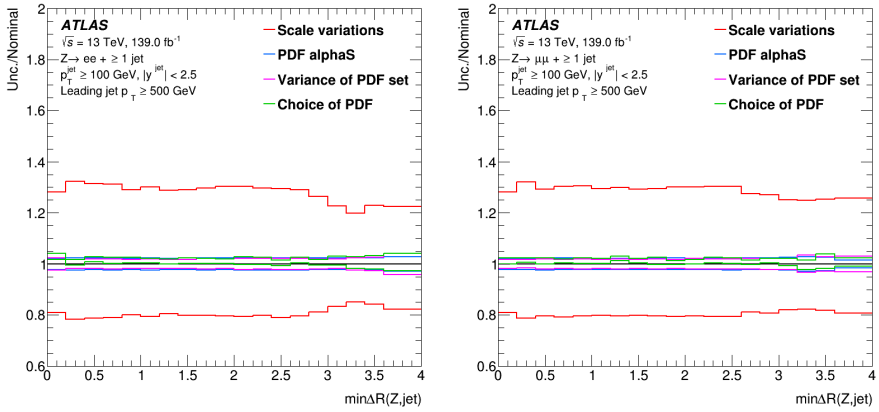

FIGURE 5.9: The contribution of the modelling uncertainties on the diboson background samples as a function of minΔR(Z,j) distribution for $p_T(leading\ jet) > 500$ GeV for the electron (left) and muon (right) decay channels [42].

5.4.2 $t\bar{t}$ Background

The dominant background in our analysis comes from $t\bar{t}$ pairs. Produced via gluon fusion or t-channel interactions, they become a potential background when both W bosons decay leptonically and into the same lepton flavour (e^+e^- or $\mu^+\mu^-$). The $t\bar{t}$ background is evaluated with a data-driven approach instead of only relying on MC prediction due to very large modelling uncertainties in the $p_T(leading\ jet) \geq 500$ GeV region (see Fig. 5.9 for example) which significantly affects the unfolded cross sections. In order to derive the $t\bar{t}$ background, a control region is constructed where $t\bar{t}$ events are enriched, by specifically selecting $e^{\pm}\mu^{\mp}$ final states. These selections are dominated by $t\bar{t}$ events with only percentage-level contributions from diboson and $Z\tau\tau$ events. After the subtraction of non-$t\bar{t}$ backgrounds, the control region (CR) data distributions are then extrapolated to the signal region by multiplying them with $ee/e\mu$ and $\mu\mu/e\mu$ scale factors for each bin, derived from $t\bar{t}$ simulation.

Both single-top (t-, Wt-, s-channel) and $t\bar{t}$ MC samples are generated using PowhegBox [236] v2 + Pythia 8.230 NLO [237–240].

Figure 5.10 shows the large modelling uncertainties of the MC $t\bar{t}$ samples. Each systematic has an "1up" and "1down" contribution, although these are not necessarily symmetrical +/- contributions about 1. The *TT_PDF* systematics describe the uncertainty from PDF variations for $t\bar{t}$ modelling. The *TT_PDF_SET* systematics account for the uncertainty in the variation between PDF sets for $t\bar{t}$ modelling. The *TT_ALPHA_S* systematics represent the uncertainty from α_S effects for $t\bar{t}$ modelling. The *TT_GEN_MATCH* systematics correspond to the uncertainty from the difference in results when matching between generators in $t\bar{t}$ modelling. The *TT_FRAG_HAD_MOD* systematics capture the uncertainty from fragmentation and hadronisation modelling for $t\bar{t}$ modelling. The *ISR* systematics outline the uncertainty from ISR effects. The *alpha_S_FSR* systematics models the uncertainty from α_S *FSR* effects [241]. From

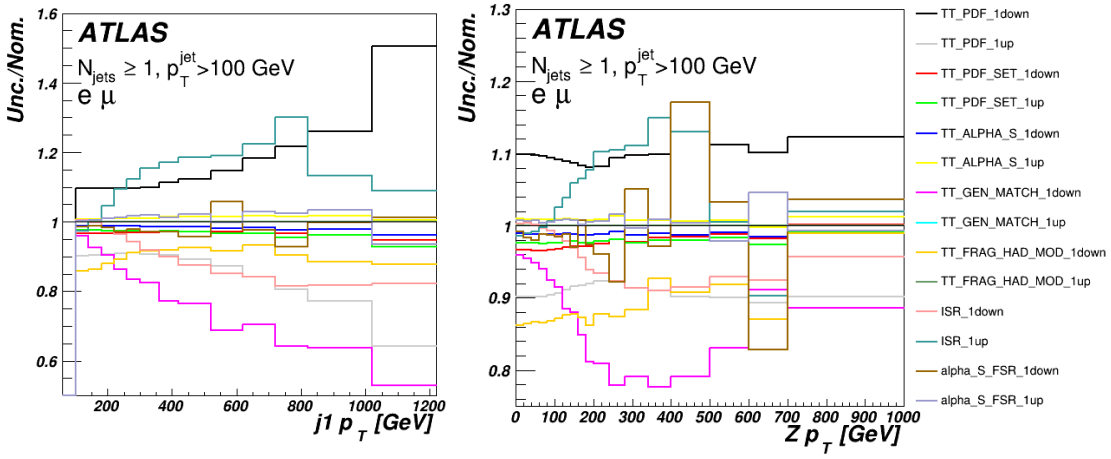

FIGURE 5.10: The relative $t\bar{t}$ theory systematics in the jet p_T and Zp_T CR distributions for leading jet $p_T > 100$ GeV . Each line represents a different $t\bar{t}$-specific modelling systematic, in addition to ISR and α_s-FSR systematics. each systematic has a "1up" and "1down" contribution.

Fig. 5.10, the generator matching systematic (*TT_GEN_MATCH_1down*) and PDF variation systematic (*TT_PDF_1down*) provide the largest uncertainty for $t\bar{t}$ modelling. These greatly contribute to the total uncertainty in the following stacked plots, motivating the data-driven approach.

Figures 5.11 and 5.12 show the distributions of data and simulation in the $e\mu$ $t\bar{t}$ CR, before subtracting backgrounds. From these we can conclude that $t\bar{t}$ MC systematics are especially large for the high-p_T region which will significantly impact the unfolded cross sections. As a result, it is difficult to trust the modelling of MC $t\bar{t}$ which is a crucial issue given that it makes up a significant contribution to the total background of this analysis, around 1/3 in some cases, as shown in Figures 5.11 and 5.12.

The trigger selectrion for the $e\mu$ "top validation" control region are given in Table 5.1, these being HLT_e17_lhloose_mu14 for 2015 and HLT_e17_lhloose_nod0_mu14" in 2016-2018.

Figure 5.13 shows the SR/CR extrapolation factors in bins of $p_T(leading\ jet)$ and $p_T(Z)$. The hashed error bars represent the detector systematics after performing the bin-by-bin division of $ee/e\mu$ and $\mu\mu/e\mu$. The naive combinatorical expectation would be ~ 0.5. This base value is implicitly folded with different electron and muon reconstruction and trigger efficiencies, leading to the trends shown in Fig. 5.13. Here we instead observe a central value around 0.6. The efficiency in the electron channel is constantly about 20% below the efficiency of the muon channel, where this drop in efficiency has been found to be caused by the electron identification and from the di-electron trigger requirement. As a result, the di-electron trigger rejects approximately double the number of events as the di-muon trigger. Consequently, the

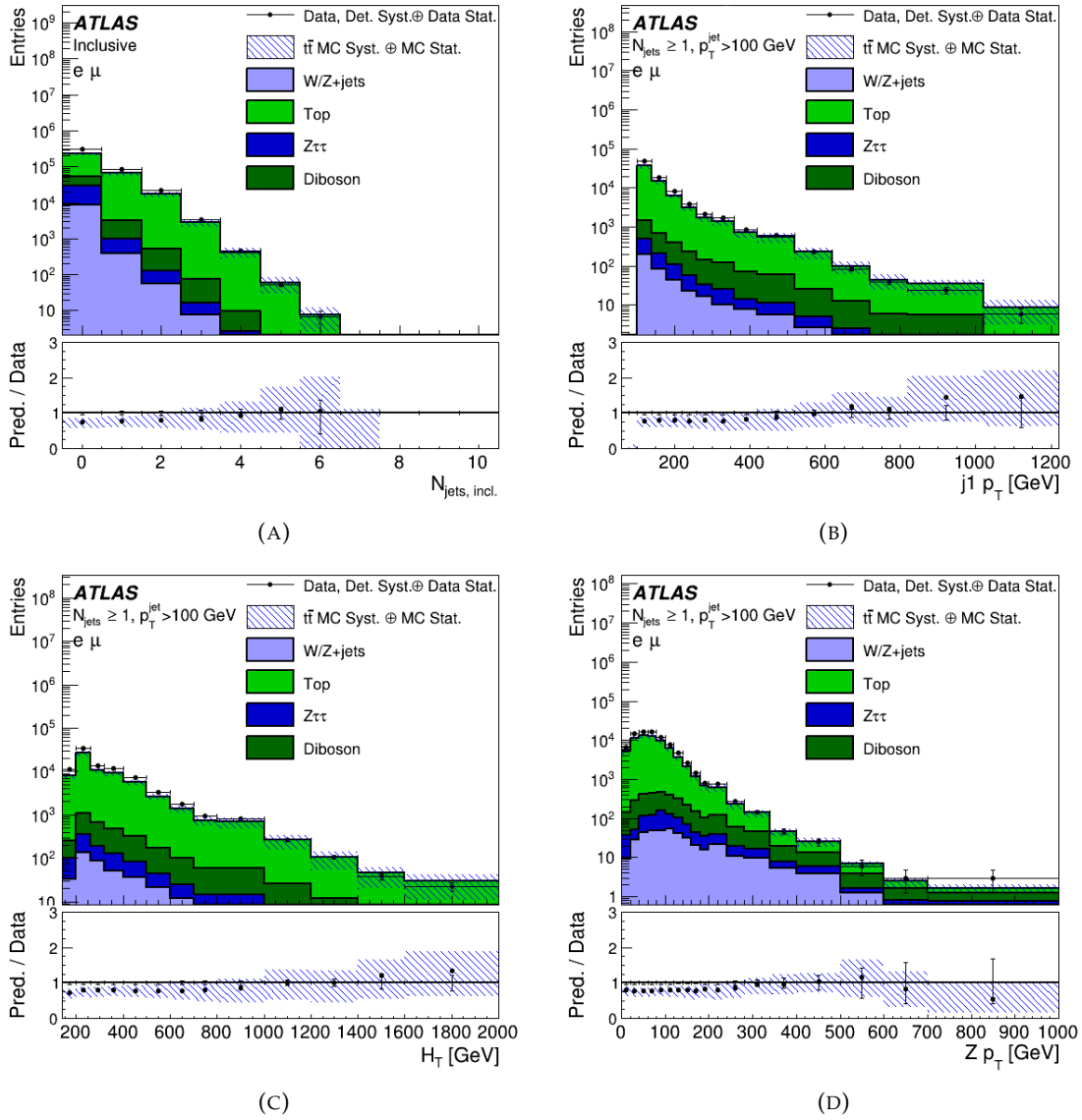

(A) (B)

(C) (D)

FIGURE 5.11: Data and stacked MC comparison in the $e\mu$ $t\bar{t}$ CR, of inclusive jet multipliciy (a), $p_T(leading\ jet)$ (b), H_T (c) and $p_T(Z)$ (d), where the latter three are in the leading jet $p_T > 100$ GeV region. All backgrounds and the signal samples are stacked to produce the figures. The bottom panels show the total MC prediction/data comparison. Top sample includes $t\bar{t}$ and single top contributions. The line error bars on uncertainty include detector systematics and data statistical uncertainty. The hashed error bars on top sample include $t\bar{t}$ modelling uncertainty and MC statistical uncertainty.

same-flavour selection has more efficient triggers, thus the
same-flavour/opposite-flavour fraction will be larger than the naive prediction.

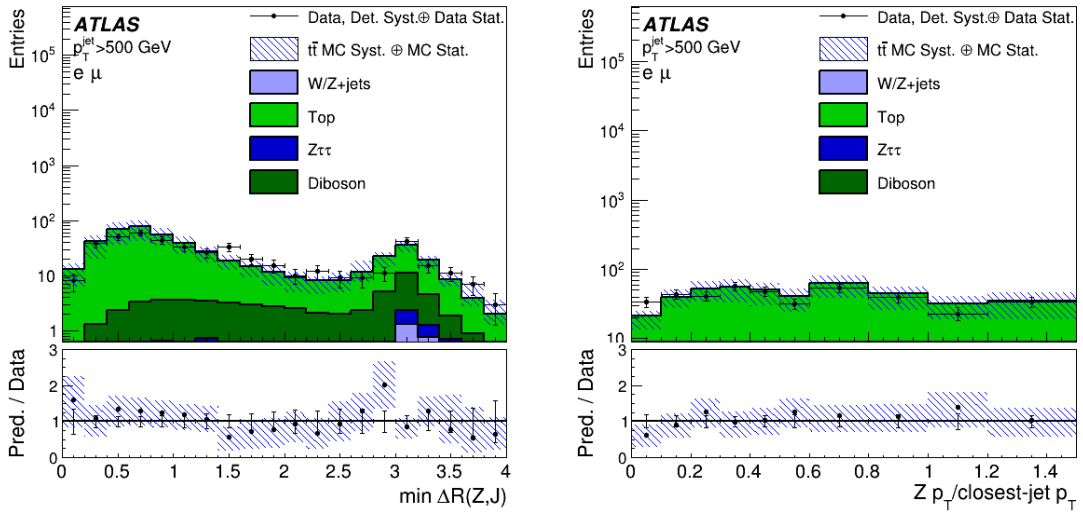

(A) (B)

FIGURE 5.12: Data and stacked MC comparison in the $e\mu$ $t\bar{t}$ CR, of the minimum ΔR between the Z and closest jet, $p_T(Z)/p_T(jet)$ both with leading jet $p_T > 500$ GeV. All backgrounds and the signal samples are stacked to produce the figures. The bottom panels show the total MC prediction/data comparison. Top sample includes $t\bar{t}$ and single top contributions. The line error bars on uncertainty include detector systematics and data statistical uncertainty. The hashed error bars on top sample include $t\bar{t}$ modelling uncertainty and MC statistical uncertainty.

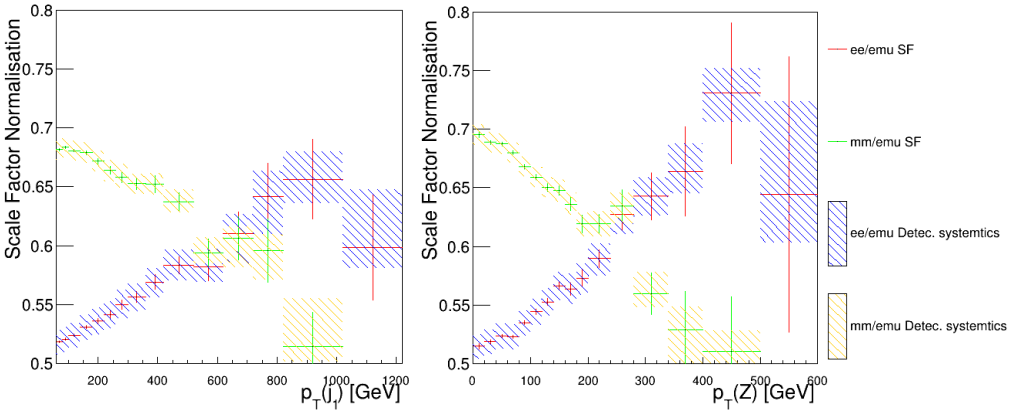

FIGURE 5.13: Extrapolation factors derived from $t\bar{t}$ MC, used in scaling the data-driven $t\bar{t}$ background in the signal regions. The hashed error bars describe the detector systematics for $ee/e\mu$ and $\mu\mu/e\mu$.

Throughout the rest of the analyses, the CR derived scale factors are applied to the MC $t\bar{t}$, and the new data-driven $t\bar{t}$ samples are then utilised in the detector-level plots presented in Fig.5.14. The inclusion of data-driven $t\bar{t}$ now results in sensible MC statistical uncertainties for detector level distributions. The inclusive region is explored here with the predicted event yield as a function of $p_T(jet)$ for $p_T(leading\ jet) > 100$ GeV. The disagreement between MC and data shows a trend where `MG+PY8 CKKW` overestimates data at larger transverse momenta regions while Sherpa 2.2.11 generally agrees with or underestimates data. These are also the regions where we expect the pQCD and EW corrections to be largest. The data/simulation comparison in the high-p_T region is also explored in Fig. 5.14, the predicted event yield as a function of $r_{Z,j}$, where there is a trend of MG5_aMC+Py8 CKKWL to over-predict the high-p_T phase space. We find that Sherpa 2.2.11 shows a good modelling of data in the high-p_T regions, and therefore can be used as a good baseline of the unfolding.

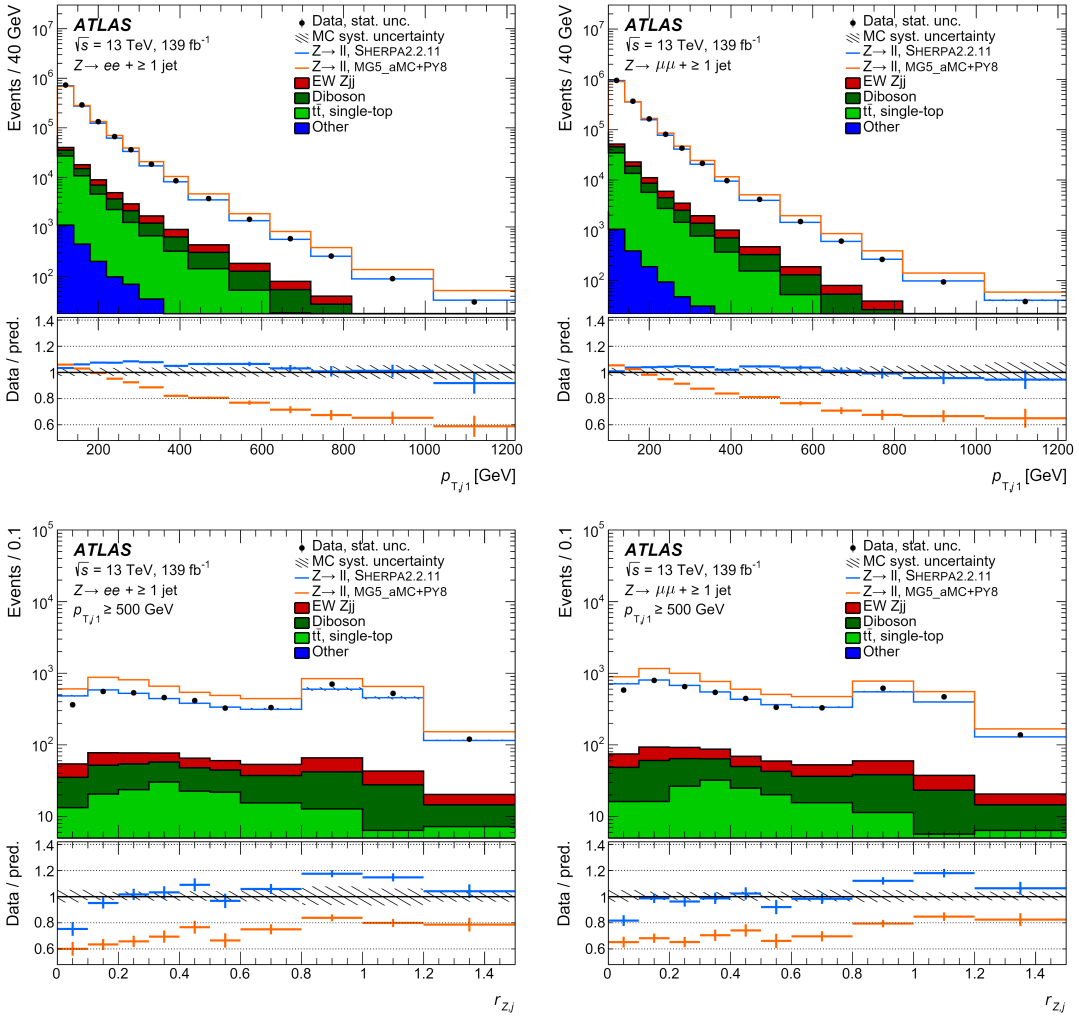

FIGURE 5.14: Event yields as a function of $p_T(jet)$ (top) and $p_T(Z)/p_T(jet)$(bottom) in the electron channel (left) and muon channel (right) in simulation and data in the inclusive region. All backgrounds and the signal samples are stacked to produce the figures. W+jets, $Z \to \tau^-\tau^+$ and $V + \gamma$ processes are combined and labelled "Other". Systematic uncertainties for the signal and background distributions are combined in the hatched band, and the statistical uncertainty is shown as error bars. The bottom panel shows the ratio between the data and two predictions, Sherpa 2.2.11 and MG+PY8 CKKWL [42].

5.4.3 Multi-jet Background

The multi-jet background to our final state comprises non-prompt leptons from hadron decays, misidentified as prompt leptons, or hadrons (and photons) which pass the requirements of lepton identification. The multijet background is assessed in a data-driven way by fitting a $m_{\ell\ell}$ template, derived in a jet-enriched control region, to the $m_{\ell\ell}$ distribution in the signal region. This template is derived by dropping lepton identification cuts.

In order to enrich the multijet background in the electron and muon channels, the nominal event selection described in Section 5.1 is applied with the following exceptions:
For the electron channel:

- Both electrons are anti-isolated.
- No electron likelihood cut.
- No vertex cuts on the impact parameters.
- No sign requirements on the electrons

and for the muon channel:

- No muon isolation requirement.
- Same signed muons.

The final multi-jets template is derived by subtracting the simulated electroweak processes from the CR data. These electroweak processes include WW,WZ,ZZ and Z+jets backgrounds.

The transfer factor between control and signal region is derived from a template fit of the CR-derived multi-jet $m_{\ell\ell}$ template to the $m_{\ell\ell}$ distribution in the signal region. In the following section, several fit strategies are tested to derive a systematic assessment. The systematic variations are formulated by varying the normalisation parameters, which can be set fixed or left floating, such as the multi-jet normalisation, the $t\bar{t}$ normalisation and the diboson normalisation. For each variation, fits are performed both for the $p_T(j) \geq 100$ GeV selection and for the $p_T(j) \geq 500$ GeV selection but due to the large statistical uncertainty the latter is only used as a rough cross check.

Sample	Scale Factor ($p_T(j) \geq 100$GeV)	Scale Factor ($p_T(j) \geq 500$GeV)
	$\mu\mu$	
Diboson	0.989 $\pm$0.0334	0.986 $\pm$2.351
ttbar	0.886 $\pm$0.0166	0.739 $\pm$0.0438
Z	1.0619 $\pm$0.009	0.829 $\pm$0.123
	ee	
Diboson	0.968 $\pm$0.101	0.984$\pm$0.119
ttbar	0.911 $\pm$0.008	0.739$\pm$0.0943
Z	1.050 $\pm$0.00169	0.826$\pm$0.0239

Sample	Integral ($p_T(j) \geq 100$GeV)	Integral ($p_T(j) \geq 500$GeV)
	$\mu\mu, 71 \leq M_{\mu\mu} \leq 111$	
Data	1673060	7896
Diboson	23905.8$\pm$809.156	430.959$\pm$1034.093
ttbar	52724.2 $\pm$988.0722	262.301$\pm$16.292
Z	1589020 $\pm$14009.591	7158.29$\pm$1074.527
	$ee, 71 \leq M_{ee} \leq 111$	
Data	1312140	7539
Diboson	18919.7$\pm$1977.635	420.999$\pm$51.149
ttbar	42506.1$\pm$405.436	262.859$\pm$35.109
Z	1244580$\pm$2008.609	6812.36$\pm$198.223

TABLE 5.7: Scale factors for $\mu\mu$, ee channel fits and contributions within $71 \leq M_{\ell\ell} \leq 111$ Z mass window, without multijet fit.

5.4.4 Non-multijet Fit

In Table 5.7 the MC is simply fit to the data, without considering multijet contributions, to obtain the normalisation used to fix in later fits.

In Fig. 5.15 the dilepton invariant mass in the multijet background control region is plotted, from which the multijet template is derived.

Because of the looser electron channel requirements, the electron channel data distribution gives about twice as many number of events compared to the muon channel data distribution. The anti-isolated electron requirement also suppresses the non-multijet electron channel samples (such as diboson or top quarks which could decay to two leptons from different sources) . The same-signed muon requirement and lack of isolation requirements still allows more non-multijet samples in the muon channel, compared to the electron channel.

5.4.5 Float Diboson, Float $t\bar{t}$

The normalisation coefficients correspond to the normalisation of the number of events. When chosen not to float, this value is set constant. In Fig. 5.16 diboson, Z, $t\bar{t}$ and multijet normalisations are left to float, with scale factors and contributions to

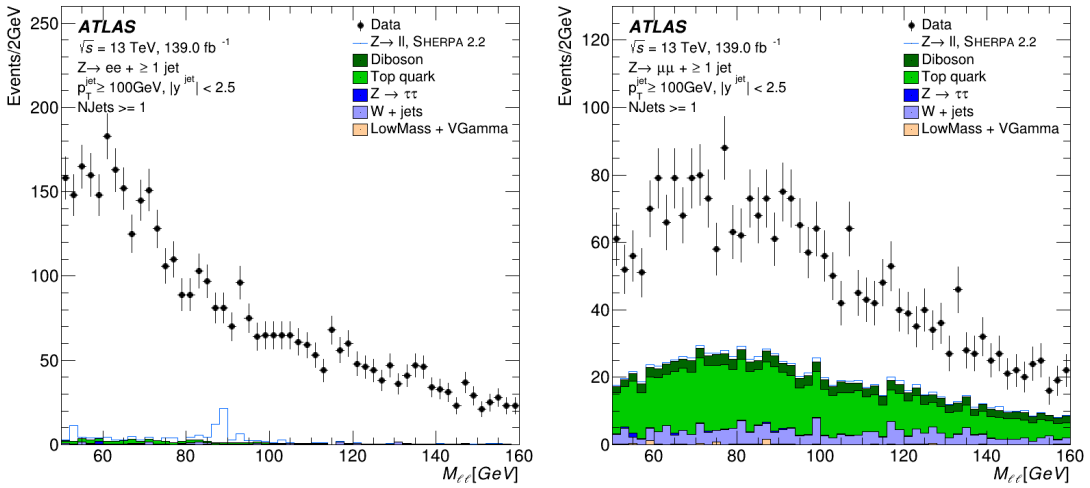

FIGURE 5.15: Measured event yield of the dilepton invariant mass in the electron (left) and muon (right) multijet background control region, with at least 1 jet, in the inclusive region. Fits are performed with Z+jets, $t\bar{t}$, diboson and multijet normalisations allowed to float independently [42].

integral within the Z mass window $71 \leq M_{\ell\ell} \leq 111$ GeV are displayed in Table C.1 for both muon channel and electron channel. The post-fit distributions in Fig. 5.16 demonstrate the downward slope in multijet events, distinct from the other stacks in the distribution for $p_T(j) \geq 100$ GeV which allows for a reasonably stable fit. Uncertainty bars in the MC/data ratio panel represent the lepton systematic uncertainties. Note that these results do not account for shape uncertainties in the fitting, which could come from experimental systematics. Template fits for $p_T(j) \geq 500$ GeV are also presented for for consistency, but the uncertainties are too large to draw a meaningful conclusion on these, so the $p_T(j) \geq 100$ GeV fits are the focus for this section.

5.4.6 Fitting Diboson+Z Together

Following these results, the fitting of EW backgrounds (diboson+Z) together is tested in Appendix C, Table C.2 and plotted in Fig.C.1. We find that there is little change in the distributions when fitting the EW samples together, with a marginal improvement to the electron channel results, and a negligible decrease in muon fit convergence. The shapes of Z+jets and diboson are similar and so this similarity in post-fit results is not surprising,

5.4.7 Float Diboson, Fixed $t\bar{t}$

For this section, the diboson normalisation is allowed to float, while the $t\bar{t}$ normalisation starting value is fixed to the integral of the $t\bar{t}$ histogram. As before, no

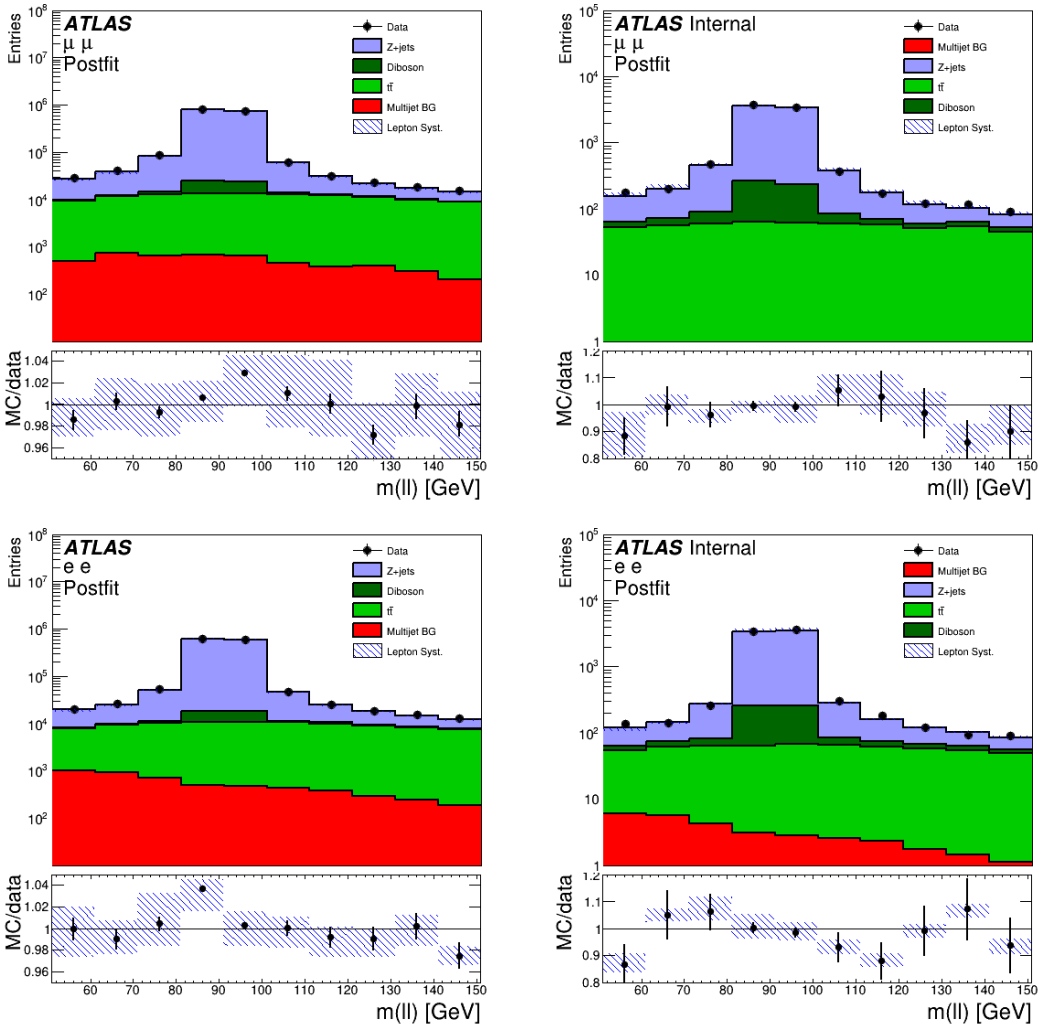

FIGURE 5.16: Muon (top) and electron (bottom) channel post-fit $m_{\ell\ell}$ distributions for signal region selection requiring one jet $p_T j \geq 100$ GeV (left) and leading jet $p_T j \geq 500$ GeV selection (right). Uncertainty bars in the MC/data ratio panel represent the lepton systematic uncertainties.

significant change is observed in the post-fit $M_{\ell\ell}$ distributions.

While the $p_T j \geq 500$ GeV fit could be compatible with 0, these results are inconclusive due to large uncertainties.

5.4.8 Fixed Diboson, Fixed $t\bar{t}$

Finally, both the diboson and $t\bar{t}$ normalisations are set fixed, with just Z and multijet normalisations left floating in Table C.5. Once again the distributions show no observable change from the previous cases.

5.4.9 Summary of Fit Results

Channel	Fit configuration	Multijet/Tot MC ($p_T j \geq 100$GeV)	Multijet/Tot MC ($p_T j \geq 500$GeV)
$\mu\mu$	All float	0.00149± 0.0007	-0.00248± 0.0229
ee	All float	0.00166± 0.0004	0.0017± 0.004
$\mu\mu$	Diboson+Z, All float	0.00144± 0.00061	-0.0107± 0.0101
ee	Diboson+Z, All float	0.00161± 0.00034	0.00172± 0.00472
$\mu\mu$	Fixed Diboson	0.00146± 0.00058	-0.00246±0.00465
ee	Fixed Diboson	0.00162± 0.00034	0.00174± 0.00484
$\mu\mu$	Fixed $t\bar{t}$	-0.000114± 0.00119	-0.00218± 0.02274
ee	Fixed $t\bar{t}$	0.000597± 0.00022	0.000603± 0.00313
$\mu\mu$	Fixed Diboson, $t\bar{t}$	0.000307± 0.00028	-0.00219± 0.00464
ee	Fixed Diboson, $t\bar{t}$	0.000611± 0.00021	0.000606± 0.00286

TABLE 5.8: Multijet background fractions summarised for all configurations and channels, showing that the Multijet/Total MC fraction in negligible in all cases. Errors represent the fit uncertainties.

These results are summarised in Table 5.8, showing the corresponding multijet fractions of the total MC for all variations of fit configurations, for both $\mu\mu$ and ee channels. There are some small variations to fractional contribution when fixing $t\bar{t}$ but not significant enough to consider in the final analysis. Overall these results show that the multijet background contributes only a small $\lesssim 1\%$ with all settings configured and tested. Therefore, it is deemed insignificant and can be treated as negligible throughout the collinear Z+jet analysis.

5.5 Unfolding and Systematics

In section 2.5.12, the most basic method of unfolding is outlined. However, for this analysis the iterative Bayesian approach (also described in section 2.5.12) is used in the unfolding. For this analysis, the fiducial acceptance region is defined by:

- Two same-flavour, opposite-charges leptons with $p_T \geq$25 GeV and $|\eta| < 2.5$
- Z mass window $71 < m_{\ell\ell} < 111$ GeV
- Jets defined with $p_T \geq 100$ GeV and $|y| < 2.5$
- At least one jet.

In addition, the high-p_T, collinear and back-to-back regions are defined as before.

Particle-level cross sections for dressed electrons and muons coming from a Z boson are investigated. These dressed leptons are defined as four-vector combinations of prompt leptons, not originating from hadron decay, τ-leptons or photon conversions, and prompt photons within a $\Delta R < 0.1$ cone. Jet clustering is implemented at the particle level, using anti-k_t algorithm with radius $R = 0.4$ for final state particles with decay lengths $c\tau$ >10 mm (with the exception of dressed Z-boson decays). Since the detector can not discriminate well between close objects in the collinear region, overlap removals are applied to particle level to best match to detector level response. An overlap removal for jets with $p_T \geq 30$ GeV within $\Delta R < 0.2$ from a dressed lepton is followed by an overlap removal of leptons within $\Delta R < 0.4$ of the remaining jets.

We use a variable bin-width for the observables such that purity is at least 60% per bin. The statistical uncertainty per bin remains below 5% for the most part. The small event yields in the some high-p_T region bins results in large statistical uncertainty, up to 13%. However, this is for individual $ee/\mu\mu$ channels and once the results are combined, this uncertainty falls to below 10%.

Background-subtracted data is unfolded using response matrices (see section 2.5.12) derived from Sherpa 2.2.11. We employ an iterative unfolding technique [242] (also see section 2.5.12) as used in the RooUnfold package [243] to account for detector effects from detector inefficiencies, resolution and systematic biases in the lepton and jet kinematic variable values. Through the iterative unfolding procedure, this iteratively updates the initial estimators for the truth-level distributions in consecutive steps in each iteration via Bayes' theorem. With this procedure, the unfolding matrix is then derived from a combination of the current truth estimator and the initial response matrix, the matrix that relates truth and reconstructed distributions for a given observable.

For p_T(leading jet), unfolding proceeds by keeping two underflow bins within $60 \geq p_T$(leading jet)$\geq$ 100 GeV due to the large bin-migration effects in the first published bin causing model dependence. These bins are then removed in the final result.

The unfolding uncertainty addresses the bias of the unfolding procedure and is derived for each unfolded observable by reweighting truth-level Sherpa 2.2.11 Z+jets MC to match the background subtracted data at reconstruction level. A 5th degree polynomial is fitted to the ratio of background subtracted data and MC at detector level to obtain a continuous reweighting function. Results in Fig.5.17 show the reweighted MC to the nominal MC and the background subtracted data as a function of p_T(leading jet) and $\Delta R^{min}_{Z,j}$ for the electron and muon channels. This is unfolded with the non-reweighted response matrix, with uncertainty from the comparison between the unfolded result and the reweighted truth distributions [42].

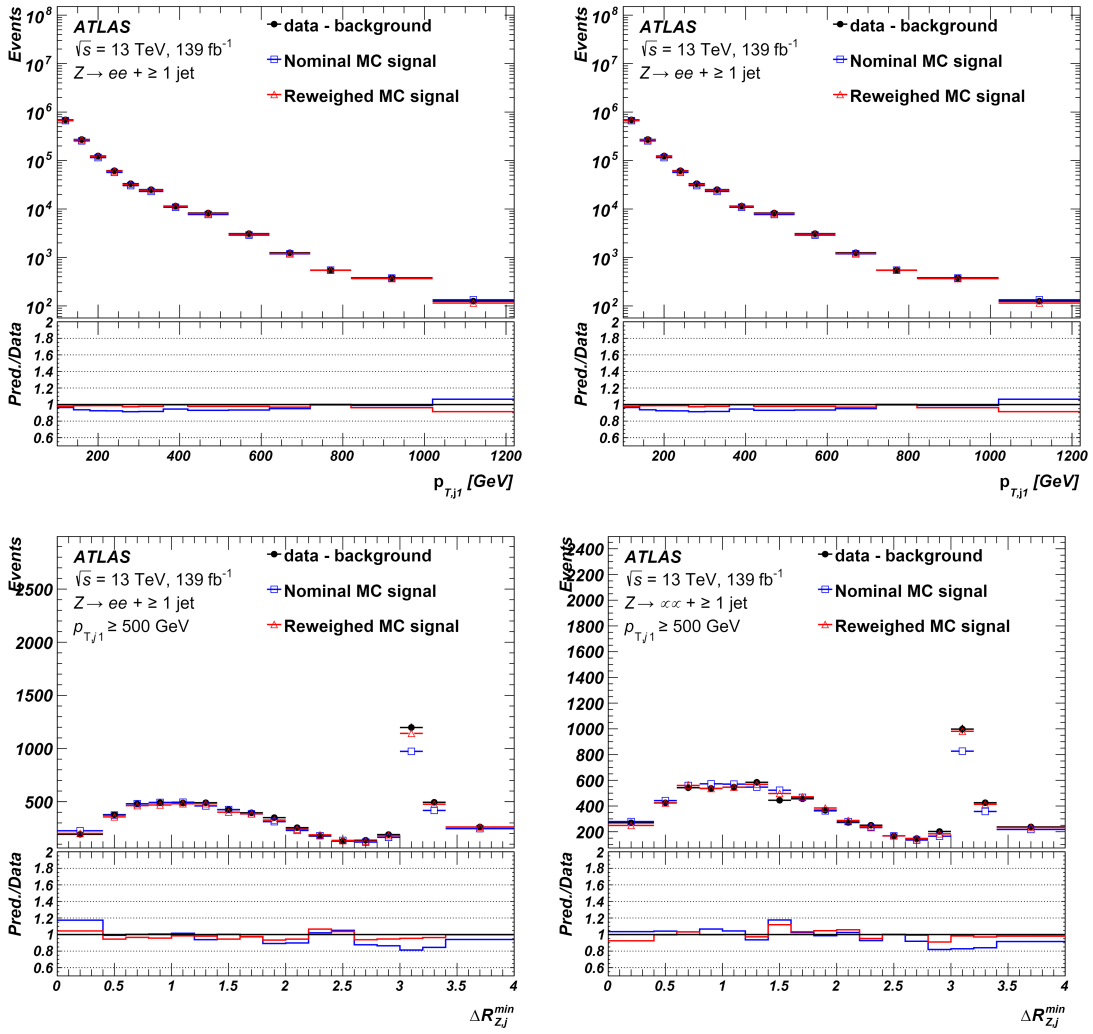

FIGURE 5.17: MC reweighting distributions to data, for the p_T(leading jet) (top) and $\Delta R^{min}_{Z,j}$ (bottom) for the electron(left) and muon channel (right). Detector level background subtracted data is plotted in black, while the original MC is plotted in blue, and reweighted in red. Z+Jets MC corresponds to Sherpa 2.2.11 samples. [42]

A toy simulation method is used to propagate the statistical uncertainties of the Sherpa 2.2.11 derived response matrices. We generate 1000 pseudo-experiments as unfolded samples and for each sample, the unfolding matrix inputs are randomly generated according to a Gaussian distribution. The mean is set to the bin content and the variance is set to the square of the bin error. We then perform unfolding on each pseudo-experiment, for which the output distribution's widths are used as a systematic uncertainty for the unfolding [42].

Fig. D.1 shows the comparison between unfolded Sherpa 2.2.1 to its truth distribution as a function of p_T(leading jet) (top) and $\Delta R^{min}_{Z,j}$ (bottom) for electron and muon channels. We observe a closure test when the unfolded and truth distributions coincide, requiring no additional uncertainties to account for any disagreement in shapes. The results in Fig. D.1 show this consistent closure within the MC statistics of

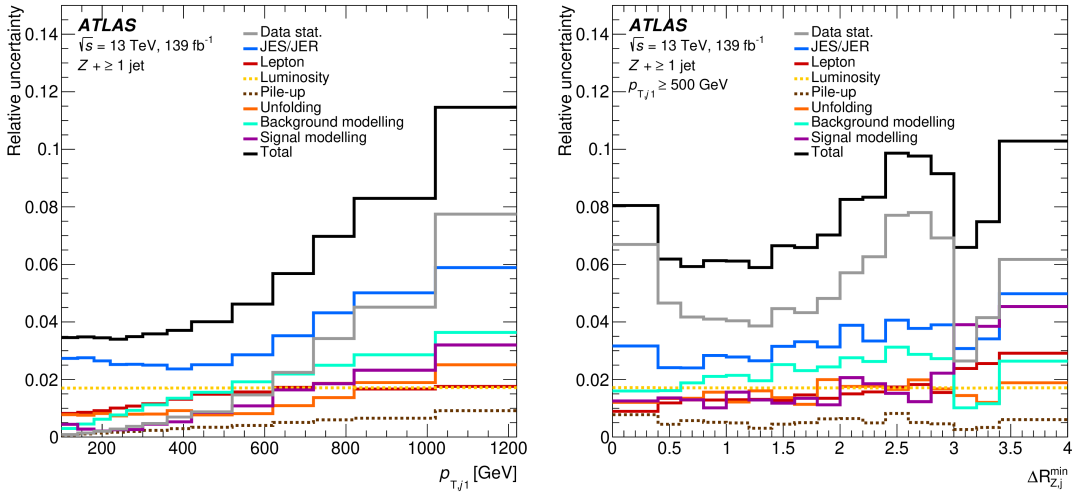

FIGURE 5.18: The systematic uncertainties on the unfolded cross section for $p_T(j)$ (left) and $\Delta R^{min}(Z,j)$ [42].

Sherpa 2.2.1 samples. We apply a few additional, symmetric uncertainties to account for all differences in other observables. This includes a flat 1% uncertainty to cover statistical variations. This covers any missed effect of the unfolding uncertainty while not impacting the final measurement precision, since unfolding uncertainty is often small.

5.6 Systematic Uncertainties On Unfolded Results

The systematic uncertainties on the differential cross-section measurements are computed using the Bayesian unfolding method (see 2.5.12) with 2 iterations. Background modelling uncertainties include the single-top normalisation uncertainty and diboson and electroweak Zjj modelling uncertainties. The Z+jets modelling uncertainty is computed from the uncertainty on the unfolded cross section from unfolding the data with the response matrix of the scale, PDF, PDF α_S and EW modelling variations of the Z+jets production.

Two examples of the systematics are shown in Fig. 5.18, which presents the stack plots for systematic uncertainties on the unfolded cross section for $p_T(j)$ and $\Delta R^{min}(Z,j)$ observables [42]. For leading jet transverse momentum, jet uncertainties (blue line) dominate up to 1 TeV, beyond which the data statistical uncertainty becomes more important. The $\Delta R^{min}(Z,j)$ observable in the high-p_T region has data statistics as the leading uncertainty, followed by jet systematics.

5.7 Results

The final results in Fig. 5.19, 5.20 and 5.21 show the unfolded differential cross sections for p_T(jet) and $\Delta R^{min}_{Z,j}$ data, compared to Sherpa 2.2.1, `MG+PY8 CKKW`, Sherpa 2.2.11 and `MG+PY8 FxFx`.

Also included are two additional samples of Z+jet events from the $NNLO_{JET}$ program [244, 245] that calculates fixed-order predictions at parton-level for inclusive jet processes at higher orders of QCD. The $NNLO_{JET}$@NNLO is a NNLO prediction at 1 parton, while the $NNLO_{JET}$@NLO is a NLO prediction at 1 parton. In this section, the LO process corresponds to Z+1 jet. These two samples utilise the NNPDF 3.1 NNLO PDF set, and are pure higher-order QCD predictions corresponding to parton or born level predictions. A born-dressed scale factor is then calculated and applied to these predictions, to match the fiducial selection for born dressed leptons. There is also an overlap removal correction factor, to correct for the difference in overlap removal procedure between these samples and the nominal ones used previously [42].

The angular distance between the Z boson and the closest jet, $\Delta R^{min}_{Z,j}$ allow to distinguish between collinear Z-boson emission and to back-to-back topologies. Collinear events are observed in the region $\Delta R^{min}_{Z,j} \leq 1.4$ while the back-to-back events are observed in $\Delta R^{min}_{Z,j} \approx \pi$. The collinear region is sensitive to logarithmic enhancements in cross section as $\sim \alpha_S ln^2 \frac{p_{T,j}}{m_Z}$ while the back-to-back region obtains non-negligible virtual EW corrections.

In Fig. 5.19 we observe mismodelling by `MG+PY8 CKKW` and Sherpa 2.2.1 in the high-p_T collinear region, while their modelling is generally better in the back-to-back region. However, both Sherpa 2.2.11 and `MG+PY8 FxFx` modelling of the collinear and back-to-back regions are largely improved over the previous generators, and consistent with data, to a high precision especially for `MG+PY8 FxFx`. The agreement to data for `MG+PY8 FxFx` and Sherpa 2.2.11 for highly collinear events implies that the resummation of additional logarithms such as those from EW showers is not required to obtain precise results.

The $NNLO_{JET}$@NNLO and $NNLO_{JET}$ model the data well in both the collinear and back-to-back regions, especially at high precision for $NNLO_{JET}$@NNLO. This is an exceptional result for collinear phase space modelling, since this region contains a large number of 3-jet events which are only simulated at LO for $NNLO_{JET}$@NNLO. In addition, we observe an overestimation of the pQCD cross section prediction without EW correction for the back-to-back region in Fig. 5.19 [42].

We find that `MG+PY8 FxFx` with matrix elements for up to 3 partons at NLO is a significant improvement in modelling to data in the high-p_T region, over `MG+PY8 CKKW` with up to 4 partons at LO, and to a much higher precision. Sherpa 2.2.11 also

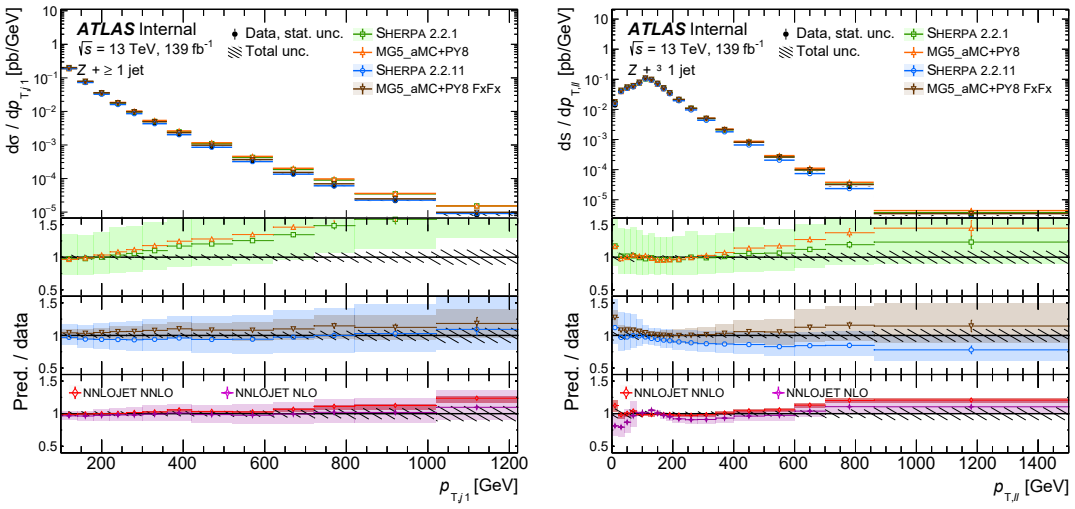

FIGURE 5.19: Differential cross sections as a function of p_T(leading jet) (left) and $p_T(Z)$ (right) for combined electron and muon channels. Unfolded data are plotted by black points, with error bars representing statistical uncertainty and the grey hashed region representing systematic uncertainties. In the upper pad, unfolded data are compared to Sherpa 2.2.1 (green squares), `MG+PY8 CKKW` (orange triangles). In the middle pad, data are compared to Sherpa 2.2.11 (blue circles) and `MG+PY8 FxFx` (brown inverted triangles). In the lower pad, data are compared to $NNLO_{JET}$@NNLO (red diamond) and $NNLO_{JET}$ (magenta cross). Error bars for the ratio pads correspond to statistical uncertainty of the prediction, while unfolded data uncertainty is given by the hashed region. Prediction uncertainties are dominated by scale uncertainties, including the quadratic sum of the PDF and scale uncertainties, while Sherpa 2.2.11 also includes uncertainties from EW contributions [42].

significantly improves over Sherpa 2.2.1 with the addition of a fifth parton at LO in the matrix element, NLO virtual EW corrections, and a new treatment of unordered histories in the parton shower. NNLO calculations at fixed order from NNLOjet [244, 245] also describe the data cross sections at a very high precision level [42].

In the next section, the second ATLAS analysis regarding an important background to BSM searches, the analysis for which I provide the unique, novel flavour fit developments and generator studies is discussed.

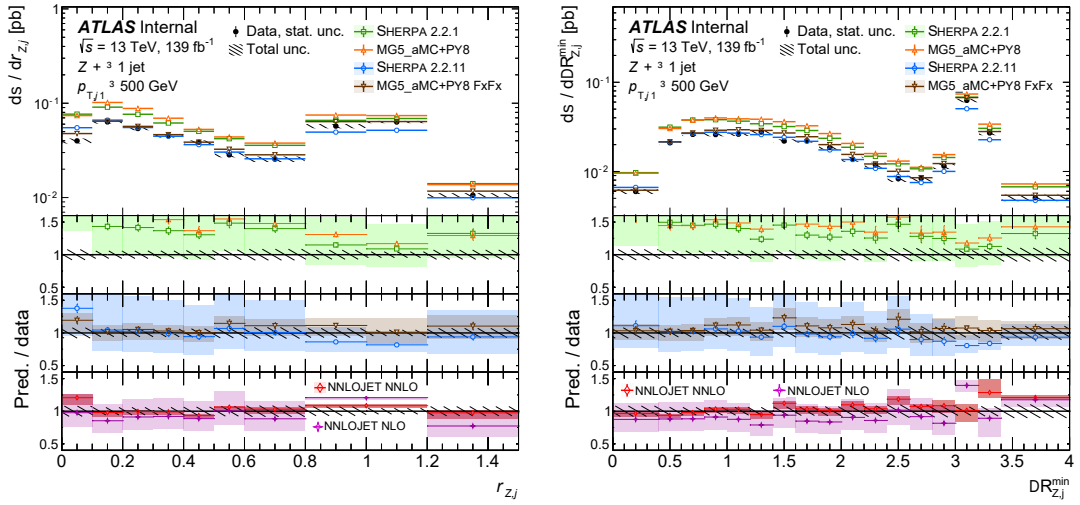

FIGURE 5.20: Differential cross sections as a function of $r_{Z,j} = p_T(Z/\text{leading jet})$ (left) and $\Delta R^{min}_{Z,j}$ (right) for combined electron and muon channels. Unfolded data are plotted by black points, with error bars representing statistical uncertainty and the grey hashed region representing systematic uncertainties. In the upper pad, unfolded data are compared to Sherpa 2.2.1 (green squares), `MG+PY8 CKKW` (orange triangles). In the middle pad, data are compared to Sherpa 2.2.11 (blue circles) and `MG+PY8 FxFx` (brown inverted triangles). In the lower pad, data are compared to $NNLO_{JET}$@NNLO (red diamond) and $NNLO_{JET}$ (magenta cross). Error bars for the ratio pads correspond to statistical uncertainty of the prediction, while unfolded data uncertainty is given by the hashed region. Prediction uncertainties are dominated by scale uncertainties, including the quadratic sum of the PDF and scale uncertainties, while Sherpa 2.2.11 also includes uncertainties from EW contributions [42].

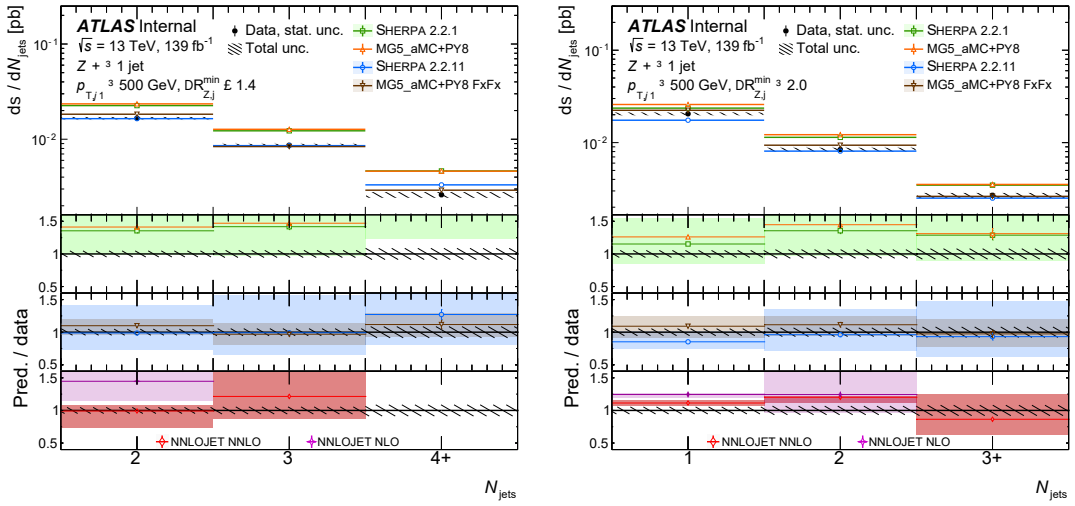

FIGURE 5.21: Differential cross sections as a function of jet multiplicity in the collinear (left) and back-to-back (right) regions for combined electron and muon channels. Unfolded data are plotted by black points, with error bars representing statistical uncertainty and the grey hashed region representing systematic uncertainties. In the upper pad, unfolded data are compared to Sherpa 2.2.1 (green squares), `MG+PY8 CKKW` (orange triangles). In the middle pad, data are compared to Sherpa 2.2.11 (blue circles) and `MG+PY8 FxFx` (brown inverted triangles). In the lower pad, data are compared to $NNLO_{JET}$@NNLO (red diamond) and $NNLO_{JET}$ (magenta cross). Error bars for the ratio pads correspond to statistical uncertainty of the prediction, while unfolded data uncertainty is given by the hashed region. Prediction uncertainties are dominated by scale uncertainties, including the quadratic sum of the PDF and scale uncertainties, while Sherpa 2.2.11 also includes uncertainties from EW contributions [42].

Chapter 6

Production of Z boson in association with b and c jets

Within the LHC, Z production is one of the most common, especially in the form of Drell-Yan neutral current processes. This requires a Z boson produced from quark-antiquark collisions, which then further decays into two same-flavour opposite-sign leptons. The Z-boson is also commonly produced in association with jets, which can be classified as heavy flavour (jets originating from b- or c-quarks) or light jets (jets originating from a gluon, u-,d- or s-quark). In contrast to the inclusive scenario studied in the previous section, this analysis focuses on the production of Z boson in association with heavy flavour quarks, both b- and c-quark jets.

In addition to probing pQCD and parton shower modelling of $Z + HF$ processes, the specific reasons for studying the $Z + b$-jet events is twofold. Firstly, since the dominant Higgs branching is $H \to bb$, the $Z + b$-jet events are a significant background to the SM precision measurement of this Higgs process, when produced via ZH. BSM searches for DM or SUSY can also possess large backgrounds coming from $Z + b$-jet events, and therefore a large systematic uncertainty for these searches. Their precise measurement would further constrain certain BSM searches (e.g. $Z(\to \nu\nu) + b$).

The second reason for interest in $Z + b$-jet production comes from their sensitivity to the difference between predictions from two different flavour schemes. These relate to the b-quark presence in the initial state proton. In pQCD calculations containing heavy flavour quarks, there are typically two schemes: the four-flavour and five-flavour number schemes (4FNS and 5FNS respectively [246]). For the 4FNS, only the parton densities of gluons and the first two quark generations are considered, forbidding the presence of a b-quark in the initial proton. Since the b-quark is much heavier than the proton, it can not be present as an initial state quark, in the matrix element of the calculation. The b-quarks could instead be produced in the final state via gluon splitting in high-Q^2 collisions. As a result, no b-quark PDF is included in the

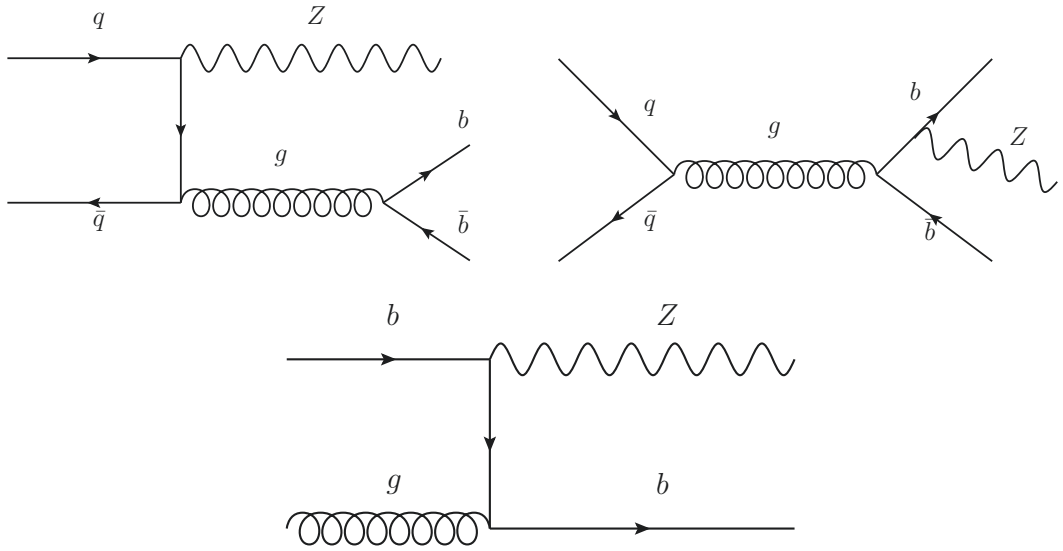

FIGURE 6.1: Diagrams for the 4-flavour number scheme (4FNS, top) and 5-flavour number scheme (5FNS, bottom) processes. The 4FNS does not allow for b-quarks in the initial state and b-quarks are only found via final state gluon splitting, while the 5FNS does allow b-quarks in the initial state.

matrix element and only the four lightest quark PDFs are included. However, this leads to a non-resummable calculation due to the non-zero b-quark mass giving rise to logarithmic divergencies at high energy, requiring NLO calculations for loop corrections of the secondary gluon vertex. Meanwhile, for the 5FNS, the b-quark density is also considered in the initial proton. Including the b-quark density in the initial state allows for possible heavy flavour production and further constraining the b-quark PDF. However, it has been shown that 5FNS predictions for differential distributions, and more exclusive observables tend to be less accurate and more involved with respect to those performed via NLO computations in the 4FNS [246]. Ideally, one should exploit the advantages of both schemes, utilising 5-flavor scheme to accurately predict the total cross section at NNLO and the corresponding 4-flavor computation at NLO. Examples of these production mechanisms are given in Fig.6.1.

The production of $Z + c$-jet events is also of great interest, and provides unique insight into the quark content of the proton. The quark has many possible bound states beyond the standard 3-quark $|uud\rangle$ bound state. These include states such as $|uudb\bar{b}\rangle$ and $|uudc\bar{c}\rangle$ where the additional quark-antiquark pair cancels out its overall charge contribution to the bound state, while contributing to the proton's overall Fock state[1]. This is know as the quarks intrinsic quark content and, although rare, is expected to provide unique phenomenology [248, 249], observable at colliders. As the c-quark mass is smaller than the b-quark mass, the effects of this intrinsic quark content, such

[1]The Fock state is also known as the number state, and is a quantum state associated with the sum of particle number in a Fock space [247].

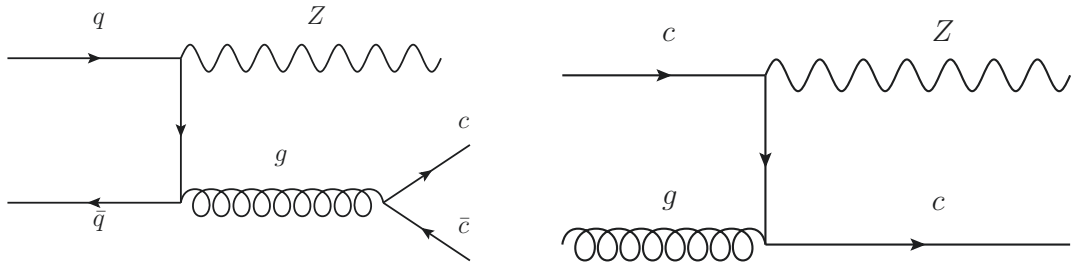

FIGURE 6.2: Two example Feynman diagrams for $Z + c(c)$ production. The left diagram shows $c\bar{c}$ production via final state gluon splitting, while the right diagram shows single c-quark production with a c-quark present in the initial state proton.

as enhancements to the c-quark PDF, can be more readily observed through c-quark jet events in experiment [250]. Example production mechanisms are given in Fig.6.2.

The variables under study for this analysis include $p_T(Z)$ for $Z+ \geq 1b$-jet, p_T (leading b-jet), $\Delta R(Z$, leading b-jet), $p_T(Z)$ for $Z+ \geq 1$ c-jet, p_T (leading c-jet), $\Delta R(Z$, leading c-jet), and in the case of ≥ 2 b-jet events, $\Delta\phi(b, b)$ and m_{bb}. The p_T (leading b-jet) variable and $p_T(Z)$ variable for $Z+ \geq 1b$-jet provide information on 5F/4F, pQCD, ME/PS and hard/soft radiation. The $\Delta R(Z$, leading b-jet) variable is then sensitive to additional radiation. For the ≥ 2 b-jet events case, $\Delta\phi(bb)$ is sensitive to parton shower effects such as gluon splitting at low $\Delta\phi$, and pQCD effects at large $\Delta\phi$. Meanwhile $m(bb)$ is useful for generator configuration and an important background for searches and Higgs signals.

The dedicated Feynman variable $x_{F,b/c}$, designed for probing heavy flavour quark content and b-/c-quark discrimination in particular, is defined as

$$x_F = \frac{2p_T \sinh(\eta)}{\sqrt{s}} \tag{6.1}$$

where p_T is the leading b/c-jet p_T, η is the leading b/c-jet pseudo-rapidity and $\sqrt{s}$ is collider energy given by 13 TeV. Sensitivity studies performed previously have shown that selecting a large enough portion of events with $x_{F,c} > 0.1$, the intrinsic charm PDF contributions to charm production is greatly enhanced, such that it can be distinguished in comparison to purely extrinsic contributions [250, 251].

Background processes to the $Z(\ell\ell) + b(b)$ or $Z(\ell\ell) + c(c)$ signal include production of dibosons, a Higgs boson, a single top quark, $t\bar{t}$, $Z \to \tau\tau$, or $W \to \ell\nu$. There is negligible background from multijet, as shown in the previous analysis. Some example Feynman diagrams for the background processes are given in Fig.6.3. The final state leptons would have the same flavour, to mimic the signal decay from a Z boson.

In summary, for the selection phase space requiring $Z+ \geq 1$ b-jet ($p_T(jet) > 20$ GeV), we measure $p_T(Z)$, $p_T(leading\ bjet)$, $\Delta R(Z, leading\ bjet)$, $x_F(leading\ bjet)$. For

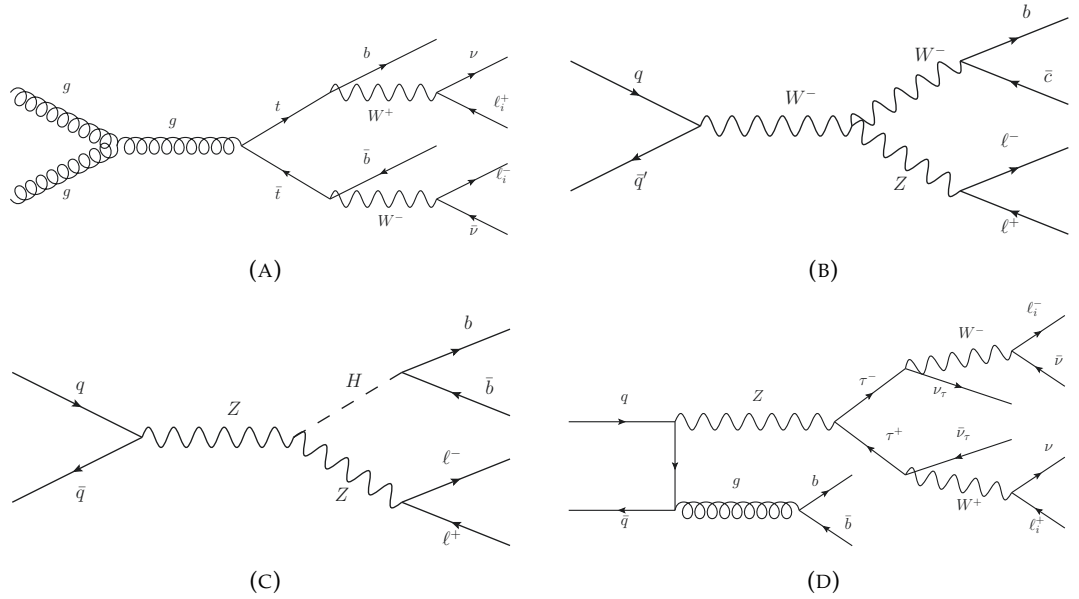

FIGURE 6.3: Examples of Feynman diagrams for the backgrounds processes, including $t\bar{t}$ (a), WZ (b), ZH (c) and $Z \to \tau\tau$ (d). In the cases where leptons come from different W boson sources, these must share the same lepton flavour (e.g. e^+e^-).

selection phase space requiring $Z+ \geq 1$ c-jet ($p_T(jet) > 20$ GeV), we measure $p_T(Z)$, x_F and for selection phase space requiring $Z+ \geq 2$ b-jet ($p_T(jet) > 20$ GeV), we measure $\Delta\phi(bb)$ and $m(bb)$.

6.1 Event Selection

Events are selected using the lowest unprescaled triggers for muon and electron channels given in Table 6.1, requiring exactly two opposite sign muons or electrons. Electrons must satisfy the tight isolation requirements and tight likelihood-based identification criteria. Electrons are selected if they fulfil $p_T > 27$ GeV and $|\eta| < 2.47$. Muons must also satisfy the tight isolation requirements while passing medium identification criteria. Muons must satisfy $p_T > 27$ GeV and $|\eta| < 2.5$ to be selected for the analysis.

Jets are reconstructed using particle flow algorithm and then clustered using anti-k_T jet clustering algorithm with radius parameter of $R = 0.4$. For jet selection we require jets with $p_T > 20$ GeV and $|\eta| < 2.5$. Overlap removal is performed such that jets within $\Delta R < 0.4$ of a lepton are removed. We require lepton pairs to satisfy a Z mass-window of $76 < m_{\ell\ell} < 106$ GeV. Additionally, events are discarded if they satisfy both $ET^{miss} > 60$ GeV and $p_T(Z) < 150$ GeV. The b-tagging uses the Deep Neural Network (DL1r) [252] with an 85% b-tag efficiency working point, 2% misidentification rate for g- and c-jets, and a 7% misidentification rate for g- and ud-jets and 4% for b-jets for c-tagging [253]. We require b- and c-quarks to be above 5

Years	Muon Channel	Electron Channel
2015-2016	HLT_mu20_iloose_L1MU15 HLT_mu50	HLT_e24_lhmedium_L1EM20VH HLT_e60_lhmedium HLT_e120_lhloose
2017-2018	HLT_mu26_ivarmedium HLT_mu50	HLT_e26_lhtight_nod0_ivarloose HLT_e60_lhmedium_nod0 HLT_e140_lhloose_nod0 HLT_e300_etcut

TABLE 6.1: The lowest unprescaled single lepton triggers for muon and electron channels [43].

GeV for ghost matching the jet flavour. This ghost matching reclusters the jets with "ghost" particles that determines the jet's flavour [254].

In this analysis, we produce a robust flavour fit in order to correct for the inaccurate flavour fraction modelling of the MC generators. In the following sections I detail my unique contributions to the $Z+$ heavy flavour quark production ATLAS analysis [43], including the MC generator comparisons followed by the novel flavour fit procedure.

6.2 FxFx and Sherpa 2.2.11 Studies

In addition to the legacy generators Sherpa 2.2.1 and MG+PY8 CKKW, the theory samples used for this analysis include Sherpa 2.2.11, and MG+PY FxFx. Below are comparisons between the new generators, using the Z+heavy flavour quark Rivet analysis [255]. The selection procedure for this Rivet analysis follows section 6.1. The distributions in Fig.6.4 show the comparisons of $p_T(Z)$ for b-jet ≥ 1 and p_T(leading b-jet) for Sherpa 2.2.11 and MG+PY8 FxFx. These are compared to a partial RunII data set [256] in the left plots, where it is shown that both Sherpa 2.2.11 and MadGraph tend to initially overestimate data but are still within statistical uncertainty. However, these lead to an underestimation above 100 GeV mostly covered by statistical uncertainty. The right plots use Sherpa 2.2.11 as the reference, showing that MG+PY8 FxFx typically predicts below Sherpa 2.2.11 for low p_T, but predicts a greater cross section as $p_T > 100$ GeV. Additionally, Sherpa 2.2.11 has much more available PDFs to contribute to the PDF uncertainty, as compared with MG+PY8 FxFx.

Following this examination of the generator performance in the $Z+$heavy flavour phase space, we proceed with the novel flavour fit procedure in the next section.

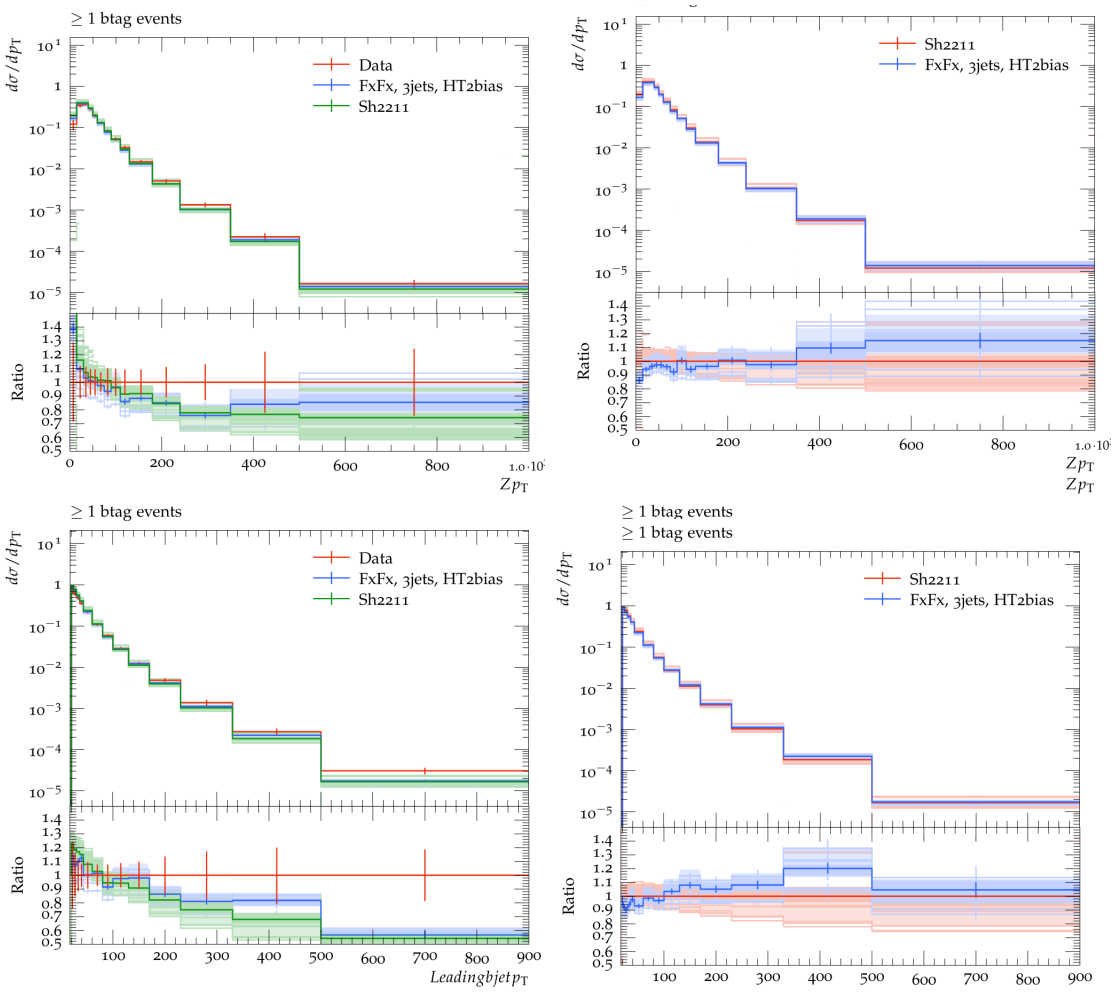

FIGURE 6.4: The left plots show comparisons to data (red) between Sherpa 2.2.11 (green) and `MG+PY8 FxFx` (blue) samples using the Z+HF analysis Rivet routine [255]. The observables plotted are $p_T(Z)$ for b-jet ≥ 1 (top) and p_T(leading b-jet) (bottom). The shaded regions indicate uncertainty due to PDF scale variations. The right plots show comparisons only between Sherpa 2.2.11(red) and `MG+PY8 FxFx` (blue), where the ratio pad uses Sherpa 2.2.11 as the reference.

6.3 Flavour Fits

Typically, we subtract Z+all flavours from data when unfolding. However, the flavour fractions are modelled incorrectly in the MC. Examples for $Z + b$ and $Z + c$ mismodelling are shown in the prefit distributions given in Fig. 6.5 for $p_T(Z)$ with ≥ 1 b-jet, b-jet p_T and x_F, where we see a significant disagreement to data, partially due to MC mismodelling of the flavour fractions in $Z + b/c$/light jet samples. Both Sherpa 2.2.11 and `MG+PY8 FxFx` overestimate compared to data at low-p_T and x_F, while they begin to underestimate compared to data as $p_T > 100$ GeV, and $x_F > 0.03$. This mismodelling is not accounted for by the statistical and systematic uncertainties associated to these generators and the background samples. This motivates the

requirement to perform the flavour fit, correcting for the flavour fraction mismodelling by the MC generators.

In order to correct for this mismodelling, it is necessary to apply corrections derived from a flavour fit to data. The unique properties of the b-quark, such as its relatively long lifetime compared to that of the c-quark, gives rise to novel signatures from b-jet events such as displaced vertices. These b-jets are then identified based on reconstructed objects at the ATLAS detector, including the tracks, primary vertex reconstruction, hadronic jets, track-jet matching and jet flavour labels. For the tracks, which are reconstructed in the ID, b-tagging algorithms are used to select decay tracks originating from b- and c-hadrons based on the kinematic properties of these decays. The primary vertex reconstruction defines the reference point for the b-jet displaced vertex to be calculated. The displaced charged-particle tracks originating from b-hadron decays are filtered for, by requiring large enough impact parameters.

The discriminants returned by the different tagging algorithms, based on various tracking information are combined using the DL1r [252, 257]. Probabilities of b-, c- or light-jet are combined to give a single output score per jet. This is the DL1r b-tagging discriminant, obtained from the DL1r algorithm and is defined as

$$D_{DL1r} = ln\left(\frac{p_b}{f_c \cdot p_c + (1 - f_c) \cdot p_{light}}\right) \tag{6.2}$$

where p_b, p_c, p_{light} are the b-jet, c-jet and light-jet probabilities respectively and f_c is the effective c-jet fraction of the background sample used for training on.

The b-jet tagging efficiency is then defined in terms of the b-tagging discriminant, with different cuts on the operating working point (OP) as

$$\epsilon^b = \frac{N^b_{pass}(D_{DL1r} > T_f)}{N^b_{total}} \tag{6.3}$$

where T_f is the cut value of the OP working points determined using a nominal $t\bar{t}$ sample. The OP working points are defined as a cut on the D_{DL1r} score for b-jet tag efficiency of 60%, 70%, 77% and 85%. The pseudo-continuous b-tagging weight (PCBT) bins can then be defined, corresponding to b-jet tag efficiencies [0%, 60%], [60%, 70%], [70%, 77%], [77%, 85%] and [85%, 100%] [258].

Utilising the DL1r derived b-tag quantile, the flavour fits are performed in the following way. First, for each bin of the observable, the b-tag quantiles (this flavour-content sensitive variable) is calculated per MC event. It is a discriminator variable, computed for each jet which is to be tagged. The b-tagging performance has dependency on jet p_T and η. At low p_T, multiple scatterings are induced, negatively impacting the b-tagging efficiency. For high p_T, there is worse resolution for b-tagging due to an increase of gluon splitting and more fragmentation leading to larger track

density and multiplicity. There is a middle-ground in which the best performance is achieved, $p_T(j) \sim 100$ GeV. The same b-tag quantile calculating procedure is performed for signal region data. These are shown in Fig. 6.6 and 6.7, where the x-axis shares the same x-axis bins as the observable and the y-axis is the number of events per quantile of the b-tag. These are separated between $Z + 1b$-jet (Fig.6.6) and $Z + 1c$-jet (Fig.6.7) for electron and muon channels.

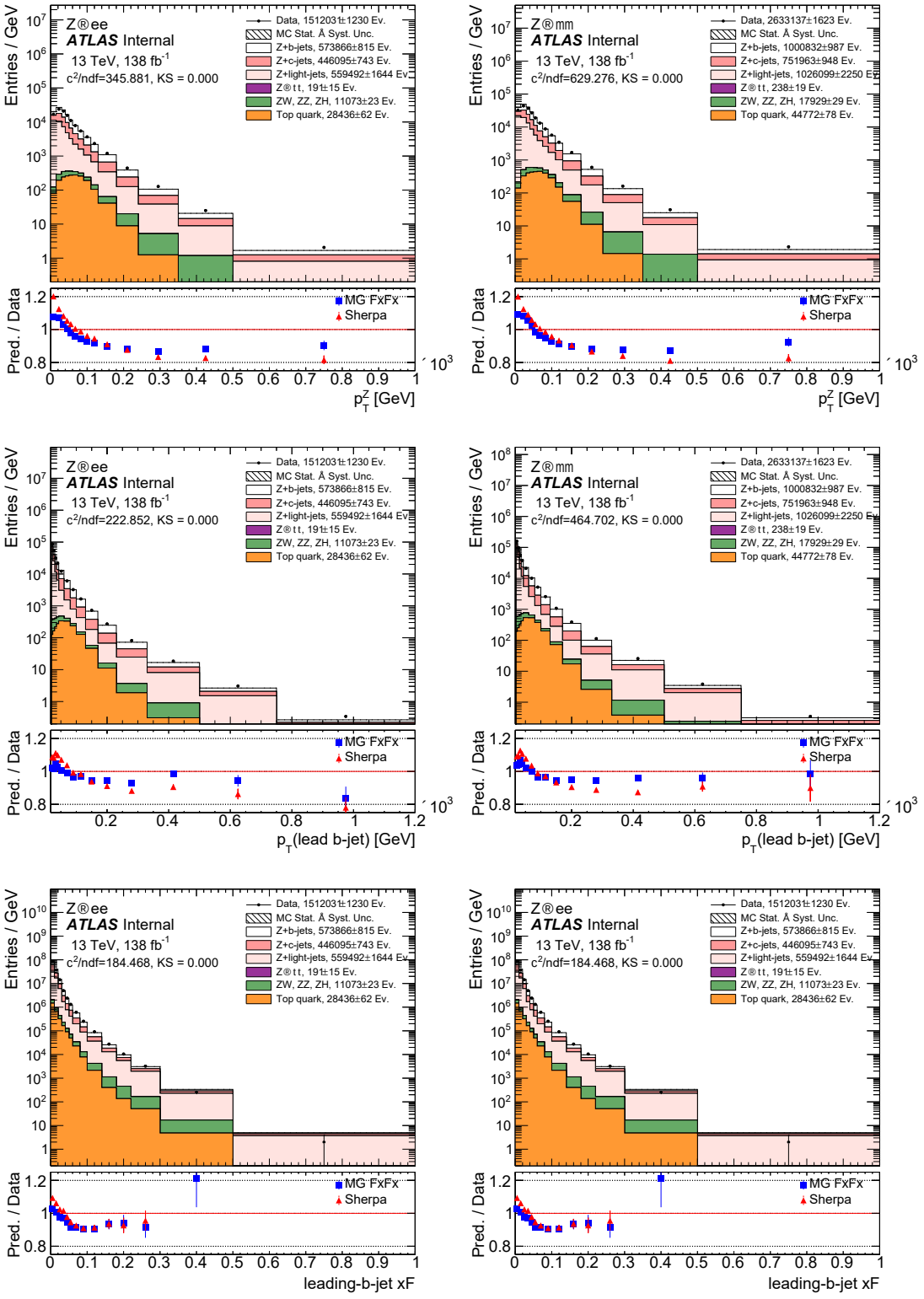

FIGURE 6.5: The prefit distributions for $p_T(Z)$ with $\geq$ 1 b-jet (top), leading b-jet p_T (middle) and x_F (bottom), for electron (left) and muon (right) channels. The stacked plot includes top quark (single top+$t\bar{t}$), diboson (ZW,ZZ) Z+Higgs and Z+b/c/light jet samples. The MC statistical and systematic uncertainty is summed in quadrature and plotted as the hashed bars. The ratio pad show the comparison between Sherpa 2.2.11, Madgraph+Pythia8 FxFx to data.

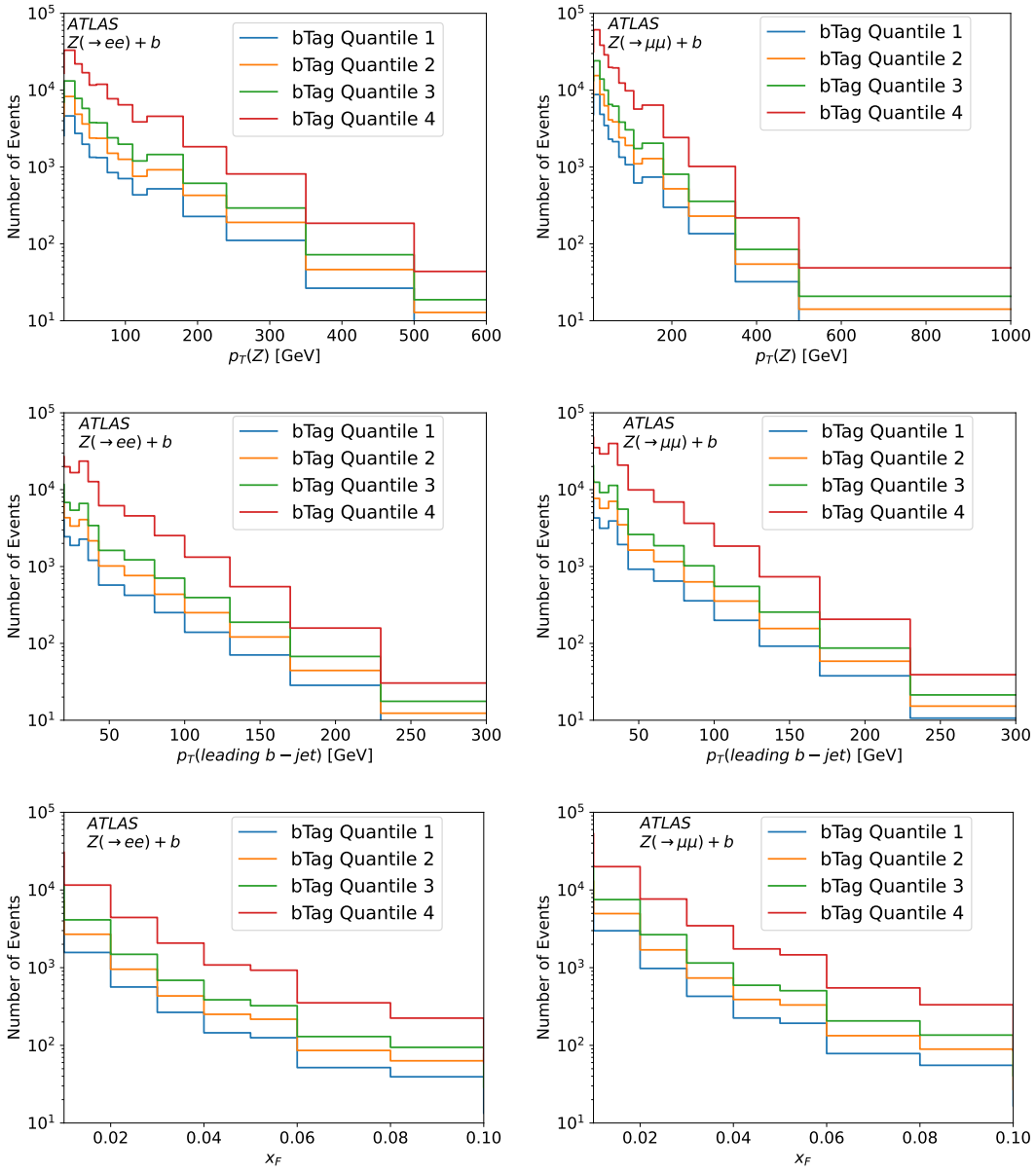

FIGURE 6.6: The $Z + 1b$ b-tag quantile distributions for $p_T(Z)$ (top), leading b-jet p_T (middle) and x_F (bottom) for electron (left) and muon (right) channels. The x-axis shares the same x-axis bins as the observable and the y-axis is the number of events per quantile of the b-tag.

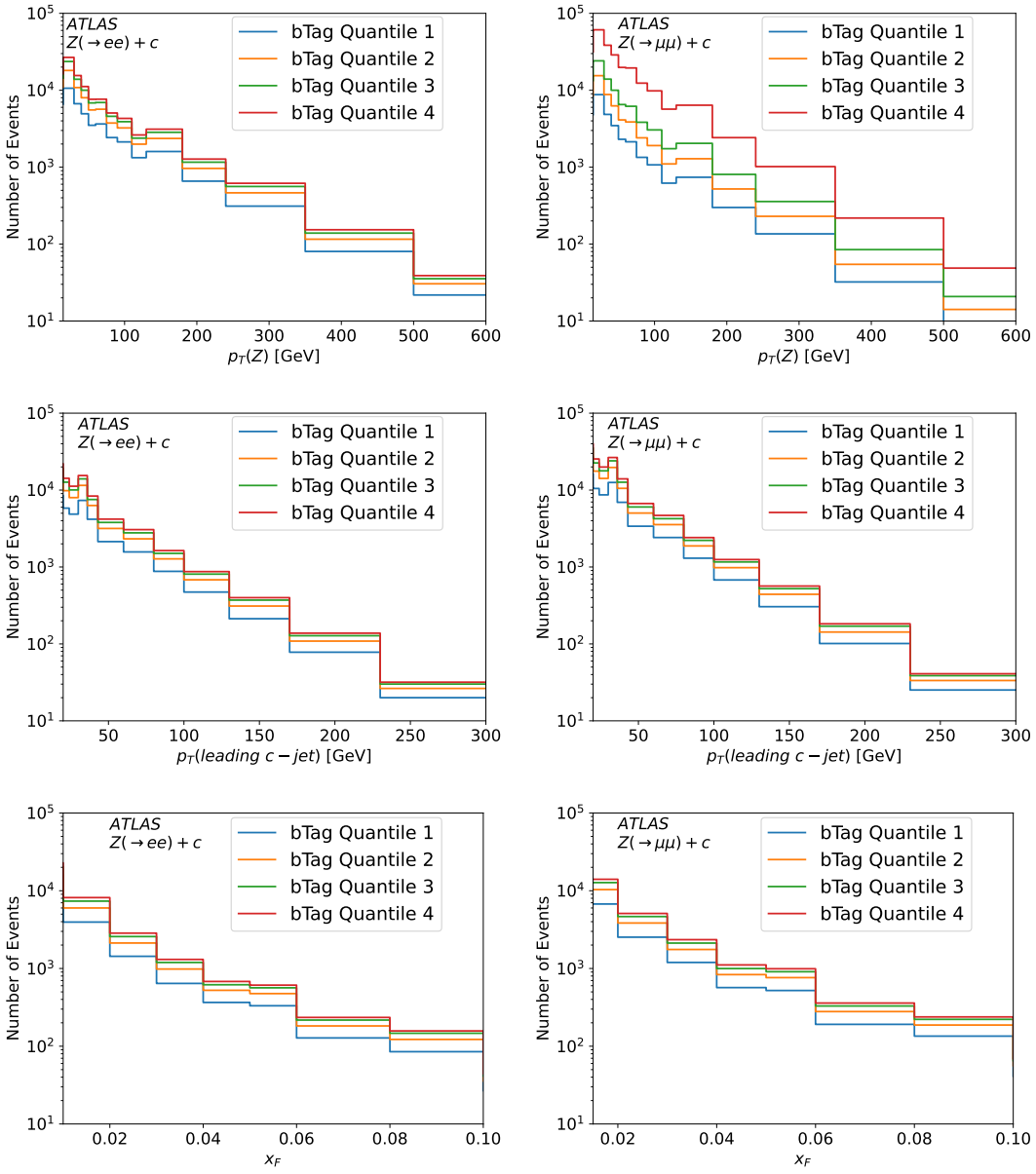

FIGURE 6.7: The $Z + 1c$ b-tag quantile distributions for $p_T(Z)$ (top), leading c-jet p_T (middle) and x_F (bottom) for electron (left) and muon (right) channels. The x-axis shares the same x-axis bins as the observable, the y-axis is the quantile of the b-tag and the z-axis is the number of events for that observable.

Using the b-tag quantile information, we perform a likelihood fit, where $Z+b$-jet, $Z+c$-jet and Z+light jet samples are set to floating normalisation. The constrained samples ($t\bar{t}$,$Z\tau\tau$,$WW/ZZ/WZ$) are set such that the fit is electroweak - background subtracted, and are fixed by a normalisation of 0.06. We then subtract a set of samples (e.g: single-top) form data before the fit, as these have fixed normalisation. This is done such that $Z+c$ is a background for $Z+b$, and $Z+b$ is a background for $Z+c$. From this fit to data, we extract scale factors for $Z+b/c$/light-jets which we apply to our MC to give the best agreement to data. Closure test plots are shown in Fig.6.8 along with comparisons between Sherpa 2.2.11 and `MG+PY8 FxFx` Z+jets fits, where we apply the extracted scale factors back onto all three of the $Z+b$.$Z+c$ and Z+light jet samples. From Fig. 6.8, it is clear that the fit passes the closure test for all observables. We expect a perfect fit, since we are just extracting the scale factors determined by the fit to data, and then re-applying this to the MC.

For the b-jet post-fit distributions, the scale factors are then applied to the backgrounds of the b-jet signal (scale factors are applied to c-jet and light-jet samples) in Fig. 6.9. Comparing the distributions in Fig.6.5 and Fig.6.9, there is a clear improvement in the modelling of the initial $p_T(Z)$ bins, and less underestimation of data around the 100 GeV region and above. The leading b-jet p_T also shows some modelling improvements, mostly for $p_T > 100$ GeV. The x_F modelling is greatly improved, in the $x_F < 0.3$ region. Some mismodelling will still persist, since the b-jet signal sample itself is not scaled to account for its own mismodelling.

Then for the c-jet post-fit distributions, the scale factors applied to the backgrounds of the c-jet signal (scale factors are applied to b-jet and light-jet samples) in Fig. 6.10. Comparing the distributions in Fig.6.5 and Fig.6.10, there is some improvement to the modelling in the $p_T(Z)$ distribution at $p_T < 100$ GeV, but underestimates data more compared to the b-jet signal plots. For the leading b-jet p_T, the scaling here causes underestimation in low p_T bins and the modelling is not improved at p_T above this. Finally, the x_F modelling is somewhat improved in the initial x_F bins, although underestimates data here. The modelling quickly falls with x_F, compared to the b-jet signal plots and the pre-fit distributions.

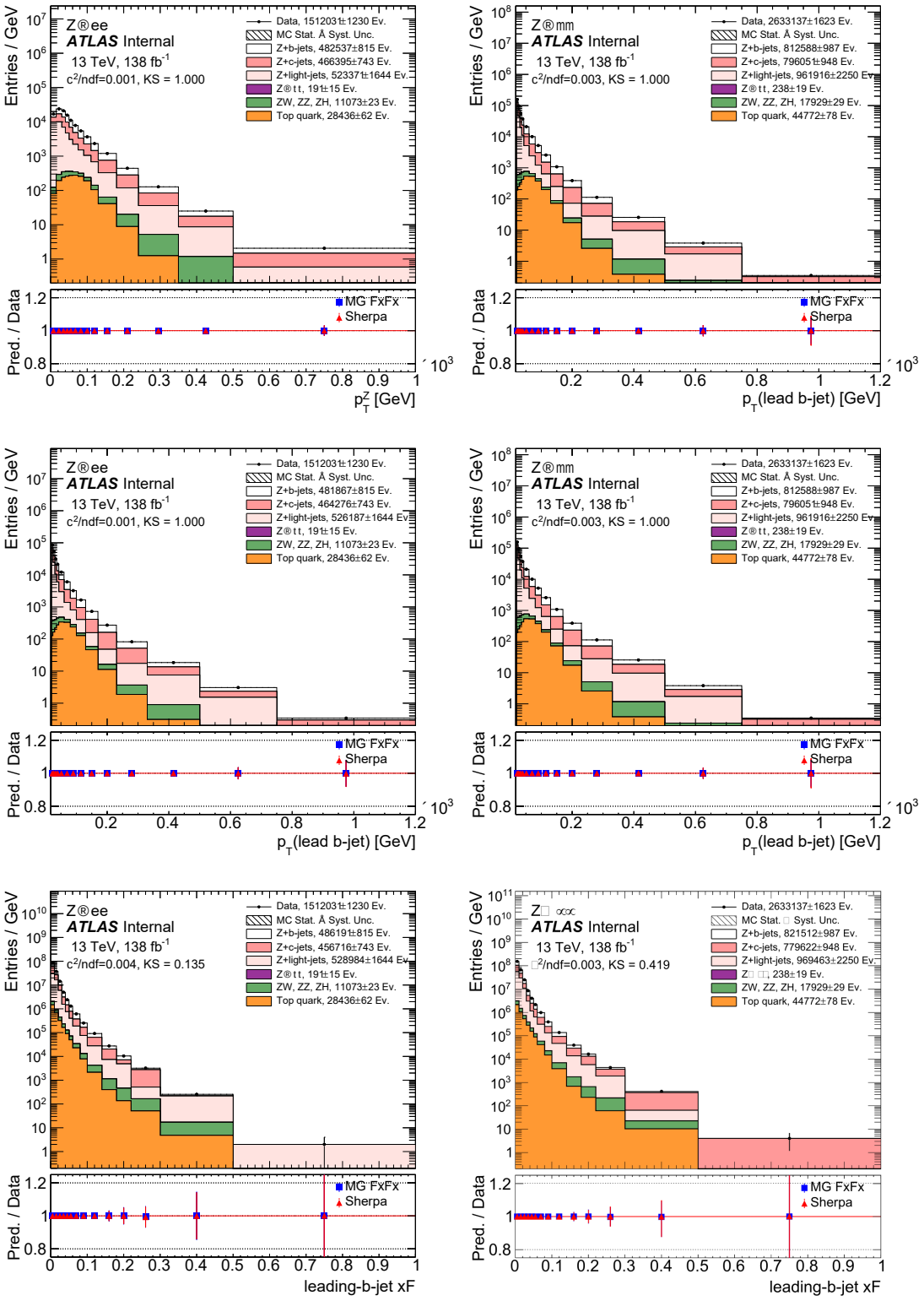

FIGURE 6.8: Closure test plots for $p_T(Z)$ (top), leading b-jet p_T (middle) and x_F (bottom) plots for electron (left) and muon (right) channels.

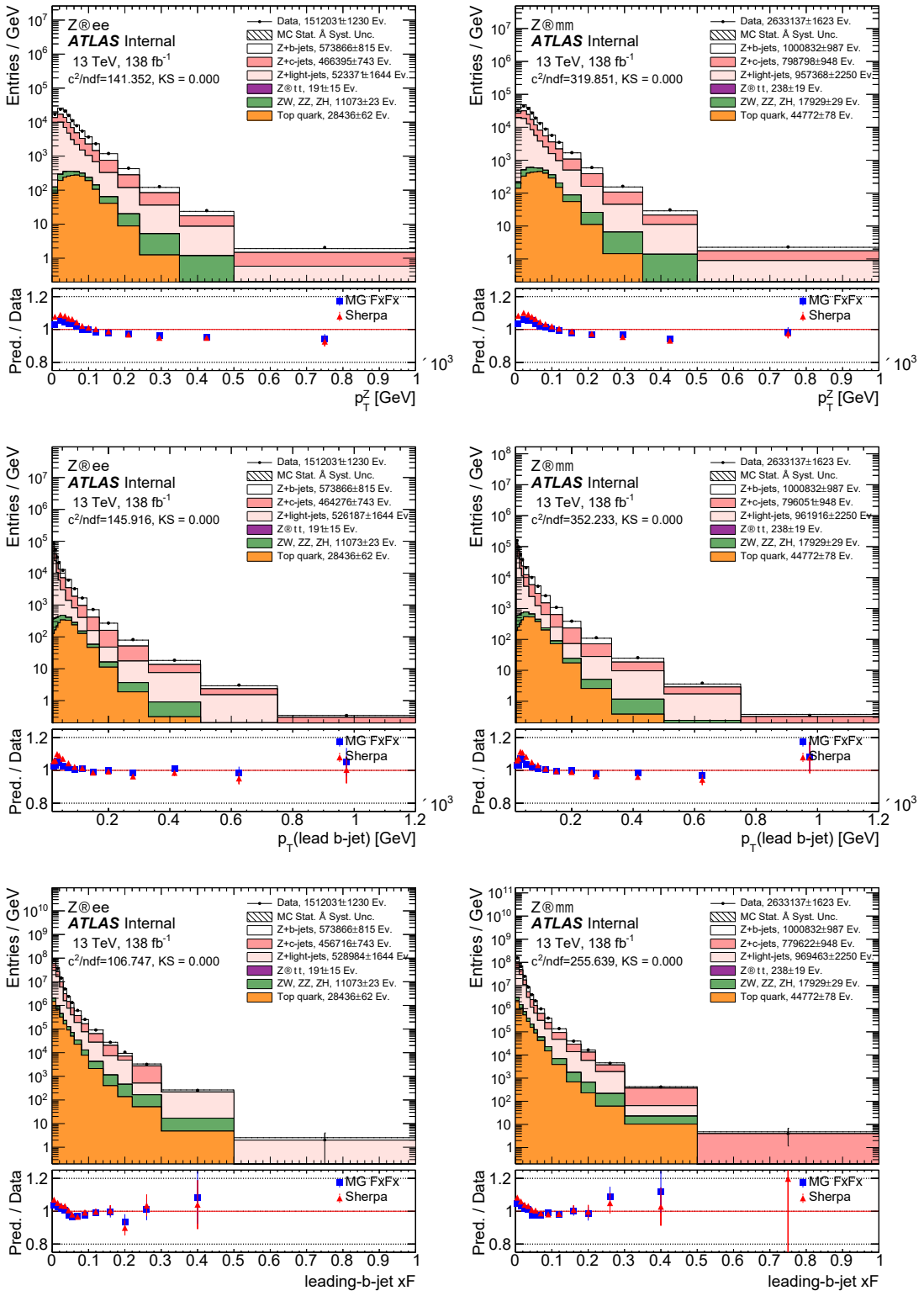

FIGURE 6.9: Post-fit plots for $p_T(Z)$ (top), leading b-jet p_T (middle) and x_F (bottom) plots for electron (left) and muon (right) channels, with scale factors applied to the backgrounds of the b-jet signal.

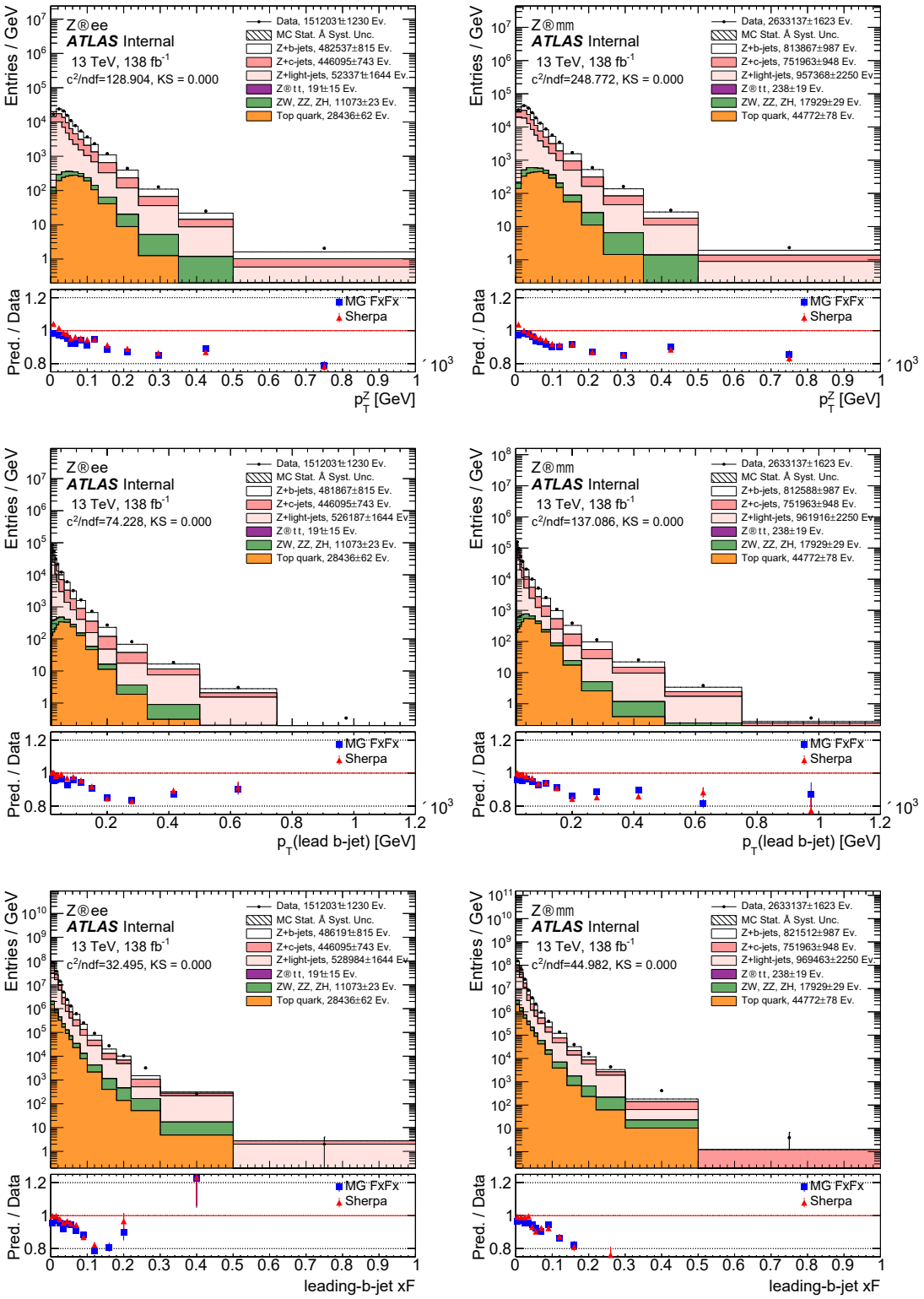

FIGURE 6.10: Post-fit plots for $p_T(Z)$ (top), leading b-jet p_T (middle) and x_F (bottom) plots for electron (left) and muon (right) channels, with scale factors applied to the backgrounds of the *c*-jet signal.

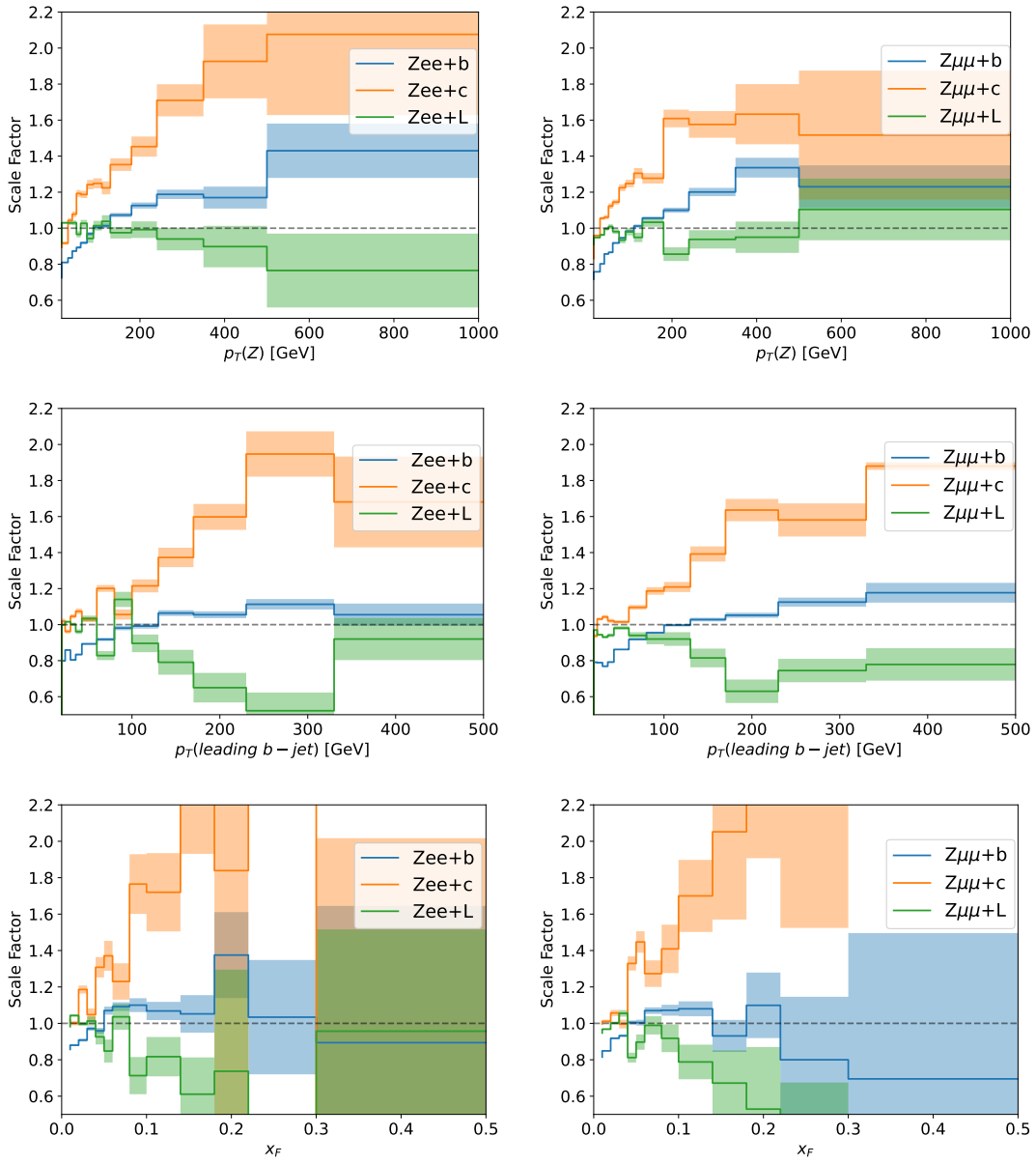

FIGURE 6.11: Scale factors plots for $p_T(Z)$ (top), $p_T(leading\ b-jet)$ (middle) and x_F (bottom) per sample. These are given for $Z+b$ (blue), $Z+c$ (orange) and Z+light (green) jet events, for electron (left) and muon (right) channels. The shaded regions correspond to the fit uncertainty.

From Fig. 6.11 it is shown that most of the correction is required for $Z + c$-jet events (orange line), compared to $Z + b$ (blue line) and Z+light (green line) jet events. Meanwhile, the $Z + b$ is fairly well predicted for p_T(leading b-jet) being within 20% and Z+light predicts $p_T(Z)$ mostly within 20%, only requiring minor scale factor corrections throughout.

These scale factors are then applied to the MC Z+jet flavour fractions to correct for flavour fraction mismodelling, which are subtracted from the data before unfolding.

6.4 Systematic Uncertainties

The systematic uncertainties for the unfolded cross section are given in Fig. 6.12. These include the b-tagging uncertainty, e/γ uncertainty, jet-related uncertainties, E_T^{miss} uncertainty, muon trigger and efficiency uncertainties, pileup reweighting (PRW) uncertainty and the unfolding uncertainty. For all observables in Fig. 6.12, the most significant systematic is the large unfolding uncertainty, especially for the last few bins of each distribution, which then propagates to the unfolded cross-section distributions in Fig. 6.13.

6.5 Unfolded Cross Section

In this section we present the unfolded cross -section distributions for a few key variables, $p_T(Z)$ for b-jets≥ 1, p_T(leading b-jet) and x_F(leading b-jet). These are shown in Fig. 6.13 and use Sherpa 2.2.11 results compared to data. These included data-driven $t\bar{t}$ and flavour fit-corrected Z+jet samples.

The results in Fig.6.13 show agreement to data, but with up to 20% discrepancy to data for $p_T(Z)$ with b-jets≥ 1 in both electron and muon channels. Similar shapes are seen for p_T(leading b-jet) and is modelled within 10% of the data uncertainty, with some close agreement in the $500 < p_T(leading\ b-jet) < 750$ GeV. The x_F variable is modelled within 10% of the data uncertainty, but suffers from some mismodelling. A few bins are in close agreement to the unfolded data for $x_F > 0.06$ for the electron channel and $0.03 < x_F < 0.8$ for the muon channel.

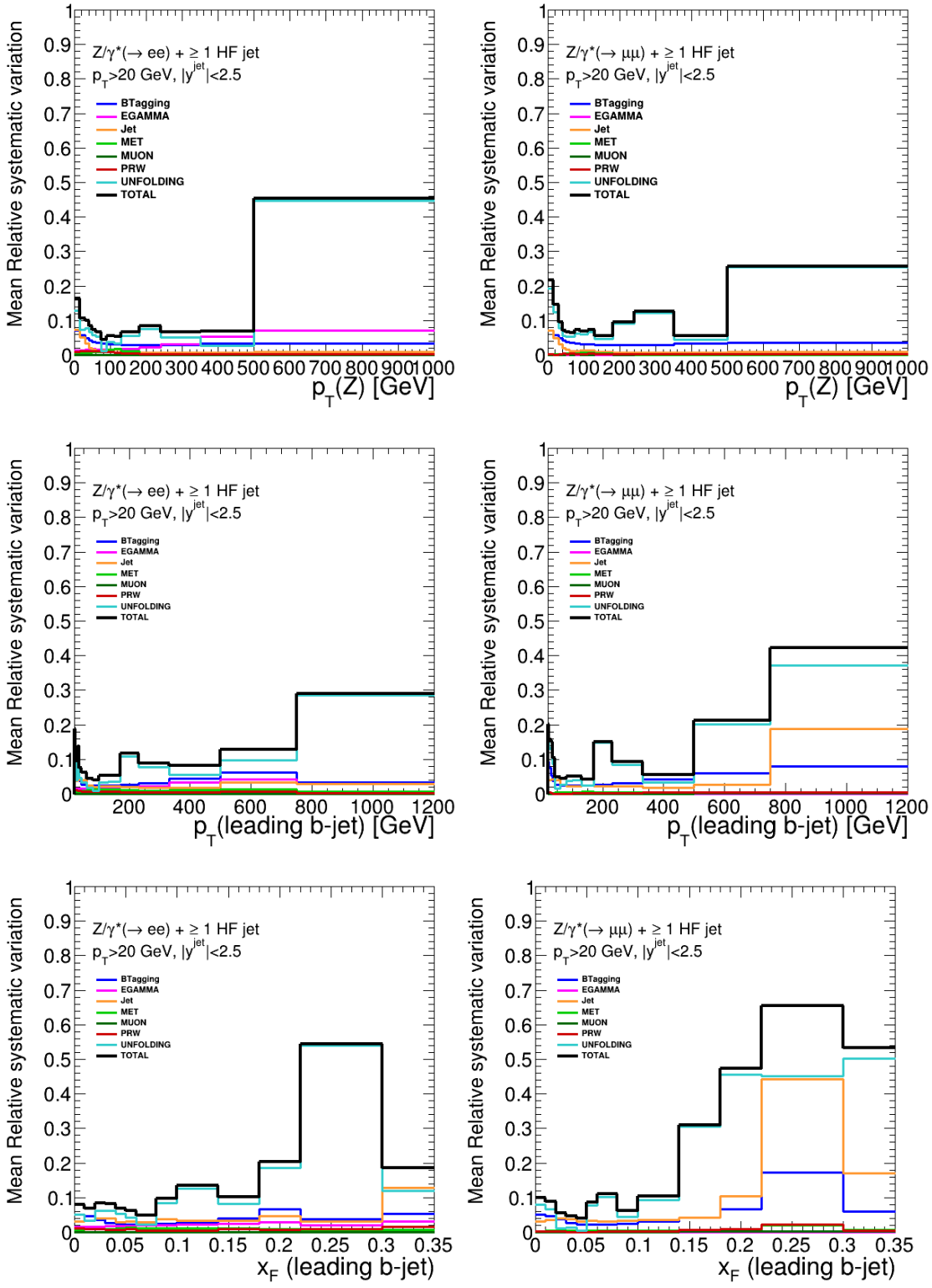

FIGURE 6.12: Systematic uncertainties for the unfolded cross section for $Z(p_T)$ (top), leading b-jet p_T (middle) and x_F (bottom) for electron (left) and muon (right) channel, as courtesy of Semen Turchikhin (JINR Dubna) [43].

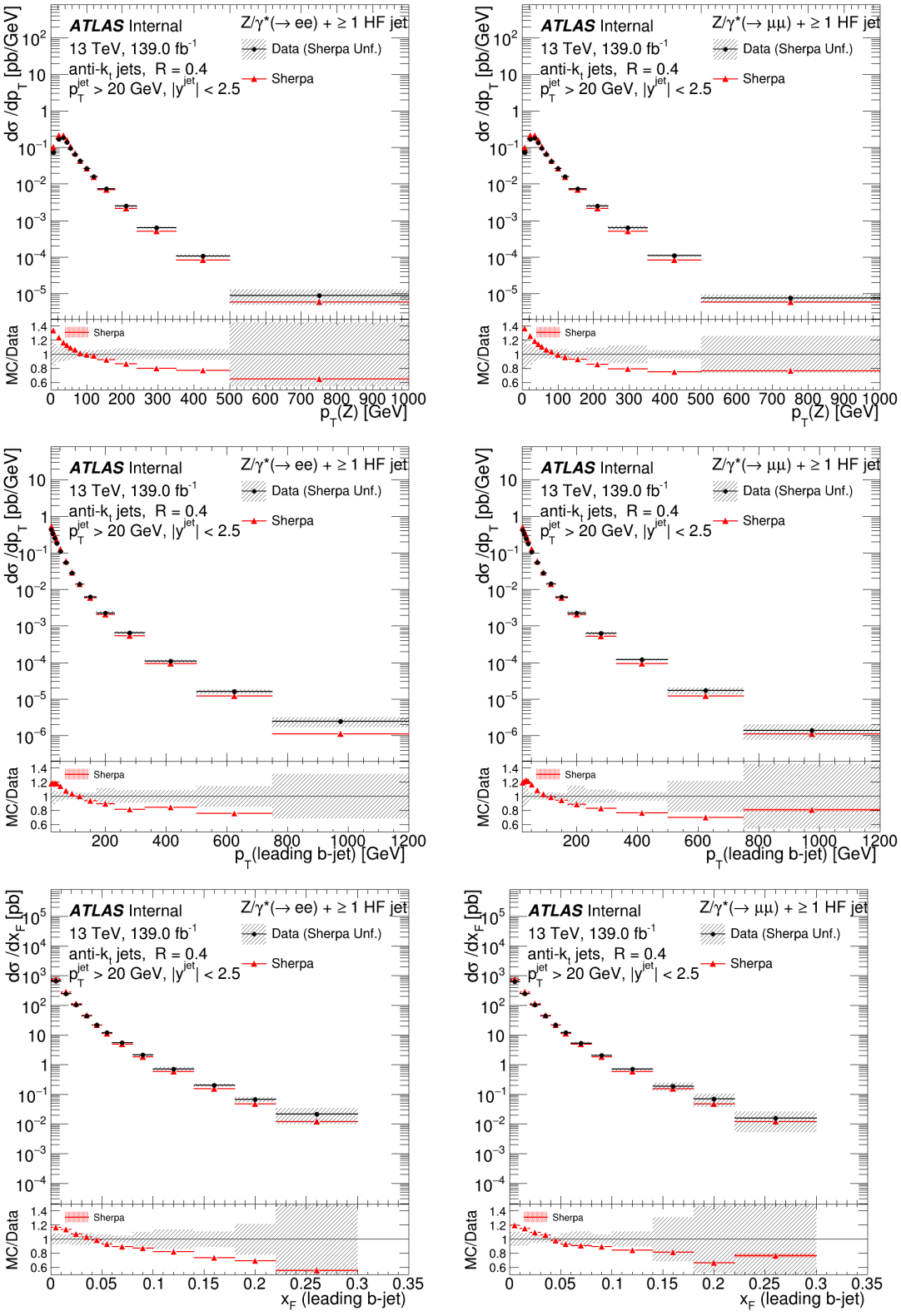

FIGURE 6.13: Differential cross sections for $Z(p_T)$ (top), leading b-jet p_T (middle) and x_F (bottom) for electron (left) and muon (right) channel, as courtesy of Semen Turchikhin (JINR Dubna) [43].

6.6 Results

In this section, we have successfully derived scale factors to correct for the MC generator mismodelling of flavour fractions in the Z+jets samples. Results show significant corrections required for certain samples and bins, up to 50% in some cases.

For the unfolded cross sections, the results in Fig. 6.13 mostly show an agreement between Sherpa 2.2.11 and data within 10-20%. However, there are discrepancies with the data typically in the $150 < p_T < 500$ GeV regions and, in comparison to the 2015/2016 results with Sherpa 2.2.1/data, the new Sherpa 2.2.11/data presented here performs somewhat worse in modelling to the data for this particular phase space. For $p_T(Z)$, Sherpa 2.2.11 shows better modelling around the $50 < p_T(Z) < 150$ GeV in the electron and muon channels of Fig. 6.13 compared to Sherpa 2.2.1 in [259], but worse modelling at $p_T(Z) < 50$ GeV and $150 < p_T(Z) < 500$ GeV. A similar trend is observed in p_T(leading b-jet), where Sherpa 2.2.11 in Fig. 6.13 performs wosre compared to Sherpa 2.2.1 in [259] for the $200 < p_T(\text{leading } b\text{-jet}) < 700$ GeV region. Presented here in Fig. 6.13 is also the x_F variable not present in the previous analysis [259]. This variable is reasonably modelled by Sherpa 2.2.11, within 20% of the data in all bins.

Beyond this section we now move to the DM signal analyses, starting with the multilepton+E_T^{miss} final state analysis at the LHC.

Chapter 7

LHC Constraints on DM Signals with Multilepton+E_T^{miss} Final States

In this section we present the multilepton + missing energy signals at the LHC, for i2HDM and MFDM models as detailed in section 3. The production and decay processes are considered inclusively and the combination gives an idea about the LHC event rate of the signatures under study. When the DM multiplet partners' mass splitting between DM and those partners is large enough, these give rise to sufficiently energetic leptons, which can originate from the following processes:

- $pp \to D_1 D^{\pm} \to D_1 D_1 W^{\pm(*)} \to D_1 D_1 \ell^{\pm} \nu$
- $pp \to D^+ D^- \to D_1 D_1 W^{+(*)} W^{-(*)} \to D_1 D_1 \ell^+ \ell^- \nu \bar{\nu}$
- $pp \to D_1 D_n \to D_1 D_1 Z^{(*)} \to D_1 D_1 \ell^+ \ell^-$
- $pp \to D^{\pm} D_n \to D_1 D_1 Z^{(*)} W^{\pm(*)} \to D_1 D_1 \ell^+ \ell^- \ell^{\pm} \nu$
- $pp \to D^{\pm} D_n \to D_1 D_1 W^{\pm} H \to D_1 D_1 W^{\pm} W^{\pm} W^{\mp *} \to D_1 D_1 \ell^{\pm} \ell^{\pm} \ell^{\mp} \nu \nu \nu$
- $pp \to D_n D_n \to D_1 D_1 Z^{(*)} Z^{(*)} \to D_1 D_1 \ell^+ \ell^- \ell^+ \ell^- / D_1 D_1 \ell^+ \ell^- q \bar{q}$

where $D_n = D_2$ or $D_n = D', D_2$ depending on the scenario, i2HDM or MFDM model, respectively. Since $D^{\pm}$ and D_n decay via Z or $W^{\pm}$ either hadronically or leptonically in association with the DM candidate, they can provide signatures with several charged leptons plus E_T^{miss}, which are the subject of this study.

7.1 Production and Decay Processes

The diagrams in common between the i2HDM and MFDM for signal production include

$$q\bar{q} \to D^+D^- \quad \text{and} \quad q\bar{q}' \to D^\pm D_2 \tag{7.1}$$

that provide the multi-lepton signatures we study here are presented in Fig. 7.1.

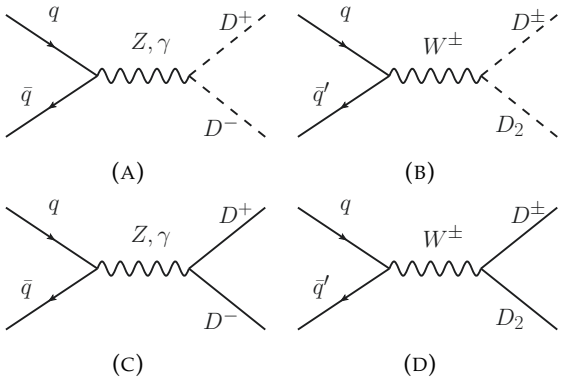

FIGURE 7.1: Feynman diagrams for D^+D^- and $D^\pm D_2$ production common to the i2HDM (top) and MFDM model (bottom).

In addition to these common Feynman diagrams, the ZD_2D_1 and ZZD_1D_1 vertices, specific only to the i2HDM, provides additional Feynman diagrams and corresponding new kinematic topologies, shown in Fig. 7.2(a) and (b). Conversely, since the MFDM model has an additional neutral DM partner, D', in contrast to the i2HDM, there are additional MFDM processes[1],

$$q\bar{q} \to D'D_1 \quad , \; q\bar{q} \to D_2D' \quad \text{and} \quad q\bar{q}' \to D^\pm D', \tag{7.2}$$

providing the required multi-lepton signatures through the topologies shown in Fig. 7.2(c), (d) and (e), respectively.

The cross sections for the above production processes presented here are calculated using CalcHEP [260], a package designed for the evaluation of the tree-level processes and their respective MC simulation. CalcHEP exploits the BSM scenarios implemented on the HEPMDB [261], allowing to cross check these in different gauges for the purpose of validating the relevant implementation, and further has an interface to LHAPDF [262] for a wide selection of PDFs, allowing to ascertain the dominant systematic error on the theoretical side[2]. The events generated by CalcHEP in Les

[1] MFDM also allows for D_2D_1 production through the HD_2D_1 vertex, but we do not study this production mode as it is highly suppressed compared to the other processes discussed here.

[2] Note that the production and decay processes exploited here are EW in nature, so that the QCD corrections to these are small, typically of order 20%, and their residual uncertainty negligible.

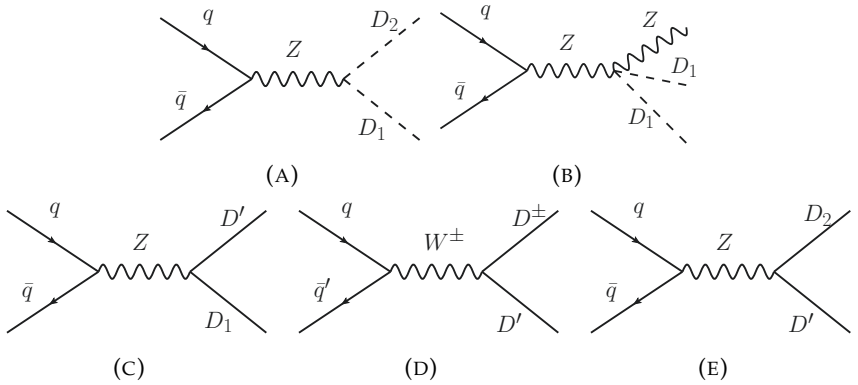

FIGURE 7.2: Feynman diagrams for D_2D_1, ZD_1D_1 production exclusive to the i2HDM, (a) and (b), and for D_1D', $D^\pm D'$ and D_2D' production exclusive to the MFDM model, (c), (d) and (e).

Houches Event (LHE) format can then be used by other tools enabling further simulations of the parton shower and detector effects. For the latter, we use here the combination PYTHIA [76] and DELPHES [263], respectively.

The relevant cross sections are presented in Fig. 7.3 as a function of the Δm^+ parameter for a 100 GeV DM mass and two values of Δm^0=1 and 100 GeV (left and right panels, respectively) for the i2HDM (top panels) and MFDM model (bottom panels). Here, one can see that for Δm^0=1, D_1D_2 production has the highest rate for the i2HDM while, in the case of the MDFM model, the analogous D_1D' channel is highly suppressed. This can be explained by the fact that the ZD_1D_2 coupling controlling this process in the i2HDM model is just a pure (weak) gauge coupling while in the MFDM model the ZD_1D' coupling is the product of a (weak) gauge coupling and the cosine of the $\chi_1^0 - \chi_s^0$ mixing angle, which is suppressed when $\Delta m^+ \gg \Delta m^0 = 1$ GeV, as shown by the blue line in Fig. 3.1(b).

In contrast, for Δm^0=1 GeV, the production cross sections for D^+D^-, $D_2D^\pm$ and $D'D^\pm$ (represented by red, green and brown lines, respectively) are close to each other in each model. This can be explained by the fact that the D^+ and D_2 masses are about the same as well as the couplings controlling these processes (which are purely (weak) gauge ones). Furthermore, one should note that the ZZD_1D_1 coupling (unique to the i2HDM) contributes to ZD_1D_1 production, the $2 \to 3$ process with a subdominant cross section in comparison with $2 \to 2$ production. However, when the $D_2 \to ZD_1$ decay is open, the ZD_1D_1 process will include the corresponding resonant $2 \to 2$ production and decay. Therefore, to avoid double counting, we do not present the cross section for this $2 \to 3$ process in Fig. 7.3(a).

For the MFDM model, the additional production process $D'D_2$ (pink line), characteristic of this scenario, has a similar cross section to D^+D^- and $D'D^\pm$ for the very same reason. One should also note that the cross sections for scalar DM production are smaller than those for fermion DM production by the spin factor $\beta^2/4$

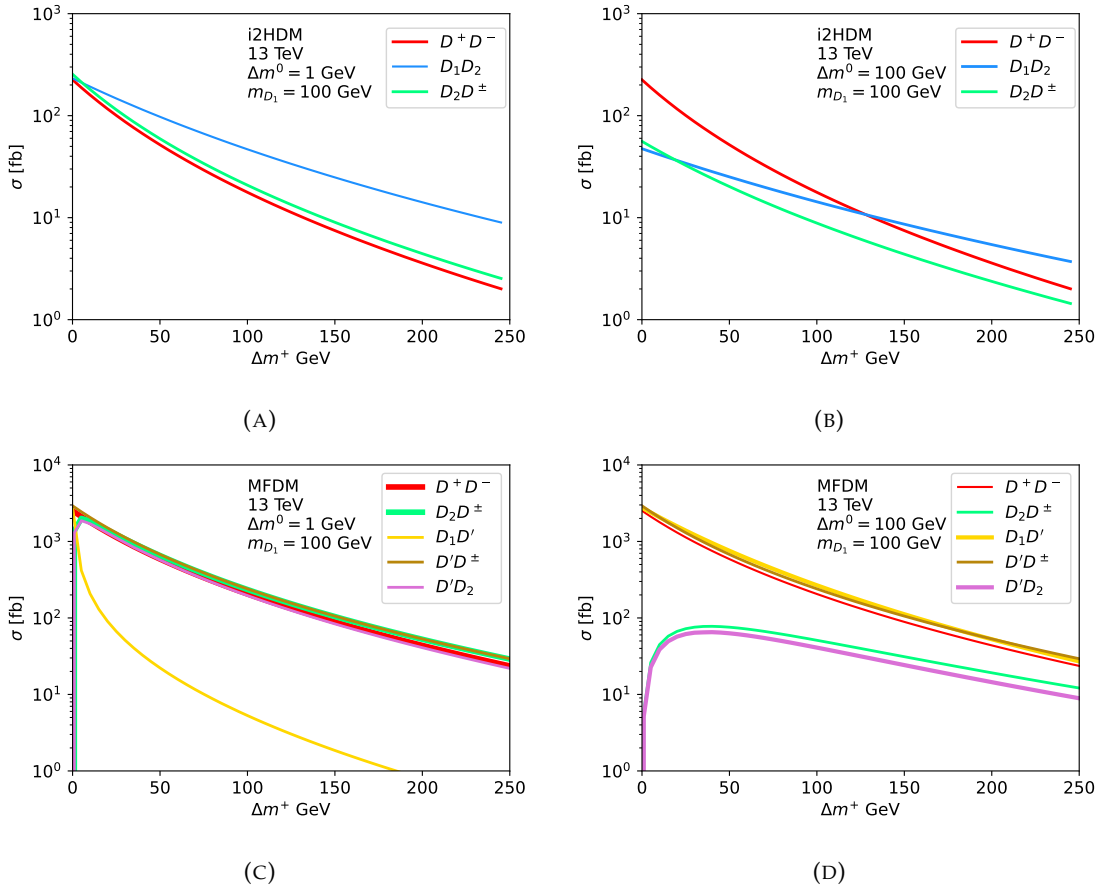

FIGURE 7.3: The cross sections for pair production of DM partners for the i2HDM (top) and MFDM model (bottom) for $\Delta m^0 = 1$ and 100 GeV (left and right panels, respectively).

(where $\beta = \sqrt{1-(m_{D_i}+m_{D_j})^2/\hat{s}}$ with m_{D_i} and m_{D_j} being the masses of DM particles in the final state), which ranges from about $1/4$ to about $1/10$, as one can see from Fig. 7.3 (left panels).

Let us now consider the Δm^0=100 GeV case presented in the right panels of Fig. 7.3. In the i2HDM, the $\Delta m^0 = 1 \to 100$ GeV change (which increases the D_2 mass) equally suppresses D_1D_2 and $D_2D^\pm$ production by about a factor of 4. For the MFDM model, the $\Delta m^0 = 1 \to 100$ GeV change affects both the D_2 mass (see Eq. (3.12)) and the $\chi_1^0 - \chi_s^0$ mixing angle θ (the ZD_2D' and $W^+D_2D^-$ couplings are both proportional to $\sin\theta$), leading to a suppression of $D'D_2$ and $D_2D^\pm$ production from both causes (see pink and green lines, respectively, in Fig. 7.3(d)). In contrast, D_1D' production is enhanced, since it is proportional to $\cos^2\theta$, which increases with Δm^0 (see Fig. 3.1(b)). Finally, the D^+D^- processes are not affected by a Δm^0 variation in both models. One should also note that in the MFDM model $D'D^\pm$ is also not affected by a Δm^0 variation since such a variation does not change the D' mass, nor the $W^+D'D^-$ coupling (which is purely weak and is not affected by the $\chi_1^0 - \chi_s^0$ mixing).

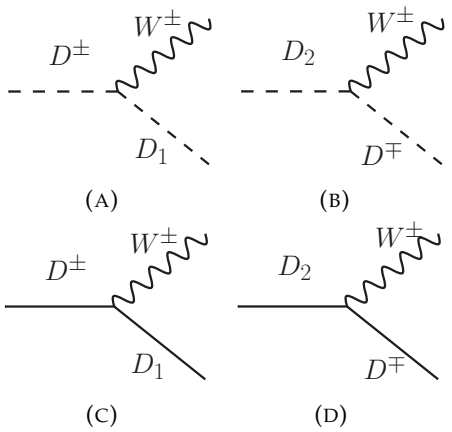

FIGURE 7.4: Decays analogous between the i2HDM (left) and the MFDM model (right).

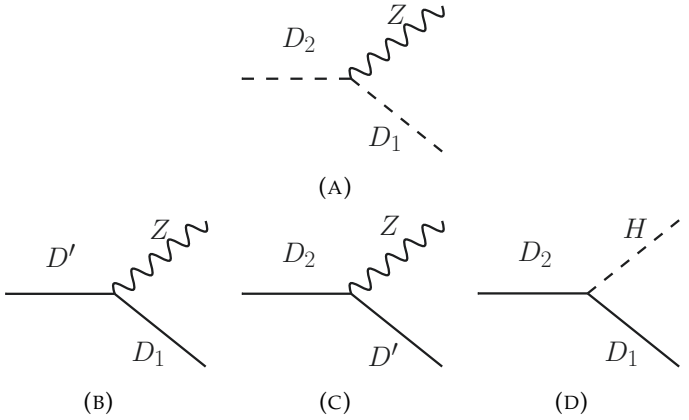

FIGURE 7.5: Decays exclusive to the i2HDM (top) and MFDM model (bottom).

In order to get an idea of the rate at which leptons are produced in the final state we also need to discuss Branching Ratios (BRs) of decay chains leading to DM particles and connect these with their pair production cross sections. In Fig. 7.4, we present the decay patterns common to both the i2HDM and MFDM model. In Fig. 7.5, we then present the unique decays of each model: the $D_2 \to ZD_1$ decay permitted in the i2HDM while the $D_2 \to HD_1$ and D' decays are so in the MFDM model.

The BRs for the decays leading to our DM signatures (see Figs. 7.4 and 7.5) are presented in Fig. 7.6 as a function of the Δm^+ parameter, again, for a 100 GeV DM mass and the two values of Δm^0=1 and 100 GeV. The $D^\pm$ decay to $W^\pm$ dominates in all cases. This is because, for the i2HDM, only $m_{D_2} > m_{D^\pm}$ is considered and so $D^\pm$ can only decay to $W^\pm D_1$ while, for the MFDM model, D' and $D^\pm$ are mass degenerate and their decay to one another is not permitted. For Δm^0=1 GeV, in the i2HDM (Fig. 7.6(a)), the D_2 decay to leptonically decaying Z and D_1 is favoured over the D_2 decay to leptonically decaying W^+ and D^- which is suppressed due to a small $D_2 - D^\pm$ mass splitting. This BR falls rapidly with increasing Δm^+, due to D^+ in the final state increasing in mass, while the mass of the D_1 in the $D_2 \to ZD_1$ final state is fixed.

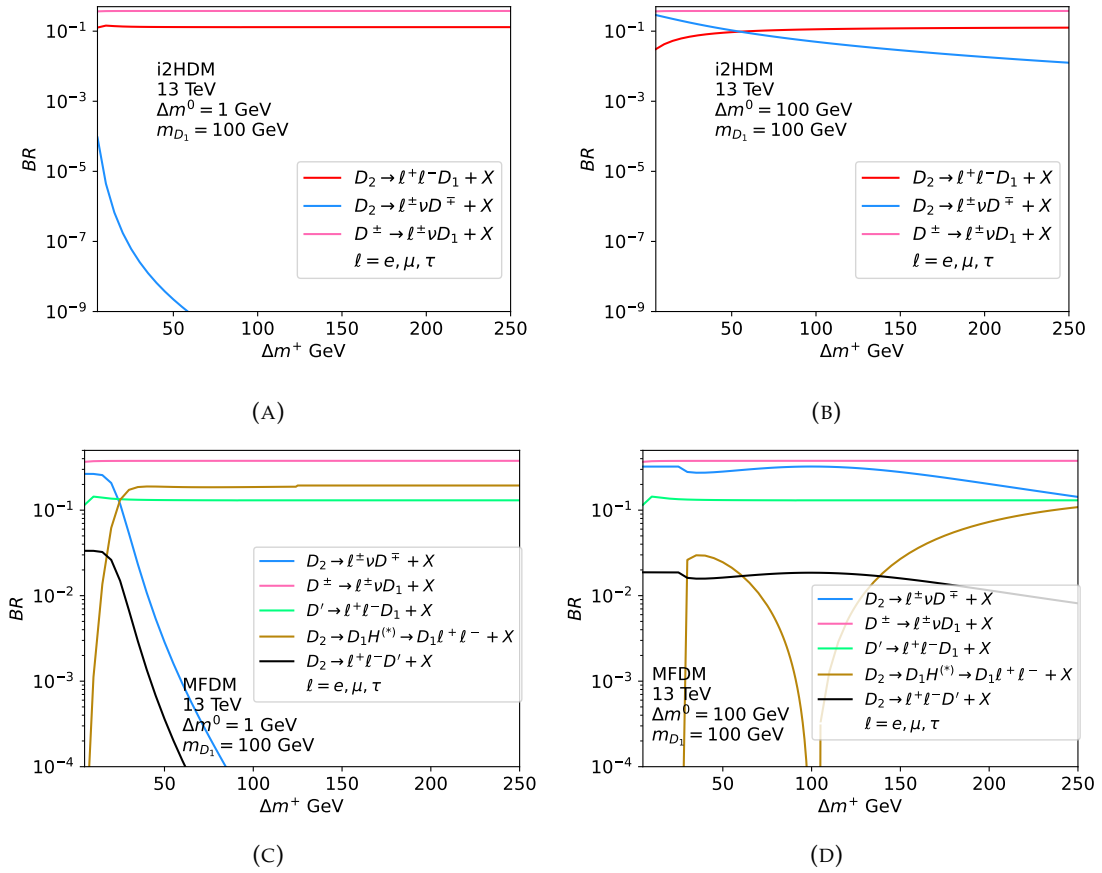

FIGURE 7.6: The BRs of leptonic decays and DM particles for the i2HDM (top) and MFDM model (bottom) for $\Delta m^0 = 1$ and 100 GeV (left and right panels, respectively).

The behaviour of the D_2 BRs changes when considering $\Delta m^0 = 1 \to 100$ GeV (Fig. 7.6(b)) since the $D_2 - D^\pm$ mass gap is increased, initially suppressing the D_2 decay to ZD_1. However, the trend over increasing Δm^+ remains the same and the two D_2 BRs cross for Δm^+ around 60 GeV. Meanwhile, for the MFDM model, the $D' \to W^+D^-$ decay is not permitted and so the BR of the D' decay to a leptonically decaying Z and D_1 remains unchanged between Fig. 7.6(c) and (d).

The MFDM model decays from D_2 include a unique Higgs interaction, $D_2 \to D_1 H^{(*)}$, where the $D_2 D_1 H$ coupling is a product of the Yukawa $Y_{\rm DM}$ (which is proportional to $\sqrt{\Delta m^0 \Delta m^+}$) and $\cos(2\theta)$ of the $\chi_1^0 - \chi_s^0$ mixing angle θ. This interplay is seen in Fig. 3.1(a) (blue line), where $Y_{\rm DM}$ suppresses this coupling at small Δm^0 and Δm^+, but the latter rises with increasing Δm^+. For Δm^0=1 GeV the shape of the $D_2 \to D_1 H^*$ (brown) line in Fig. 7.6(c) follows the trend just described, then it levels out as $\sqrt{\Delta m^+}$. As the Higgs boson becomes on-shell with increasing Δm^+, a jump in the BR of leptonic decays via $D_2 \to D_1 H$ is observed in Fig. 7.6(c), due to the additional contribution $H \to W^+W^-$. Meanwhile, the D_2 decays to W^+D^- and ZD' are both controlled by the sine of the mixing angle, i.e., the amount by which the D_2 is χ_1^0. Therefore, their shapes are similar to one another but the blue and black lines fall as

the $D_2 \to D_1 H$ brown line increases with Δm^+ (note that the $D_2 \to W^+ D^-$ BR is a factor ~ 8 larger than the $D_2 \to D' Z$ one due to combinatorics and the ratio m_Z / m_W).

Now, considering $\Delta m^0 = 100$ GeV for the MFDM model, D_2 decays are strongly affected by any Δm^0 variation. In Fig. 7.6(d), $D_2 \to Z D'$ and $D_2 \to W^+ D^-$ are now on-shell and these decays are then enhanced. When $\Delta m^+ = 30$ GeV and $m_{D_2} - m_{D_1} = 130$ GeV, the $D_2 \to H D_1$ decay (brown line) becomes on-shell and boosted, reducing the other D_2 decays proportionally. However, D_2 changes from mostly χ_s^0 to mostly χ_1^0 as Δm^+ reaches Δm^0 from below, where the coupling reaches zero at $\Delta m^+ = \Delta m^0 = 100$ GeV (see Fig. 3.1(a) red line). Beyond this value of Δm^+, the coupling then increases with $\sqrt{\Delta m^+}$ as $\Delta m^+ > \Delta m^0$ which in turn reduces the $D_2 \to Z D'$ and $D_2 \to W^+ D^-$ leptonic BRs above $\Delta m^+ > 100$ GeV as seen in Fig. 7.6(d).

The discussed combinations of production and decay rates provide the expected rates for the 2- and 3-lepton signatures which we study below at the (fast) detector level and compare to published LHC data.

In order to understand the constraints on the models we study in this analysis, we reinterpret existing multi-lepton searches at the LHC. We first provide a brief summary of the models, then describe briefly the reinterpretation tools for this work, finally followed by an assessment of the impact of these searches on our two benchmark models.

7.1.1 LHC Searches and Tools

We begin by identifying the LHC searches that can potentially be useful to constrain the latter. For the i2HDM, constraints were derived previously in [264] by reinterpreting 8 TeV 2- and 3-lepton searches using MadAnalysis5 [265, 266]. In preparation for this publication, the previous work is verified using the public recast tool CheckMATE [267] (see Appendix K). The corresponding recast software is publicly available at [268, 269]. In this paper, we extend this result to 13 TeV for both the i2HDM and MFDM model based on searches available in CheckMATE.

Analysis	Description	Final States	Lumi. [fb^{-1}]
atlas_1609_01599 [270]	$t\bar{t}V$ cross-section measurement at 13 TeV	two or three leptons(one OSSF pair)+bjets	3.2
atlas_conf_2016_076 [271]	direct top squark pair + DM production	two leptons + jets + E_T^{miss}	13.3
atlas_conf_2016_096 [272]	EW production of charginos and neutralinos	two or three leptons $+E_T^{miss}$	13.3
atlas_1712_08119 [273]	EWinos search with soft leptons	two soft OSSF leptons $+E_T^{miss}$	36.1
cms_sus_16_039 [274]	EWinos in multilepton final state	$\geq$two leptons + τ $+E_T^{miss}$	35.9
cms_sus_16_025 [275]	EWino and stop compressed spectra	two soft OS leptons $+E_T^{miss}$	12.9
cms_sus_16_048 [276]	Search for new physics in events with soft leptons	two soft OS leptons $+E_T^{miss}$	35.9

TABLE 7.1: The relevant 13 TeV ATLAS and CMS analyses which are sensitive to the DM signatures under study in this paper.

In Table. 7.1, we identify the 13 TeV searches that are relevant for the reinterpretations in this paper. The most stringent constraints for these models are expected to emerge

from LHC Supersymmetry searches targeting EW gauginos. Since we are investigating models with a variety of mass gaps in this paper, we look for searches that constrain both small and large mass gaps. We therefore note the following.

- For small mass gaps the CMS [125] soft lepton searches `cms_sus_16_025` [275] and `cms_sus_16_048` [276] can potentially constrain the parameter space under study here. The search `cms_sus_16_025` constrains $\chi_1^+\chi_2^0$ pair production followed by decay to leptons and missing energy via off-shell $W^\pm$ and Z bosons for mass gaps $\simeq 5-50$ GeV. It also constrains direct stop pair production followed by a decay to leptons via off-shell $W^\pm$'s for mass gaps up to 70 GeV. The search `cms_sus_16_048` targets the same EWino pair production as above and constrains mass gaps up to about 50 GeV at an integrated luminosity of 35.9 fb^{-1}. Both of the above searches require Opposite Sign (OS) $ee/\mu\mu/e\mu$ with leading leptons $p_T < 20$ GeV, $E_T^{miss} < 200$ GeV and at least one jet.
- For large mass gaps the ATLAS [119] search `atlas_conf_2016_096` [272] as well as the CMS search `cms_sus_16_039` [274] are the most constraining ones. These publications target EWino pair production with the same decay pattern as the soft lepton searches. The searches look for OS leptons and constrain mass gaps above 50 GeV.

The i2HDM and MFDM model input LHE files were produced with different mass parameters, as described in section 7.1, with CalcHEP [260]. This is followed by showering and hadronisation using PYTHIA8 [183]. Jets, with final-state hadrons are constructed using FASTJET [171], while detector simulation is performed using DELPHES [263]. The entire process (barring parton level event generation) is performed within CheckMATE. The built-in AnalysisHandler processes the detector-level events with the user selected analyses. The signal size is determined based on the efficiency, acceptance, signal cross section and integrated luminosity [277] of the analysis.

7.2 Constraints on the i2HDM and MFDM Model

In this section, we present the results of our study for the i2HDM and MFDM model. For each of these scenarios, we constrain the parameter space in the $(m_{D_1}, \Delta m^+)$ plane using the searches quoted above to calculate the *r-value*:

$$r = \frac{S_{DM}}{S_{95}}, \tag{7.3}$$

where S_{DM} is the number of DM events expected to pass the signal selection and S_{95} is the 95% Confidence Level (CL) upper limit on the number of selected events. Any point with $r > 1$ is excluded by current LHC limits.

This criterion is then used in the following sections where the new limits for i2HDM and MFDM scenarios with multilepton+E_T^{miss} final states at 13 TeV are presented.

7.2.1 Constraints on the i2HDM at 13 TeV

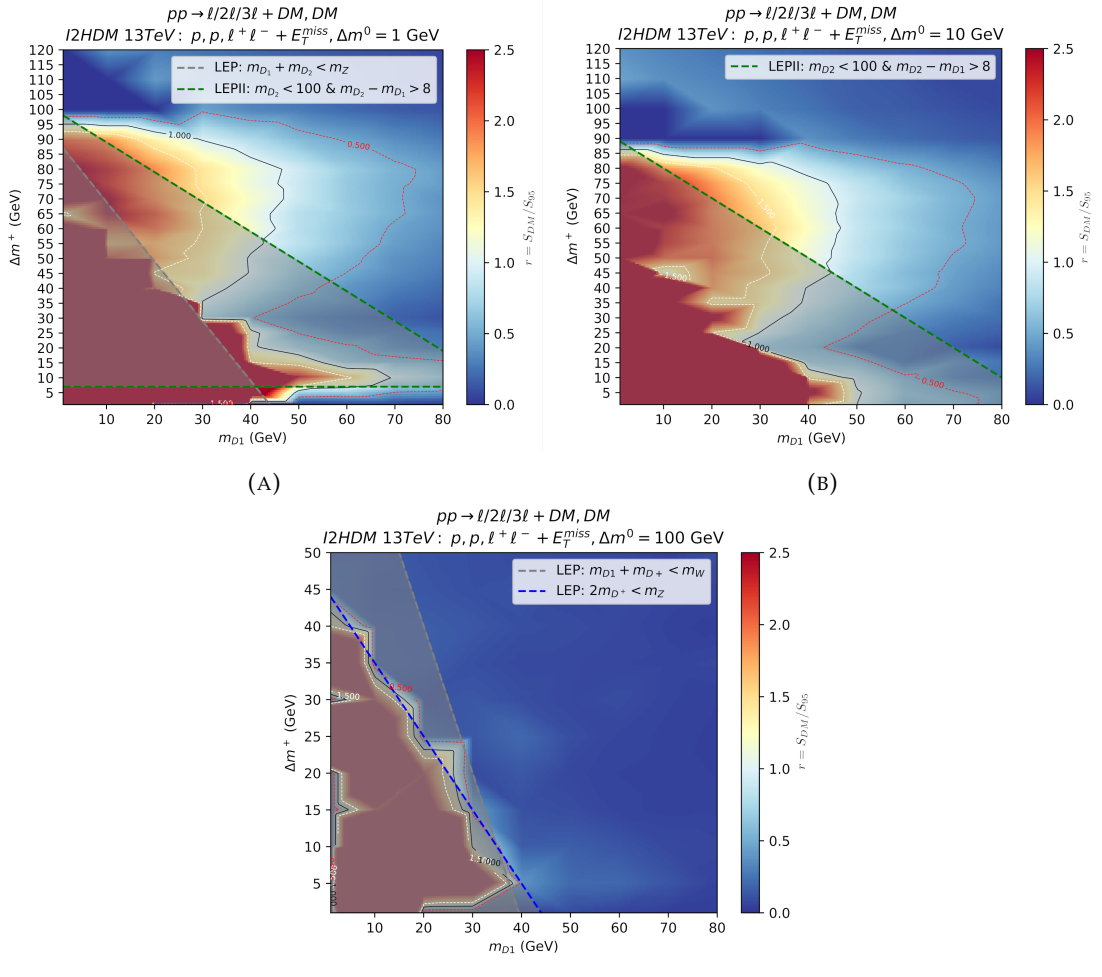

FIGURE 7.7: i2HDM 13 TeV r-value contour plots for 2- and 3-lepton final states as a function of Δm^+ and m_{D1} for $\Delta m^0 = 1$ (a), $\Delta m^0 = 10$ (b) and $\Delta m^0 = 100$ (c) GeV. These are overlaid with limits from the LEP I and LEP II experiments [278], [279]. This includes $m_{D_1} + m_{D_2} < m_Z$ (grey line) and $2m_{D^+} < m_Z$(blue), from LEP I Z boson width measurements forbidding on-shell $Z \to D_1 D_2$ and $Z \to D^+ D^-$ decay. The same applies to W width measurement forbidding on-shell $W^\pm \to D^\pm D_1$ decay. The exclusion region $m_{D_1} < 80$ GeV *and* $m_{D_2} < 100$ GeV *and* $m_{D_2} - m_{D_1} > 8$ GeV (green lines) are excluded by LEP II observations. Where these lines are absent, they are overlapped completely by the other LEP limits.

Using the re-parametrisation of Eq. (3.12), Fig. 7.7 (overlaid with total cross-section yields in Fig. N.1 of Appendix N), show the *r*-value (see Eq. (7.3)) of the i2HDM 2- and 3-lepton signatures discussed in section 7.1 as a function of Δm^+ and m_{D1} for various choices of Δm^0. The 3-lepton contributions to the *r*-value are important, reaching up to $\sim 70\%$ of the 2-lepton-only *r*-values. However, 2-lepton-only *r*-values still dominate throughout the i2HDM contour plots.

For $\Delta m^0 = 1$ GeV, the dominant DM pair production process is $D_2 D_1$ (see Fig. 7.3(a)) and the dominant D_2 decay contribution is $D_2 \to Z D_1$ (see Fig. 7.6(a)), providing two leptons. The 3-lepton final states can be provided by the second largest DM production process, $D_2 D^\pm$, with decays as $D_2 \to Z D_1$ and $D^\pm \to W^\pm D_1$. This process and its decays can also fulfil the 2-lepton criteria if the W decays hadronically, or a lepton is misidentified.

The horizontal wedge of large *r*-value in Fig. 7.7(a) within $\Delta m^+ < 60$ GeV, $m_{D1} < 70$ GeV is excluded by analyses `cms_sus_16_025` [275] and `cms_sus_16_048` [276], both with signal region `SR1_weakino_1low_mll_2`, requiring two leptons with $m_{ll} < 20$ GeV and at least one jet. In the i2HDM, this signature would be mostly provided by the leptonic Z decay and the hadronic W decay in the $D_2 D^\pm$ pair production. Most of this phase space is already excluded by LEP-II observations [278] (green line) and LEP-I limits from Z width measurements (grey line), excluding on-shell $Z \to D_2 D_1$ decays. However, at $\Delta m^+ < 8$ GeV, there is a small wedge of allowed phase space from soft leptons, when $m_{D_1} > 50$ GeV and $\Delta m^+ < 8$ GeV which is not covered by the LEP-I or LEP-II limits. The second, broader region of large *r*-value around $40 < \Delta m^+ < 100$ GeV is excluded by analysis `atlas_conf_2016_096` [272], signal region `2LASF`. The dominant $D_2 D_1$ process with leptonic Z decay provides a signal that strongly contributes to the *r*-value in this region. Note that a significant portion in Fig. 7.7(a) within the region $60 < \Delta m^+ < 95$ GeV and $m_{D_1} < 50$ GeV not excluded by LEP, is excluded by these LHC limits.

Similar excluded regions are found for $\Delta m^0 = 10$ GeV in Fig. 7.7(b), but without the region of allowed phase space at small Δm^+, for which the LEP-II limit now overlaps with this region (the grey line corresponding to the LEP limit $m_{D_1} + m_{D_2} < m_Z$ in Fig. 7.7(a) would be overlapped completely in Fig. 7.7(b) by the green line, so is not plotted here). Again, we see a significant contribution from LHC limits in $60 < \Delta m^+ < 95$ GeV and $m_{D_1} < 50$ GeV where LEP does not already exclude.

As Δm^0 is increased further to 100 GeV in Fig. 7.7(c), the $D_2 D_1$ and $D_2 D^\pm$ cross sections are now suppressed at small Δm^+ (see Fig. 7.3(b)) compared to the dominant production $D^+ D^-$ for $\Delta m^+ < 130$ GeV, with decays $D^\pm \to W^\pm D_1$ (see Fig. 7.6(b)). The $M_{ll} > 100$ GeV cut applied in the `atlas_conf_2016_096` [272] analysis now removes all events for larger Δm^+ in Fig. 7.7(c), as heavier D_2 production cross section

with harder lepton decays has decreased. In addition, the combination of LEP limits covers the totality of LHC limits for $\Delta m^0 = 100$ GeV in Fig. 7.7(c).

7.2.2 Constraints on the MFDM at 13 TeV

Based on the re-parametrisation of Eq. (3.23), Fig. 7.8 (overlaid in Fig. N.2 of Appendix N with cross-section yields) shows the r-value exclusion contours of the MFDM model 2- and 3-lepton signatures discussed in section 7.1 as a function of Δm^+ and m_{D1} for various choices of Δm^0. The LEP-II limit in the MFDM model case corresponds to bounds on fermionic DM [279], which covers $m_{D^+} < 100$ GeV, a smaller Δm^+ range than the LEP limits for the i2HDM. Since we allow DM-Higgs coupling, the Higgs-to-invisible limit [280] of ~ 0.15 BR (magenta region) is also plotted.

Contributions to the 2-lepton r-value are provided by the dominant D^+D^- production (see Fig. 7.3(c)-(d)) with its leptonic decays $D^\pm \to W^\pm D_1$ (see Fig. 7.6(c)-(d)), by $D'D^\pm$ and, specifically for $\Delta m^0 = 1$ GeV, $D_2D^\pm$ productions, where the latter two require D' and D_2 to decay leptonically. Cascades from $D'D_2$ production can also contribute to 2-lepton final states for $\Delta m^0 = 1$ GeV. However, $D_2D^\pm$ and $D'D_2$ production become suppressed with $\Delta m^0 = 100$ GeV (see Fig. 7.3(d)). Meanwhile, $D'D_1$ production, which is suppressed for $\Delta m^0 = 1$ GeV, becomes enhanced with $\Delta m^0 = 100$ GeV as detailed in section 7.1, contributing to 2-lepton final states. Contributions to the 3-lepton r-value are provided by the $D'D^\pm$ production with fully leptonic decays, although these are less likely to satisfy the signal regions that require τ-leptons than $D'D_2$ and $D_2D^\pm$ production with $D_2 \to D_1H^* \to D_1\tau\tau$ decay. However, as stated, D_2 productions become suppressed with $\Delta m^0 = 100$ GeV (see Fig. 7.3(d)).

For $\Delta m^0 = 1$ GeV, the sharp excluded region of large r-value in Fig. 7.8(a) within $\Delta m^+ < 30$ GeV, $m_{D_1} < 150$ GeV was seen similarly for the i2HDM case in Fig. 7.7. As with the i2HDM case, this signal of soft leptons for the MFDM model in Fig. 7.8(a) is also excluded by the 2-lepton analyses `cms_sus_16_048` and `cms_sus_16_025` both with signal regions `stop_1low_pt`, `weakino_1low_mll`. These require two leptons and at least one jet, a signal also provided by the $D'D^\pm$ pair production, dominant here in the MFDM model (see Fig. 7.3(c)).

As Δm^+ increases, the 3-lepton r-value becomes larger than the 2-lepton-only r-value in the region $30 < \Delta m^+ < 100$ GeV and $m_{D_1} < 80$ GeV, excluded by the `cms_sus_16_039` [274] analysis signal regions requiring three leptons including τ. This is where the most dominant decay of D_2 changes from 1-lepton final states to 2-lepton final states including τ-leptons through virtual Higgs decays, as detailed in section 7.1 and Fig. 7.6(c). This gives more 3-lepton final states, with τ-leptons, from D^+D_2 production. The additional third excluded area of smaller r-value than the previous

two areas in Fig. 7.8(a), but still within an excluded region $120 < \Delta m^+ < 260$ GeV, $m_{D_1} < 100$ GeV has contributions to the signal from on-shell Higgs decay, where D_2 changes from decaying through H^*, into decaying to real Higgs which further decays to two W bosons or τ-leptons. This contributes more to the r-value as $\Delta m^+ > M_H$ for real Higgs production as detailed in section 7.1. This region is also excluded by analysis `cms_sus_16_039` [274], with its 3-lepton (including one τ) signal regions.

As Δm^0 is further increased to 10 GeV and 100 GeV in Fig. 7.8(b) and (c) respectively, the same r-value exclusion patterns are consistently observed. This no-lose theorem appears with the 2-lepton r-value due to the following scenarios: for small Δm^0, the cross section is large for light D_2 production, but with suppressed coupling between $D_1 - D'$ (see Fig. 7.6(c)). Then, for large Δm^0, this coupling is increased and (see Fig. 7.6(d)), while the heavy D_2 leads to suppressed production cross section.

For the 3-lepton r-value, while D_2 production becomes suppressed for increasing Δm^0 as shown in Fig. 7.3, its decays $D_2 \to W^+ D^-$ and $D_2 \to Z D'$ are enhanced, which can easily provide three leptons, including τ-leptons required by the relevant signal regions. In addition, $D' D^\pm$ production cross section is not affected by the Δm^0 variation.

As Δm^0 is increased, the Higgs-to-invisible limit [280] of ~ 0.15 BR excludes larger regions in Fig. 7.8(c)-(f), where $H \to D_1 D_1$ becomes the Higgs' dominant decay channel (since this coupling is proportional to Y_{DM}), until D_1 is too heavy to be produced on-shell. Other than this, the similarities in r-value plots for these three Δm^0 scenarios means we only need to consider the 2D plane $(\Delta m^+, m_{D1})$.

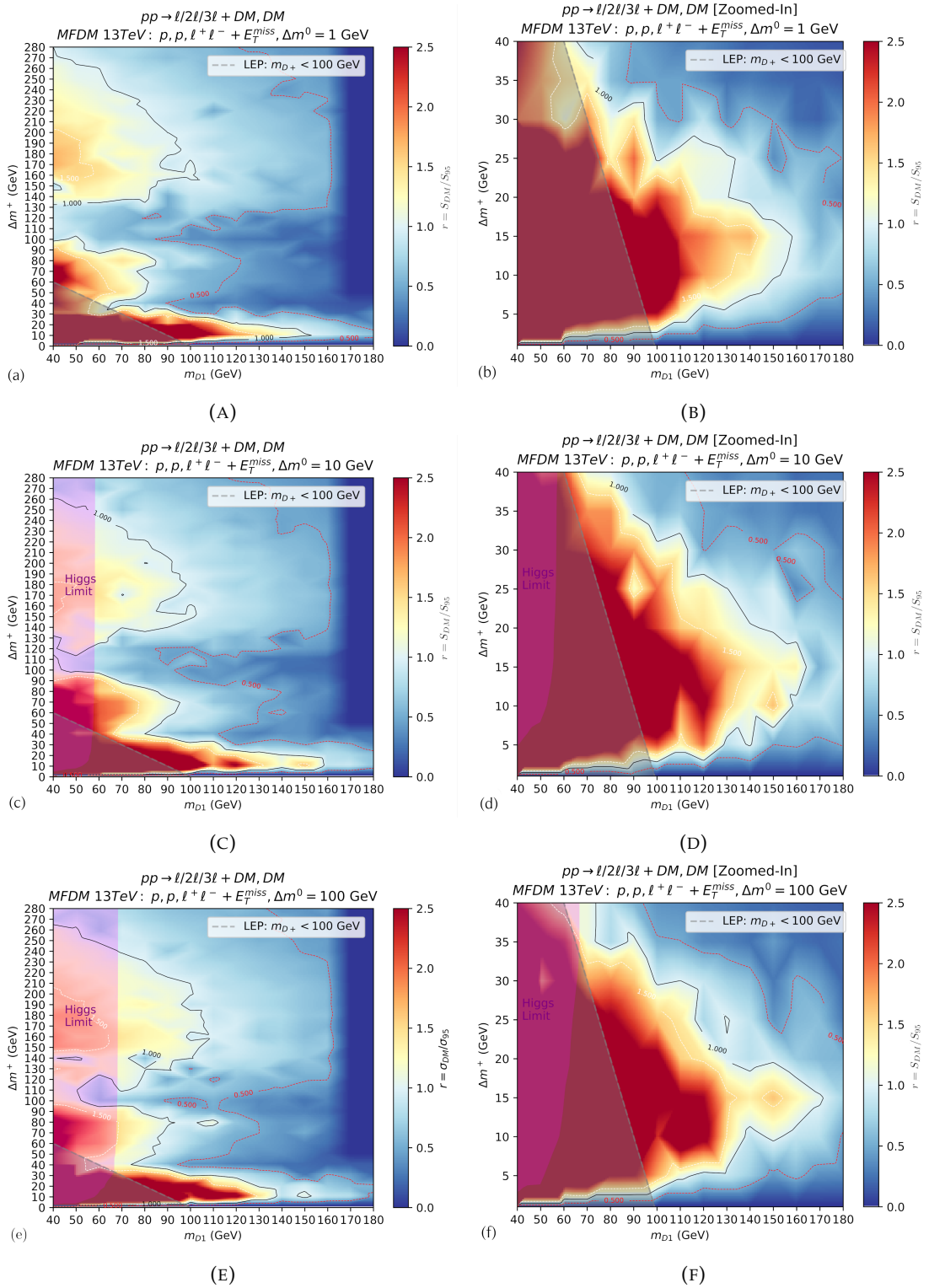

FIGURE 7.8: MFDM 13 TeV r-value contours as a function of Δm^+ and m_{D1} for $\Delta m^0 =$ 1(a), $\Delta m^0 = 10$(c) and $\Delta m^0 = 100$(e) GeV. Also presented is a zoomed in region ($0 < \Delta m^+ < 40$, $40 < m_{D1} < 180$) for each Δm^0 to the right of the respective original plot. The vertical magenta shaded region in plots (c), (d), (e) and (f) indicate the current Higgs-to-invisible limit [280] of 0.15 branching fraction. The LEP bounds on charginos for the fermionic DM case [279] are also plotted in grey.

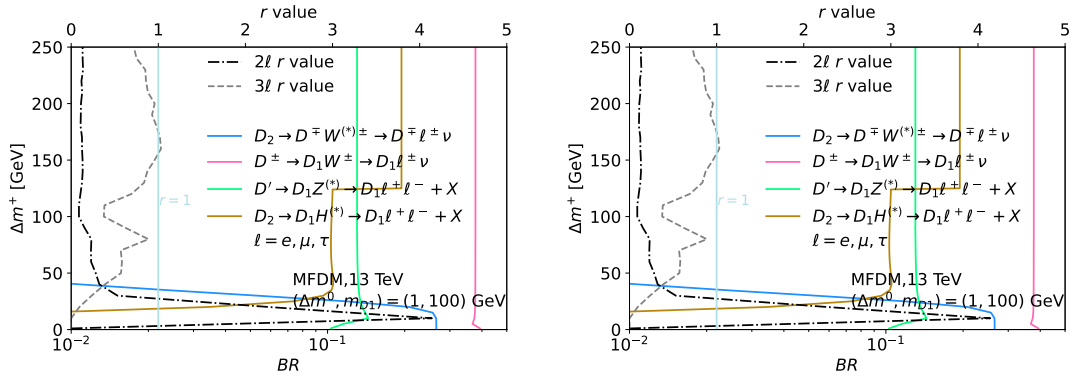

(A) (B)

FIGURE 7.9: Branching ratios (BR) as a function of the mass split Δm^+ for various decays of D_2, superimposed with the 2- and 3-lepton r-values, for $\Delta m^0 = 1$ GeV(a) and $\Delta m^0 = 100$ GeV(b). DM mass is fixed to $m_{D_1} = 100$ GeV, corresponding to a vertical slice of Fig.7.8(a) and (e).

Fig. 7.9 visualises the relation of r-values and BR by superimposing the decay BR from Fig. 7.6, rotated to match the contour plots in Fig. 7.8, with the 2-(dot-dashed line) and 3-(dashed line) lepton r-values from a vertical slice of Fig. 7.8 at $m_{D_1} = 100$ GeV as a function of Δm^+.

For $\Delta m^0 = 1$ GeV (Fig. 7.9(a)), the dominant contribution to the r-value switches from 2-lepton final states to 3-lepton final states around $\Delta m^+ > 45$ GeV, due to the change in dominant branching of $D_2 \to D^{\mp} W^{*\pm} (\to l\nu)$ (blue line) to $D_2 \to D_1 H^* (\to \tau^+\tau^-)$ (brown line) as Δm^+ (and m_{D2}) increases. This corresponds to a phase space excluded specifically by the analysis `cms_sus_16_039` [274], requiring three leptons with at least one τ-lepton, which can be provided in significant quantities by the H^* decay. Since the dominant productions at $\Delta m^0 = 1$ GeV include $D_2 D^+$ and $D_2 D'$ (see Fig. 7.3(c)), the dominating contribution to the r-value changes from $D_2 D^+ \to l\nu D^+ l\nu D_1 + X$ (total of two charged leptons) to $D_2 D^+ \to llD_1 l\nu D_1 + X$ and $D_2 D' \to \tau^+\tau^- D_1 llD_1$ (total of at least three charged leptons, including τ-leptons). As the Higgs boson becomes on-shell at $\Delta m^+ > 130$ GeV, the $H \to W^+W^-$ channel opens, in addition to the real $H \to \tau^+\tau^-$, noticeably contributing further to the 3-lepton r-value line in Fig. 7.9(a).

For $\Delta m^0 = 100$ GeV in Fig. 7.9(b), while D_2 production is suppressed (see Fig. 7.3(d)), the co-dominant pair production $D' D^{\pm}$ also provides three leptons via $D' \to D_1 Z$ (green line) and $D^{\pm} \to D_1 W^{\pm}$ (pink line). In addition, although D_2 production being suppressed, the D_2 decays $D_2 \to D^{\pm} W^{\pm} (\to l\nu)$ and $D_2 \to D' Z (\to ll)$ become strongly enhanced throughout (since W and Z are on-shell). Combined, they provide enough leptons, including τ-leptons, to compensate for the suppression of D_2 production and maintain a significant contribution to the 3-lepton r-value with increasing Δm^0. As Δm^+ increases, an increase in the $D_2 \to D_1 H$ branching, which also decreases the $D_2 \to D^{\pm} W^{\pm} (\to l\nu)$ branching, contributes with τ-leptons to the 3-lepton r-value

around $40 < \Delta m^+ < 60$ GeV. As detailed in section 7.1, the $D_2 D_1 H$ coupling falls to zero again as Δm^+ reaches $\Delta m^0 = 100$ GeV where the mixing angle θ is such that $\cos(2\theta)$ and therefore the $D_2 D_1 H$ coupling falls to zero (see Fig. 3.1(a) red line). This decrease does not occur for the $\Delta m^0 = 1$ GeV case (see Fig. 3.1(a) blue line), since $\Delta m^+ > \Delta m^0$. However, this reduced contribution in Fig. 7.9(b) is compensated by the increase in $D_2 \to W^\pm D^\mp$ and $D_2 \to Z D'$. Finally, there is a boost in the 3-lepton r-value for $\Delta m^+ > 100$ GeV where the $D_2 D_1 H$ coupling becomes more enhanced.

In the next section, we further explore the MFDM model and its non-LHC constraints, including limits from relic density, direct and indirect detection constraints.

Chapter 8

Non-collider Probe of MFDM Model and Their Complementarity to LHC Constraints

In addition to the LHC collider constraints obtained in section 7, it is vital to consider the non-collider constraints from relic density requirements, direct detection and indirect detection experiments and CMB results. In this section we outline the current and future limits on MFDM, starting with relic density constraints.

8.1 Relic Density Constraints

The current measurements taken by the PLANCK satellite telescope put precise limits on DM relic density $\Omega_{DM}^{obs}h^2 = 0.1185 \pm 0.0015$ to 68% C.L. [281]. In the MFDM, contributions to relic density come from annihilation cross sections, governed by the 7 different vertices shown in Fig. 8.1 with the largest contribution coming from the $D_1D^{\pm}W^{\pm}$ and $D_1D^{\pm}W^{\pm}$ vertices. This is due two the fact that D_1D_1 annihilation, which is dominant, occurs most readily by the top-left process of Fig. 8.1, and by its D_2-exchanging counterpart on the bottom-left. The transferred momentum in this t-channel process is much smaller than in s-channel processes like $D_1D_1 \longrightarrow H$, so the subsequent propagator is much larger, giving rise to a larger cross section. They are also the vertices governing D_1D_2 and D_1D^+ co-annihilation, usually the second and third most common annihilations. All the vertices only pick up parameter dependence through factors dependent on the mixing angle, which is dependent only on the mass differences. The mass m_{D_1} then affects matrix elements only through the propagator, which depends on the annihilation channel.

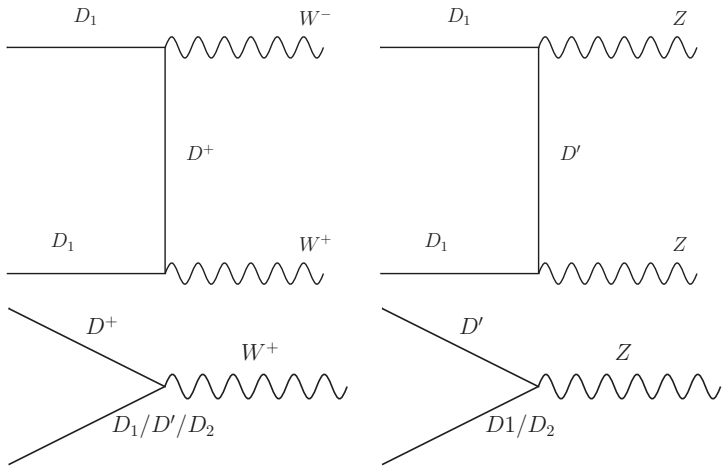

FIGURE 8.1: Feynman diagrams for the MFDM DM annihilation processes.

We evaluate $\Omega_{DM}h^2$ with the micrOMEGAs package [282], reading model files CalcHEP format. Contour plots of sensitivity from relic density contributions, across the $m_{D_1} - \Delta m^+$ plane, are presented in Fig.8.2. We find the following

- For small m_{D_1}, neither DM self-annihilation channels nor co-annihilation channels can open, leaving relic over abundant.
- Increasing m_{D_1} above ~ 6 GeV threshold opens $D_1D_1 \to H^*$, $D_1D_1 \to W^+W^-$ and $D_1D_1 \to ZZ$ annihilation channels sufficient enough to satisfy relic.
- For too large m_{D_1}, DM itself becomes overabundant and is unable to satisfy relic constraints.
- For increasing Δm^+ and large enough m_{D_1}, the $D_1D^+ \to W^+$ and $D_1D' \to Z$ processes, dependent on the $D_1D^+W^+$ and D_1D_2Z couplings respectively, are enhanced, suppressing relic.
- For too large Δm^+ relic can no longer be satisfied again, as more D_1 is produced from heavier dark sector partners decaying to D_1.
- A region around $m_{D_1} \sim m_H/2$ corresponds to the opening of $D_1D_1 \to H$ annihilation, satisfying relic constraints along this funnel region. This expands slightly with increasing Δm^0 due to enhanced D_1D_1H coupling proportional to $\sqrt{\Delta m^0}$ and mixing angle θ.
- As Δm^0 is increased, DM-Higgs couplings are enhanced, from the combination of large Δm^+ and Δm^0 as observed in Fig.3.1 and visible as an additional allowed region in Fig.8.2 for $\Delta m^0 = 100$ GeV, $\Delta m^+ > 100$ GeV.

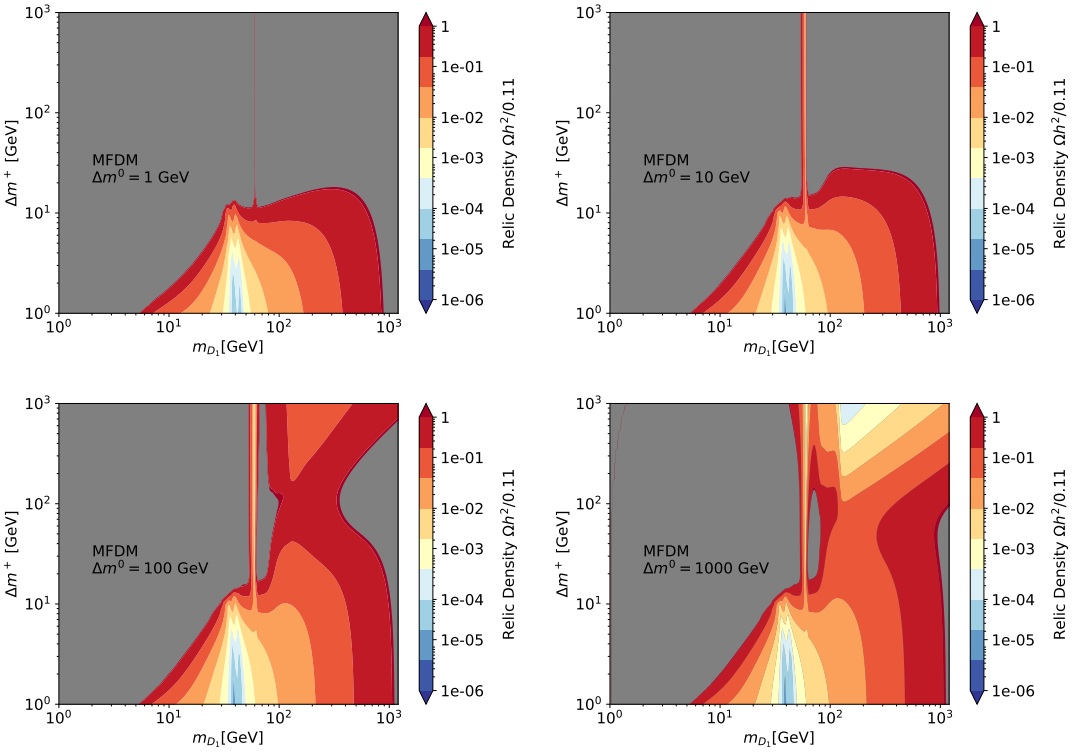

FIGURE 8.2: Colour maps of the relic density limits for Δm^0 =1(a),10(b),100(c) and 1000(d) GeV. Excluded region is plotted in grey, to 68% C.L. on the exclusion boundary [281].

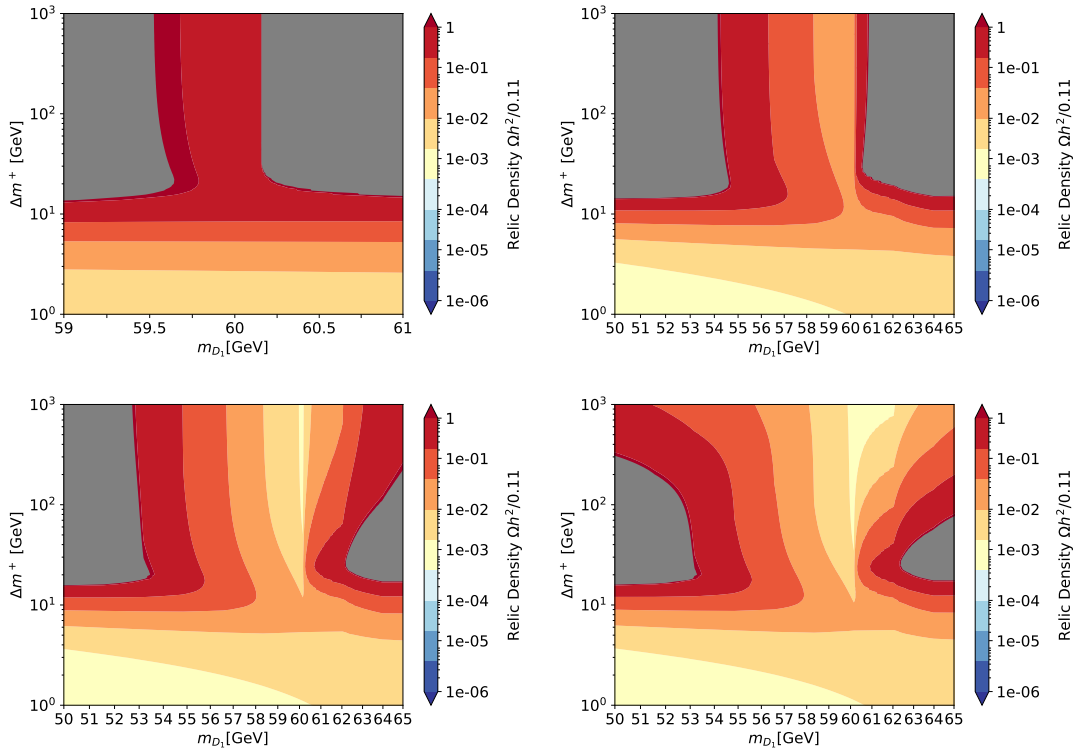

FIGURE 8.3: Colour maps of the relic density limits for Δm^0 =1(a),10(b),100(c) and 1000(d) GeV within a zoomed region. Excluded region is plotted in grey, to 68% C.L. on the exclusion boundary [281].

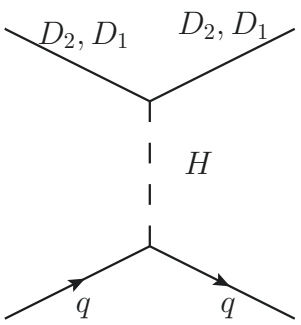

FIGURE 8.4: Feynman diagrams for the DM-SM scattering processes in MFDM providing DD.

8.2 DM Direct Detection Constraints

Next, we check the consistency of MFDM with the bounds set by direct detection (DD) limits. The DD bounds on the MFDM model only come from DM-Higgs scatterings in the case of large mass split between $D_1 D'$ where scattering through Z-boson is suppressed. The $D_1 D_2 H$ coupling depends on both the Yukawa coupling Y_{DM} Eq. 2.64 and $cos^2\theta$ of the $\chi_1^0 - \chi_s^0$ mixing angle and its behaviour as a function of Δm^+ is presented in Fig. 3.1. In addition, both the $D_1 D_1 H$ and $D_2 D_2 H$ couplings are proportional to $\cos\theta \sin\theta Y_{DM}$.

Fig.8.4 shows the relevant Feynman diagram for DD scattering in MFDM. Evaluating the spin-independent proton scattering cross section σ_{SI}^p using the micrOMEGAs package, we present the contour plots of sensitivity from DD experiment XENON1T [283] in Fig.8.6. The sensitivity is in terms of

$$\frac{\hat{\sigma}^{DD}_{MFDM}}{\sigma^{DD}_{XENON1T}} = \frac{\sigma_{SI,\,MFDM} \times \Omega_{DM}/0.11}{\sigma_{SI,\,XENON1T}} \tag{8.1}$$

where DM σ_{SI} is scaled to take into account the scenario where D_1 representing only a part of the total DM budget. The observations are similar to that of the relic density distributions, but with a few major differences:

- The m_{D_1} threshold for allowed DD rates is ~ 3 GeV for small Δm^+, as D_1 and D_2 become energetic enough to each scatter with Higgs
- The DD rates remain allowed for a larger m_{D_1} and Δm^+, up to Δm^+ =40 GeV for $m_{D_1} = 1000$ GeV, $\Delta m^0 = 1$ GeV, as opposed to the sharp cut-off for RD constraints in Fig.8.2(a) at ~ 900 GeV.
- The excluded region between $100 < m_{D_1} < 1000$ GeV, $20 < \Delta m^+ < 1000$ GeV remains similar with increasing Δm^0 (with the exception of $\Delta m^0 = 1000$ GeV, in contrast to RD constraints.)

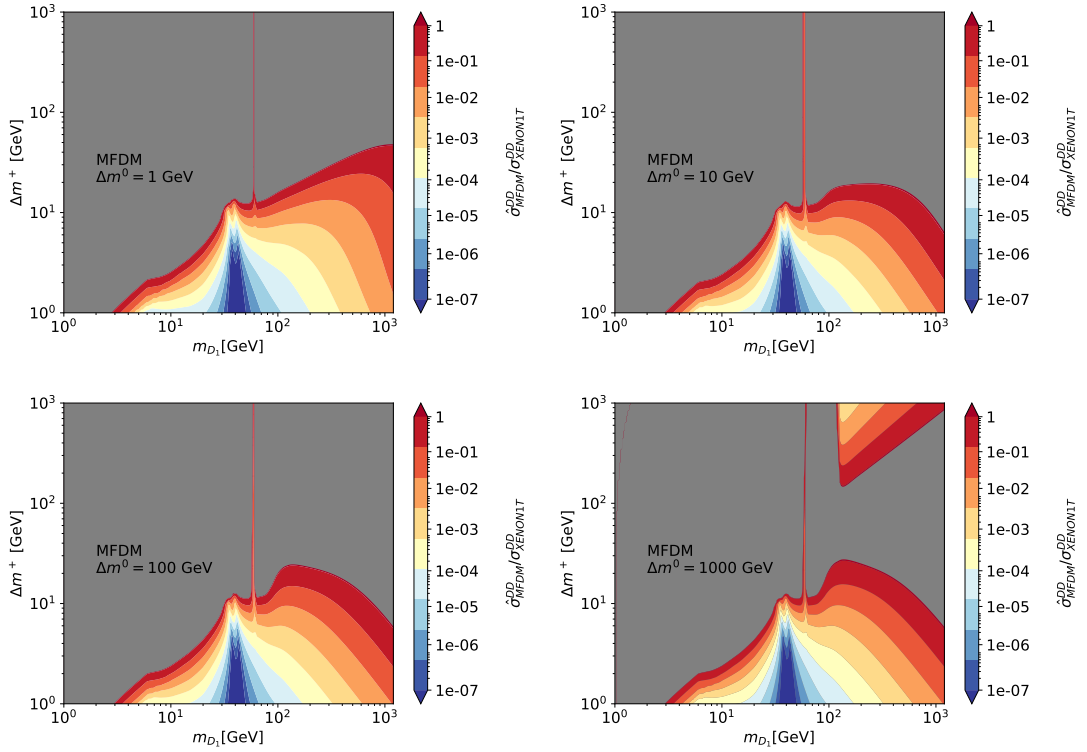

FIGURE 8.5: Colour maps of the direct detection limits for Δm^0 =1(a),10(b),100(c),1000(d) GeV. Excluded region is plotted in grey at 90% C.L. on the exclusion boundary [283].

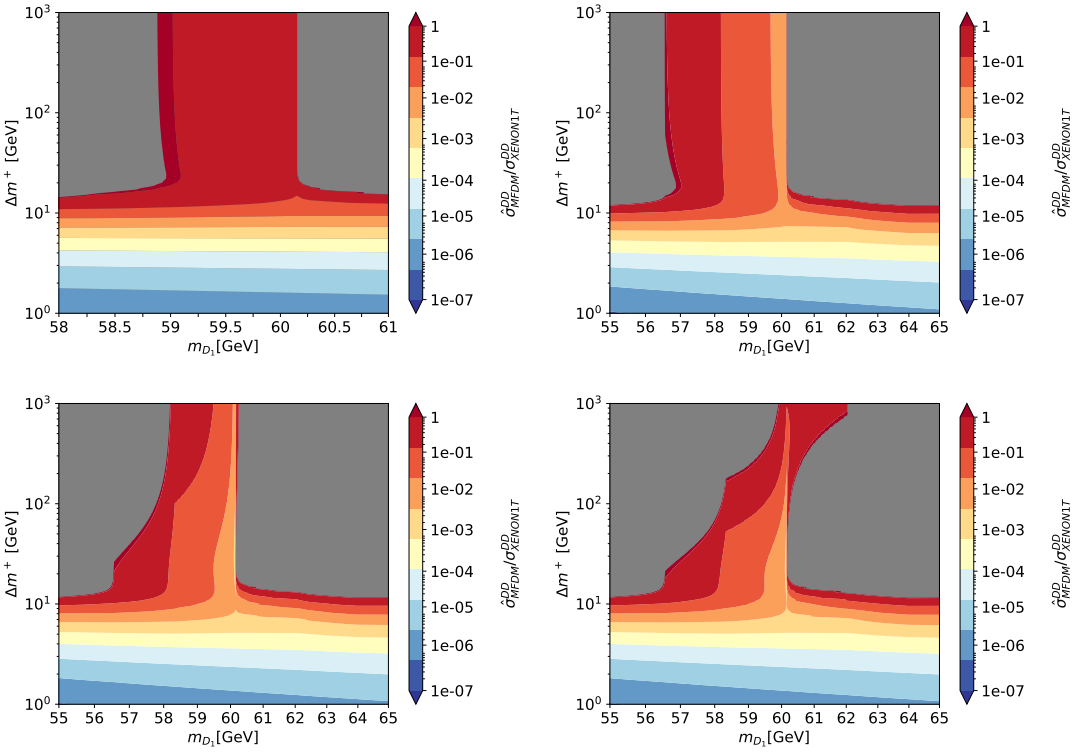

FIGURE 8.6: Colour maps of the direct detection limits for Δm^0 =1(a),10(b),100(c) and 1000(d) GeV in the zoomed region around the Higgs funnel $56 < m_{D1} < 64$ GeV. Excluded region is plotted in grey at 90% C.L. on the exclusion boundary [283].

8.3 Indirect Detection Constraints

8.3.1 CMB Constraints

DM annihilation and decay by-products can potentially be observed in astrophysical objects. Such observations (or non-observations) set bounds on the DM annihilation cross section, dependent on the distribution of DM within the astrophysical object.

The cosmic microwave background (CMB), precisely measured by WMAP, ACBAR and BOOMERANG experiments [284], can provide competitive constraints when chosen as the target astrophysical object and, as previous analyses have shown, the production of a leading DM signal occurs at redshift of $z \sim 600$ [285]. The leading bound on the thermally averaged annihilation cross-section at redshift 600 is given by [286]

$$p_{ann} = \sum_j f_j(600, m_{D_1}) \frac{\langle \sigma v \rangle_j (600)}{m_{D_1}} \tag{8.2}$$

where $f_j(600, m_{D_1})$ is the fraction of annihilation energy absorbed by the plasma, at the chosen redshift of $z \sim 600$ and $\langle \sigma v \rangle_j$ is the j-th channel thermally averaged partial annihilation cross section at this redshift.

The limit on p_{ann} is set by [281]

$$p_{ann} < 3.2 \times 10^{-28} \frac{\text{cm}^3}{\text{s GeV}} \text{ at 95\% C.L.} \tag{8.3}$$

where we take values of $f_j(z, m_{D_1})$ from digitising the upper plot of Fig. 4 in [287].

Using micrOMEGAs [282] we scan over the parameter space for $\langle \sigma v \rangle$ and contribution DM annihilation channels. After scaling again with

$$p_{ann}^{rescaled} = p_{ann} \times (\Omega h^2 / 0.11)^2 \tag{8.4}$$

the result shown in Fig.8.7 show

- No constraint from this limit in our given parameter space
- Some sensitivity in the $m_{D_1} \sim m_H/2$ region from Higgs contributions.
- All other sensitivity comes mostly from W^+W^- contributions as $m_{D_1} > 80$ GeV.
- An increase in Δm^0 increases sensitivity as couplings dependent on Δm^0 increase.

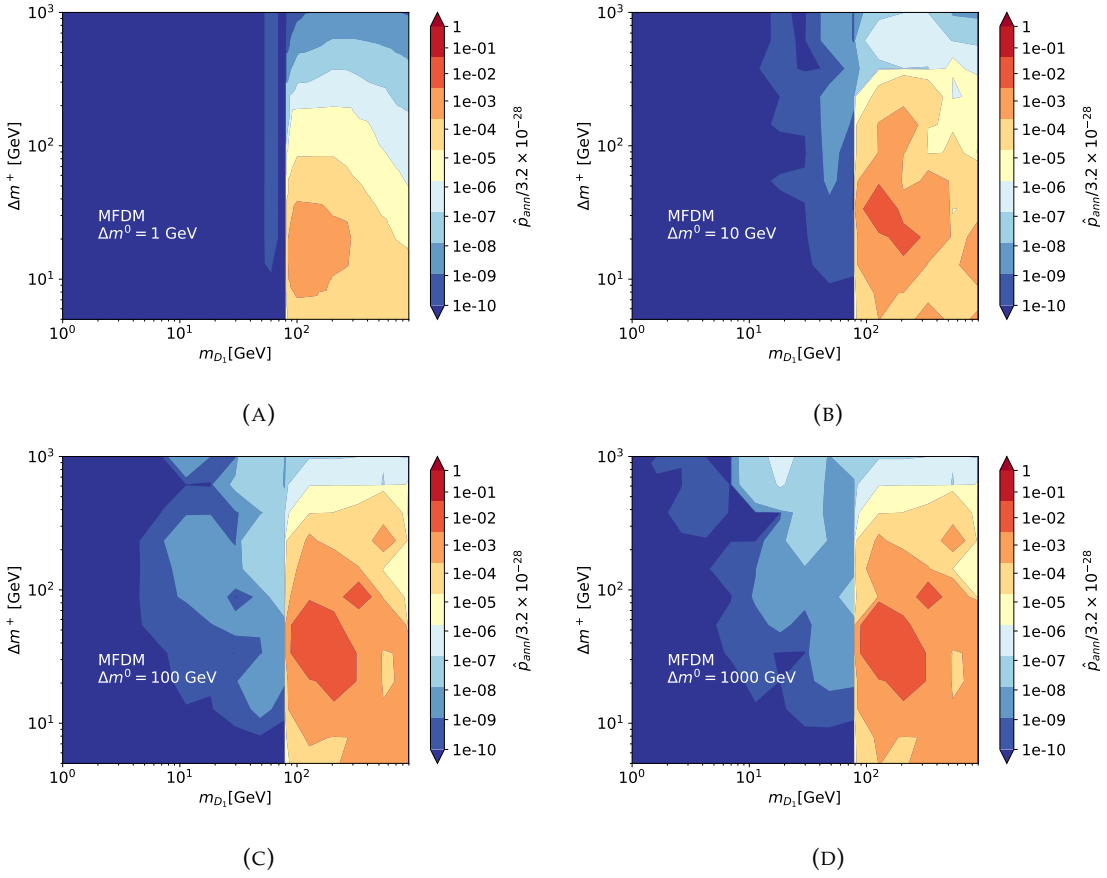

FIGURE 8.7: Scaled p_{ann}^{scaled} values ($p_{ann} \times (\Omega h^2/0.12)^2$) for MFDM parameter space. Plots (a),(b), (c) and (d) show regions for $\Delta m^0 = 1$, 10, 100 and 1000 GeV respectively, at 95% C.L. on the exclusion boundary [281].

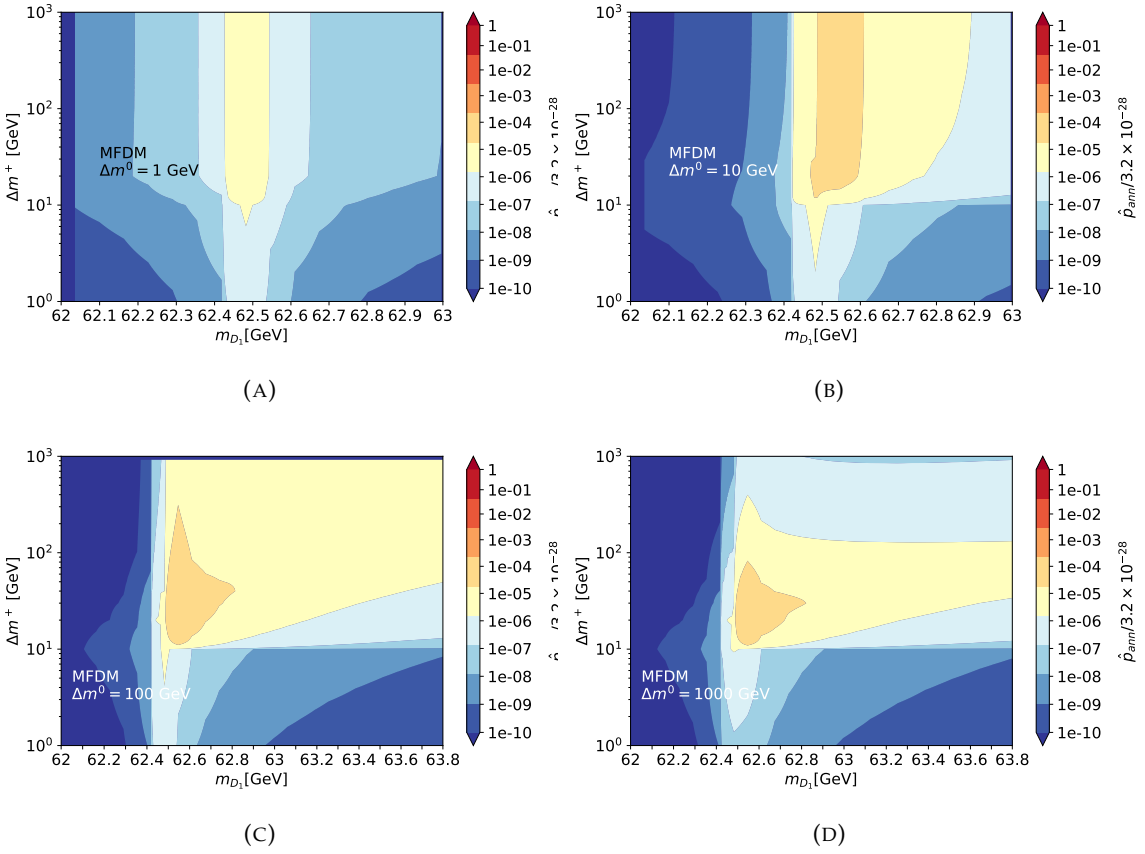

(A) (B)

(C) (D)

FIGURE 8.8: Scaled p_{ann}^{scaled} values ($p_{ann} \times (\Omega h^2/0.12)^2$) for MFDM parameter space. Plots (a),(b),(c) and (d) show regions for $\Delta m^0 = 1$, 10, 100 and 1000 GeV respectively, at 95% C.L. on the exclusion boundary [281].

8.3.2 Future CTA Limits

Indirect detection can also be probed with future projections of indirect detection experiments, such as the Cherenkov Telescope Array (CTA) [288–290].

The measured $\langle \sigma v \rangle$ values from the model is compared to that found in telescope searches The experimental sensitivities are based on DM annihilation into specific standard model particles such that their specific branching ratios are taken into account when comparing the model's data with the experimental data. Gamma ray signals are a common and promising detection channel as they travel long distances while having a short wavelength (less than 10^{-11}metres), and the highest energy in the electromagnetic spectrum, making them the most sensitive to probes. Also, they are always inevitably produced from annihilation processes due to the fact that charged particles radiate photons, which generate smooth distributions of gamma ray energies. However, since D_1 is not charged, photon products are heavily suppressed.

The annihilation cross section for gamma ray detection measured from Earth comes from cones of Cherenkov light, the radiation caused when a charged particle is travelling through a medium at velocities faster than the speed of light in the medium. In this case, it comes from gamma rays causing electromagnetic cascades in the atmosphere, where gamma rays produce pairs of cosmic electrons and positrons, which in turn produce gamma rays decaying into lower energy electron/positron pairs. This so called air showering of all these particles generates cones of Cherenkov light at an angle with respect to the particle's direction [291]. The intensity, angle, and shape of this Cherenkov light can give information about the energy and direction of the arrival of the gamma rays. These jets have different features that can be measured to estimate the original particle's mass by looking for spectral features and lines associated with the original particles. In this case DM particles [292]. However, one can not be sure that the original particle is DM since it does not interact via the electromagnetic spectrum. To combat this, two areas of similar astrophysical emission but different amounts of DM annihilation are focused on and compared. The area with the least amount of this annihilation is used as 'background' signal, to attempt to focus solely on the signals from DM annihilation [293].

Fig. 8.9 shows the relevant contributing processes from $D_1 D_1 \to W^+W^-$ annihilation.

In Fig.8.10 we present the sensitivity on DM indirect detection from future CTA experiment projections. Plotted here is

$$\frac{\sigma^{ID}_{MFDM}}{\sigma^{ID}_{CTA}} = \frac{\sigma^{ann}_{MFDM} \times BR(\to W^+W^-)_{MFDM}}{\sigma^{ID}_{CTA,W^+W^-}} \tag{8.5}$$

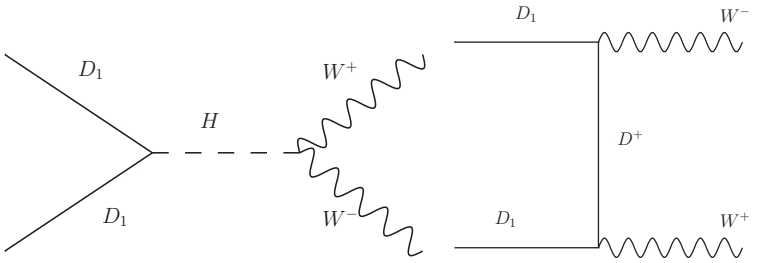

FIGURE 8.9: Feynman diagrams for the contributing $D_1 D_1 \rightarrow W^+W^-$ annihilation process.

where σ^{ann} is the annihilation cross section of MFDM DM and σ^{ID}_{CTA,W^+W^-} is the projections from CTA for the W^+W^- annihilation channel which provides the strongest limits due to decays to harder gamma rays.

The results show that

- Sensitivity only begins for $m_{D_1} > 80$ GeV from the W^+W^- contribution.
- As m_{D_1} becomes too large, there is a decrease of the $\langle \sigma v \rangle$.
- Sensitivity falls with increasing Δm^+ as this controls the t-channel diagram in Fig.8.9(b)
- Increasing Δm^0 also increases the range of Δm^0 that is sensitive to ID limits, as the $D^+ D_1 W^-$ is proportional to $\cos(\theta)$ of the mixing angle θ which increases with Δm^0(see Fig.3.1).

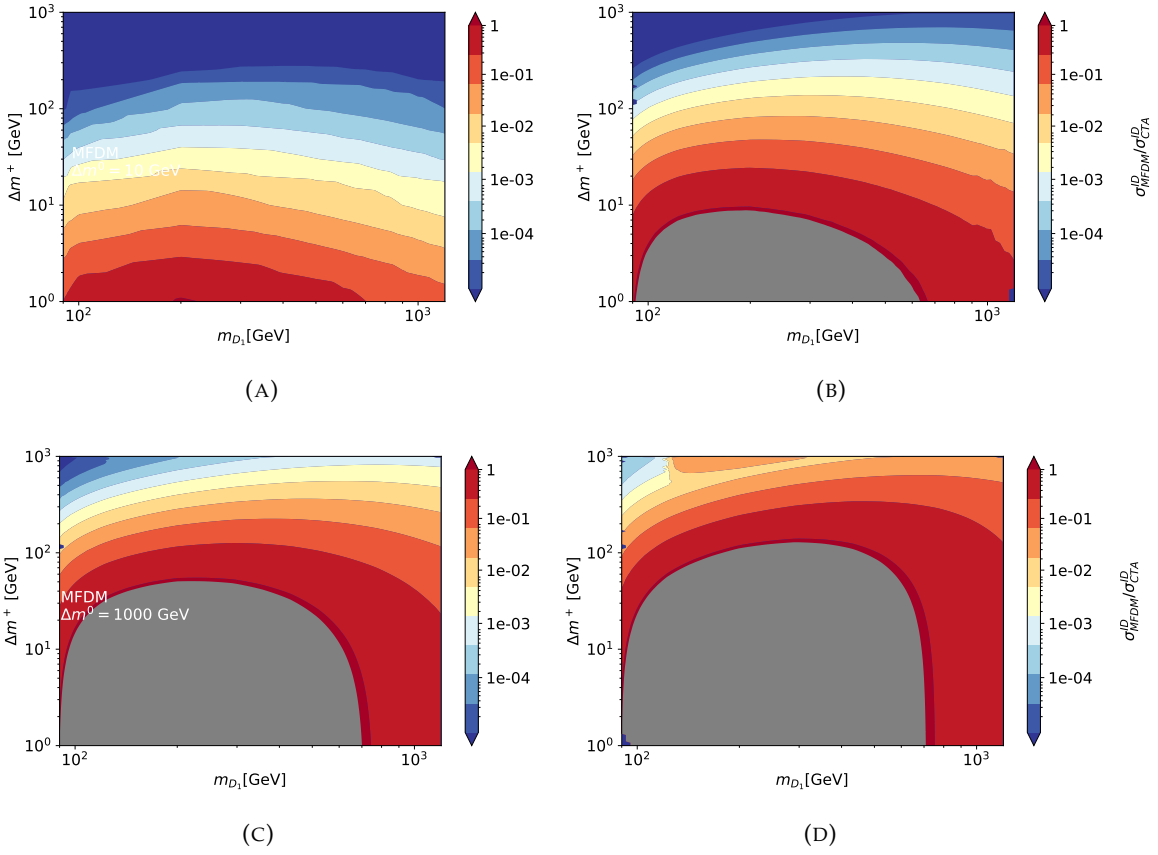

FIGURE 8.10: Indirect detection limits on $\sigma(D_1 D_1 \to W^+W^-)$ for MFDM parameter space, from future CTA [289, 290] projections at 95% C.L. on the exclusion boundary. Plots (a),(b) (c) and (d) show regions for $\Delta m^0 = 1$, 10, 100 and 1000 GeV respectively Excluded region is plotted in grey.

8.3.3 Combined LHC and Non-collider Constraints

We now present the results from Fig. 7.7 combined with the non-collider constraints on the i2HDM DM masses and mass splitting. Fig. 8.11 shows the excluded regions from relic density (RD: orange) LEP (grey) and LHC limits (pink). The allowed regions include predicted DM that explains $< 95\%$ of observed DM (blue) and DM that explains 95%-100% of observed DM (green). Since we assume that $\lambda_{345} \sim 0$, DM direct detection does not constrain the rest of the the parameter space of i2HDM model for our scenario. As discussed in the context of Fig. 8.11, the LEP limits cover the majority of the LHC exclusion region, with the exception of a small region with $m_{D_1} > 40$ GeV, $2 < \Delta m^+ < 8$ GeV for $\Delta m^0 = 1$ GeV, and a region around $\Delta m^+ > 60$ GeV, $m_{D_1} < 50$ GeV for $\Delta m^0 = 1, 10$ GeV. The relic density constraint sets the lower limit about 6 GeV on m_{D_1}, below which DM annihilation and co-annihilation channels are suppressed and, therefore the relic density is over abundant. The regions with higher DM mass open DM annihilation channels $D_1 D_1 \to H^* \to b\bar{b}$ and $D_1 D_1 \to H^* \to \tau^+\tau^-$ enough to satisfy relic. The increase of Δm^+ on one hand suppresses $D_1 D^\pm$ co-annihilation, while on the other hand enhances the couplings relevant for co-annihilation. As a result of this interplay, the relic density becomes too high in the large Δm^+ region for $m_{D_1} \lesssim 60$ GeV, since the co-annihilation channel is exponentially suppressed due to the Boltzmann factor. On the other hand, starting from $m_{D_1} \gtrsim 60$ GeV the $D_1 D_1 \to H^*$ annihilation becomes relevant, providing either correct or even under abundant amount of relic density. DM annihilation is especially enhanced by the narrow resonant annihilation region for m_{D_1} around $M_H/2$. The region with $m_{D_1} > M_W$ opens $D_1 D_1 \to W^+W^-$ annihilation channel followed by $D_1 D_1 \to ZZ$ channel for $m_{D_1} > M_Z$ which further suppresses relic density. The region with $m_{D_1} > 500$ GeV and Δm^+ in the 1-10 GeV range can provide the right amount of DM relic density as one can see in the right corner of Fig. 8.11 (a) and (b). In this region the relic density is controlled mainly by the $D_1 D_1 \to HH$ annihilation channel which is defined by the couplings determined by the Δm^+ and Δm^0 values. However if Δm^+ and/or Δm^0 values are too low then the DM annihilation is suppressed and relic density is over-abundant.

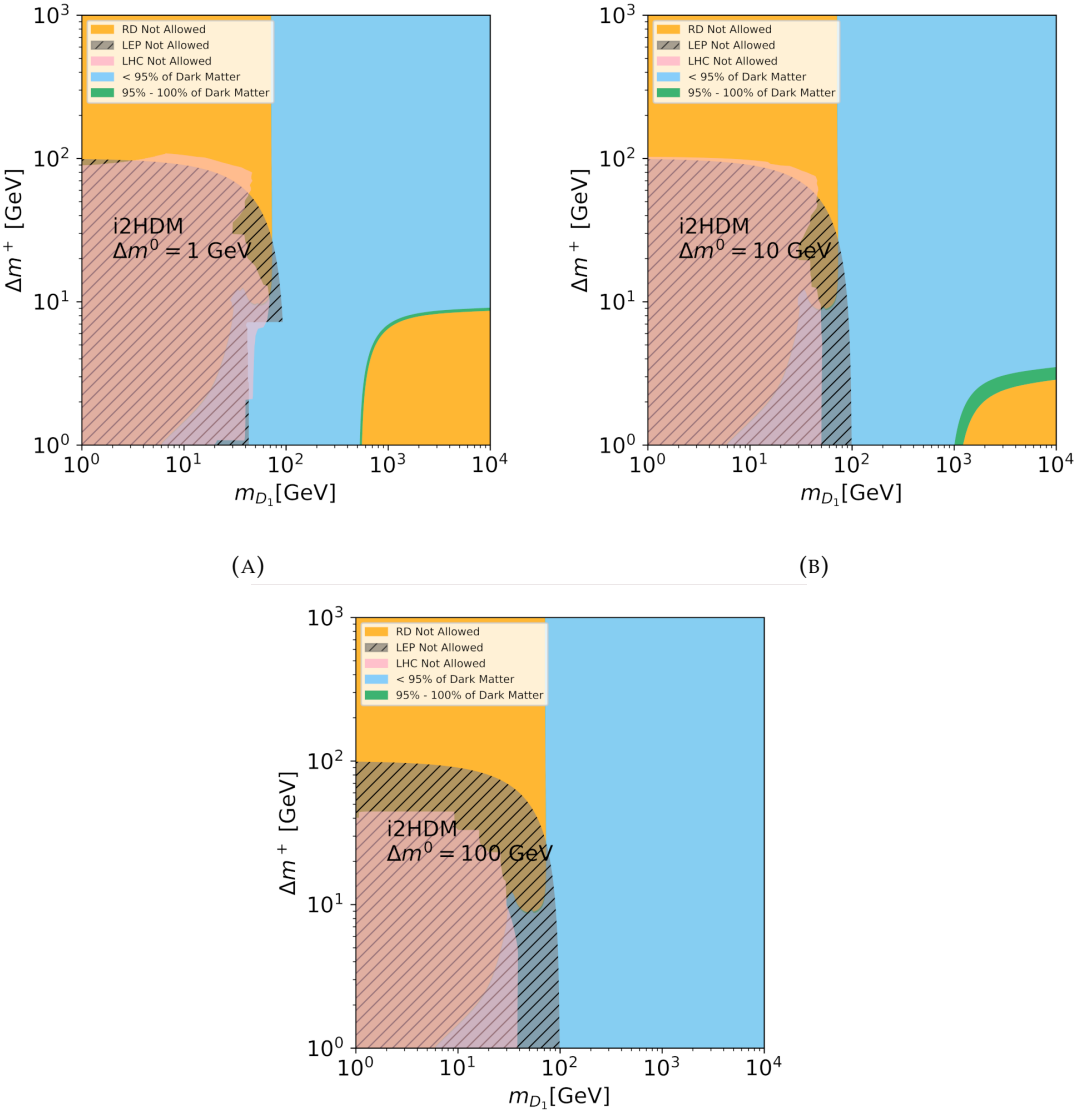

(A) (B)

(C)

FIGURE 8.11: LHC potential to exclude i2DM parameter space complementing non-collider constraints direct detection (DD), relic density (RD), LEP and LHC limits. Plots (a),(b),(c) and (d) show regions for $\Delta m^0 = 1$, 10, 100 GeV respectively.

In Fig. 8.12, we now present the results from Fig. 7.8 combined with the non-collider constraints on the MFDM model DM masses and mass splitting. Again, the allowed regions include predicted DM that explains ¡95% of observed DM (blue) and DM that explains 95%-100% of observed DM (green). Relic density (orange), LEP limits (grey) and LHC limits (pink) are also displayed presented in Fig. 8.12. For the MFDM model we now include regions excluded from direct detection (DD: red) since we allow $D_1 D_1 H$ interactions for this model. As discussed in the context of Fig. 7.8, the new LHC limits extend the phase-space coverage significantly beyond the LEP limits, including a substantial portion of the Higgs-funnel region around $m_{D_1} = m_H/2$.

The direct detection from XENON1T [294] constrains the region with large values of Δm^+ and Δm^0 parameters corresponding to large values of Yukawa coupling Y_{DM} (see Eq. (2.64)), since direct detection is defined by Higgs-DM coupling. The exclusion takes place for $\Delta m^+ \gtrsim 10$ GeV. As in i2HDM case, the relic density constraint sets the lower limit also about 6 GeV on DM mass for MFDM. The larger DM masses open various thresholds for DM annihilation via Higgs resonance as well as via WW, ZZ pairs. The region with $m_{D_1} > 800$ GeV is excluded by the relic density constraints since it becomes over abundant due to the large DM mass. The relic density constraints define also the upper limit on $\Delta m^+ \lesssim 10$ GeV, above which the DM co-annihilation with D^+ is not effective enough and therefore the relic density is too high. The only exception is the $D_1 D_1 \to H$ resonant annihilation region represented by the narrow band with m_{D1} around around $M_H/2$. This region is allowed for any large values of Δm^+. It is especially relevant to our study and partly covered by the LHC constraints.

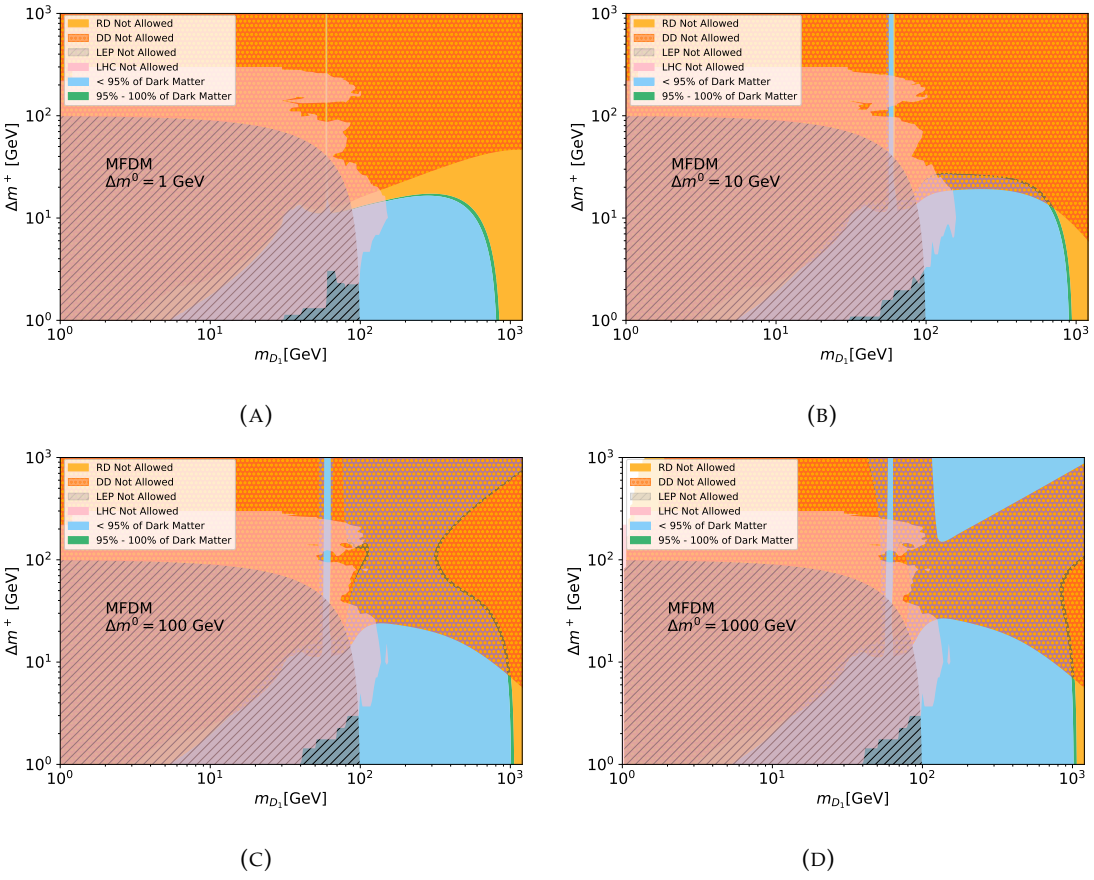

FIGURE 8.12: LHC potential to exclude MFDM parameter space complementing non-collider constraints direct detection (DD), relic density (RD), LEP and LHC limits. Plots (a),(b) and (c) show regions for $\Delta m^0 = 1,\ 10,\ 100$ GeV respectively.

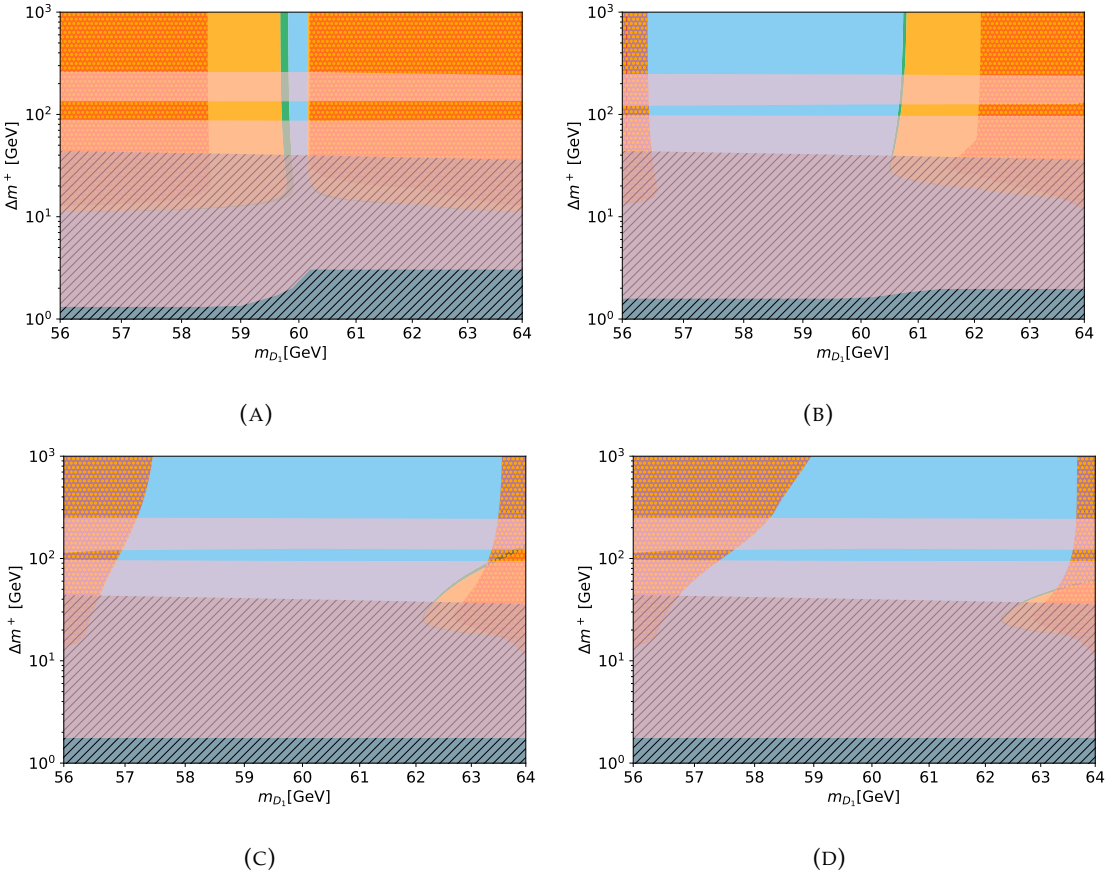

(A) (B)

(C) (D)

FIGURE 8.13: LHC potential to exclude MFDM parameter space complementing non-collider constraints direct detection (DD), relic density (RD), LEP and LHC limits. Plots (a),(b),(c) and (d) show regions for $\Delta m^0 = 1,\ 10,\ 100$ and 1000 GeV respectively.

We then overlay these distributions with the future projections from CTA limits in Fig 8.14. This expected exclusion limit from CTA covers a significant region of the still allowed parameter space, for $\Delta m^0 \geq 10$ GeV. Specifically this is the previously allowed (if under abundant) region between $100 < m_{D_1} < 1000$ GeV and $\Delta m^+ < 10$ GeV.

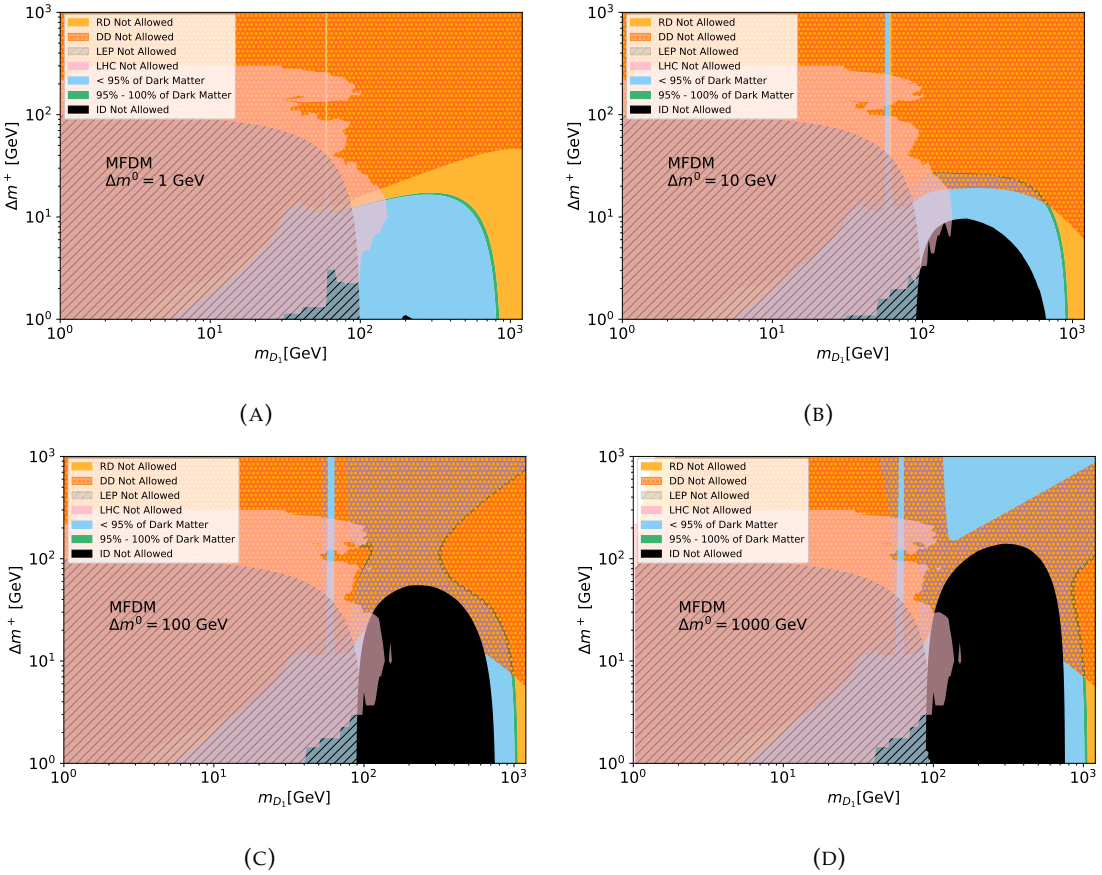

FIGURE 8.14: LHC potential to exclude MFDM parameter space complementing non-collider constraints direct detection (DD),indirect detection (ID) from CTA projections, relic density (RD), LEP and LHC limits. Plots (a),(b),(c) and (d) show regions for $\Delta m^0 = 1,\ 10,\ 100$ and 1000 GeV respectively.

Following this section, we further study the future prospects of these two models. Specifically, we next study the ability to discern mass and spin at future e^+e^- colliders.

Chapter 9

Future e^+e^- Collider Studies: DM Mass and Spin discrimination

In addition to the previous analyses, the search for DM can also be complimented by potential signals at future colliders, such as e^+e^- colliders. Future colliders could probe higher energies or different aspects of the phase space for a given model, and so is a vital addition to the constraining of DM models. In this section we study the i2HDM (sec. 3.1), MFDM (sec. 3.2) models' possible signals at an e^+e^- collider with 500 GeV centre of mass energy. In addition to DM mass determination by fitting to muon decay energy distributions, it is found that DM spin (0 and 1/2 for i2HDM and MFDM respectively) can also be distinguished at future e^+e^- colliders (such as the International Linear Collider (ILC) [295]) using a key angular variable. This is the escape angle of $D^\pm$ in $e^+e^- \to D^+D^-$ process. Additionally, escape angle of $W^\pm$ from $D^\pm$ decay can tell one about the polarisation of $D^\pm$, allowing one to distinguish vector DM from fermion and scalar DM.

9.1 Benchmark Points

For this study we chose two benchmark points with different Δm^+ mass splits. The first benchmark point, BP1, allows for on-shell $D^+ \to D_1 W$ decays. The second benchmark point, BP2, instead has off-shell W-boson in the final state. All model parameters are chosen such that they can provide the right amount of relic density and satisfy direct detection constraints from XENON1T. These benchmark points are given in Table.9.1 for the relevant i2HDM and MFDM parameters. The I2HDM model has two additional parameters compared to MFDM model, these being λ_{345} and λ_2. We chose m_{D_1}, Δm^+ and Δm^0 such that the relic density is consistent with the results from PLANCK for MFDM model, then use additional parameter λ_{345} from I2HDM to make the relic density from this model consistent with PLANCK. The other parameter

Parameter	BP1	BP2
m_{D_1}	60 GeV	60 GeV
Δm^+	100 GeV	60 GeV
Δm^0	0.85 GeV	0.85 GeV
λ_{345}	6.5×10^{-4}	7×10^{-4}
λ_2	1.0	1.0

TABLE 9.1: Benchmark points for the i2HDM and MFDM models for realistic parameters that allow for DM observables with relic and DD constraints.

λ_2 , which controls the self-interaction of DM, is not relevant to collider phenomenology. In this case, we keep $\lambda_2 = 1$ without loss of generality[1] since it does not affect any conclusions for this section. We chose the same D_1 mass and Δm^+, Δm^0 mass splits for both models with the aim to explore the ILC potential in distinguishing theories with same mass but different spin of the DM sector. Once again, we use micrOMEGAs package [282] for the relic density Ωh^2 and spin-independent proton scattering cross section σ^p_{SI}.

From section 7 the existing SUSY analyses using CheckMATE2 were recasted, where we found the most sensitive search for BP1 and BP2 is the CMS 13 TeV search for elecotroweak production of charginos and neutralinos in multilepton final states [274], which gives an r-value of 0.325 and 0.664 respectively. Many of the most strinegent LHC constraints on electroweak scale WIMP masses arise from decays mediated by sleptons and sneutrinos of mass $\sim$ 500GeV. In the scenarios explored here we assume that all additional SUSY particles (or analogous particles which could appear in the I2HDM extension) are decoupled. It is worth noting that the global scan of electroweakino DM by the GAMBIT collaboration shows favoured parameter points around our benchmarks [296].

9.2 Signal Process

To measure the $e^+e^- \to D^+D^-$ cross section at the experimental level one should measure the sum over all processes with signatures

$$e^+e^- \to D^+D^- \to D_1D_1W^+W^- \to D_1D_1(W^+ \to q\bar{q}')(W^- \to q\bar{q}'), \tag{9.1}$$

$$e^+e^- \to D^+D^- \to D_1D_1W^+W^- \to D_1D_1(W \to \ell\nu)(W \to q\bar{q}') \tag{9.2}$$

where Eq.9.1 gives two di-jets $+E_T^{miss}$ and Eq.9.2 gives a di-jet + e or μ + E_T^{miss} with each di-jet or lepton having energy $< \frac{\sqrt{s}}{2}$. In total, this is about 7/9 of the total cross section of D^+D^- production, since our signature does not include dilepton final state which is

[1] Although we do not study these effects here, the large value of λ_2 could potentially affect the DM density profile and loop-induced DM annhillation into SM particles.

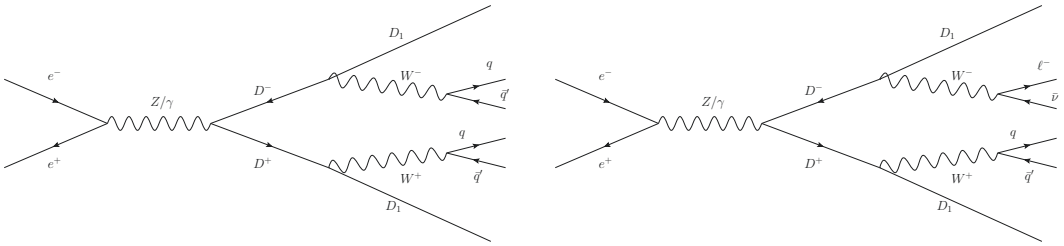

FIGURE 9.1: Feynman diagrams for the signal processes of D^+D^- production and W^+W^- decays. The left diagram depicts process 9.1 while the right diagram depicts process 9.2.

$\sqrt{s}$/GeV	300	500	500	500
m_{D^+}/GeV	120	120	160	200
SDM: σ/ fb	81.0	87.7	58.9	28.0
FDM: σ/ fb	1188.6	508.1	480.8	411.3

TABLE 9.2: Examples of cross sections $\sigma(e^+e^- \to D^+D^-)$

$2 \times (3/9 \times 3/9) = 2/9$. We instead consider the combination of dijet and lepton final state as this gives us both a precise energy measurement from the lepton decay, and more information from the jets to reconstruct the W boson. Considering only jets would give poor energy resolution, while relying only on leptonic final states loses information needed to properly reconstruct the W direction and angluar distributions.

Diagrams for these processes are given in Fig.9.1.

When masses m_{D+} is measured, the cross section of $\sigma(e^+e^- \to D^+D^-)$ process can be calculated and compared with the measured one. Since the difference between the MFDM and i2HDM signal is about one order of magnitude, the knowledge of the cross section would allow to distinguish DM spin for these two models. One should note, that in case of SUSY the MFDM cross section can be modified by t-channel diagrams with the sleptons, which could reduce the cross section by about factor of two, which however would still allow to discriminate MFDM from i2HDM case.

The expected $e^+e^- \to W^+W^-$ leading SM background and $e^+e^- \to D^+D^-$ signal cross section distributions are given in Fig.9.2 as a function of $\sqrt{s}$ in the left plot and as a function of D^+ mass in the right plot. Some examples of $e^+e^- \to D^+D^-$ cross sections are also given in Table 9.2. Fig.9.2.

For our benchmarks, the $e^+e^- \to D^+D^-$ cross section for the fermion DM (FDM) case is about 1 order of magnitude higher than the scalar DM (SDM) case The annual integrated luminosity L for the ILC project [297] is expected to be 500 fb^{-1} which provides of the order 10^5 and 10^4 events for FDM and SDM cases, respectively. The initial ratios of the FDM and SDM signals to the $e + e^- \to W^+W^-$ background are about 1/10 and 1/100, respectively.

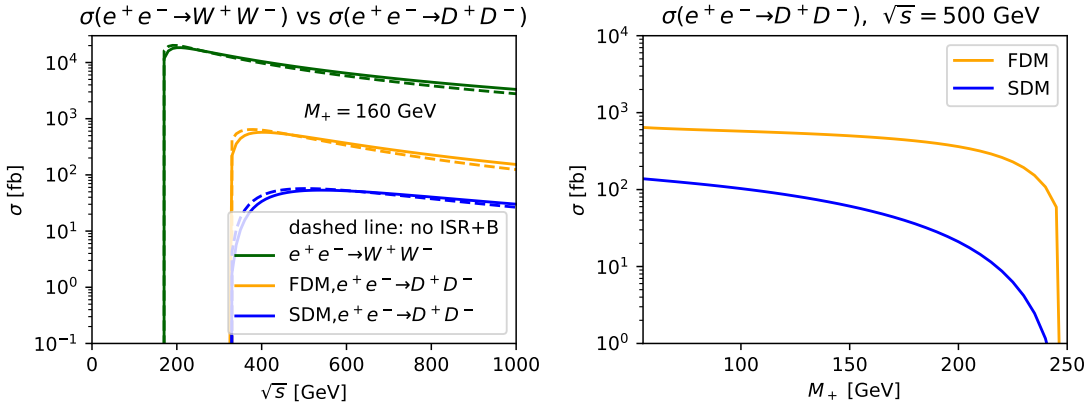

FIGURE 9.2: Left: cross section versus $\sqrt{s}$ for background $e^+e^- \to W^+W^-$ process (green) compared to the cross section of $e^+e^- \to D^+D^-$ signal processes for fermion (orange) and scalar (blue) dark matter for BP1 ($m_{D^+} = 160$ GeV). Solid (dashed) lines present results for ISR + B effects switched on (off), respectively. Right: $e^+e^- \to D^+D^-$ cross section versus m_D^+

9.3 *W* and charged lepton energy distribution and Dark Matter mass reconstruction

We proceed with a discussion of the features of the W and charged lepton energy distributions for processes (9.1) and (9.2), comprising the positions of discontinuities and end-points, expressions for which are derived using simple kinematics.

9.3.1 *W* Energy Distributions

First we consider the energy distribution of W (which may be virtual) with mass m_W^*. In the regime where W may be produced on-shell (i.e $m_{D+} - m_{D_1} > m_W$), then $m_W^* = m_W$. However, when W is produced off-shell its maximum effective mass is $m_W^* = m_{D+} - m_{D_1}$ for W^* at zero momentum. In the rest frame of $D^\pm$ we have a two-particle decay $D^\pm \to DW^\pm$. The energy and three-momentum of the W boson in the $D^\pm$ rest frame (labelled by superscript D) are given by:

$$E_W^D(m_W^*) = \frac{m_{D+}^2 + m_W^{*2} - m_{D_1}^2}{2m_{D+}}, \quad p_W^D(m_W^*) = \frac{\sqrt{(m_{D+}^2 - m_W^{*2} - m_{D_1}^2)^2 - 4m_{D_1}^2 m_W^{*2}}}{2m_{D+}}. \tag{9.3}$$

Denoting θ as the W^+ escape angle in the D^+ rest frame with respect to the direction of D^+ motion in the laboratory frame, and using $c \equiv \cos\theta$, we find the energy of W^+

in the laboratory frame to be:

$$E_W = \gamma_D(E_W^D + c\beta_D p_W^D) \Rightarrow \quad E_W^{(-)}(m_W^*) < E_W < E_W^{(+)}(m_W^*), \tag{9.4}$$

where

$$E_W^{(\pm)}(m_W^*) = \gamma_D(E_W^D \pm \beta_D p_W^D) \ , \tag{9.5}$$

with $\gamma_D = \dfrac{\sqrt{s}}{2m_{D+}}$, $\beta_D = \sqrt{1 - 4m_{D^+}^2/s}$.

For the on-shell W ($m_W^* = m_W$) case, the kinematical edges of the W energy distribution are

$$E_W^{(\pm)} = \frac{E}{2}\left[1 + \frac{m_W^2 - m_{D_1}^2}{m_{D+}^2} \pm \frac{\sqrt{(m_{D+}^2 - m_W^2 - m_{D_1}^2)^2 - 4m_{D_1}^2 m_W^2}}{m_{D+}^2}\sqrt{1 - \frac{m_{D+}^2}{E^2}}\right] \tag{9.6}$$

where E is the $D^\pm$ energy, which is quite different from delta-function shape of the background distribution, peaking at E in the absence of ISR+B. We show the W-boson energy distribution in Fig.9.3 for both i2HDM and MFDM cases. In reality ISR+B, as we show later, introduces an important smearing which makes the background non-negligible.

For the off-shell case ($m_{D+} - m_{D_1} < m_W$) although these equations hold for events with both a virtual W and real D produced at rest in the $D^\pm$ frame, the kinematic edges are smeared as a result of variation the final state momenta (and consequently the four-momentum of the virtual W) over the phase-space. This is demonstrated below in Fig.9.6 where the kinematic edges are not clearly visible.

In a well known approach, one measures edges in the energy distributions of dijets, representing W coming from $D^\pm \to DW^\pm$ decay([36,298] for MSSM and [**?**,299,300] for IDM). However, the individual jet energies and, consequently, invariant masses of dijets cannot be measured with a high precision. The observed lower edge of the W energy distribution in the dijet mode is smeared because of this. One can only hope for a sufficiently accurate measurement of the upper edge of the W energy distribution, E_W^+ given by Eq. (9.6). Therefore we suggest to extract the second quantity for derivation of masses from the lepton energy spectra. The lepton energy is measurable with a higher accuracy in comparison to the di-jet one. We will show that the singular points of the energy distribution of the leptons in the final state with signature (9.2) are kinematically determined, and therefore can be used for a mass measurement.

9.3.2 Charged lepton energy distributions from $e^+e^- \to D^+D^-$

We next study the distribution of events over the muon energy, E_μ. The fraction of such events for each separate lepton, e^+, e^-, μ^+ or μ^-, is about 0.08, while their sum is about 0.33 of the total cross section of the process.

In the following sections we consider only muons, so that in the W rest frame and the laboratory system with W energy E_W respectively, we have

$$E_\mu^W = |\mathbf{p}|_\mu^W = m_W^{(*)}/2\,, \qquad \gamma_W = E_W/m_W^{(*)},\ \ \beta_W = \sqrt{1-\gamma_W^{-2}}. \tag{9.7}$$

Just as before, we denote θ_1 as the escape angle of μ relative to the direction of the W in the laboratory frame and use $c_1 = \cos\theta_1$. The muon energy in the laboratory frame is

$$E_\mu = \frac{E_W}{2}\left(1 + c_1\beta_W\right). \tag{9.8}$$

Muon energies lie between energies $\frac{1}{2}\left(E_W \pm \sqrt{E_W^2 - m_W^{(*)2}}\right)$. The maximum muon energy, E_μ^{max}, may be determined from the highest value of W energy , i.e $E_W = E_W^{(+)}$ from Eq. (9.6) (see appendix S.1):

$$E_\mu^{max} = \frac{E}{2}\left(1+\beta_D\right)\left(1 - \frac{m_{D_1}}{m_{D+}}\right). \tag{9.9}$$

With a shift of E_W from these boundaries inwards, the density of states in the E_μ distribution grows monotonically due to contributions of smaller E_W values up to $E_\mu^{(\pm)}$ values, corresponding to the lowest value of W energy $E_W^{(-)}$ from Eq. (9.6). At these points the energy distributions of muons have kinks, located at $E_\mu^{(\pm)}$. Between these kinks, the E_μ-distribution is approximately flat. The following equation (derived in appendix S.2):

$$E_\mu^{(\pm)} = \frac{E_W^{(-)} \pm \sqrt{(E_W^{(-)})^2 - m_W^2}}{2} \tag{9.10}$$

gives the upper and lower bounds in the muon energy distributions.

At $m_{D+} - m_{D_1} > m_W$, the positions of upper edge in the dijet energy distribution $E_W^{(+)}$ (9.6) and the lower kink in the muon energy distribution $E_\mu^{(-)}$ (9.10) give us two equations necessary for determination of m_{D_1} and m_{D+} (derived in appendix S.3):

$$m_{D_1}^2 = m_W^2 - m_{D+}^2\left[\frac{1}{E}\left(\alpha+\beta\right) - 1\right], \tag{9.11}$$

$$m_{D+}^2 = 2\left[\frac{E^2\left(\alpha\beta + m_W^2\right) - \sqrt{E^4(\alpha^2 - m_W^2)(\beta^2 - m_W^2)}}{(\alpha+\beta)^2}\right], \tag{9.12}$$

where α and β are defined as:

$$\alpha = \frac{4E_\mu^{(+)2} + m_W^2}{4E_\mu^{(+)}}, \qquad \beta = \frac{4E_\mu^{(-)2} + m_W^2}{4E_\mu^{(-)}}. \tag{9.13}$$

The position of the upper edge in the dijet energy distribution $E_W^{(+)}$ should be extracted from all events with signatures 9.1, 9.2, while the position of the lower kink in the muon energy distribution $E_\mu^{(-)}$ can be extracted from events with signature 9.2 only.

If a D_2 particle is absent or $m_{D_2} > m_{D+}$, the results (9.8)-(9.10) are valid since one can neglect the interference between the signal and SM diagrams as we discuss below. The shape of the energy distribution of leptons (with one peak or two kinks) allows to determine which case is realized, $m_{D+} - m_{D_1} > m_W$ or $m_{D+} - m_{D_1} < m_W$. The energy distributions (without ISR+B effects) of muons E_μ alongside E_W are presented in Fig.9.3 for both i2HDM and MFDM cases.

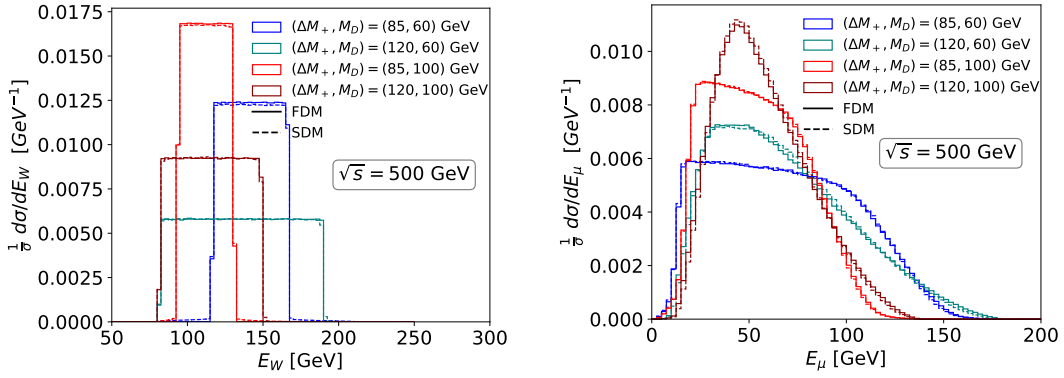

FIGURE 9.3: The energy spectra (without ISR+B) of the W (left) and muon (right) for different DM mass, m_{D_1}, and mass split with its charged partner, Δm^+. Solid and dashed lines correspond to FDM and SDM respectively.

While spin does not affect the shape of distributions in Fig. 9.3, the different DM masses and mass split scenarios can be easily distinguished by using both energy spectra E_W and E_μ. For the W energy distributions in the left plot, increasing Δm^+ spreads the energy distribution across a larger range. The W is produced nearly at rest when near the D-D^+ mass split but can have a larger range when given more energy and is more boosted.

This is opposite in the case of muon energy distributions in the right plot, where increasing Δm^+ narrows the distributions. When the width of E_W is minimal, this

maximises the width of E_μ because the muon can go exactly along W or opposite this direction, making the muon distribution as wide as possible. If W has larger phase space then it is not aligned along the direction of D^+. In this case the W energy is not fixed and can be varied which leaves less phase space to muon for its energy variation.

In the W energy distributions, increasing DM mass shifts the distributions to lower energies. This is also the case for muon energy distributions, as the tails extend to higher energies for smaller DM mass. Since a heavier DM is produced, this takes a larger fraction of the system's energy, giving less energy to the W and muons for the same input energy.

The low and high end kinks can be very close or even overlap either for E_W or E_μ energy distributions, which would eventually spoil m_{D^+} and m_{D_1} determination. The key point we stress here is that these kinks *never overlap for both distributions simultaneously*, as is demonstrated in Fig. 9.4, meaning that m_{D^+} and m_{D_1} masses can be always reconstructed. When kinematic edges are not distinguishable in the E_μ energy distribution, the E_W distribution displays a maximal separation of kinematic edges and vice versa. This is an important feature of the signal which highlights the complementary power of the two observables which allows to effectively extract DM masses in the whole parameter space relevant to the ILC signal under study.

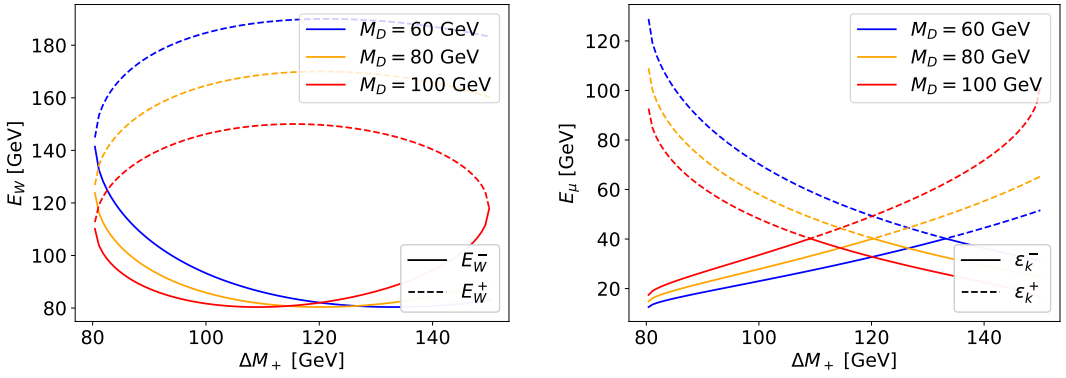

FIGURE 9.4: The dependence of position of kink of the W(left) and muon(right) energy distributions on the DM mass, m_{D1}, and mass split with its charged partner, ΔM_+. Here solid(dashed) lines correspond to lower(upper) kinks of the respective energy distributions.

Observation of events with signature 9.1, 9.2 will be a clear signal for DM particle candidates. The non-observation of such events will allow to find lower limits for masses m_{D+}, like [**?**,299,300]. At $m_{D+} < \frac{\sqrt{s}}{2}$, the cross section $e^+e^- \to D^+D^-$ is a large fraction of the total cross section of e^+e^- annihilation, making this observation a very realistic task.

9.3.3 Distortion of the energy distributions from width effects, ISR+B and intermediate τs

A more detailed analysis reveals two main sources of distortion of the energy distributions, neglected from our preliminary analysis.

1. The final width of W and $D^{\pm}$ leads to a blurring of the singularities derived. This effect increases with the growth of $m_{D^+} - m_{D_1}$.
2. The energy spectra under discussion will be smoothed due to QED initial state radiation (ISR) and beamstrahlung (B).
3. Smearing from intermediate τ leptons in the cascade $\boldsymbol{D^- \to D_1 W^- \to D_1 \tau^- \nu \to D_1 \mu^- \nu \nu}$

For the on-shell W energy distributions with scalar and fermion DM shown in Fig. 9.5 the upper and lower edges in E_W are clearly visible. However, the ISR+B smearing effect increases the uncertainty in edge identification, especially for the upper edge in E_W. For the off-shell W case, its energy distributions in Fig. 9.6 show no visible kinks

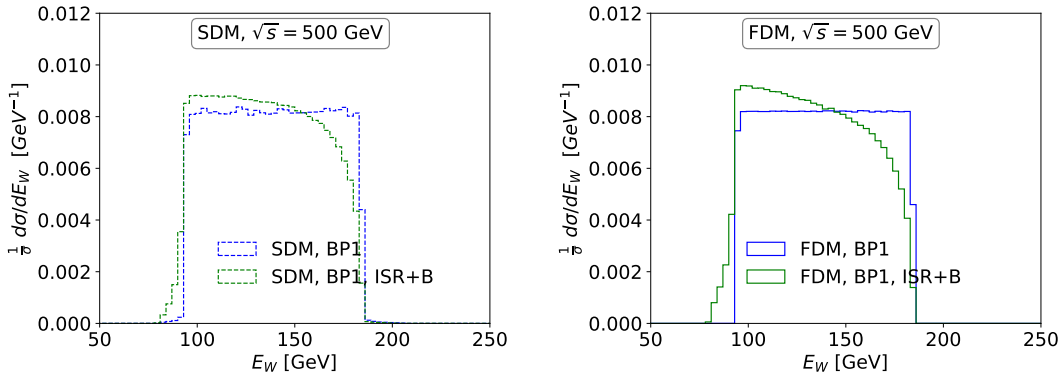

FIGURE 9.5: The W energy distribution for BP1, the on-shell W case, for i2HDM (left) and MFDM (right).

or edges, making it impossible to determine DM masses, regardless of ISR+B effects.

The effect of ISR+B which distorts the parton level muon energy distributions is presented in Fig. 9.7 left and right for i2HDM and MFDM respectively (for BP1). The blue line corresponds to production of $D^{\pm} D W^{\mp}$ and subsequent decay of W boson, i.e W-width effects are not included. The yellow line corresponds to simulation of the full production cross-section, taking into account all widths. This effect smooths $E_{\mu}^{(+)}$ considerably, but the dominant distortion comes from the effects of ISR+B, as shown by the green line. In CalcHEP, ISR is modelled using equation by Jadach, Skrzypek, and Ward [301], and Bremsstrahlung by that of P. Chen [302]. The key observation here is that the left hand kink, $E_{\mu}^{(-)}$, remains visible.

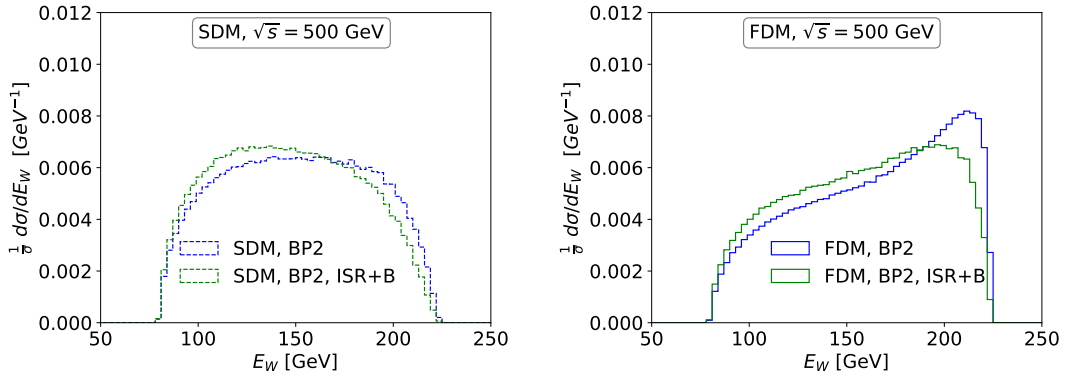

FIGURE 9.6: The W energy distribution for BP2, the off-shell W case, for i2HDM (left) and MFDM (right).

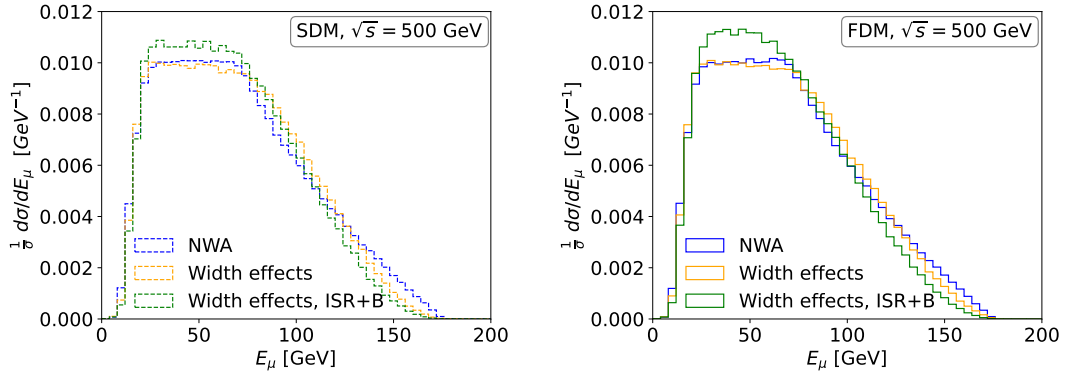

FIGURE 9.7: Muon energy distribution at BP1 for i2HDM (left) and MFDM (right).

The process $D^- \to D_1 W^- \to D_1 \tau^- \nu \to D_1 \mu^- \nu\nu\nu$ also modifies the spectra just discussed. The energy distribution of τ produced in the decay $W \to \tau\nu$ is the same as that for μ or e (within the accuracy of $\sim (m_\tau/m_W^*)^2$). Once produced, τ decays to $\mu\nu\nu$ in 17 % of cases (the same for decay to $e\nu\nu$). These muons are added to those discussed above. In the τ rest frame, the energy of muon is $E_\mu^\tau = y\, m_\tau/2$ with $y \leqslant 1$. The energy spectrum of muons is $dN/dy = 2(3-2y)y^2$. The signal evaluation is presented as energy distributions of muons in the Lab frame. It is clear that this contribution is strongly shifted towards the soft end of the entire muon energy spectrum.

In Fig. 9.8, we compare the normalised muon energy distributions for SDM and FDM, including all width and ISR+B effects. Since positions of kinks are kinematically determined, it is not surprising that calculations for distinct models (containing different angular dependence) demonstrate variations in shapes, but do not perturb the position of kinks. We see that for MFDM, $E_\mu^{(+)}$ is less well preserved than for i2HDM. Also, the higher energy tail demonstrates small difference in behaviour, however does not change the endpoint, $E_\mu^{(+)}$, required for measurement of mass. This small difference between overall shapes suggests that muon energy is not a good observable to differentiate between spins of DM, but conversely that it is a good

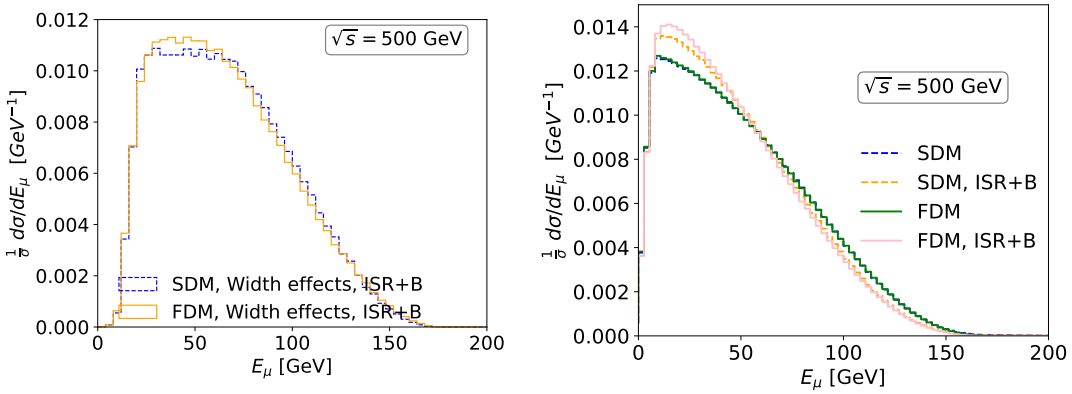

FIGURE 9.8: Comparing i2HDM and MFDM normalised muon energy distributions for BP1 (left) and BP2 (right) values, including width and ISR+B effects.

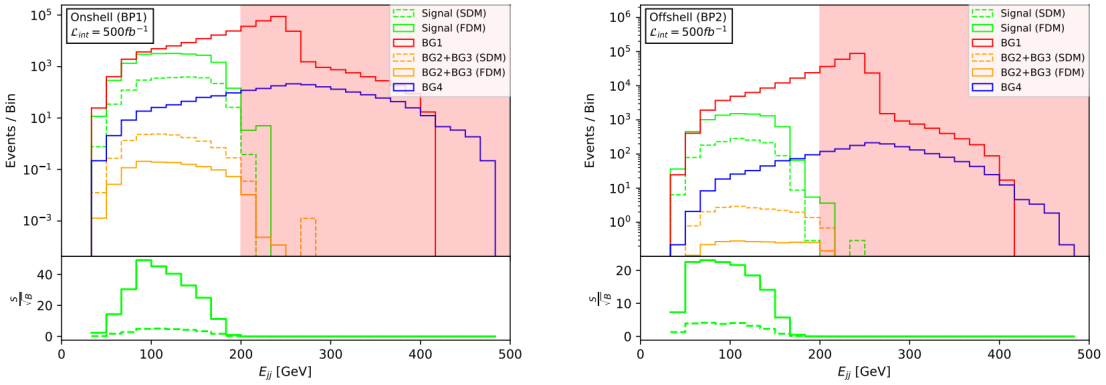

FIGURE 9.9: Energy of W boson reconstructed from dijet, for onshell (left) and offshell (right) benchmark points. BG1 corresponds to $e^+e^- \to W^+W^-$ signature 9.1 or 9.2. BG2 refers to $e^+e^- \to (W^- \to \mu\bar{\nu})(W^+ \to D_1(D^+ \to D_1W^+ \to D_1q\bar{q}))$. BG3 is the $e^+e^- \to D_1D_2 \to D_1D^+W^- \to D_1D_1W^+W^-$. BG4 then corresponds to the SM process with signature 9.1 or 9.2 but with large missing energy carried by neutrinos.

observable for spin-independent measurements of mass. Note that spin correlations were taken into account from $2 \to 4$ process.

The right plot in Fig. 9.8 shows the muon energy distribution for the off-shell W decay case. In this case, $E_\mu^{(-)}$ is easily distinguishable between DM spins, including some differences in the shapes of the distribution tails. However, $E_\mu^{(+)}$ does not exist in this case, so one must rely solely on $E_\mu^{(-)}$ for mass and spin determination for the off-shell case.

We also look at the signal-to-background comparison for energy distributions from W as reconstructed dijet in Fig.9.9. After performing $S/\sqrt{B}$ analysis on the mass peak region, one can see in the ratio pad that the FDM can still be distinguished, at least for the lower mass peak and peaks around 50 $S/\sqrt{B}$. Meanwhile, the SDM $S/\sqrt{B}$ distribution is mostly washed away by the various backgrounds, only reaching around 10 $S/\sqrt{B}$.

In the next section we discuss the observable which can be used for DM spin determination.

9.4 Angular distributions for DM spin discrimination

We have found that the remarkable observable, which can distinguish the spin of DM, is the angular distribution of W-boson with respect to the electron beam in the lab frame. We found that D^+ angular distribution is determined by the spin of DM (and in case of s-channel SM vector mediators – photon and Z-boson). By computing the $2\to 2$ matrix element squared, analytically or via CalcHEP, we obtain the differential cross sections for spin zero and spin one-half of DM:

$$\frac{d\sigma}{d\cos\theta_{D^\pm}} \propto \begin{cases} 1-\cos^2\theta_{D^\pm}, & \text{for scalar } D^\pm \\ 1+\dfrac{s-4m^2_{D^+}}{s+4m^2_{D^+}}\cos^2\theta_{D^\pm}, & \text{for fermion } D^\pm. \end{cases} \tag{9.14}$$

On the other hand, the angular distribution of W-boson from $D^\pm$ decay is strongly correlated with $D^\pm$ one. This can be observed from Fig. 9.10(left), where we present normalised angular distributions for $D^\pm$ and $W^\pm$ for two benchmarks of the fermion and scalar DM cases. One can see that the shapes of the $D^\pm$ distributions, given by Eq.(9.14) determines the angular distribution of its decay product, $W^\pm$, whose angular distribution is very close to its parent, $D^\pm$. While the (inverted parabolic) shape of $D^\pm$ angular distribution is the same for different masses of DM in case of scalar DM, the shape of angular distribution for the fermion DM case has mild dependence on DM mass and in the extreme case of the $D^\pm$ production at the threshold it becomes flat, but still clearly distinguishable from the inverted parabolic shape of the angular distribution for the scalar DM case.

The different shapes of the distributions for DM with different spins have a very simple physical explanation. Since the mediator for D^+D^- production is the spin-one SM vector bosons – photons and Z-boson, only left-left(LL) or right-right(RR) spin configuration for the initial e^+e^- state is allowed. In case of scalar DM, the forward-backward scattering of D^+D^- pair is forbidden, since forward-backward D^+D^- pair can not form orbital momentum equal to one to match the spin of the mediator. This angular momentum conservation is reflected in $(1-\cos^2\theta)$ dependence of the angular distribution of the scalar $D^\pm$ particles. At the same time, in case of fermion DM the forward-backward scattering of D^+D^- with their LL or RR final state spin configuration (matching spin one mediator) is naturally allowed, which is reflected in $\left(1+\dfrac{s-4m^2_{D^+}}{s+4m^2_{D^+}}\cos^2\theta\right)$ functional form of the angular distribution of the fermion $D^\pm$ particles.

It is important to stress that angular distributions of $W^\pm$ are very close to $D^\pm$ ones for both on-shell and off-shell W-boson cases. This makes the approach of distinguishing

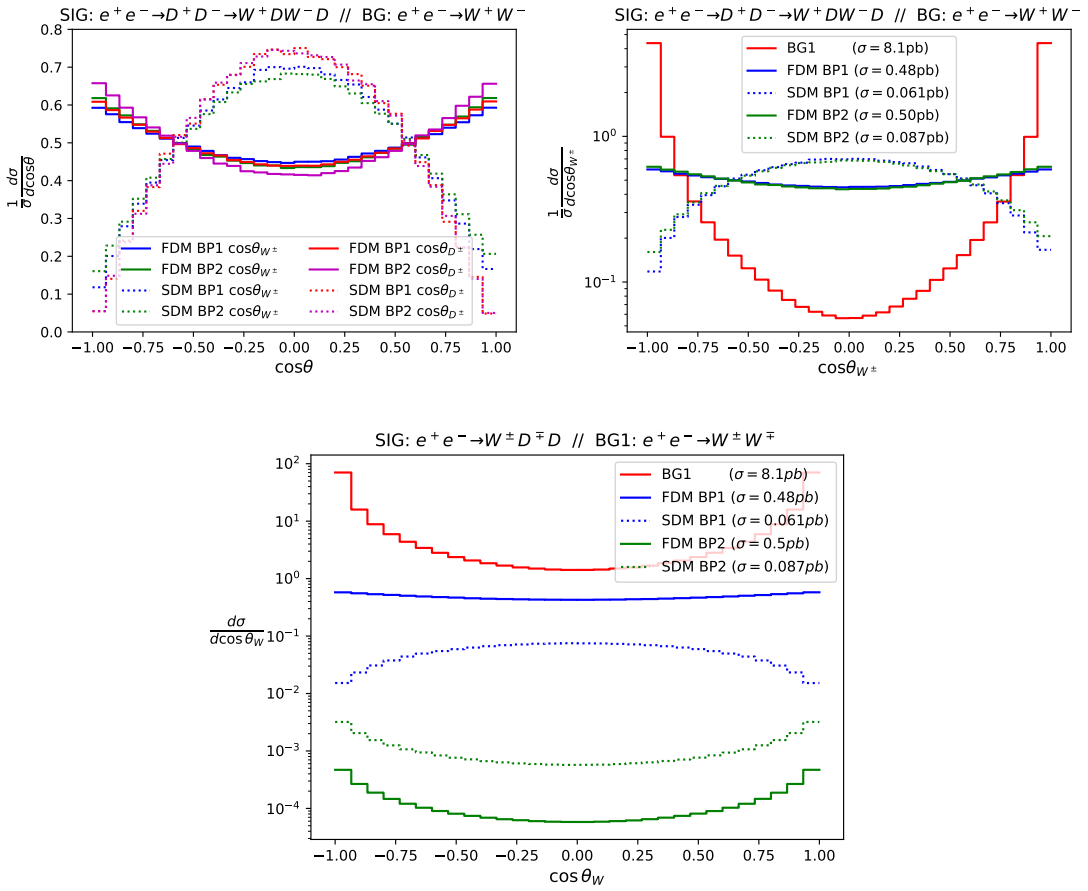

FIGURE 9.10: Left: comparison of the $W^\pm$ and $D^\pm$ angular distributions respect to beam direction in the lab frame. Right: the angular distribution of $W^\pm$ with respect to beam direction in the lab frame for signal and background processes. Bottom: Non-normalised version of the $W^\pm$ angular distribution plots.

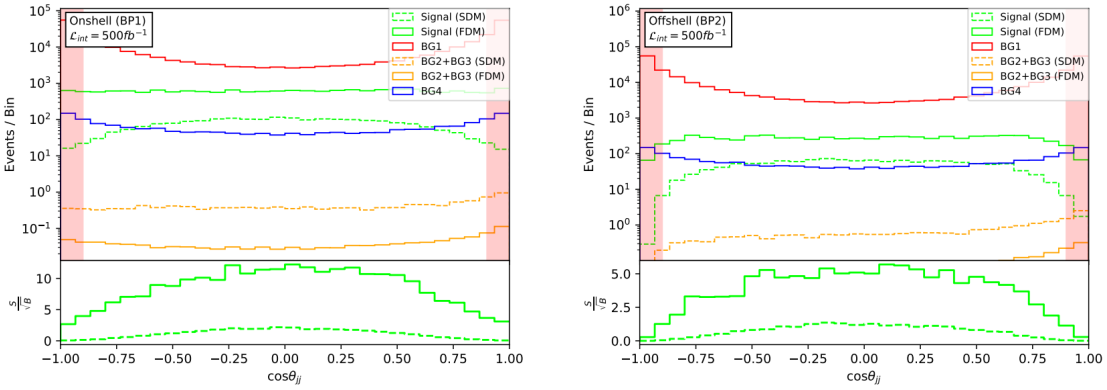

FIGURE 9.11: Scattering angle of W as reconstructed from a dijet, for onshell (left) and offshell (right) benchmark points. BG1 corresponds to $e^+e^- \to W^+W^-$ signature 9.1 or 9.2. BG2 refers to $e^+e^- \to (W^- \to \mu\bar{\nu})(W^+ \to D_1(D^+ \to D_1W^+ \to D_1q\bar{q}))$. BG3 is the $e^+e^- \to D_1D_2 \to D_1D^+W^- \to D_1D_1W^+W^-$. BG4 then corresponds to the SM process with signature 9.1 or 9.2 but with large missing energy carried by neutrinos.

DM with different spins applicable to the whole model parameter space, once W-boson (on-shell or off-shell) is reconstructed from the di-jet.

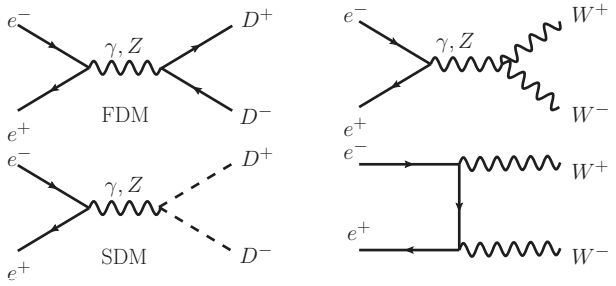

FIGURE 9.12: Signal (left) and background (right) diagrams

Another remarkable property of the signal angular distributions for both spin zero and spin one-half DM is that they are very different from the the background. This is demonstrated in Fig. 9.10(right), where we present normalised angular distributions for $W^\pm$ for both benchmarks from both DM models as well as the leading $e^+e^- \to W^+W^-$ background. One can see that the background distribution has very pronounced forward-backward peak even in comparison with the distribution for the fermion DM. The reason for this is the t-channel diagram with the electron exchange for the background, shown in Fig. 9.12(right) which plays an important role and provides the gauge invariance together with the s-channel γ/Z diagram. This is contrary to the signal case, which has only s-channel γ/Z diagram (Fig. 9.12(left)) for the D^+D^-. In case of an additional t-channel diagram for sleptons production which could take place in case of Supersymmetry, the angular $D^\pm$ and respectively $W^\pm$ distributions will be still quite different from W^+W^-, as shown in [32]. In Fig.9.11 we present the W scattering angle as reconstructed from a dijet, comparing the expected signal and backgrounds for each model. One can see from the ratio pad of $S/\sqrt{B}$ that the FDM angular distribution is much more pronounced than the SDM case, reaching over 10 $S/\sqrt{B}$. However, the SDM case still shows a significant distribution that would indeed be discernible behind its strong background.

Therefore, the angular distribution of $W^\pm$ from $D^\pm$ is very powerful observable to discriminate the spin of DM. Moreover, as we have found in our study, this variable is the generic one for the whole parameter space of a given model and therefore it allows one to successfully distinguish signal models as well as background between each other. Using one of the W's dijet final state, one can reconstruct the momentum of the two jets and their angular distributions observable at colliders to give an idea of the direction of the W they originate from.

9.5 Discussions

In this section we have considered both scalar (i2HDM) and fermionic (MFDM) DM models where DM particles are stabalised by conservation of a new quantum number, D-parity. Both of these models also include charged particles $D^{\pm}$ with the same D-parity. As a results, this setup is fairly model independent, and can be applied for more complex, SUSY-like models such as MSSM. We have studied the energy distributions of single lepton in the process $e^+e^- \to D^+D^- \to D_1D_1W^{\pm}(\to qq)W^{\mp}(\to \ell\nu)$, which provides a large enough cross section. Our analysis has shown that the energy distributions of these single leptons provide singular points, kinks, peaks and end-points which are driven only by kinematics, making them model independent. We therefore propose a new method for precise DM mass measurements using these distributions at future e^+e^- colliders, such as ILC and CLIC.

This method also provides unique improvements over previous approaches, including:

- Using leptons which are provided in abundance and can be accurately measured in comparison to QCD jets which can only be measured at low precision.
- Utilising singularities which are robust and can be distinguished under any smooth background.

Additionally we have discussed the angular observable suitable for distinguishing DM spin, between spin-0 and spin-1/2.

Chapter 10

Conclusions

Particle DM is highly motivated by the multitude of gravitational observations, and its potential collider and non-collider phenomenology is rich with unique signatures. However, an extension of the SM is required to facilitate its existence. In this thesis we have detailed two potential MCDM models for study with potential LHC and non-LHC signals. These models provide great insight into the interplay between cosmological observations of DM and their collider phenomenology, while also integratable into more complex SUSY-like models. We present a model-independent method for distinguishing DM mass and spin, using kinematic features of the energy spectra of DM-induced charged lepton cascades in e^+e^- colliders. Using benchmark points that satisfy relic abundance and DD bounds, this method provides a robust way to distinguish these crucial properties of DM, which can then be used to help disentangle the complex collider signatures. In particular, we discovered the ability to discriminate between spins by measuring the $W^\pm$ angular distributions, from reconstructed jets or charged leptons. We have also explored the full 3D parameter space of both the i2HDM and MFDM models at the LHC, presenting new limits from DM production with both 2- and 3-lepton final states + E_T^{miss}. In addition, we have studied the non-collider constraints, including relic density, direct and indirect detection, CMB and future CTA projections. We show that, while the i2HDM is highly constrained in many aspects, the MFDM still has great potential for further exploration at higher energies.

We have also studied the important SM production of Z in association with high-p_T jets, which significantly contributes to the background of such BSM signatures. Many aspects of the production were fully explored, including non-perturbative correction studies, data-driven $t\bar{t}$ and multijet background modelling, and thorough MC generator performance comparisons. We also detailed the unfolding procedure, and impacts from systematic uncertainty on our final results. In this analysis we showed that the cutting-edge MC generators, Sherpa 2.2.11 and MadGraph+Pythia 8 FxFx, perform excellently when modelling to data in the high-p_T phase space. With these

results, the two regions of interest, the collinear and back-to-back regions, can be identified and the high-p_T phases space can be well understood. We also analyse an additional SM production, namely Z production in association with heavy flavour (b and c) jets. We performed a unique, novel and robust flavour fit to correct for the mismodelling of flavour fractions by the MC generators.

The studied MCDM models are the perfect starting point for exploring BSM models, given that they are the some of the most minimal extensions one can make to include DM candidates. One can then add additional particles to these models to construct more complex BSM models with viable DM candidates, while many of the limits presented in this thesis will apply. Therefore, with this work, I give physicists a great insight as to where to search first, in terms of viable parameter space and suitable search strategies for these and for more complex models with DM candidates. In particular, the results from Chapter 7 present the ruled-out parameter spaces for multilepton final states for spin-1/2 and spin-0 minimal DM models. These could then be applied to SUSY-like models to avoid re-searching the already excluded regions and improve the analysis efficiency. Results in chapter 8 further assist physicists in discovering which non-collider constraints are already covered for these minimal scenarios, and to consider regions to explore further or model mechanisms to provide the correct limits. Finally, chapter 9 results show how one can experimentally measure the mass of their DM candidate and distinguish the DM spin in their minimal model from other spins of DM, in a model-independent way. Therefore, the results presented in this thesis are vital for the future of DM searches going forward. An important addition would be to, not only explore further in the DM mass-split axis, but also to explore similar limits for spin 1 vector DM to increase the number of models these limits are applicable for. And with higher collider energies attainable in the near future, larger DM masses and mass-splits can be probed.

In summary, this thesis is a great starting point for all particle-DM candidate BSM model builders, presenting new results on collider and non-collider sensitivity to two highly adaptable and well-motivated MCDM models while giving further insights into some of there background processes. This thesis greatly motivates the further study of DM at colliders, non-collider experiments and future colliders and indicates their unprecedented potential to discover DM in the near future.

Appendix A

Studies into HDF5 Format for ATLAS Athena Framework

This note reports on the task of implementing HDF5 reading and processing compatibility, within Athena. This involved developing code for reading information of parton-level events generated on high-performance computers (HPC) outside of the Athena framework. The results have been proven successful in reading leading-order MC predictions and merging with up to nine final state jets.

Additional investigations include the highly compressed HDF5 format [303] of event files by HPCs allows for faster computations and storing larger samples of more events than the previous standards. As the inclusive number of jets in the final states of V+jets production increases, computation time increases drastically, especially at higher order computations. As the current MC generators advance to higher precision capabilities, with more complex topologies and higher jet multiplicities, these requirements must be fulfilled to provide practical and efficient production in the near future.

The ATLAS qualification task was to develop a HDF5 file reader to work in the ATLAS Athena software, to then be showered via Pythia8 [183]. This was planned to be completed in the form of a UserHook script for Pythia reading of the Sherpa V+jets HDF5 samples. The result is a header code, which works similar to the existing LHE reading options for Athena, allowing for further Pythia input parameters from the user. These options are given as a standard job options file, an example of which is shown in this note, for jet matching and merging through Pythia.

While working with Holger Schulz's [304] reader libraries and successful compilation on a local setup, sample Z/W+jets HDF5 files were correctly read for testing purposes. Modifications to the code to output a file for plotting were made to validate the results. Dependencies on parallelisation were successfully removed, while

external packages were also accounted for, as required by Athena software. The code includes Holger's reader libraries, without parallelisation requirements, but still relies on external plugins. These packages are available in Athena setups which have been successfully found and linked to when compiling the code. The code has also been compiled and tested on ATLAS computer systems, and within an Athena setup. The code was then converted into a more standard, user-friendly tool for reading input HDF5 with user settings and showering all within the Athena generate job.

The format of the example HDF5 samples, and generators used to produce them are described in Section A.1. This note then explains the inner-working of the code, and parameters of the HDF5 reader in Section A.2. The process of installation and user implementation is then described in Section A.3, with an example of reading files given in Section A.4. The results from these examples are detailed in Section A.5.

A.1 Sample HDF5 Events

As detailed in [304], the $Z/W + 9$ jets HDF5 samples used as an input for particle-level simulation testing, demonstrate the reading procedure of the new Athena code. These samples were generated outside of Athena using modified Sherpa's Comix code and parallelisation of Alpgen code. A brief overview of the MC generators and High Energy Physics (HEP) tools used is discussed in the next few sections.

A.1.1 Sherpa Generation

Sherpa [172] is a modular program for MC generation, consisting of two matrix element generators, Comix and AMEGIC++, while also including the phase-space generator Phasic for tree-level amplitude computation. Sherpa also includes multiple merging algorithms of its own, for dealing with multijet production. While AMEGIC++ was the original matrix element generator implemented in Sherpa, the newer Comix module takes advantage of the color dressed Berends-Giele recursive relations [221] to compute multi-leg matrix elements with recursively computed phase-space weights.

A modified version of Sherpa 2.2.4 is used to produce the HDF5 files, incorporating Comix for the parton event generation. Jet definitions include k_T clustering with $R = 0.4$, and cuts on $pT(j) > 20$ GeV and $|\eta(j)| < 6$. The renormalization and factorization scales are then set to half the scalar sum of final state transverse momenta, $H'_T/2$.

A.1.2 Pythia Showering

Pythia [183] is another HEP tool for MC event generation, ideal for processes with complex multiparticle final states. It contains multiple libraries, including several algorithms for matching and merging between the hard process and parton showers. In addition, Pythia has the ability to read in external event files of various formats, and perform showering and jet matching appropriately, taken advantage of for the development of the code presented in this note

Various matching algorithms, such as the CKKW-L method [185], provide the link between the final jets after parton-showering and jet clustering, to the original partons described in the matrix element. The procedure of jet matching/merging between the hard matrix element computation and the patron showers is required to avoid double counting of a parton shower generated emission that is already accounted for by the hard interaction included in the matrix-element calculation. This is done for a tree-level matrix element generated process, by then producing the same process with up to N additional partons and regularising this via a cut on the jets involved. The scale at which the jet transverse momenta are cut, and merging applied is t_{MS}, for which a parton shower with emissions below this scale is added to the hard partons. This then models the soft and collinear emissions more accurately than the original hard matrix element calculation

A.1.3 LHE and HDF5 Event Files

The previous standard for storing MC event files as Les Houches Event (LHE) [305] files are currently produced by most generators, and can be easily passed between more general-purpose generators, for applying the user's preferred parton showering and detector-level effects. These files contain commonblocks, containers for initialisation information such as incoming beam properties, and another for information on each separate event, such as the number of particles and their properties. In Pythia for example, these are read and stored as Les Houches Accord (LHA) [306] objects of input parton-level information from a matrix element generator, ready for parton showering. While based on XML format ideal for XML parsers but still readable by Fortran and C++ code, LHE files however bring with them inefficiencies when parallelising the reading process.

The Hierarchical Data Formats (HDF) [303] were created as an effort to easily communicate and organise large volumes of information, accessible between many programming languages. These hierarchically organised databases group and contain datasets as multidimensional arrays, similar to a standard filesystem structure. This allows for easy access and reading by many tools in an intuitive way. The HDF5 format of event files are designed with HPC machines in mind, used to dealing with

large quantities of data with many number of events. It also avoids the I/O problems that come with the traditional LHE format for HPCs. The database-like structure of these HDF5 event files are visualised in the Table A.1, displaying the substructure of the parton-level event information.

A.1.4 HDF5 group: *event*

Within the *event* HDF5 group, the *aqcd* and *aqed* datasets describes which α_{strong} and α_{EM} were used, and which to set for the LHA object. These are the strong and electro-magnetic coupling constants respectively. The $fscale$ sets μ_F, the factorisation scale while *rscale* sets μ_R, the regularisation scale. Then the *scale* variable sets the scale at which the process occurred. The datasets $npLO$ and $npNLO$ then set N^pLO and N^pNLO used for LesHouches merging. The number of particles involved in the process is defined by $nparticles$, and *pid* is the process's identification code. The $trials$ equates to the number of MC trials, which is used in the weighting process, in combination with the *weights* variable.

A.1.5 HDF5 group: *index*

The particle info is read in, one by one, and stored as a LHA object in Pythia. For each event, *start* labels the beginning of the event, while *end* labels the end, used for indicating the inputs event-by-event information contained in the other HDF5 groups.

A.1.6 HDF5 group: *init*

This group of global properties give details on the initial state of the process. The $PDFgroupA$ and $PDFgroupB$ are used in combination with $PDFsetA$ and $PDFsetB$ to define the PDFs used for the incoming beams. These then have energies $energyA$ and $energyB$, and consist of particles $beamA$, $beamB$ respectively. The $weightingStrategy$ sets the input process weight strategy.

HDF5 group	HDF5 Dataset	Short Description	Type
event	aqcd	α_{strong}	double
	aqed	α_{EM}	double
	fscale	μ_F	double
	npLO	N^pLO	int
	npNLO	N^pNLO	int
	nparticles	Number of particles	int
	pid	Particle identification number	int
	rscale	μ_R	double
	scale	Upper restriction to showers and emissions	double
	trials	Used in weighting	double
	weights	Event-by-event weights	double
index	end	Label for start of event	int
	start	Label for end of event	int
init	PDFgroupA	Used for PDF selection for beam A	int
	PDFgroupB	Used for PDF selection for beam B	int
	PDFsetA	PDF used for beam A	int
	PDFsetB	PDF used for beam B	int
	beamA	beam A particle	int
	beamB	beam B particle	int
	energyA	Energy of beam A, GeV	double
	energyB	Energy of beam B, GeV	double
	numProcesses	Number of input processes	int
	weightingStrategy	Event weighting strategy	int
particle	color1	Colour of first particle	int
	color2	Colour of second particle	int
	e	EM charge	double
	id	Particle label	int
	lifetime	Particle's invariant lifetime $c\tau$	double
	m	Effective mass	double
	mother1	Position of first parent of particle	int
	mother2	Position of second parent of particle	int
	px	x component of particle's momentum	double
	py	y component of particle's momentum	double
	pz	z component of particle's momentum	double
	spin	Spin/helicity information of the particle	double
	status	Particles status code/state of the parton	int
procInfo	error	Total MC eror of the cross0section	double
	procid	Identification number of the total process	int
	unitWeight	1 if unit weighting is applied	double
	xSection	Total cross-section of the process	double

TABLE A.1: HDF5 event database-like format, comprised of HDF5 groups and their corresponding HDF5 dataset. The *event* and *index* datasets contain details of each event, the *particle* dataset describes all particles involved in the processes, while the *init* and $procInfo$ datasets give global information to the simulated processes.

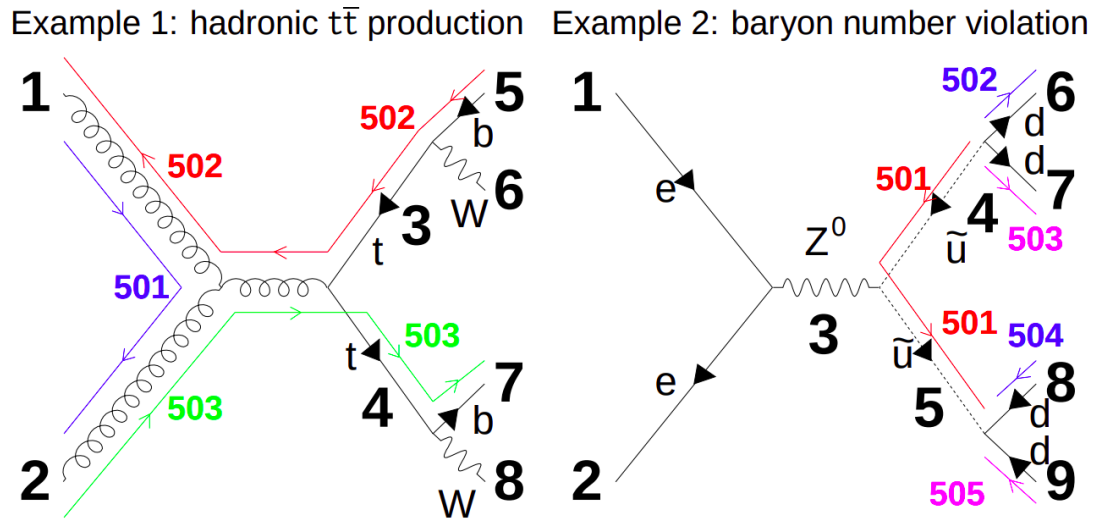

FIGURE A.1: Examples of the standard numbering system used for the *particle* group properties. [307] This includes *color* line tags, e.g.: 501, 502, and particle *id* number 1,2, which are then used as the mother numbers for particles 3, 4 e.t.c.

A.1.7 HDF5 group: *particle*

For each pair of particles for each event, *color*1 and *color*2 refer to the colours of particles 1 and 2. As displayed in Figure A.1, these came from mothers with positions *mother*1 and *mother*2. The *e*, *spin* and *m* variables define its EM-charge, spin and mass respectively. The momentum in each Cartesian direction is set with *px*,*py* and *pz*. Type of particle is identified with *id*, with a set $lifetime$. The *status* code is defined as follows: -1 is an incoming parton, 1 is a final-state parton and 2 is an intermediate resonance with preserved *m*. The *numProcesses* sets the number of separate input user processes

A.1.8 HDF5 group: *procInfo*

This group describes global properties of the total process. The *xSection* term gives the final cross-section, with *error* as the total uncertainty and is scaled with *unitWeight*. The *procid* is the total process's identification code.

A.2 Details on the Reader Code

The reader code itself is located in: *athena/Generators/Pythia8_i/src/UserHooks* (`https://gitlab.cern.ch/afreegar/athena/-/tree/21.6_Pythia8_hdf5_compatibility/Generators/Pythia8_i/src/UserHooks/hdf5readHook.h`) which first includes code required for HighFive functionality.

Relying on this, the *lheh*5 is then defined for reading HDF5 files. This is done by creating the standard structure of the events, in terms of the previously defined *particle* variables *id*, *status*,*mother*1 and so on. This then includes an event header, for the global event information such as *nparticles*, *pid*, *weight*, e.t.c.

The $LHAupH5$ object is then defined, a form of the $LHAup$ object which can be read by Pythia. This is a standard way for inputting parton level information from matrix-elements-based generators into Pythia. It assigns the corresponding event and particle properties from the HDF5 groups into event slices which are ready one-by-one with $Pythia :: next()$. The $m\_hdf5File$ variable is defined within *athena*/*Generators*/*Pythia*8_*i*/*Pythia*8_*i*/*Pythia*8_*i.h*
as the private string with $std :: string\ m\_hdf5File$;. Minor modifications are made to the source Pythia8 i code located in *athena*/*Generators*/*Pythia*8_*i*/*src*/*Pythia*8_*i.cxx*. The reader code is included by the line

```
#include "src/UserHooks/hdf5readHook.h"
```

and the reading process is carried out if the $m\_hdf5File$ is not empty, and $Pythia8\_i.HDF5File$ is set by the user in the job options file

```
if(m_hdf5File != ""){
        ATH_MSG_INFO("Input file is: "+ m_hdf5File);
        HighFive::File file(m_hdf5File, HighFive::File::ReadOnly);
        int numEvents = m_pythia.settings.mode("Main:numberOfEvents");
        size_t eventOffset = 0;
        LHAupH5* LHAup = new LHAupH5( &file , eventOffset, numEvents);
        m_pythia.setLHAupPtr(LHAup);
        m_pythia.settings.mode("Beams:frameType", 5);
}
```

which tells Pythia to read the settings from the LHA object, thus the HDF5 file inputted.

A.3 Setting-up the Code

In order to build the HDF5 reading compatible version of Athena, the following set-up can be implemented. First pull the HDF5 compatible Athena git branch with

```
setupATLAS
lsetup git
git atlas init-workdir
https://:@gitlab.cern.ch:8443/athena.git
cd athena
git checkout -b 21.6_Pythia8_hdf5_compatibility
upstream/21.6 --no-track
git atlas addpkg Pythia8_i
git pull origin 21.6_Pythia8_hdf5_compatibility
```

At this stage, create two additional directories such that the current directories show: *athena build run*, and set a release in the *build* directory

```
cd ../
mkdir build run
cd build
asetup 21.6.33,AthGeneration
```

It is then required to call the relevant packages needed specifically for the reader, such as the HDF5 libraries

```
lsetup "gcc gcc620_x86_64_slc6"
lsetup "cmake 3.11.0"
lsetup "boost boost-1.54.0-python2.7-x86_64-slc6-gcc47"
lsetup "hdf5 1.10.0.patch1-slc6"
```

Then, within the *build* folder, the code is compiled with the cmake commands

```
cmake ../athena/Projects/WorkDir
source x86_64*/setup.sh
make
```

Once compiling is complete, the code is ready for testing within the *run* directory.

A.4 Example of Reading a File

A.4.1 Job Options

This example uses the following job options *run*/100001/*mc.hdf5_matchmerge.py* for the Z+0jets file, setting a maximum of 2 jets for matching/merging.

```
evgenConfig.description = "hdf5 read test"
evgenConfig.keywords = ["Z", "Jets", "SM"]
include("Pythia8_i/Pythia8_Base_Fragment.py")
Pythia8_i.HDF5File = "Z0.hdf5"
genSeq.Pythia8.Commands += [
"Merging:doKTMerging = on",
"Merging:ktType = 1",
"Merging:Process=pp>e+e-",
"Merging:TMS=20",
"Merging:nJetMax=2"]
```

The user implemented Pythia8 commands tell the Pythia module to look for Z events when kT matching and merging jets, for 2 maximum jets at $t_{MS} = 20$ GeV cut-off scale.

A.4.2 Pythia 8 Commands

Pythia8 uses CKKW-L merging [184] in order to shower files with additional jets without double counting.

The **Merging:KTMerging** option is the switch used to apply merging with respect to the k_T cut variable. This is used when the input files are regulated by a k_T cut, which is the case here.

The **Merging:ktType** option then determines the precise definition of $k_T = min[\sqrt{p}_{Tkin,min}{}^2, \sqrt{p}_{Tlon,min}{}^2]$ used in merging, with respect to kinematic p_{Tkin} and longitudinal p_{Tlon}. Option 1, the default option applied here, uses the definition of longitudinally invariant k_T as the square root of the minimum of minimal jet kinematic $p_T(p^2_{Tkin,min} = min[p^2_{T,i}])$ and $p^2_{Tlon,min} = min[min[p^2_{T,i}, p^2_{T,j}] * [(\Delta y_{ij})^2 + (\Delta\phi_{ij})^2]/D^2]$ using the true rapidity y_{ij} of partons. Option 2 then uses the definition in terms of jet kinematics, using the pseudo-rapidity η_{ij} of partons. Option 3 uses the hyperbolic cosh function of the partons' pseudo-rapidity.

The **Merging:Process** option, which tells the Pythia8 program what matrix element hard process to look for, is set to $pp > e + e-$ to indicate Z production, in association to the matched jets.

The **Merging:TMS** variable is then the choice of merging scale. This is the k_T-cut variable in GeV units, and 20 GeV matches the choice from [304] for the original files.

The **Merging:nJetMax** option determines the maximum allowed number of jets to consider in the matrix element. The $nJetMax$ parameter for the merging must be set to at least the highest parton level number of jets that is to be encountered in the input sample production. In order to mix and match samples of different multiplicities, this must be the same in all cases, equal to the largest multiplicity of all the input files. For example, if the file $Wp2.hdf5$ corresponding to the process $p, p \to W^+, j, j$ is showered with $nJetMax = 2$, this would be valid for merging with the lower multiplicity files $Wp1.hdf5$ and $Wp0.hdf5$ (so long as these have been showered with $nJetMax = 2$ also). However, if one wants to add an additional multiplicity with $Wp3.hdf5$ for 3 partons in the final state, this would not be valid, and the previous files must also all be showered with $nJetMax = 3$.

The **Merging:nJetMinWinnerTakesAll** tells Pythia8 the minimum number of jets in the matrix element to perform winner-takes-all clustering on. This is required to be set for the split files with 7,8 and 9 jets to optimise the clustering process. "Winner Takes All" is a method in computing that takes only the most competitive neural network neuron, keeping it activated, while the rest are deactivated. In terms of clustering algorithms, a four-vector from pair-wise recombinations (taken to be massless) with momentum pointing in the direction $\hat{n}$ of the harder particle is defined as

$$p_{T,WTA} = p_{T,1} + p_{T,2}, \quad \hat{n}_{WTA} = \begin{cases} \hat{n}_1 & \text{if } p_{T,1} > p_{T,2} \\ \hat{n}_2 & \text{if } p_{T,2} > p_{T,1} \end{cases}. \tag{A.1}$$

Applied to the k_T or anti$-k_T$ algorithms, it recombines the particles directions to always align with one of the input particles. This method of finding the winner-take-all axis is also faster computationally than previous methods, and thus uses less cpu time for these files. [308] [309]

A.4.3 Generate Command

This is then used in the Athena generate transform command with

```
Gen_tf.py --ecmEnergy=14000. --firstEvent=1 --maxEvents=10000
--randomSeed $RANDOM --jobConfig=100001
--outputEVNTFile=Z0_2jmax.EVNT.root
```

The **ecmEnergy** option sets the centre of mass energy to 14 TeV, in agreement with the original HDF5 files being read. The **firstEvent** option allows for the choice of event to being processing on. The **maxEvents** option is set to tell the generators how many evens to expect, which should be set to avoid crashing. The **randomSeed** option is used to differentiate runs of similar processes, to avoid any cross-over in parameters for event generation. The **jobConfig** is used to chose the job options folder for reading the correct pythia options described above. Finally, the **outputEVNTFile** option is used to name the output file, as root format, usually named with the suffix ".EVNT.root" for the standard Athena EVNT format.

A.5 Results

The Pythia framework with HDF5 compatibility has been tested on HDF5 samples of inclusive $W^+ + 9$ jets parton level events at 14 TeV [310] to validate its functionality. Figure A.2 shows the leading jet p_T spectra results from showering different final multiplicity states of the inclusive $W^+ + N$ jets HDF5 files, and the affect of choosing different $nJetmax$ values.

The effect observed in the difference between jet multiplicities of the files is clearly seen across the different plots. There is a large fluctuation for just 1 jet and $nJetMax$ of 1 compared to $nJetMax > 1$, as observed in original plots in [304]. Fluctuation between $nJetMax$ settings then begin to diminishes for 2 jets, also observed in original plots. For 3 jets these fluctuations mostly occur after 100 GeV. The plots then begin to diverge for 4 jets and onward. With more files available for showering when considering higher multiplicities, this also results in higher statistics for these distributions. Taking the fluctuations due to this into account, the distributions are smooth, with few major kinks. This suggests the Athena incorporation of the HDF5 reading code is working in accordance to the original, and the merging process is being applied as expected.

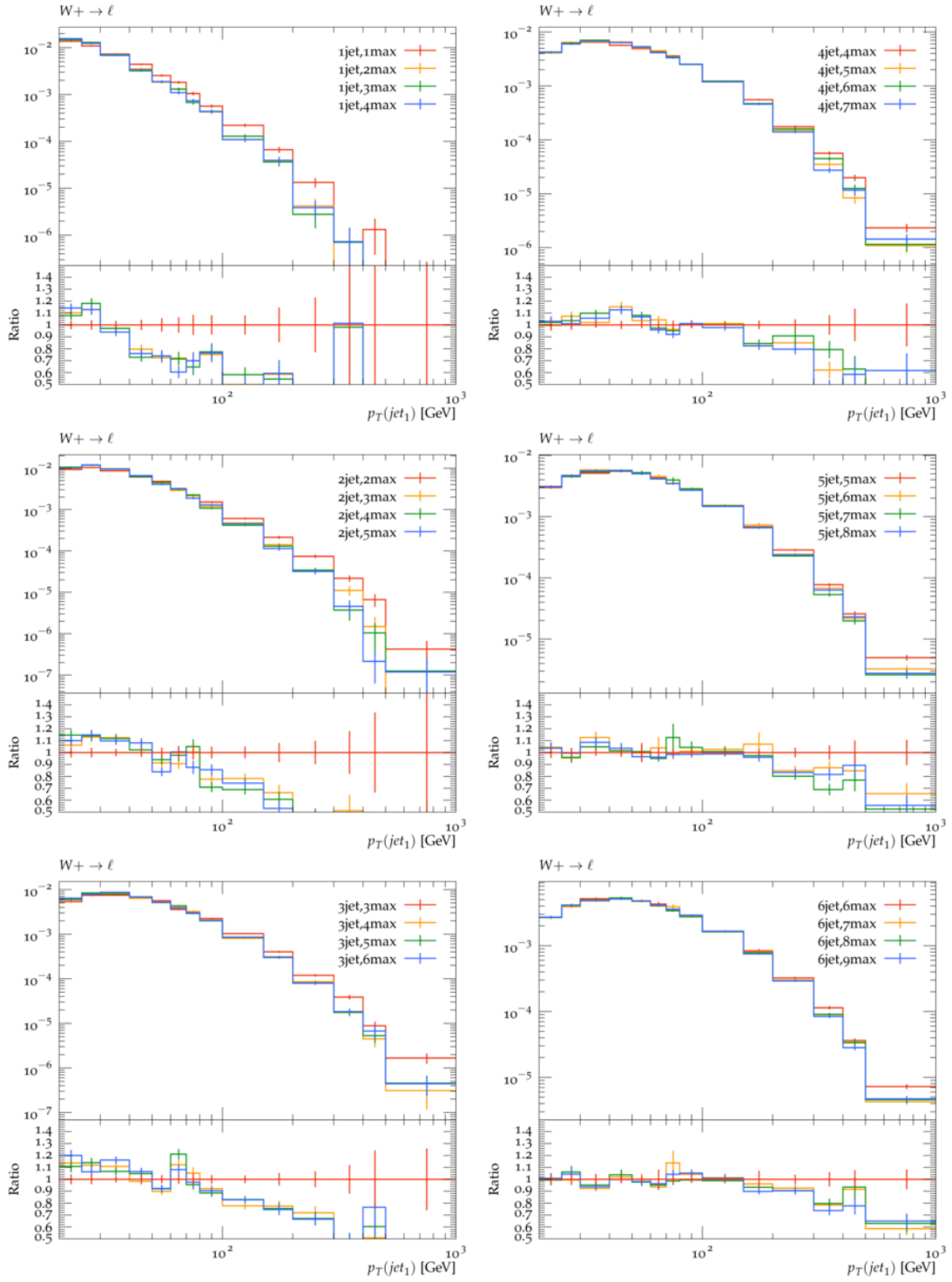

FIGURE A.2: Jet p_T distributions for different $W^+ + N$ jets final state jet multiplicities and maximum jets set for the matrix element in Pythia8.

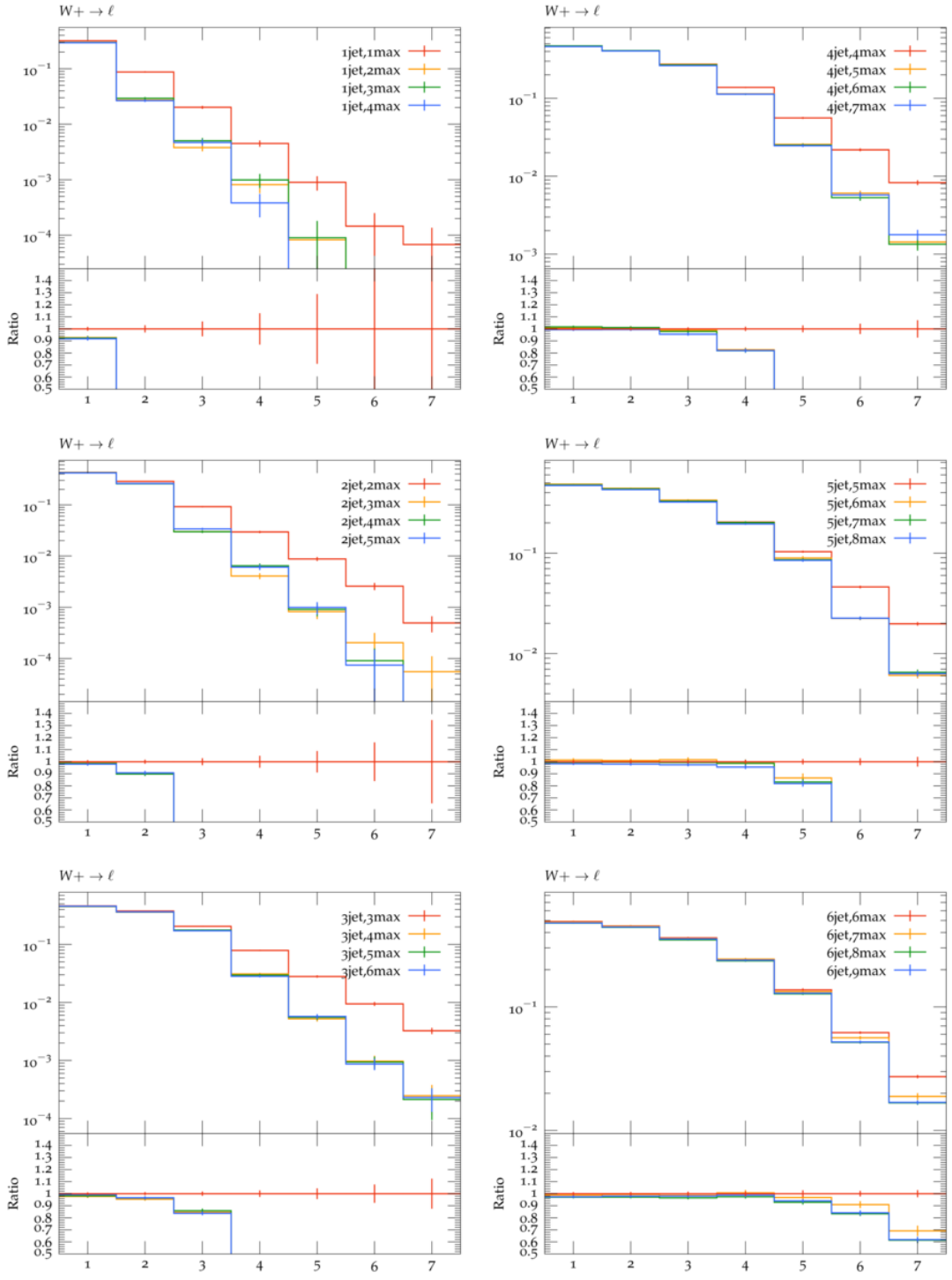

FIGURE A.3: Jet multiplicity distributions for different $W^+ + N$ jets multiplicities (prior to showering) and maximum jets set for the matrix element in Pythia8.

The plots in Fig.A.3 show the differences found in jet multiplicity for the number of jets showered on, as well as the effect of setting jet max. Similar to the effects in jet p_T distributions, the jet multiplicity is overestimated for 1 jet processes, where $nJetMax$ is 1, compared to higher $nJetMax$ values. If the $nJetMax$ is set to a higher value than the number of partons showered on, the generator expects more events from these

missing, higher multiplicity files, and so takes this into account by providing less events in these distributions. It expects the additional samples to compensate for these lack of events, but these are not provided. Conversely, when $nJetMax$ matches the number of partons showered on, the generators know not to expect more samples, and the total events are accounted for. This effect diminishes as the number of jets in the final state input file is increased, and diverges as it reaches 6 jets

The showered output of the Wp0.hdf5 file (7.7 GB) with 850 events is 31 MB. Regarding computing time of the operation, while running on the ATLAS lxplus system, showering the Z0 file with 800 events took 6 minutes. When then showering the Z1 file with 600 events, this then took 4 minutes. These are relatively fast times, when compared to LHE file reading, but more example statistics in HDF5 format are needed to test for more number of events. In comparison, for the Wp0.hdf5 file, now for 10,000 maximum number of events after showering, this gives an output file of 356 MB, and took 54 minutes. These then have to be merged with the other files (after a Rivet run and yodamerge on these .yoda files), depending on the number of max jets requested for the desired study.

This note has documented the successful processing and showering of HDF5 files with Pythia8 via the ATLAS Athena framework. The distributions have shown good agreement with the distributions in Figure A.4 from [304], with smooth plots containing few kinks. The time taken to shower these files is also reportedly faster than the pre-existing LHE file reading by comparison. The code itself has been shown to be simple to implement and control by the user, as it also functions similarly to the LHE reading already included in Athena.

For the future, it is proposed to move forward with considering large scale production. The recommended settings will still need to be discussed on a case-by-case basis, but the examples used here show consistent results.

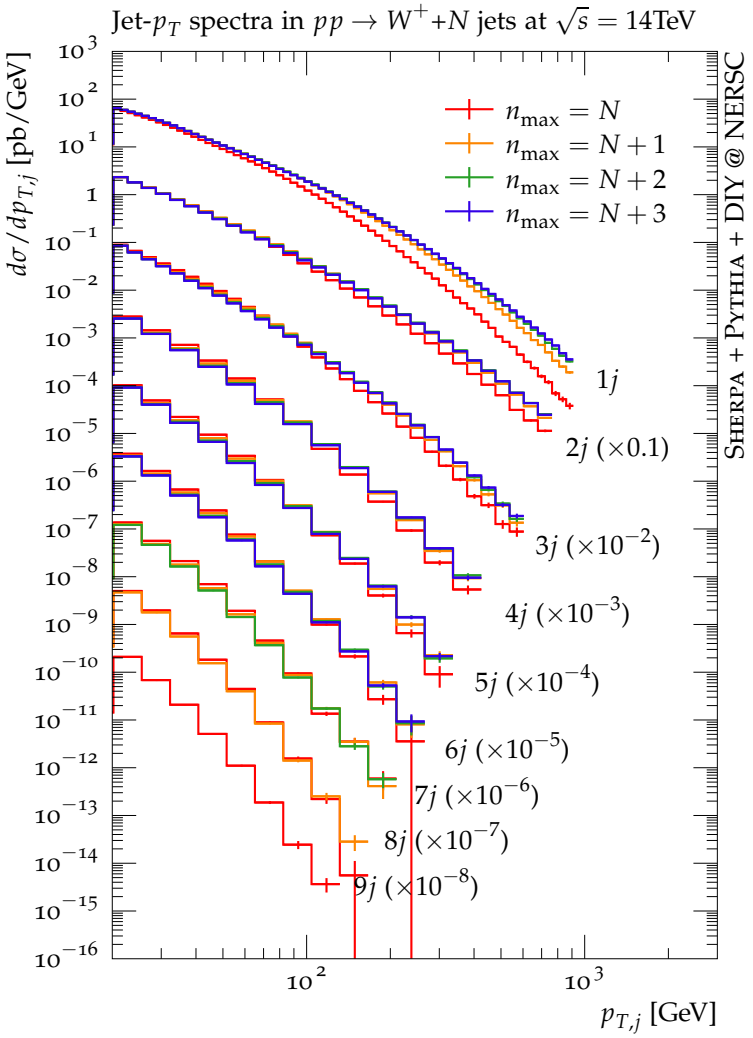

FIGURE A.4: Inclusive jet multiplicity and jet p_T for up to $W + 9$jets hdf5 files showered through Athena.

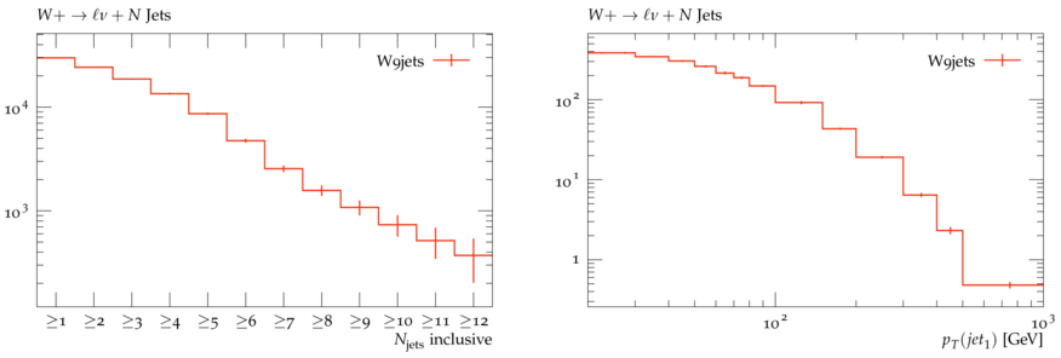

FIGURE A.5: Inclusive jet multiplicity and jet p_T for the $W + 9$jets hdf5 files showered through Athena.

Input W^++Partons	σ (pb)	Sum of Weights	Sum Of Sqr Weights	CPU time	Events	Size
0 (1 jmax)	63540	7.40E+08	5.48E+13	3835.53	10,000	356M
0 (2 jmax)	63640	7.40E+08	5.48E+13	3976.4	10,000	360M
1 (1 jmax)	328200	3.77E+09	1.44E+15	2047.62	10,000	397M
1 (2 jmax)	245600	3.85E+09	1.51E+15	2602.2	10,000	389M
1 (3 jmax)	246400	3.85E+09	1.51E+15	2660.06	10,000	390M
2 (2 jmax)	1548000	2.12E+10	6.93E+16	1950.46	10,000	423M
2 (3 jmax)	1105000	2.25E+10	7.49E+16	2718.93	10,000	413M
2 (4 jmax)	1120000	2.24E+10	7.47E+16	2800.43	10,000	411M
3 (3 jmax)	2288000	4.27E+10	1.11E+18	2138.86	10,000	456M
3 (4 jmax)	1499000	4.43E+10	2.53E+17	3208.41	10,000	441M
3 (5 jmax)	1514000	4.44E+10	2.61E+17	4944.71	10,000	444M
4 (4 jmax)	1652000	4.48E+10	2.91E+17	2297.61	10,000	488M
4 (5 jmax)	1068000	4.83E+10	3.52E+17	3704.19	10,000	469M
4 (6 jmax)	1037000	4.75E+10	3.30E+17	3700.12	10,000	470M
5 (5 jmax)	1110000	4.38E+10	7.96E+17	3744.51	10,000	523M
5 (6 jmax)	681000	4.82E+10	9.56E+17	6321.91	10,000	502M
5 (7 jmax)	673800	4.80E+10	1.05E+18	6291.31	10,000	504M
6 (6 jmax)	408600	2.44E+10	2.72E+17	14811.63	10,000	556M
7 1 (9 jmax)	2345	7643.29	1.54E+07	1.32E+12	400	25M
7 2 (9 jmax)	22500	1.87E+08	2.75E+14	16653.98	400	26M
7 1 (9 jmax, WTA)	2093	1.46E+07	8.98E+11	8043.01	400	25M
7 2 (9 jmax, WTA)	25900	1.86E+08	1.78E+14	14320.33	400	26M
7 3 (9 jmax, WTA)	2524	1.87E+07	1.46E+12	11409.95	400	24M
7 4 (9 jmax, WTA)	24300	1.09E+08	3.25E+14	7869.18	400	25M
7 5 (9 jmax, WTA)	1565	8.40E+06	4.30E+11	6440.72	400	23M
9 1 (9 jmax, WTA)	386.4	3.46E+06	5.36E+11	43051.73	400	29M
9 2 (9 jmax, WTA)	3646	3.42E+07	2.68E+13	79006.23	400	30M
9 3 (9 jmax, WTA)	344.9	3.05E+06	1.14E+11	58273.63	400	27M
9 4 (9 jmax, WTA)	1379	1.24E+07	1.40E+12	69421.8	400	29M
9 5 (9 jmax, WTA)	203.5	1.97E+06	1.18E+11	63575.48	400	27M

TABLE A.2: Cross sections, weights and cpu times for the different $W^+ + N$ jets for a chosen final number of events, and maximum ME jets.

Appendix B

Z+jets Non-perturbative Corrections at Low p_T

$p_T(jet)$ (GeV)	O_{parton}/O_{hadron}	H_T(GeV)	O_{parton}/O_{hadron}
20.02-21.2	0.78±0.05	20-22.5	0.80±0.03
21.2-22.5	0.84±0.05	22.5-25.2	0.86±0.04
22.5-23.8	0.77±0.05	25.2-28.3	0.91±0.05
23.8-25.3	0.87±0.06	28.3-31.8	0.85±0.05
25.3-26.7	0.87±0.06	31.8-35.7	0.93±0.06
26.7-28.3	0.89±0.06	35.7-40.0	0.86±0.06
28.3-30.0	0.89±0.06	40.0-44.9	0.92±0.07
30.0-31.8	0.77±0.06	44.9-50.5	0.91±0.06
31.8-33.7	0.89±0.07	50.5-56.6	0.86±0.06
33.7-35.7	0.86±0.07	56.6-63.6	0.82±0.06
35.7-37.8	0.90±0.07	63.6-71.4	0.93±0.06
37.8-40.1	0.82±0.06	71.4-80.1	0.89±0.05
40.1-42.5	1.05±0.08	80.1-90.0	0.93±0.04
42.5-45.0	0.85±0.07	90.0-101.0	0.92±0.04
45.0-47.7	1.01±0.08	101.0-113.4	0.91±0.03
47.7-50.5	1.02±0.08	113.4-127.3	0.94±0.03
50.5-53.5	0.86±0.07	127.3-142.9	0.94±0.03
53.5-56.7	0.93±0.08	142.9-160.4	0.92±0.02
56.7-60.1	0.81±0.07	160.4-180.1	0.93±0.02
60.1-63.7	0.95±0.08	180.1-202.2	0.92±0.02
63.7-67.4	0.96±0.07	202.2-227.0	0.97±0.02
67.4-71.5	1.09±0.07	227.0-254.8	1.01±0.02
71.5-75.7	0.90±0.05	254.8-286.1	0.97±0.02
75.7-80.2	0.96±0.04	286.1-321.2	0.99±0.02
80.2-85.0	0.94±0.03	321.2-360.6	1.00±0.02
85.0-90.1	0.98±0.03	360.6-404.8	1.00±0.02
90.1-95.4	0.98±0.03	404.8-454.4	0.99±0.02
95.4-101.1	0.98±0.03	454.4-510.1	0.98±0.02
101.1-107.1	0.97±0.03	510.1-572.7	0.97±0.02
107.1-113.5	0.93±0.03	572.7-642.9	0.93±0.02
113.5-120.3	1.01±0.03	642.9-721.8	1.01±0.01
120.3-127.4	0.98±0.03	721.8-810.3	0.98±0.01
127.4-135.0	0.96±0.03	810.3-909.6	0.96±0.01
135.0-143.0	1.01±0.03	909.6-1021.2	1.01±0.02
143.0-151.6	0.97±0.03	1021.2-1146.4	0.97±0.01
151.6-160.6	0.97±0.03	1146.4-1287.0	0.97±0.02
160.6-170.1	1.00±0.03	1287.0-1444.9	1.00±0.02
170.1-180.3	0.96±0.03	1444.9-1622.0	0.96±0.02
180.3-191.0	1.01±0.03	1622.0-1821.0	1.01±0.03
191.0-202.4	1.03±0.03	1821.0-2044.3	1.03±0.04
202.4-214.4	0.97±0.03	2044.3-2295.0	0.97±0.03

TABLE B.1: For MG+P8 LO, leading jet $p_T > 20$ GeV and H_T.

Appendix C

Z+jets Multijet Background Fits

Sample	Scale Factor ($p_T j \geq 100$GeV)	Scale Factor ($p_T j \geq 500$GeV)
	$\mu\mu$	
Diboson	0.989± 0.0334	0.986± 2.351
ttbar	0.854± 0.0166	0.744± 0.0438
Z	1.061 ±0.009	0.832± 0.123
Multijet	3.25± 1.106	-0.502± 3.174
	ee	
Diboson	0.737± 0.101	0.984± 0.119
ttbar	0.869± 0.008	0.702± 0.0943
Z	1.053± 0.00169	0.826± 0.0239
Multijet	1.305± 0.186	0.157± 0.306

Sample	Integral ($p_T j \geq 100$GeV)	Integral ($p_T j \geq 500$GeV)
	$\mu\mu, 71 \leq M_{\mu\mu} \leq 111$	
Data	1673060	7925
Diboson	23905.8 ±809.156	433.854 ±1034.093
ttbar	50823.7± 988.0722	276.348± 16.292
Z	1588290± 14009.591	7217.15± 1074.527
Multijet	2431.88 ±826.805	-19.617± 123.975
TotMC	1665451.38± 570138.678	7907.7347± 53425.464
Multijet/TotMC	0.00146± 0.00070	-0.00248± -0.0230
	$ee, 71 \leq M_{ee} \leq 111$	
Data	1312140	7577
Diboson	14428.9± 1977.635	423.743± 51.149
ttbar	40525.9± 405.436	261.272± 35.109
Z	1248860± 2008.609	6832.89± 198.223
Multijet	2135.71± 304.534	13.2208± 25.809
TotMC	1305950.51± 258633.184	7531.1258± 14766.355
Multijet/TotMC	0.00164± 0.00040	0.00176± 0.00486

TABLE C.1: Scale factors for $\mu\mu$, ee channel fits and contributions within Z mass window $71 \leq M_{ee} \leq 111$, with four floating parameters, including $t\bar{t}$. Errors here represent the fit uncertainties.

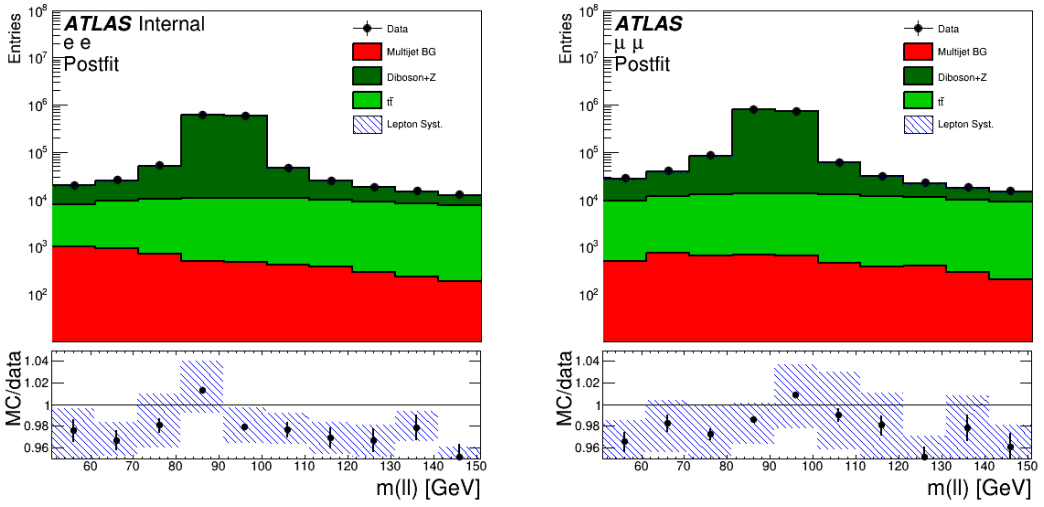

FIGURE C.1: Electron (left) and muon (right) channel multijet post-fit $m_{\ell\ell}$ distributions, with diboson and Z+jets combined. Here diboson+Z+jets and $t\bar{t}$ are left floating. Uncertainty bars in the MC/data ratio panel represent the lepton systematic uncertainties.

Sample	Scale Factor ($p_T j \geq 100$GeV)	Scale Factor ($p_T j \geq 500$GeV)
	$\mu\mu$	
Diboson+Z	1.0604± 0.0009	0.8391± 0.0105
ttbar	0.8526± 0.0105	0.9284± 0.1313
Multijet	3.228± 0.9622	-2.2637± 1.4871
	ee	
Diboson+Z	1.049± 0.0009	0.834± 0.0104
ttbar	0.863± 0.0085	0.7156± 0.088
Multijet	1.287± 0.1897	0.1584± 0.305

Sample	Integral ($p_T j \geq 100$GeV)	Integral ($p_T j \geq 500$GeV)
	$\mu\mu, 71 \leq M_{\mu\mu} \leq 111$	
Data	1673060	7896
Diboson+Z	1612290± 1370.673	7610.93± 95.2534
ttbar	50735± 628.7872	329.505± 46.6015
Multijet	2413.73± 719.359	-84.6137± 55.587
TotMC	1665438.73± 496778.353	7855.8213± 5280.039
Multijet/TotMC	0.00145± 0.00061	-0.0108± 0.01012
	$ee, 71 \leq M_{ee} \leq 111$	
Data	1312140	7539
Diboson+Z	1263440± 1188.158	7228.72± 90.274
ttbar	40261.4± 397.4205	254.432± 31.446
Multijet	2106.86± 310.486	12.958± 24.974
TotMC	1305808.26± 192871.047	7496.1102± 14476.936
Multijet/TotMC	0.00161± 0.00034	0.00173± 0.00472

TABLE C.2: Scale factors for $\mu\mu$, ee channel fits and contributions within Z mass window $71 \leq M_{ee} \leq 111$, fitting Diboson+Z together. Errors represent the fit uncertainties.

C.0.1 Fixed Diboson, Float $t\bar{t}$

In the next set of results shown Table.C.3 $t\bar{t}$ Z and multijet normalisations are then allowed to float, keeping diboson normalisation fixed. We find no significant variation to the post-fit $m_{\ell\ell}$ distributions, and so they been omitted from this work.

Sample	Scale Factor ($p_T j \geq 100$GeV)	Scale Factor ($p_T j \geq 500$GeV)
	$\mu\mu$	
ttbar	0.854± 0.0101	0.7444± 0.04988
Z	1.061± 0.0009	0.832± 0.0109
Multijet	3.254± 0.9185	-0.4981± 0.6649
	ee	
ttbar	0.865± 0.00852	0.7027± 0.0882
Z	1.05 ±0.001	0.826± 0.0109
Multijet	1.289± 0.1897	0.155± 0.305

Sample	Integral ($p_T j \geq 100$GeV)	Integral ($p_T j \geq 500$GeV)
	$\mu\mu, 71 \leq M_{\mu\mu} \leq 111$	
Data	1673060	7925
Diboson	23905.8	433.858
ttbar	50822.2± 603.142	276.348± 18.515
Z	1588300± 1363.103	7216.88± 95.198
Multijet	2433.21± 686.661	-19.456± 25.967
TotMC	1665461.21 ±470417.198	7907.629± 10567.363
Multijet/TotMC	0.00146± 0.00058	-0.00246±0.00465
	$ee, 71 \leq M_{ee} \leq 111$	
Data	1312140	7577
Diboson	18919.8	423.744
ttbar	40359.3± 397.421	261.396± 32.816
Z	1244460± 1189.914	6832.84± 90.345
Multijet	2110.21± 310.488	13.113± 25.768
TotMC	1305849.31± 192571.687	7531.093± 14829.646
Multijet/TotMC	0.00162± 0.00034	0.00174± 0.00484

TABLE C.3: Scale factors for $\mu\mu$, ee channel fits and contributions within Z mass window $71 \leq M_{ee} \leq 111$, with three floating parameters, including $t\bar{t}$. Errors represent the fit uncertainties.

C.0.2 Float Diboson, Fixed $t\bar{t}$

For this section, the diboson normalisation is allowed to float, while the $t\bar{t}$ normalisation starting value is fixed to the integral of the $t\bar{t}$ histogram. As before, no significant change is observed in the post-fit $m_{\ell\ell}$ distributions.

Sample	Scale Factor ($p_T j \geq 100$GeV)	Scale Factor ($p_T j \geq 500$GeV)
	$\mu\mu$	
Diboson	1.396± 0.724	0.986± 2.272
Z	1.055 ±0.0110	0.832± 0.1239
Multijet	-0.253± 1.868	-0.443227± 3.174
	ee	
Diboson	0.989± 0.00148	0.984722± 0.0706
Z	1.04895± 0.00195	0.827± 0.0212
Multijet	0.476± 0.1266	0.0538± 0.1975

Sample	Integral ($p_T j \geq 100$GeV)	Integral ($p_T j \geq 500$GeV)
	$\mu\mu, 71 \leq M_{\mu\mu} \leq 111$	
Data	1673060	7925
Diboson	33738.7± 17487.953	433.851± 999.617
ttbar	52724.3	274.385
Z	1579250± 16471.228	7216.77 ±1074.527
Multijet	-189.078± 1396.702	-17.3108± 123.976
TotMC	1665523.922± 12333340.77	7907.6952± 59503.53
Multijet/TotMC	-0.000114± 0.00119	-0.00219± 0.02274
	$ee, 71 \leq M_{ee} \leq 111$	
Data	1312140	7577
Diboson	19328.2± 28.923	423.745± 30.378
ttbar	42506.1	275.014
Z	1242910 ±2313.143	6826.26 ±175.352
Multijet	779.776± 207.263	4.547 ±16.674
TotMC	1305524.076± 347019.233	7529.566± 27616.849
Multijet/TotMC	0.000597± 0.00022	0.000603± 0.00313

TABLE C.4: Scale factors for $\mu\mu$, ee channel fits and contributions within Z mass window $71 \leq M_{ee} \leq 111$, with floating diboson parameters. Errors represent the fit uncertainties.

While the $p_T j \geq 500$ GeV fit could be compatible with 0, these results are inconclusive due to large uncertainties.

C.0.3 Fixed Diboson, Fixed $t\bar{t}$

Finally, both the diboson and $t\bar{t}$ normalisations are set fixed, with just Z and multijet normalisations left floating in Table.C.5. Once again the distributions show no observable change from the previous cases.

Sample	Scale Factor ($p_T j \geq 100$GeV)	Scale Factor ($p_T j \geq 500$GeV)
	$\mu\mu$	
Z	1.0614± 0.00091	0.832± 0.0109
Multijet	0.686± 0.441	-0.444± 0.6648
	ee	
Z	1.0492± 0.000988	0.825± 0.0107
Multijet	0.488± 0.1164	0.0540± 0.1805

Sample	Integral ($p_T j \geq 100$GeV)	Integral ($p_T j \geq 500$GeV)
	$\mu\mu, 71 \leq M_{\mu\mu} \leq 111$	
Data	1673060	7925
Diboson	23905.8	433.858
ttbar	52724.3	274.385
Z	1588220± 1363.116	7217.33± 95.199
Multijet	512.674± 329.793	-17.357± 25.966
TotMC	1665362.774± 1071295.822	7908.2157± 11830.983
Multijet/TotMC	0.000307± 0.00028	-0.00219± 0.00464
	$ee, 71 \leq M_{ee} \leq 111$	
Data	1312140	7577
Diboson	18919.8	423.744
ttbar	42506.1	275.014
Z	1243310± 1170.868	6825.82± 88.628
Multijet	798.186± 190.583	4.562± 15.240
TotMC	1305534.086± 311725.233	7529.1402± 25151.413
Multijet/TotMC	0.000611± 0.00021	0.000606± 0.00286

TABLE C.5: Scale factors for $\mu\mu$, ee channel fits and contributions within Z mass window $71 \leq M_{ee} \leq 111$, with floating Z and multijet parameters. Errors represent the fit uncertainties.

Appendix D

Z+jets Cross Section Results

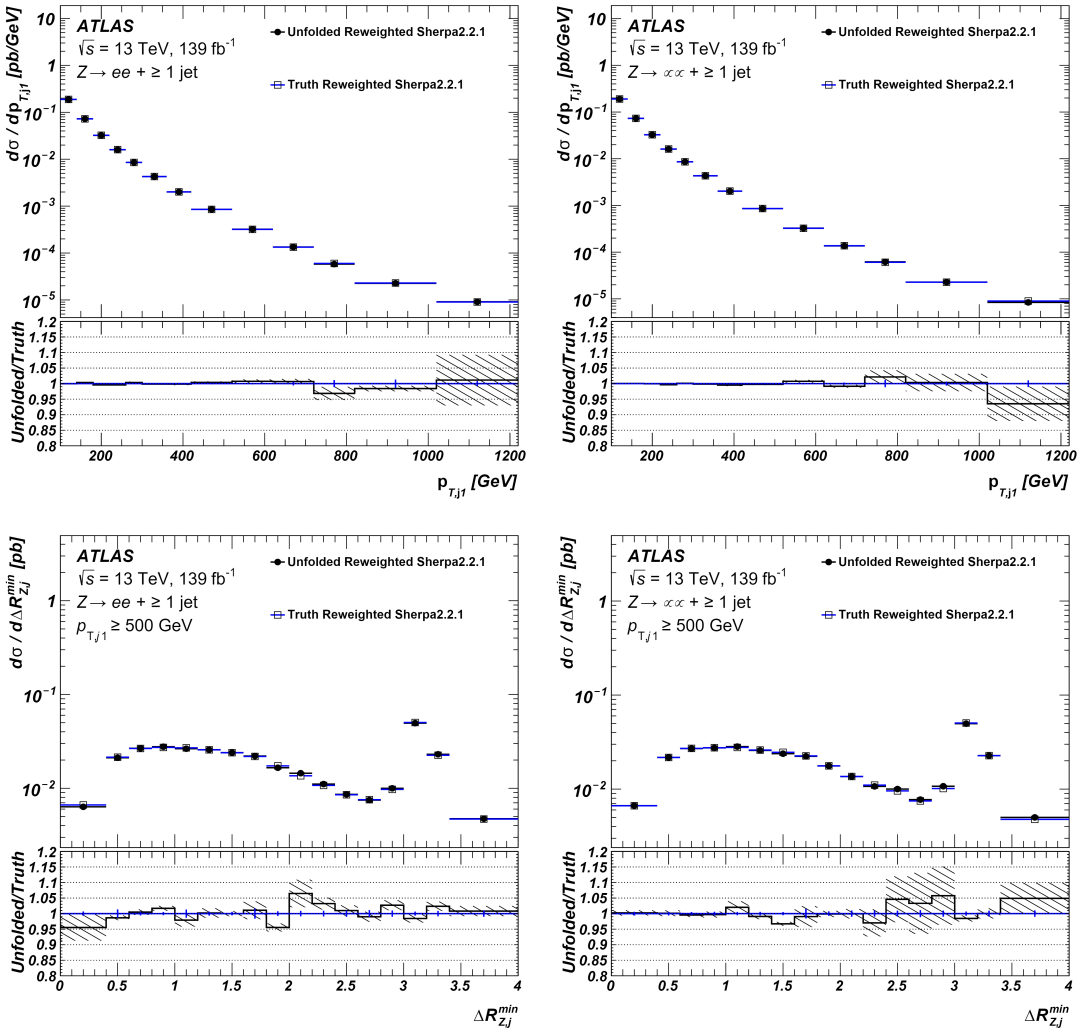

FIGURE D.1: Closure test for truth reweighted and unfolded reweighted differential cross sections from Sherpa 2.2.1 MC distributions, for the p_T(leading jet) (top) and $\Delta R^{min}_{Z,j}$ (bottom) for the electron(left) and muon channel (right). [42]

Appendix E

8 TeV Validation: i2HDM

Appendix K details the validation of our CheckMATE recast for 8 TeV LHC exclusion limits for 2-lepton final states by comparing with the existing MadAnalysis implementation [311]. The CheckMATE analysis code was written based on and validated with the original experimental results, which searched for direct production of charginos, neutralinos and sleptons in final states with two leptons and missing transverse momentum [312] at the LHC. This was implemented using the CheckMATE's AnalysisManager in the current public build, and the SUSY analysis is available at [268]. The cutflows are given in tables K.1 and K.2.

Global Cut	
E_T^{miss}	> 0 GeV
Base leptons	2
e^+e^- trigger	97%
$\mu^+\mu^-$ trigger	89%
$e\mu$ trigger	75%
Signal leptons	2
Leading lepton p_T	> 35 GeV
sub-leading lepton p_T	> 20 GeV
$M_{\ell\ell}$	> 20 GeV
jets	0
$\lvert M_{\ell\ell} - M_Z \rvert$	> 10 GeV

TABLE E.1: Cutflow for all events in the 8 TeV ATLAS SUSY analysis for 2-lepton+E_T^{miss} finals states, implemented in CheckMATE.

SR	m_{T2}^{90}	m_{T2}^{120}	m_{T2}^{150}	WWa	WWb	WWc	Zjets
$M_{\ell\ell}$				< 120	< 170		
$p_T(\ell\ell)$				> 80			> 80
$E_T^{miss,rel}$				> 80			> 80
m_{T2}	> 90	> 120	> 150		> 90	> 100	

TABLE E.2: Cutflows used for the specific signal regions in the 8 TeV ATLAS SUSY analysis for 2-lepton+E_T^{miss} finals states, implemented in CheckMATE.

The 8 TeV ATLAS analysis searching for invisible decays of a Higgs boson produced in association with Z [312], previously recasted for MadAnalysis [313] was also written for the CheckMATE analysis performed here, as it also looks for final states with two leptons and missing energy. The public code of the Higgs analysis is available at [269]. The cutflow is given in table K.3.

Global Cut	
Base leptons	2
Lepton p_T	> 20 GeV
Z-window	$76 < M_{\ell\ell} < 106$ GeV
E_T^{miss}	> 90 GeV
$d\phi(E_T^{miss}, p_T^{miss})$	< 0.2
$\Delta\phi(p_T(\ell\ell), E_T^{miss})$	> 2.6
$\Delta\phi(\ell, \ell)$	< 1.7
$\lvert\frac{E_T^{miss} - p_T(\ell\ell)}{p_T(\ell\ell)}\rvert$	> 0.2
jets	0

TABLE E.3: Cutflow for all events in the 8 TeV ATLAS Higgs analysis for 2-lepton+E_T^{miss} finals states, implemented in CheckMATE.

The events used for the validations were generated with CalcHEP, with 100000 events produced for each 9 benchmark points, using the SLHA files provided from HepData [314] and 1 benchmark point for $HZ \to$ invisible, with $M_H = 125.5$ GeV. Leptonic decays of Z in the HZ production, $\chi^{\pm}\chi 2$ production and W in the $\chi^+\chi^-$, were also specified in CalcHEP to improve efficiency, which were then showered with CheckMATE's built-in PYTHIA8 module. Detector effects are also applied via CheckMATE with a DELPHES module. Validation for the SUSY analysis is available at [315] and Higgs analysis available at [316].

The motivation behind fixing m_{D+} is because it is mostly only important for D^+D^- production, which give an additional EW coupling factor compared to D_2D_1 production, only providing significant contributions to r-value at very light m_{D+}. The ZD_1D_1 production is also less dominant as the ZZD_1D_1 coupling is quadratic and therefore weak compared to other couplings. The lowest allowed LEP limit of $m_{D+} = 85$ GeV is used and the higher value of $m_{D+} = 150$ GeV for comparison.

The r-value contour plots for $m_{D+} = 85$ GeV in Fig. K.1(a) for the WWb signal region shows that the Run 1 ATLAS 2-lepton analysis excludes for the lightest DM mass of $m_{D1} \leq 35$ GeV for $m_{D2} = 100$ GeV, reaching a maximum of ~ 40 GeV as m_{D2} is increased. In the case of Fig. K.1(b), the WWc signal region reports stronger limits, excluding the lightest DM mass of $m_{D1} \leq 40$ GeV for $m_{D2} = 100$ GeV, reaching a maximum of ~ 45 GeV as m_{D2} is increased. For $m_{D1} \to 0$ GeV, both cases exclude up to a mass of $m_{D2} = 130$ GeV.

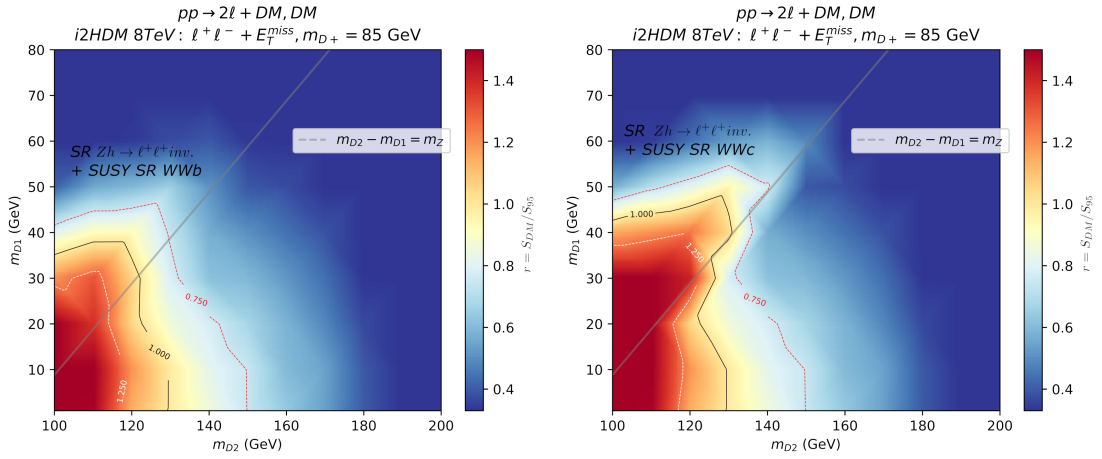

(A) (B)

FIGURE E.1: r-value Exclusion plots as a function of m_{D_2} in i2HDM at 8 TeV, $m_{D+} = 85$ GeV, signal regions WWb+Higgs (a) and WWc+Higgs (b).

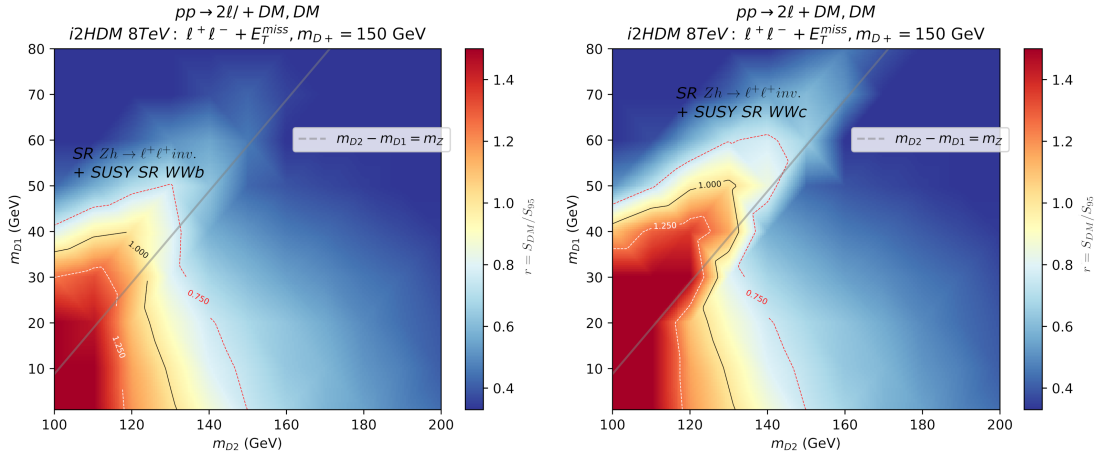

(A) (B)

FIGURE E.2: r-value exclusion plots as a function of m_{D_2} in i2HDM for 8 TeV, $m_{D+} = 150$ GeV, signal regions WWb+Higgs (a) and WWc+Higgs (b).

By increasing m_{D^+} to 150 GeV in Fig. K.2(a), the WWb signal region excludes up to $m_{D1} = 35$ GeV at $m_{D2} = 100$ GeV, to $m_{D1} = 40$ GeV with increasing m_{D2}. In comparison, the WWc signal region excludes masses from $m_{D1} = 40$ GeV at $m_{D2} = 100$ GeV, to $m_{D1} = 50$ GeV as m_{D2} is increased.

Constraints increase with larger m_{D+} in both WWb and WWc signal regions, due to increased contributions from D^+D^- production and from D_2D^+ production.

For larger m_{D2}, the signal events coming from D_2D_1 production is smaller as the Z decay from D_2 is replaced in favour of W decay to D^+ and its decay to an additional W^+ and D_1, which produces much softer leptons than required by the signal region cuts.

As m_{D2} is increased, m_{D1} is further constrained when considering the phase space above $m_{D2} - m_{D1} = m_Z$, due to harder lepton production Z decaying from D_2. Beyond this line, for a large enough $m_{D2} - m_{D1}$ mass splitting, the Z-veto required by the SUSY analysis is no longer fulfilled by the signal, as real Z decay emerges in the production. Instead, the Z-window required by the Higgs analysis accepts these events, and becomes the dominant signal region as the mass splitting is further increased, independent of m_{D+}.

From Fig. K.1(a) and K.2(a) the WWb+Higgs analyses agree with the general shape in [264] Fig. 1, for both $m_D+ = 85$ GeV and 150 GeV, but with lower r-value overall. However, results with larger r-value are obtained when considering WWc+Higgs signal regions in Fig. K.1(b) and K.2(b). While [264] considered both WWb and the $HZ \rightarrow$invisible, they did not consider the WWc signal region. This is because, although the WWc signal region gives a larger observed r value than WWb, the expected r value is lower than WWb (deeming it the better channel by analysis tools). It is worth noting that the MadAnalysis validation for this signal region is overestimated compared to the experimental paper by a small amount, while the CheckMATE analysis implemented is closer to the experimental findings for survived number of MC events. Contour exclusion limits for WWc, where a higher m_T2 cut on the leptons is implemented, shows higher observed r-value than the original paper's WWb contour exclusion limits.

Appendix F

i2HDM 13 TeV, 2- or 3-lepton Final states

In appendix L the analysis in [264] is then extended to higher centre of mass energies, using all available ATLAS and CMS 13 TeV analyses in CheckMATE. There is no equivalent to the Higgs $ZH \to \ell^+\ell^-$+ invisible recasted code as of writing, which is why the r-value beyond the $m_{D2} - m_{D1} = m_Z$ line is negligible.

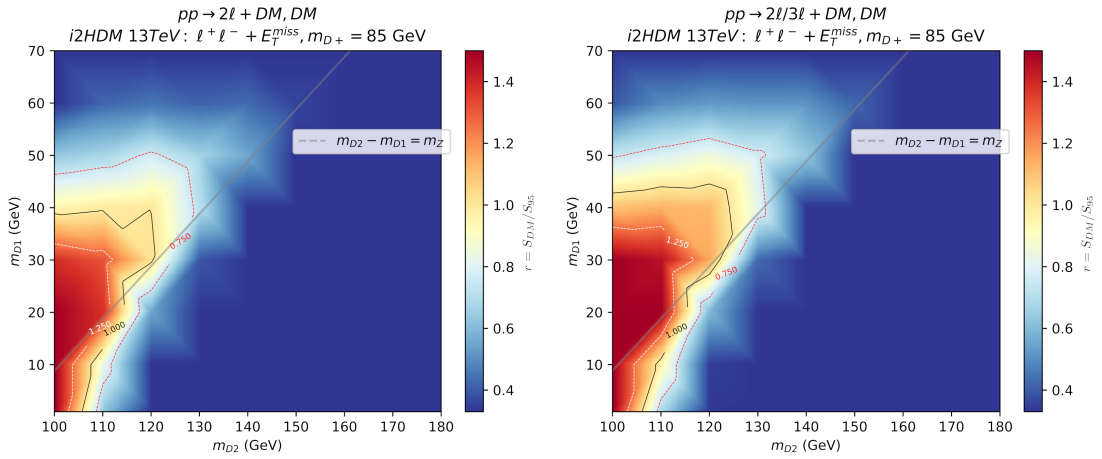

(A) (B)

FIGURE F.1: r-value exclusion plots in i2HDM for 13 TeV, $m_{D+} = 85$ GeV, using signal regions with the highest r-values for two leptons (a) and 2- or 3-lepton (b) final states.

Extended to 13 TeV, Fig. L.1 shows that this does not necessarily improve results, due to scaling of vector boson backgrounds in this phase space. Also shown between Fig. L.1(a) and (b) is the improvement to r-value due to the inclusion of 3-lepton final states. This introduces 6 additional contributing diagrams where D_2,D^+ production plays an important role. D_2 provides two leptons via $D_2 \to Z(\ell^+\ell^-), D_1$ and D^+ gives one extra lepton via $D^+ \to W^+(\ell^+\nu), D_1$ which contributes in heavier D_1 (and thus softer leptons) phase spaces than 2-lepton exclusive searches.

If D^+ is heavy enough, it can decay via D_2, but this only occurs in Fig L.2. The m_{D1} extends from 40 GeV to 45 GeV limit, while m_{D2} can extend from 120 GeV to 125 GeV.

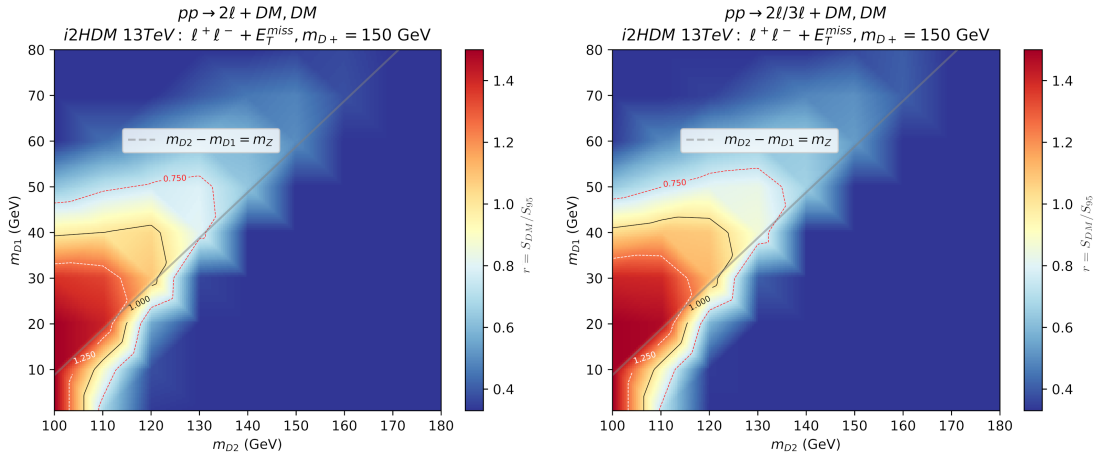

(A) (B)

FIGURE F.2: r-value exclusion plots in i2HDM for 13 TeV, $m_{D+} = 150$ GeV, using signal regions with the highest r-values for two leptons (a) and 2- or 3-lepton (b) final states.

Shown in Fig. L.2 is the improvement from increasing lepton multiplicity for the larger m_{D+} value. Although less apparent than in Fig. L.1, there are extensions to exclusion limits from under $m_{D1} = 40$ GeV to above the 40 GeV line and similarly small extensions to the m_{D2} limit.

The diagrams with three leptons in the final state can now contribute to the relevant phase space, but as this chain of decays contains more steps than other contributions, the soft leptons it produces mostly do not pass the cuts here. Contrary to the 8 TeV case, there is not much increase in limits when moving to heavier D_2. In fact, for 2- and 3-lepton searches, Fig. L.1(b) has limits of $m_{D1} = 44 - 45$ GeV for $m_{D2} = 100$ GeV, while for $m_{D+} = 150$ GeV figure L.2(b) only has limits reaching $m_{D1} = 40 - 41$ GeV due to more processes that do not necessarily fulfil the signal criteria.

In principle one would combine 13 TeV result with the 8 TeV exclusion limits for a comprehensive picture of LHC limits. Although 8 TeV limits are stronger than 13 TeV limits for the phase space in [264] and in this appendix, 8 TeV results do not improve within the phase pace of our 13 TeV results in new parametrisation, shown in section 7.

Appendix G

MFDM 8 TeV

In appendix M 8 TeV r-value contour plots for MFDM are next discussed, starting with the same 8 TeV analyses that were used in the i2HDM case.

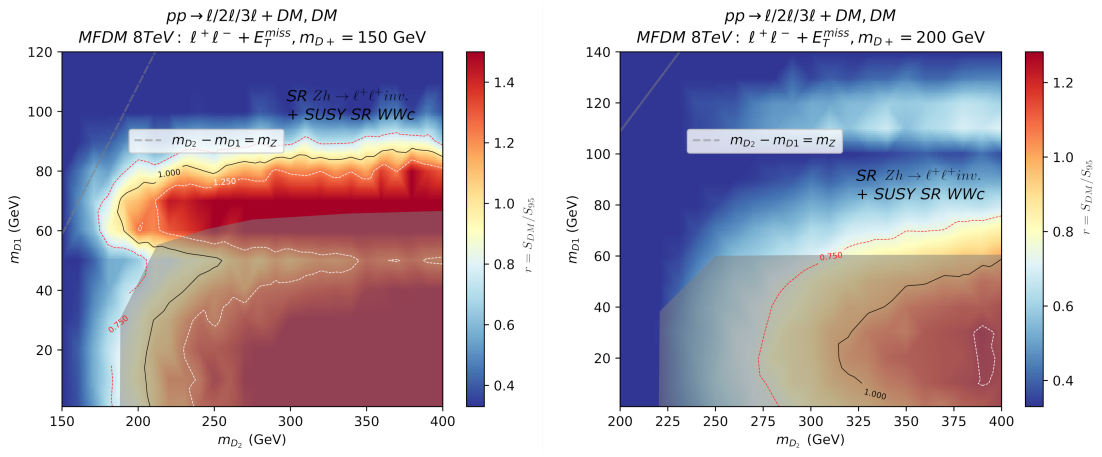

(A) (B)

FIGURE G.1: The r-value exclusion plots in MFDM for 8 TeV, $m_{D+} = 150$ GeV (a) and $m_{D+} = 200$ GeV (b), from the signal regions WWc+Higgs.

Plots in Fig. M.1 show fixed m_{D+} results, with scans in the m_{D_1}-m_{D_2} plane. The shaded region shows the Higgs to invisible excluded region, covering a large phase space of the CheckMATE excluded region. In figure M.1(a), where $m_{D^+} = 150$ GeV, the region above $m_{D_1} = 60$ GeV has limits reaching to $m_{D_1} < 85$ GeV excluded while $m_{D_2} > 180$ excluded. As m_{D_2} increases, this increases the split between D_2 and D^+/D', increasing the Yukawa coupling in Eq. (2.64). This facilitates more decays that would lead to leptonic final states, thus r-value is increased in the positive x-axis direction. In the y-axis, as DM mass is increased, the exclusion changes from `atlas_higgs_2013_03` analysis at low DM mass, to the `atlas_1403_5294` analysis at higher DM mass. Looking at Tables K.1, K.3, this is due to the Z-window changing to a Z-veto with

softer leptons being produced in association with harder DM for the same input energy.

Fig. M.1(b) shows $m_{D^+} = 200$ GeV, where no exclusion outside of the Higgs to invisible limit of $m_{D_1} < 60$ GeV excluded for $m_{D_2} > 220$ GeV. This is because m_{D^+} and $m_{D'}$ become too heavy to produce at these masses, so the sources of leptonic final states are suppressed.

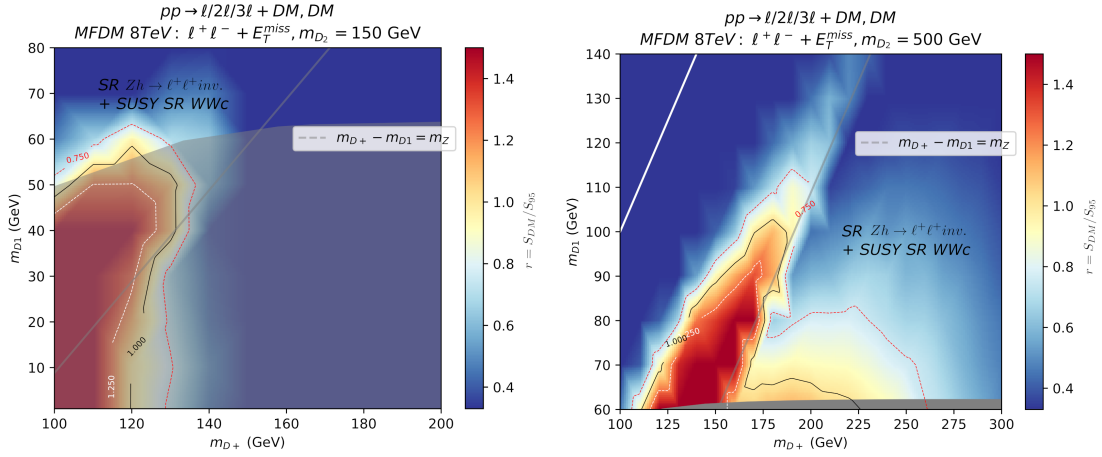

(A) (B)

FIGURE G.2: r-value exclusion plots in MFDM for 8 TeV, $m_{D_2} = 150$ GeV (a), $m_{D_2} = 500$ GeV (b) from signal regions WWc+Higgs.

The plots in Fig. M.2 for MFDM at 8 TeV with fixed m_{D_2}, showing the m_{D_1}-m_{D^+} plane, are more analogous to those displayed for the i2HDM results shown previously. Figure M.2(a) with $m_{D_2} = 150$ GeV is mostly excluded by Higgs to invisible limits, of $m_{D_1} < 60$ GeV excluded.

On the other hand, Fig. M.2(b) limits, for $m_{D_2} = 500$ GeV, extend much further. It excludes a peak at $m_{D_1} = 100$ GeV, $m_{D^+} = 180$ GeV, and follows along M_Z in terms of the mas split between m_{D^+} and m_{D_1}. This is when D' can decay via real Z boson to two leptons, and D_1 in the final state. It is also close to when this mass split equals M_W, facilitating two $D^\pm$ decays via real $W^\pm$ to a charged lepton and neutrino, along with D_1 in the final state.

In Fig. M.2(b) there is an additional region of large r-value at 160 GeV $< m_{D^+} <$ 225 GeV, with a limit of $m_{D_1} = 65$ GeV excluded, coming from the `atlas_higgs_2013_03` analysis with harder leptonic decays, and lighter D_1.

Appendix H

Numerical Overlaid Plots

In appendix N we present the exclusion plots overlaid with cross sections in fb for 2 or 3-leptonic final states. We first present the results for i2HDM in Fig.N.1 and MFDM in Fig.N.2.

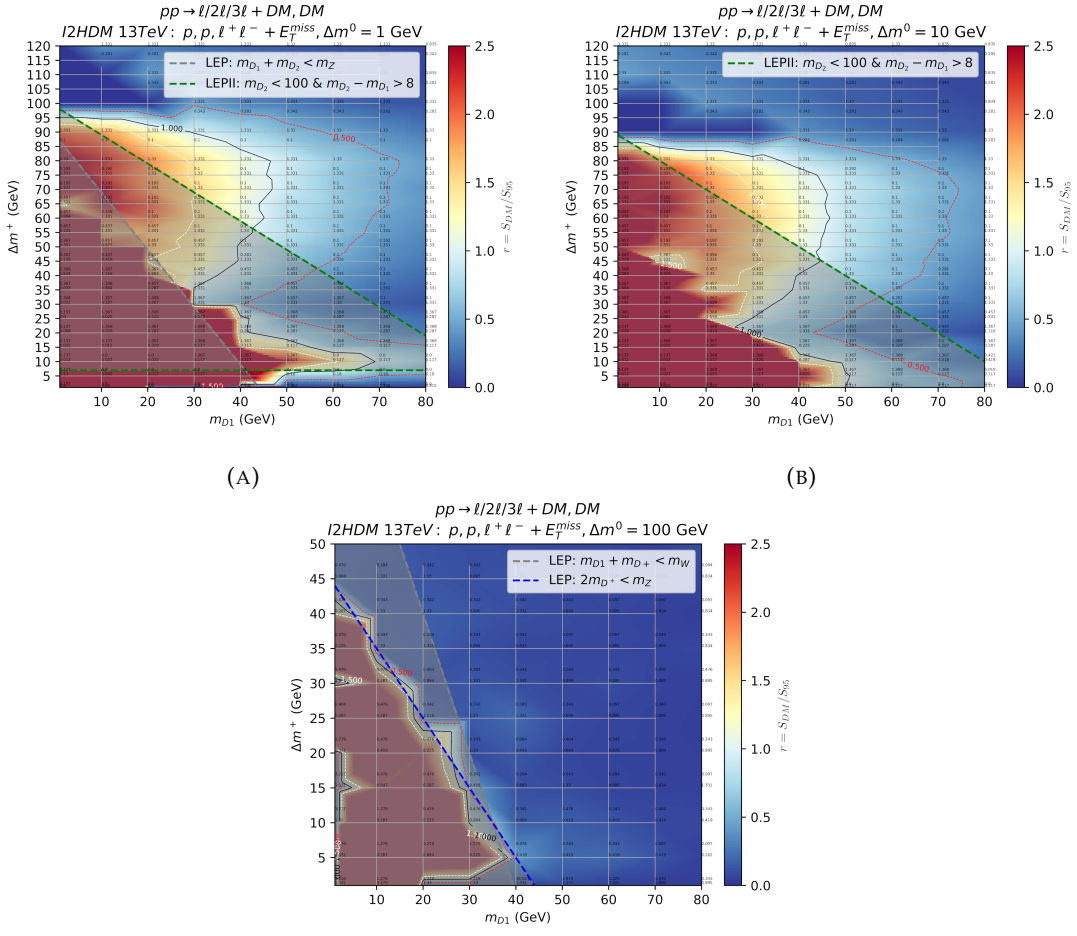

(A) (B)

(C)

FIGURE H.1: i2HDM 13 TeV r-value exclusion plots, overlaid with total cross-section yields from 2-lepton(top number) and 3-lepton (bottom number) contributions to r-value. This is with the parametrisation in terms of Δm^+ Δm^0. Plot (a) shows the case where $\Delta m^0 = 1$ GeV, while plot (b) shows $\Delta m^0 = 10$ GeV and plot (c) shows $\Delta m^0 = 100$ GeV. These are overlaid with limits from LEP I, LEP II experiments [278, 279].

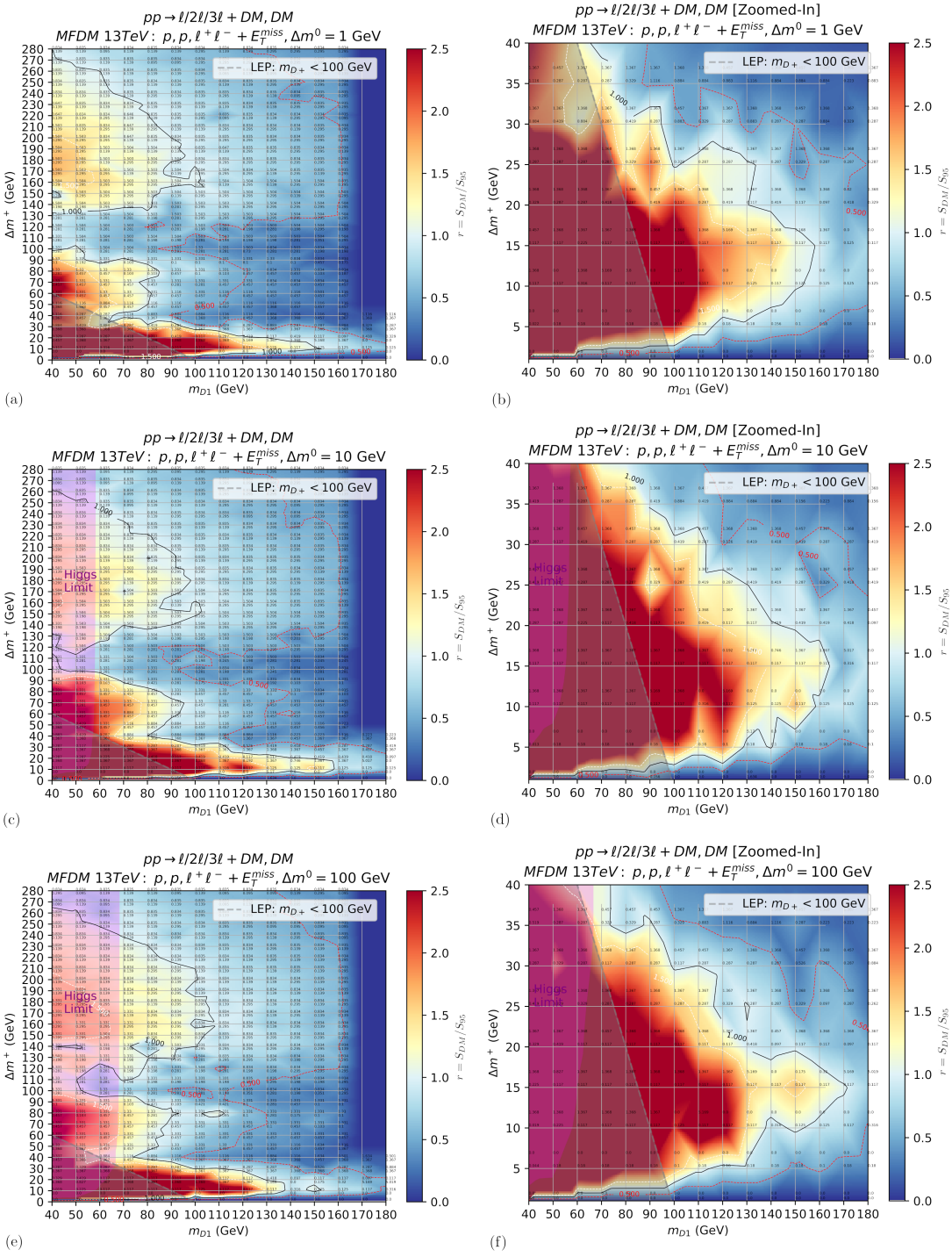

FIGURE H.2: MFDM 13 TeV r-value exclusion plots overlaid with cross-section yields from 2-lepton(top number) and 3-lepton (bottom number) contributions, for parameter space Δm^+-m_{D1} for $\Delta m^0 = 1$(a)-(b), 10(c)-(d), 100(e)-(f) GeV. The magenta region and grey region indicate the current Higgs-to-invisible limit [280] of 0.15 branching fraction and LEP bounds on charginos for the fermionic DM case [279] respectively.

Appendix I

Sample Exclusion Formulae

In appendix O we describe the samples and formulae used to understand the tables presented [44]. The input samples are separated between A,B and C, in both i2HDM and MFDM cases to improve efficiency.

For i2HDM, set A produces 50,000 events of D^+D^- and D_1D_2 pairs, while specifying the decays $D^\pm \to \ell^\pm, \nu, D_1$ (via W)and $D_2 \to \ell^+, \ell^-, D_1$ (via Z). Set B produces 150,000 events of $D^\pm D_2$, while specifying $D_2 \to \ell^+, \ell^-, D_1$ (via Z) to obtain at least two leptons. Set C produces 100,000 events of the D_1D_1Z production, while specifying leptonic Z decay.

For MFDM, set A produces 50,000 total events, of D^+D^- and D_1D' pairs, while specifying decays of $D^\pm \to \ell^\pm, \nu, D_1$ (via W) and decays $D' \to \ell^+, \ell^-, D_1$ (via Z). Set B produces 150,000 $D'D_2$ events, without specifying decays. Set C produces 100,000 events of $D^\pm D'$ and $D^\pm D_2$ pairs, while requiring $D' \to \ell^+, \ell^-, D_1$ decays, $D_2 \to \ell^\pm, \nu, D^\pm$ (via W) or $D_2 \to \ell^-, \ell^+, D'$ decays (via Z). This last set means D' or $D^\pm$ coming from D_2 can also decay hadronically, to fulfil more 2-lepton and 3-lepton thresholds of the analyses.

The exclusion limits between input samples, for the same signal region of a given analysis, can be related by the equation

$$\sigma_A^{95}\epsilon_A = \sigma_B^{95}\epsilon_B = \sigma_C^{95}\epsilon_C \tag{I.1}$$

allowing for exclusion r values to be calculated, also noting that

$$r = r_A + r_B + r_C = \frac{\sigma_A^{DM}}{\sigma_A^{95}} + \frac{\sigma_B^{DM}}{\sigma_B^{95}} + \frac{\sigma_C^{DM}}{\sigma_C^{95}}. \tag{I.2}$$

Appendix J

Example Analyses and Cutflows

In appendix P we present examples of the 13 TeV analyses used for the presented exclusion limits and their cutflows as implemented in CheckMATE.

Analysis: cms_sus_16_048, Signal Region: SR1_weakino_1low_mll_1

	Cuts
$mT(\ell[0]/\ell[1],\ E_T^{miss})$	< 70 GeV
$mT(p_{\ell[0]},\ E_T^{miss}$	< 70 GeV
$mT(p_{\ell[1]},\ E_T^{miss})$	< 70 GeV
E_T^{miss}	< 200 GeV
$M_{\ell\ell}$	< 10 GeV

TABLE J.1: Cutflow for cms_sus_16_048, SR1_weakino_1low_mll_1

Analysis: `cms_sus_16039`**, Signal Region:** `SR_A02`

Two out of the three leptons (e or μ) will form an OSSF pair. This is signal region "A" One of the $m_{\ell\ell}$ bins is defined to be below the Z mass ($M_l l < 75$ GeV).

	Cuts
MT	$0 < MT < 100$ GeV
p_T^{miss}	$200 < p_T^{miss} < 250$ GeV
$M_{\ell\ell}$	< 75 GeV

TABLE J.2: Cutflow for `cms_sus_16039`, `SR_A02`

Analysis: cms_sus_16_025, Signal Region: SR2_stop_1low_pt_1

The second category corresponds to the two leptons stemming from two different particles, as in the decays of two top squarks, or in two cascades like $\chi^{\pm}$ to W, χ_1. In these cases, the leptons are not required to have the same flavour.

Analysis: atlas_conf_2016_096, Signal Region: 2LASF

	Cuts
E_T^{miss}	< 200GeV
$p_T(\ell[0])$	< 12 GeV

TABLE J.3: Cutflow for `cms_sus_16_025`, `SR2_stop_1low_pt_1`

	Cuts
$\|mll - mZ\|$	> 10 GeV
$mT2$	> 90 GeV

TABLE J.4: Cutflow for `atlas_conf_2016_096`, `2LASF`

This analysis searches for D^+, D^- with two lepton final states.

Analysis: atlas_conf_2016_096, Signal Region: 3LI

This signal region consists of three leptons, targeting the intermediate mass splitting between D2, D1 of order $2 \times m_Z$.

	Cuts
mT	> 110 GeV
$M(SFOS), E$	$[81.2, 101.2]$ GeV
$pT(3rd\ lep)$	> 30 GeV
E_T^{miss}	> 120 GeV

TABLE J.5: Cutflow for `atlas_conf_2016_096`, `3LI`

Analysis: cms_sus_16_039, Signal Region: SR_A03

This analysis looks for electrowekinos in multilepton final states. This particular signal region requires three e/μ forming at least one opposite-sign same-flavour pair.

	Cuts
MT	$0 < MT < 100$ GeV
p_T^{miss}	$150 < p_T^{miss} < 200$
$M_{\ell\ell}$	< 75 GeV

TABLE J.6: Cutflow for `cms_sus_16_039`, `SR_A03`

Appendix K

8 TeV Validation: i2HDM

Appendix K details the validation of our CheckMATE recast for 8 TeV LHC exclusion limits for 2-lepton final states by comparing with the existing MadAnalysis implementation [311]. The CheckMATE analysis code was written based on and validated with the original experimental results, which searched for direct production of charginos, neutralinos and sleptons in final states with two leptons and missing transverse momentum [312] at the LHC. This was implemented using the CheckMATE's AnalysisManager in the current public build, and the SUSY analysis is available at [268]. The cutflows are given in tables K.1 and K.2.

Global Cut	
E_T^{miss}	> 0 GeV
Base leptons	2
e^+e^- trigger	97%
$\mu^+\mu^-$ trigger	89%
$e\mu$ trigger	75%
Signal leptons	2
Leading lepton p_T	> 35 GeV
sub-leading lepton p_T	> 20 GeV
$M_{\ell\ell}$	> 20 GeV
jets	0
$\lvert M_{\ell\ell} - M_Z \rvert$	> 10 GeV

TABLE K.1: Cutflow for all events in the 8 TeV ATLAS SUSY analysis for 2-lepton+E_T^{miss} finals states, implemented in CheckMATE.

SR	m_{T2}^{90}	m_{T2}^{120}	m_{T2}^{150}	WWa	WWb	WWc	Zjets
$M_{\ell\ell}$				< 120	< 170		
$p_T(\ell\ell)$				> 80			> 80
$E_T^{miss,rel}$				> 80			> 80
m_{T2}	> 90	> 120	> 150		> 90	> 100	

TABLE K.2: Cutflows used for the specific signal regions in the 8 TeV ATLAS SUSY analysis for 2-lepton+E_T^{miss} finals states, implemented in CheckMATE.

The 8 TeV ATLAS analysis searching for invisible decays of a Higgs boson produced in association with Z [312], previously recasted for MadAnalysis [313] was also written for the CheckMATE analysis performed here, as it also looks for final states with two leptons and missing energy. The public code of the Higgs analysis is available at [269]. The cutflow is given in table K.3.

Global Cut	
Base leptons	2
Lepton p_T	> 20 GeV
Z-window	$76 < M_{\ell\ell} < 106$ GeV
E_T^{miss}	> 90 GeV
$d\phi(E_T^{miss}, p_T^{miss})$	< 0.2
$\Delta\phi(p_T(\ell\ell), E_T^{miss})$	> 2.6
$\Delta\phi(\ell, \ell)$	< 1.7
$\lvert\frac{E_T^{miss} - p_T(\ell\ell)}{p_T(\ell\ell)}\rvert$	> 0.2
jets	0

TABLE K.3: Cutflow for all events in the 8 TeV ATLAS Higgs analysis for 2-lepton+E_T^{miss} finals states, implemented in CheckMATE.

The events used for the validations were generated with CalcHEP, with 100000 events produced for each 9 benchmark points, using the SLHA files provided from HepData [314] and 1 benchmark point for $HZ \to$ invisible, with $M_H = 125.5$ GeV. Leptonic decays of Z in the HZ production, $\chi^{\pm}\chi 2$ production and W in the $\chi^+\chi^-$, were also specified in CalcHEP to improve efficiency, which were then showered with CheckMATE's built-in PYTHIA8 module. Detector effects are also applied via CheckMATE with a DELPHES module. Validation for the SUSY analysis is available at [315] and Higgs analysis available at [316].

The motivation behind fixing m_{D+} is because it is mostly only important for D^+D^- production, which give an additional EW coupling factor compared to D_2D_1 production, only providing significant contributions to r-value at very light m_{D+}. The ZD_1D_1 production is also less dominant as the ZZD_1D_1 coupling is quadratic and therefore weak compared to other couplings. The lowest allowed LEP limit of $m_{D+} = 85$ GeV is used and the higher value of $m_{D+} = 150$ GeV for comparison.

The r-value contour plots for $m_{D+} = 85$ GeV in Fig. K.1(a) for the WWb signal region shows that the Run 1 ATLAS 2-lepton analysis excludes for the lightest DM mass of $m_{D1} \leq 35$ GeV for $m_{D2} = 100$ GeV, reaching a maximum of ~ 40 GeV as m_{D2} is increased. In the case of Fig. K.1(b), the WWc signal region reports stronger limits, excluding the lightest DM mass of $m_{D1} \leq 40$ GeV for $m_{D2} = 100$ GeV, reaching a maximum of ~ 45 GeV as m_{D2} is increased. For $m_{D1} \to 0$ GeV, both cases exclude up to a mass of $m_{D2} = 130$ GeV.

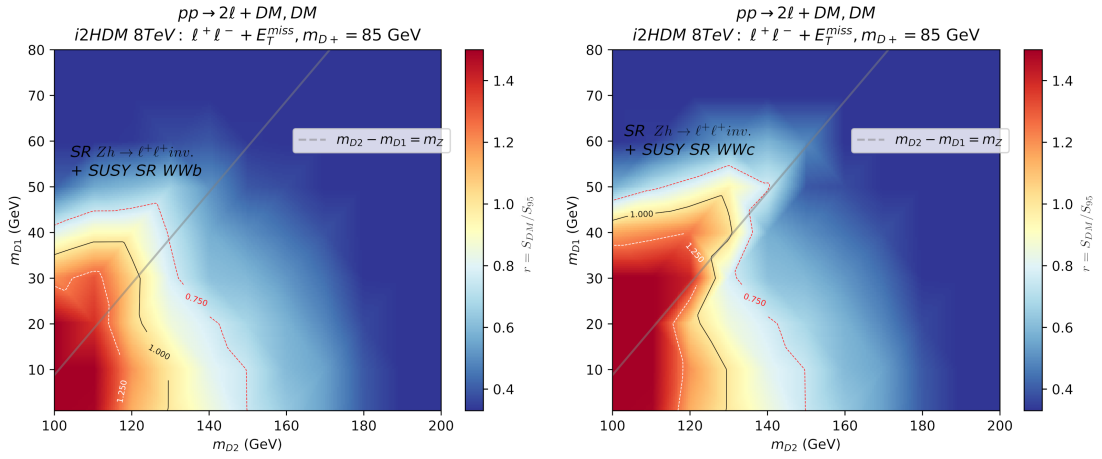

(A) (B)

FIGURE K.1: r-value Exclusion plots as a function of m_{D_2} in i2HDM at 8 TeV, $m_{D+} = 85$ GeV, signal regions WWb+Higgs (a) and WWc+Higgs (b).

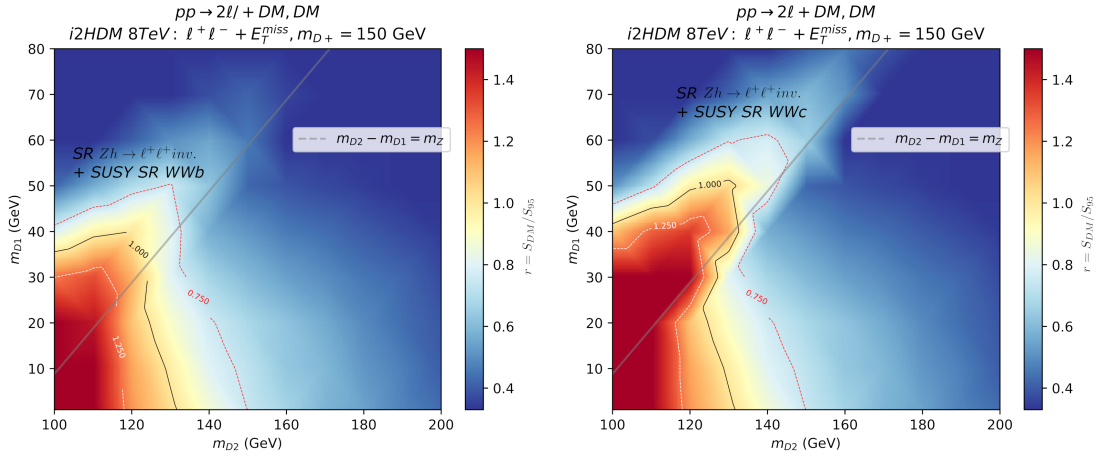

(A) (B)

FIGURE K.2: r-value exclusion plots as a function of m_{D_2} in i2HDM for 8 TeV, $m_{D+} = 150$ GeV, signal regions WWb+Higgs (a) and WWc+Higgs (b).

By increasing m_{D^+} to 150 GeV in Fig. K.2(a), the WWb signal region excludes up to $m_{D1} = 35$ GeV at $m_{D2} = 100$ GeV, to $m_{D1} = 40$ GeV with increasing m_{D2}. In comparison, the WWc signal region excludes masses from $m_{D1} = 40$ GeV at $m_{D2} = 100$ GeV, to $m_{D1} = 50$ GeV as m_{D2} is increased.

Constraints increase with larger m_{D+} in both WWb and WWc signal regions, due to increased contributions from D^+D^- production and from D_2D^+ production.

For larger m_{D2}, the signal events coming from D_2D_1 production is smaller as the Z decay from D_2 is replaced in favour of W decay to D^+ and its decay to an additional W^+ and D_1, which produces much softer leptons than required by the signal region cuts.

As m_{D2} is increased, m_{D1} is further constrained when considering the phase space above $m_{D2} - m_{D1} = m_Z$, due to harder lepton production Z decaying from D_2. Beyond this line, for a large enough $m_{D2} - m_{D1}$ mass splitting, the Z-veto required by the SUSY analysis is no longer fulfilled by the signal, as real Z decay emerges in the production. Instead, the Z-window required by the Higgs analysis accepts these events, and becomes the dominant signal region as the mass splitting is further increased, independent of m_{D+}.

From Fig. K.1(a) and K.2(a) the WWb+Higgs analyses agree with the general shape in [264] Fig. 1, for both $m_D+ = 85$ GeV and 150 GeV, but with lower r-value overall. However, results with larger r-value are obtained when considering WWc+Higgs signal regions in Fig. K.1(b) and K.2(b). While [264] considered both WWb and the $HZ \rightarrow$invisible, they did not consider the WWc signal region. This is because, although the WWc signal region gives a larger observed r value than WWb, the expected r value is lower than WWb (deeming it the better channel by analysis tools). It is worth noting that the MadAnalysis validation for this signal region is overestimated compared to the experimental paper by a small amount, while the CheckMATE analysis implemented is closer to the experimental findings for survived number of MC events. Contour exclusion limits for WWc, where a higher m_T2 cut on the leptons is implemented, shows higher observed r-value than the original paper's WWb contour exclusion limits.

Appendix L

i2HDM 13 TeV, 2- or 3-lepton Final states

In appendix L the analysis in [264] is then extended to higher centre of mass energies, using all available ATLAS and CMS 13 TeV analyses in CheckMATE. There is no equivalent to the Higgs $ZH \to \ell^+\ell^-$+ invisible recasted code as of writing, which is why the r-value beyond the $m_{D2} - m_{D1} = m_Z$ line is negligible.

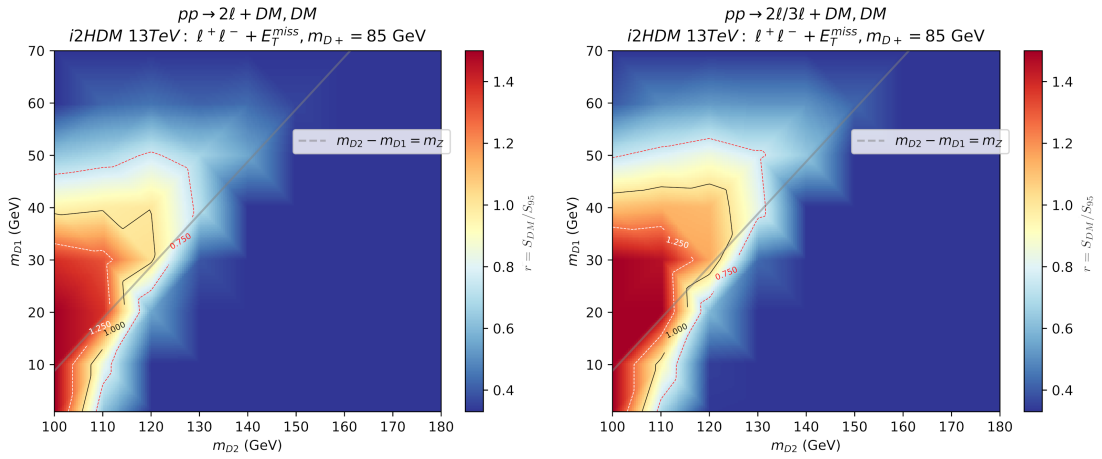

(A) (B)

FIGURE L.1: r-value exclusion plots in i2HDM for 13 TeV, $m_{D+} = 85$ GeV, using signal regions with the highest r-values for two leptons (a) and 2- or 3-lepton (b) final states.

Extended to 13 TeV, Fig. L.1 shows that this does not necessarily improve results, due to scaling of vector boson backgrounds in this phase space. Also shown between Fig. L.1(a) and (b) is the improvement to r-value due to the inclusion of 3-lepton final states. This introduces 6 additional contributing diagrams where D_2,D^+ production plays an important role. D_2 provides two leptons via $D_2 \to Z(\ell^+\ell^-), D_1$ and D^+ gives one extra lepton via $D^+ \to W^+(\ell^+\nu), D_1$ which contributes in heavier D_1 (and thus softer leptons) phase spaces than 2-lepton exclusive searches.

If D^+ is heavy enough, it can decay via D_2, but this only occurs in Fig L.2. The m_{D1} extends from 40 GeV to 45 GeV limit, while m_{D2} can extend from 120 GeV to 125 GeV.

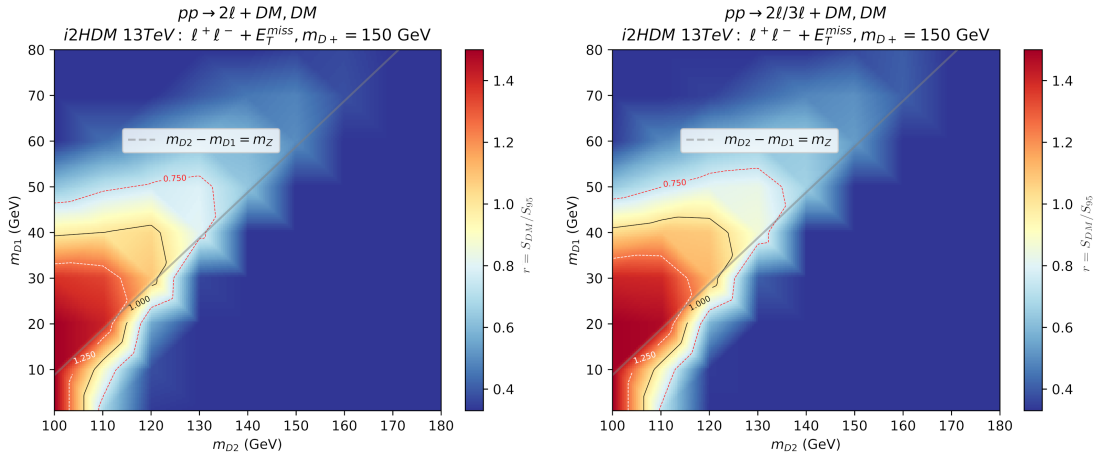

(A) (B)

FIGURE L.2: r-value exclusion plots in i2HDM for 13 TeV, $m_{D+} = 150$ GeV, using signal regions with the highest r-values for two leptons (a) and 2- or 3-lepton (b) final states.

Shown in Fig. L.2 is the improvement from increasing lepton multiplicity for the larger m_{D+} value. Although less apparent than in Fig. L.1, there are extensions to exclusion limits from under $m_{D1} = 40$ GeV to above the 40 GeV line and similarly small extensions to the m_{D2} limit.

The diagrams with three leptons in the final state can now contribute to the relevant phase space, but as this chain of decays contains more steps than other contributions, the soft leptons it produces mostly do not pass the cuts here. Contrary to the 8 TeV case, there is not much increase in limits when moving to heavier D_2. In fact, for 2- and 3-lepton searches, Fig. L.1(b) has limits of $m_{D1} = 44 - 45$ GeV for $m_{D2} = 100$ GeV, while for $m_{D+} = 150$ GeV figure L.2(b) only has limits reaching $m_{D1} = 40 - 41$ GeV due to more processes that do not necessarily fulfil the signal criteria.

In principle one would combine 13 TeV result with the 8 TeV exclusion limits for a comprehensive picture of LHC limits. Although 8 TeV limits are stronger than 13 TeV limits for the phase space in [264] and in this appendix, 8 TeV results do not improve within the phase pace of our 13 TeV results in new parametrisation, shown in section 7.

Appendix M

MFDM 8 TeV

In appendix M 8 TeV r-value contour plots for MFDM are next discussed, starting with the same 8 TeV analyses that were used in the i2HDM case.

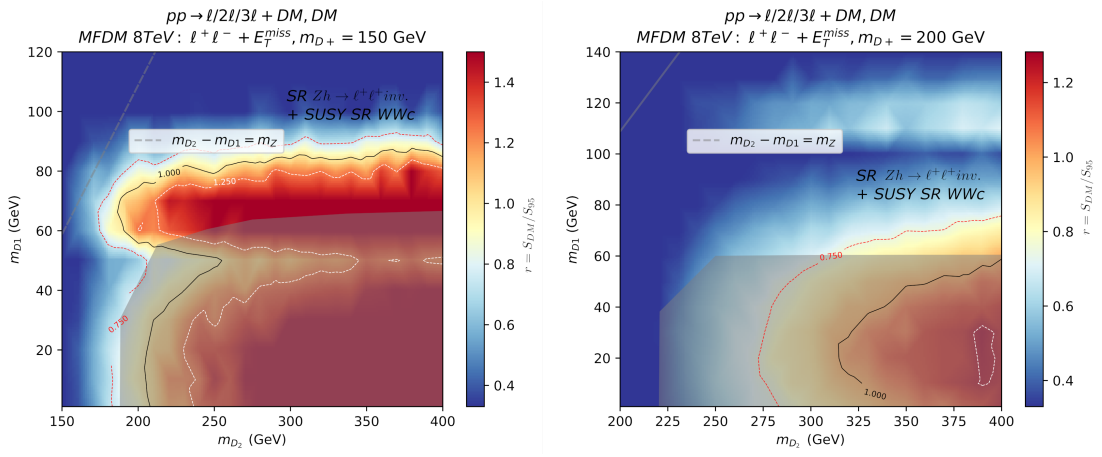

(A) (B)

FIGURE M.1: The r-value exclusion plots in MFDM for 8 TeV, $m_{D+} = 150$ GeV (a) and $m_{D+} = 200$ GeV (b), from the signal regions WWc+Higgs.

Plots in Fig. M.1 show fixed m_{D+} results, with scans in the m_{D_1}-m_{D_2} plane. The shaded region shows the Higgs to invisible excluded region, covering a large phase space of the CheckMATE excluded region. In figure M.1(a), where $m_{D^+} = 150$ GeV, the region above $m_{D_1} = 60$ GeV has limits reaching to $m_{D_1} < 85$ GeV excluded while $m_{D_2} > 180$ excluded. As m_{D_2} increases, this increases the split between D_2 and D^+/D', increasing the Yukawa coupling in Eq. (2.64). This facilitates more decays that would lead to leptonic final states, thus r-value is increased in the positive x-axis direction. In the y-axis, as DM mass is increased, the exclusion changes from `atlas_higgs_2013_03` analysis at low DM mass, to the `atlas_1403_5294` analysis at higher DM mass. Looking at Tables K.1, K.3, this is due to the Z-window changing to a Z-veto with

softer leptons being produced in association with harder DM for the same input energy.

Fig. M.1(b) shows $m_{D^+} = 200$ GeV, where no exclusion outside of the Higgs to invisible limit of $m_{D_1} < 60$ GeV excluded for $m_{D_2} > 220$ GeV. This is because m_{D^+} and $m_{D'}$ become too heavy to produce at these masses, so the sources of leptonic final states are suppressed.

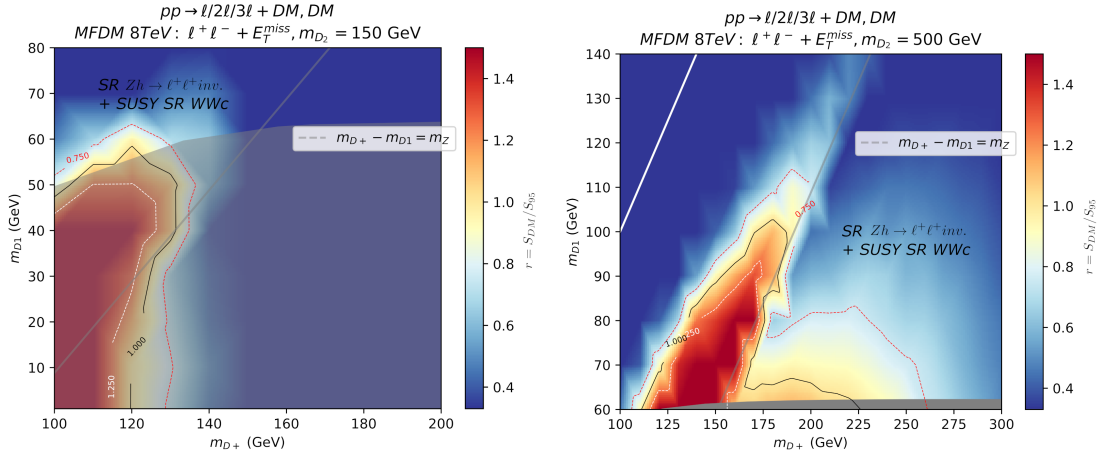

(A) (B)

FIGURE M.2: r-value exclusion plots in MFDM for 8 TeV, $m_{D_2} = 150$ GeV (a), $m_{D_2} = 500$ GeV (b) from signal regions WWc+Higgs.

The plots in Fig. M.2 for MFDM at 8 TeV with fixed m_{D_2}, showing the m_{D_1}-m_{D^+} plane, are more analogous to those displayed for the i2HDM results shown previously. Figure M.2(a) with $m_{D_2} = 150$ GeV is mostly excluded by Higgs to invisible limits, of $m_{D_1} < 60$ GeV excluded.

On the other hand, Fig. M.2(b) limits, for $m_{D_2} = 500$ GeV, extend much further. It excludes a peak at $m_{D_1} = 100$ GeV, $m_{D^+} = 180$ GeV, and follows along M_Z in terms of the mas split between m_{D^+} and m_{D_1}. This is when D' can decay via real Z boson to two leptons, and D_1 in the final state. It is also close to when this mass split equals M_W, facilitating two $D^\pm$ decays via real $W^\pm$ to a charged lepton and neutrino, along with D_1 in the final state.

In Fig. M.2(b) there is an additional region of large r-value at 160 GeV $< m_{D^+} <$ 225 GeV, with a limit of $m_{D_1} = 65$ GeV excluded, coming from the `atlas_higgs_2013_03` analysis with harder leptonic decays, and lighter D_1.

Appendix N

Numerical Overlaid Plots

In appendix N we present the exclusion plots overlaid with cross sections in fb for 2 or 3-leptonic final states. We first present the results for i2HDM in Fig.N.1 and MFDM in Fig.N.2.

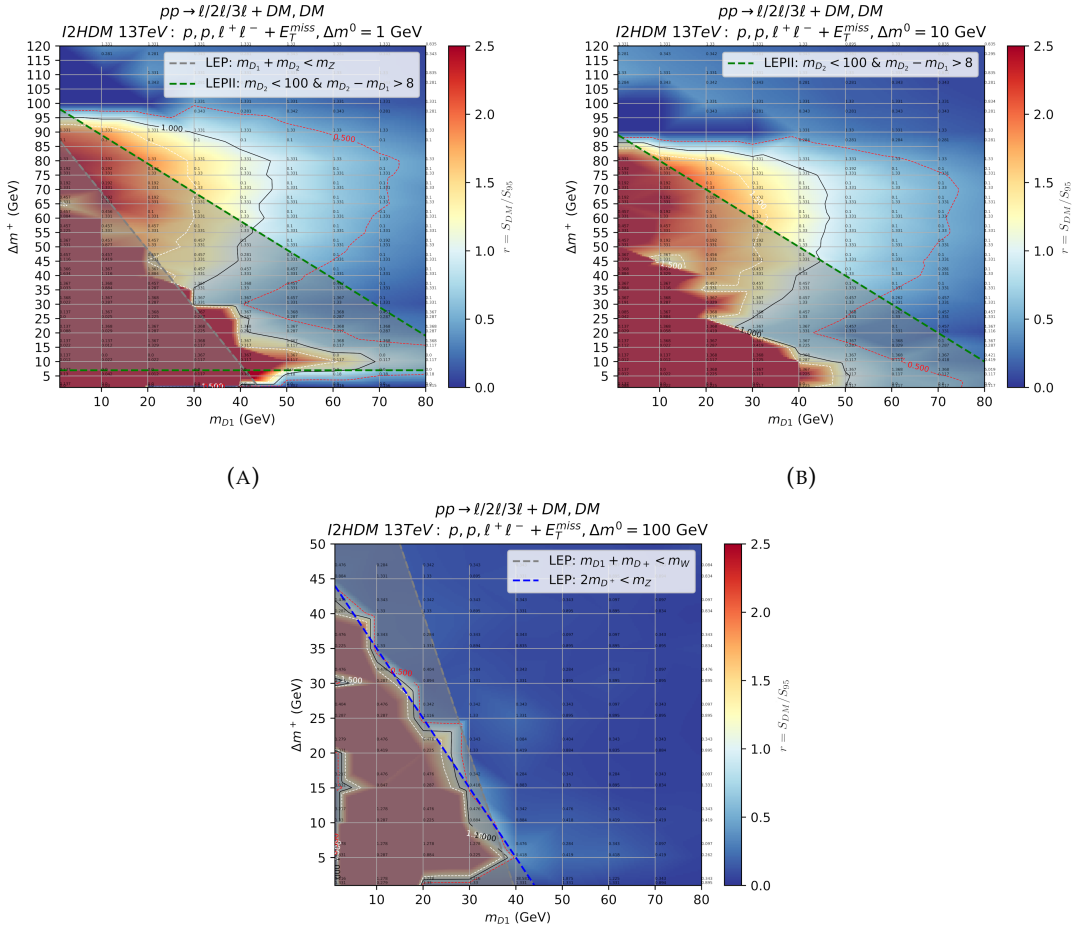

(A) (B)

(C)

FIGURE N.1: i2HDM 13 TeV r-value exclusion plots, overlaid with total cross-section yields from 2-lepton(top number) and 3-lepton (bottom number) contributions to r-value. This is with the parametrisation in terms of Δm^+ Δm^0. Plot (a) shows the case where $\Delta m^0 = 1$ GeV, while plot (b) shows $\Delta m^0 = 10$ GeV and plot (c) shows $\Delta m^0 = 100$ GeV. These are overlaid with limits from LEP I, LEP II experiments [278, 279].

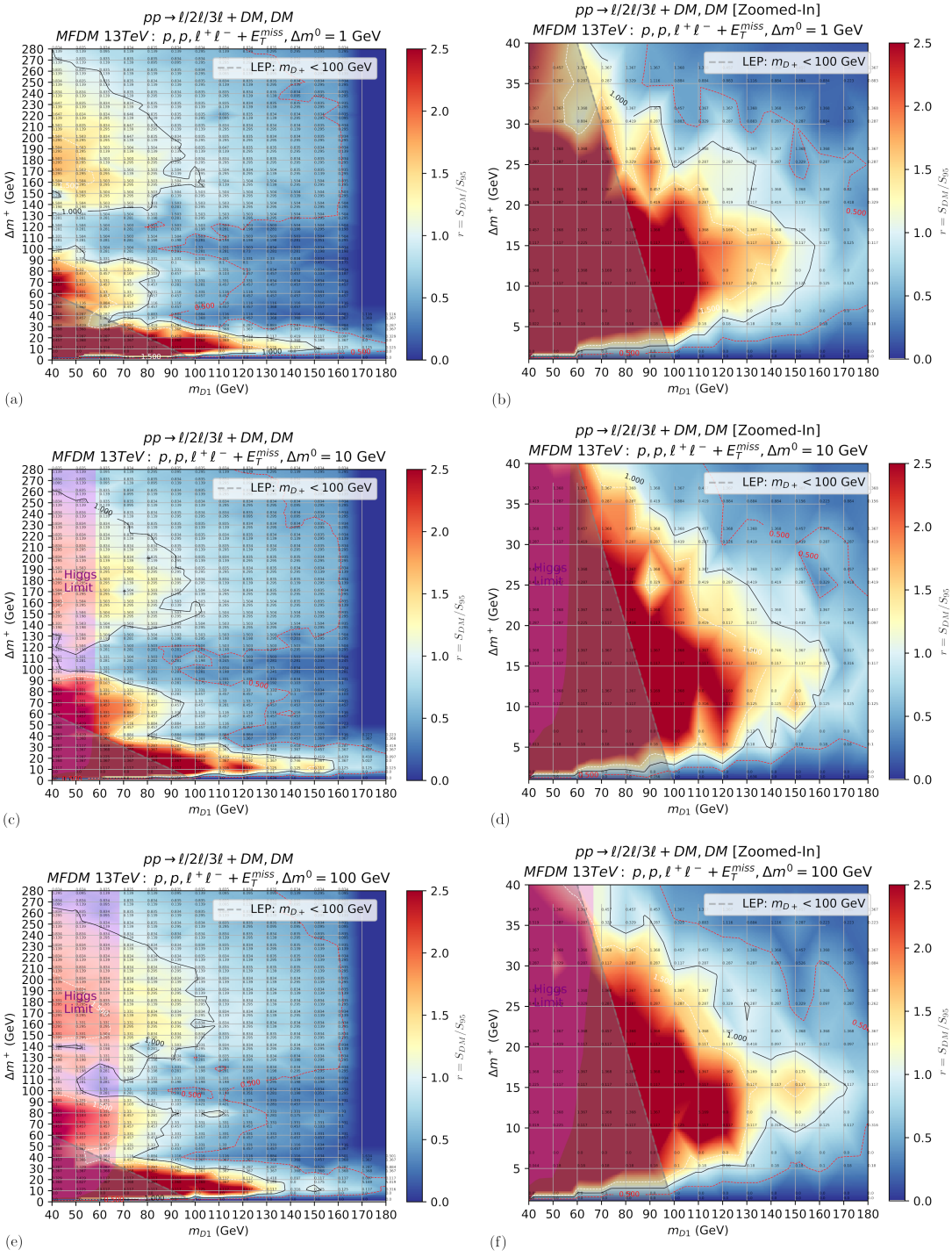

FIGURE N.2: MFDM 13 TeV r-value exclusion plots overlaid with cross-section yields from 2-lepton(top number) and 3-lepton (bottom number) contributions, for parameter space Δm^{+}-m_{D1} for $\Delta m^{0} = 1$(a)-(b), 10(c)-(d), 100(e)-(f) GeV. The magenta region and grey region indicate the current Higgs-to-invisible limit [280] of 0.15 branching fraction and LEP bounds on charginos for the fermionic DM case [279] respectively.

Appendix O

Sample Exclusion Formulae

In appendix O we describe the samples and formulae used to understand the tables presented [44]. The input samples are separated between A,B and C, in both i2HDM and MFDM cases to improve efficiency.

For i2HDM, set A produces 50,000 events of D^+D^- and D_1D_2 pairs, while specifying the decays $D^\pm \to \ell^\pm, \nu, D_1$ (via W)and $D_2 \to \ell^+, \ell^-, D_1$ (via Z). Set B produces 150,000 events of $D^\pm D_2$, while specifying $D_2 \to \ell^+, \ell^-, D_1$ (via Z) to obtain at least two leptons. Set C produces 100,000 events of the D_1D_1Z production, while specifying leptonic Z decay.

For MFDM, set A produces 50,000 total events, of D^+D^- and D_1D' pairs, while specifying decays of $D^\pm \to \ell^\pm, \nu, D_1$ (via W) and decays $D' \to \ell^+, \ell^-, D_1$ (via Z). Set B produces 150,000 $D'D_2$ events, without specifying decays. Set C produces 100,000 events of $D^\pm D'$ and $D^\pm D_2$ pairs, while requiring $D' \to \ell^+, \ell^-, D_1$ decays, $D_2 \to \ell^\pm, \nu, D^\pm$ (via W) or $D_2 \to \ell^-, \ell^+, D'$ decays (via Z). This last set means D' or $D^\pm$ coming from D_2 can also decay hadronically, to fulfil more 2-lepton and 3-lepton thresholds of the analyses.

The exclusion limits between input samples, for the same signal region of a given analysis, can be related by the equation

$$\sigma_A^{95}\epsilon_A = \sigma_B^{95}\epsilon_B = \sigma_C^{95}\epsilon_C \tag{O.1}$$

allowing for exclusion r values to be calculated, also noting that

$$r = r_A + r_B + r_C = \frac{\sigma_A^{DM}}{\sigma_A^{95}} + \frac{\sigma_B^{DM}}{\sigma_B^{95}} + \frac{\sigma_C^{DM}}{\sigma_C^{95}}. \tag{O.2}$$

Appendix P

Example Analyses and Cutflows

In appendix P we present examples of the 13 TeV analyses used for the presented exclusion limits and their cutflows as implemented in CheckMATE.

Analysis: cms_sus_16_048, Signal Region: SR1_weakino_1low_mll_1

	Cuts
$mT(\ell[0]/\ell[1],\ E_T^{miss})$	< 70 GeV
$mT(p_{\ell[0]},\ E_T^{miss}$	< 70 GeV
$mT(p_{\ell[1]},\ E_T^{miss})$	< 70 GeV
E_T^{miss}	< 200 GeV
$M_{\ell\ell}$	< 10 GeV

TABLE P.1: Cutflow for cms_sus_16_048, SR1_weakino_1low_mll_1

Analysis: `cms_sus_16039`**, Signal Region:** `SR_A02`

Two out of the three leptons (e or μ) will form an OSSF pair. This is signal region "A" One of the $m_{\ell\ell}$ bins is defined to be below the Z mass ($M_l l < 75$ GeV).

	Cuts
MT	$0 < MT < 100$ GeV
p_T^{miss}	$200 < p_T^{miss} < 250$ GeV
$M_{\ell\ell}$	< 75 GeV

TABLE P.2: Cutflow for `cms_sus_16039`, `SR_A02`

Analysis: cms_sus_16_025, Signal Region: SR2_stop_1low_pt_1

The second category corresponds to the two leptons stemming from two different particles, as in the decays of two top squarks, or in two cascades like $\chi^{\pm}$ to W, χ_1. In these cases, the leptons are not required to have the same flavour.

Analysis: atlas_conf_2016_096, Signal Region: 2LASF

	Cuts
E_T^{miss}	< 200GeV
$p_T(\ell[0])$	< 12 GeV

TABLE P.3: Cutflow for `cms_sus_16_025`, `SR2_stop_1low_pt_1`

	Cuts
$\|mll - mZ\|$	> 10 GeV
$mT2$	> 90 GeV

TABLE P.4: Cutflow for `atlas_conf_2016_096`, `2LASF`

This analysis searches for D^+, D^- with two lepton final states.

Analysis: atlas_conf_2016_096, Signal Region: 3LI

This signal region consists of three leptons, targeting the intermediate mass splitting between D2, D1 of order $2 \times m_Z$.

	Cuts
mT	> 110 GeV
$M(SFOS), E$	$[81.2, 101.2]$ GeV
$pT(3rd\ lep)$	> 30 GeV
E_T^{miss}	> 120 GeV

TABLE P.5: Cutflow for `atlas_conf_2016_096`, `3LI`

Analysis: cms_sus_16_039, Signal Region: SR_A03

This analysis looks for electrowekinos in multilepton final states. This particular signal region requires three e/μ forming at least one opposite-sign same-flavour pair.

	Cuts
MT	$0 < MT < 100$ GeV
p_T^{miss}	$150 < p_T^{miss} < 200$
$M_{\ell\ell}$	< 75 GeV

TABLE P.6: Cutflow for `cms_sus_16_039`, `SR_A03`

Appendix Q

Evaluation of the S and T parameters for MFDM

To find the contribution of new physics to the oblique parameters one should evaluate quantum corrections to the masses of vector bosons and their mixings, $\Pi_{ZZ}(p^2)$, $\Pi_{Z\gamma}(p^2)$, $\Pi_{\gamma\gamma}(p^2)$, $\Pi_{WW}(p^2)$ (or in unbroken gauge basis, 3,0 labels refer to W^3, B gauge bosons respectively), defined by the effective Lagrangian

$$\mathcal{L}_{\text{oblique}} = \frac{1}{2} Z_\mu \Pi_{ZZ}(p^2) Z^\mu + \frac{1}{2} \gamma_\mu \Pi_{\gamma\gamma}(p^2) \gamma^\mu + Z_\mu \Pi_{Z\gamma}(p^2) \gamma^\mu + W^+_\mu \Pi_{WW}(p^2) W^{-\mu} \ , \tag{Q.1}$$

where vacuum polarisation functions Π's can be expanded in powers of p^2:

$$\Pi(p^2) = \Pi(0) + p^2\, \Pi'(0) + \frac{(p^2)^2}{2}\, \Pi''(0) + \dots \ , \tag{Q.2}$$

since the new physics scale is expected to be high. As for I2HDM, for MFDM we are evaluating here S, T, and U observables [116] among the complete set of seven oblique parameters [317] which are related to Π functions as follows:

$$S \equiv \frac{4 c_W^2 s_W^2}{\alpha} \left[\Pi'_{ZZ}(0) - \frac{c_W^2 - s_W^2}{c_W s_W} \Pi'_{Z\gamma}(0) - \Pi'_{\gamma\gamma}(0) \right] = \frac{4 s_W^2}{\alpha} \frac{g}{g'} \Pi'_{30}(0) \tag{Q.3}$$

$$T \equiv \frac{1}{\alpha} \left[\frac{\Pi_{WW}(0)}{M_W^2} - \frac{\Pi_{ZZ}(0)}{M_Z^2} \right] = \frac{1}{\alpha} \frac{\Pi_{33}(0) - \Pi_{WW}(0)}{M_W^2} \tag{Q.4}$$

$$U \equiv \frac{4 s_W^2}{\alpha} \left[\Pi'_{WW}(0) - \frac{c_W}{s_W} \Pi'_{Z\gamma}(0) - \Pi'_{\gamma\gamma}(0) \right] - S = \frac{4 s_W^2}{\alpha} \left[\Pi'_{WW}(0) - \Pi'_{33}(0) \right] \tag{Q.5}$$

where $\alpha = \alpha_{em}(m_Z)$. In the following expressions we adopt $\Pi^{(\prime)}(0) \equiv \Pi^{(\prime)}$ notation, i.e. omit (0) argument of $\Pi^{(\prime)}$ functions,

To find S, T, and U values we have calculated Π functions for the interaction Lagrangian of the general form:

$$\mathcal{L}_{V\psi\psi} = \bar{\psi}_1 \left(g_V \gamma^\mu - g_A \gamma^\mu \gamma^5\right) \psi_2 V_\mu + h.c. \tag{Q.6}$$

using dimensional regularisation. We have found that

$$\Pi^{(\prime)} = \frac{1}{4\pi^2} \left(\left(g_V^2 + g_A^2\right) \Pi^{(\prime)}_{V+A} + \left(g_V^2 - g_A^2\right) \Pi^{(\prime)}_{V-A} \right) \ , \tag{Q.7}$$

with $\Pi^{(\prime)}_{V\pm A}$ given by

$$\Pi_{V+A} = -\frac{1}{2}\left(m_1^2 + m_2^2\right)(div + L) - \frac{1}{4}(m_1^2 + m_2^2) - \frac{\left(m_1^4 + m_2^4\right)}{4\left(m_1^2 - m_2^2\right)} \ln\left(\frac{m_2^2}{m_1^2}\right) \tag{Q.8}$$

$$\Pi_{V-A} = m_1 m_2 \left(div + L + 1 + \frac{\left(m_1^2 + m_2^2\right)}{2\left(m_1^2 - m_2^2\right)} \ln\left(\frac{m_2^2}{m_1^2}\right) \right) \tag{Q.9}$$

$$\Pi'_{V+A} = \left(\frac{1}{3} div + \frac{1}{3} L\right) + \frac{m_1^4 - 8m_1^2 m_2^2 + m_2^4}{9\left(m_1^2 - m_2^2\right)^2} + \frac{\left(m_1^2 + m_2^2\right)\left(m_1^4 - 4m_1^2 m_2^2 + m_2^4\right)}{6\left(m_1^2 - m_2^2\right)^3} \ln\left(\frac{m_2^2}{m_1^2}\right) \tag{Q.10}$$

$$\Pi'_{V-A} = m_1 m_2 \left(\frac{\left(m_1^2 + m_2^2\right)}{2\left(m_1^2 - m_2^2\right)^2} + \frac{m_1^2 m_2^2}{\left(m_1^2 - m_2^2\right)^3} \ln\left(\frac{m_2^2}{m_1^2}\right) \right), \tag{Q.11}$$

where $div = \dfrac{1}{\epsilon} + ln(4\pi) - \gamma_\epsilon$, $L = \ln\left(\dfrac{\mu^2}{m_1 m_2}\right)$ and m_1, m_2 are the fermion masses in the loop. For $m_1 = m_2 \equiv m$ the expressions for $\Pi^{(\prime)}_{V\pm A}$ are given by

$$\Pi_{V+A} = -m^2 div - m^2 \ln\left(\tfrac{\mu^2}{m^2}\right) \ , \qquad \Pi_{V-A} = m^2 div + m^2 \ln\left(\frac{\mu^2}{m^2}\right) \tag{Q.12}$$

$$\Pi'_{V+A} = \tfrac{1}{3} div + \tfrac{1}{3} \ln\left(\tfrac{\mu^2}{m^2}\right) - \tfrac{1}{6} \ , \qquad \Pi'_{V-A} = \frac{1}{6} \tag{Q.13}$$

One should note that in [318] the identical expressions have been found in the context of generic model with vector-like fermions, with the exception of two errors/typos in the expressions for Π'_{V+A} given by Eqs. (Q.10) and (Q.13). The modification of Π'_{V+A} presented in [318] such that $L \to L/3$ in addition to squaring the denominator of the third term gives results identical to our independent calculation. We assume these mistakes are typos as taking the limit of their complete expression for Π'_{V+A} gives rise to a further divergence, and the equal mass limit presented in [318] has inconsistent dimensionality.

For the model with vector-like fermions ($g_V = 1, g_A = 0$) such as MFDM, the expressions for S and T observables are given in terms of

$$\Pi^{(\prime)}_V = \Pi^{(\prime)}_{V+A} + \Pi^{(\prime)}_{V-A} \tag{Q.14}$$

which follows from Eq. Q.7. Using Eqs. (Q.8-Q.13) and Eq. Q.14. one finds the following expressions for S and T observables for MFDM:

$$S = \frac{1}{\pi}\left[\cos^2\theta\Pi'_V(M_{D'},M_D)+\sin^2\theta\Pi'_V(M_{D'},M_{D_2})-\Pi'_V(M_+,M_+)\right] \quad \text{(Q.15)}$$

$$T = \frac{1}{4\pi M_W^2 s_W^2}\left[\Pi_V(M_+,M_{D'})+\cos^2\theta\Pi_V(M_+,M_D)+\sin^2\theta\Pi_V(M_+,M_{D_2})\right.$$
$$\left.-\Pi_V(M_+,M_+)-\cos^2\theta\Pi_V(M_{D'},M_{D_1})-\sin^2\theta\Pi_V(M_{D'},M_{D_2})\right] \quad \text{(Q.16)}$$

where θ is the χ^0-χ^0_s mixing angle defined by Eq. 3.16. The coefficients infront of Π and Π' functions in Eqs. (Q.15,Q.16) are defined by the Lagrangian of MFDM model 3.13, the complete set of Feynman rules for which is given in HEPMDB.

Recalling that $m_{D^+} = M_{D'}$ from Eq. Q.16 it follows that

$$T \equiv 0 \ . \quad \text{(Q.17)}$$

This important feature of MFDM takes place because one of the down parts of the vector-like doublet, corresponding to the neutral Majorana fermion, does not mix and has the same mass as the charged fermion. For the same reason

$$U \equiv 0 \quad \text{(Q.18)}$$

for MFDM. One should also note that for the expressions for S, T and U observables both div and $\ln(\mu^2)$ terms cancel out as expected, confirming the consistency and correctness of our evaluation.

Appendix R

Process $e^+e^- \to Z \to DD_2 \to DDZ$

One more process leading to production of D-odd particles at ILC is also observable at $M_{D_2} + M_D < \sqrt{s}$ (in particular, at $\frac{\sqrt{s}}{2} > M_+ > M_{D_2}$):

$$e^+e^- \to Z \to DD_2 \to DDZ. \tag{R.1}$$

This process has a clear signature in the modes suitable for observation:

The e^+e^- or $\mu^+\mu^-$ pair with large and large $M()$ + *nothing*. The effective mass of this dilepton is $\leqslant M_Z$, its energy is typically less than $\frac{\sqrt{s}}{2}$.	(R.2a)

A quark dijet with large and large $M()$ + *nothing*. The effective mass of this dijet is $\leqslant M_Z$, its energy is typically less than $\frac{\sqrt{s}}{2}$.	(R.2b)

At $M_{D_2} < M_+$ the BR for channel with signature (R.2a) is 0.06, for the channel with signature (R.2b) – 0.7. We skip channel $Z \to \tau^+\tau^-$ with BR=0.03, 20% of decays of Z are invisible ($Z \to \nu\bar{\nu}$).

At $M_{D_2} > M_+$ BR's for processes with signature (R.2) become less, since new decay channels $D_2 \to D^{\mp}W^{\pm} \to DW^+W^-$ are added with signature:

$e^+e^- \to DD_2 \to DDW^+W^-$: Two quark dijets or dijet + single lepton or two leptons in one hemisphere with large and large $M()$ + *nothing*. The effective mass of this system is $\leqslant M_Z$, its energy is typically less than $\frac{\sqrt{s}}{2}$.	(R.3)

The cross section of the process $e^+e^- \to DD_2$ is model dependent. In the IDM it is determined unambiguously, in MSSM result depends on mixing angles and on the nature of fermions D and D_2 (Dirac or Majorana). In all considered cases at $\sqrt{s} > 200$ GeV this cross section is smaller than $0.1\sigma_0$. Since the BR for events with signature (R.2a) is 0.06, at the 500 fb^{-1} luminosity the number of events with this

signature is of the order of 10^3 which is not enough for high precision measurements (but certain limits on the masses can be obtained (cf. [**?**,**?**,**?**] for LEP)).

Nevertheless we describe, for completeness, the energy distributions of Z in this process. The obtained equations are similar to (9.3)–(9.6) for new kinematics.

The γ-factor and velocity of D_2 in c.m.s. for e^+e^- are

$$\gamma_{D_2} = \frac{s + M_{D_2}^2 - M_D^2}{2\sqrt{s}M_{D_2}}, \quad \beta_{D_2} = \frac{\sqrt{(s^2 - M_{D_2}^2 - M_D^2)^2 - 4M_D^2 M_{D_2}^2}}{s + M_{D_2}^2 - M_D^2}. \tag{R.4}$$

For production of Z with an effective mass M_Z^* ($M_Z^* = M_Z$ at $M_{D_2} - M_D > M_Z$ and $M_Z^* \leqslant M_{D_2} - M_D$ at $M_{D_2} - M_D < M_Z$) in the rest frame of D_2

$$E_Z^D = \frac{M_{D_2}^2 + M_Z^{*2} - M_D^2}{2M_{D_2}}, \qquad p_Z^D = \frac{\sqrt{(M_{D_2}^2 - M_Z^{*2} - M_D^2)^2 - 4M_D^2 M_Z^{*2}}}{2M_{D_2}}. \tag{R.5}$$

At $M_{D_2} - M_D > M_Z$ the Z-boson energy E_Z lies within the interval with edges

$$E_Z^{(-)} = \gamma_{D_2}(E_Z^D - \beta_{D_2}|\mathbf{p}|_Z^D), \quad E_Z^{(+)} = \gamma_{D_2}(E_Z^D + \beta_{D_2}|\mathbf{p}|_Z^D). \tag{R.6}$$

At $M_{D_2} - M_D < M_Z$ similar equations are valid for each value of M_Z^*. Absolute upper and lower edges of the energy distribution of Z are reached at $M_Z^* = 0$:

$$E_Z^{(\pm)} = \gamma_{D_2}(1 \pm \beta_{D_2})(M_{D_2}^2 - M_D^2)/(2M_{D_2})\,. \tag{R.7}$$

The peak in the energy distribution of dilepton appears at $M_Z^* = M_{D_2} - M_D$:

$$E_Z = \gamma_{D_2}(M_{D_2} - M_D)\,. \tag{R.8}$$

At first sight, measurement of kinematical edges of the dilepton spectrum (R.6) (at $M_{D_2} - M_D > M_Z$) gives two equations for M_D and M_{D_2}, allowing for determination of these masses. At $M_{D_2} - M_D < M_Z$, the same procedure can be performed separately for each value of the effective mass of dilepton [319]. In the latter case, the absolute edges of the dilepton energy spectrum (R.7) and the position of the peak in this spectrum (R.8) could be also used for measuring M_D and M_{D_2}.

In any case, the upper edge in the dijet energy spectrum $E_Z^{(+)}$ (R.6), (R.7) (signature (R.2)) gives one equation, necessary to find M_{D_2} and M_D. In principle, necessary additional information gives position of lower edge in the dilepton energy spectrum $E_Z^{(-)}$. However, as it was noted above, the anticipated number of events with signature (R.2a) looks insufficient for obtaining precise results. Together with good results for M_D and M_+, one can hope to find an accurate value of M_{D_2}.

Appendix S

Derivations

S.1 E_μ end-point: E_μ^{max}

In this section we present the derivation for the maximum muon energy, E_μ^{max}, which is achieved when mass of virtual W boson M_W^* reaches its maximum value of $M_+ - M_D$. We start with the muon energy in the laboratory frame:

$$E_\mu = \gamma_W(1 + c_1\beta_W)(M_W^{(*)}/2), \tag{S.1}$$

where c_1 is $cos\theta_1$ of the escape angle of μ relative to the direction of the W in the laboratory frame. We then substitute the γ_W and β_W variables for the edge, given by:

$$\gamma_W = E_W/M_W^{(*)} = E(1 - M_D/M_+)/M_W^{(*)}, \tag{S.2}$$

$$\beta_W = \sqrt{1 - M_W^{(*)2}/E_W^2} = \sqrt{1 - \frac{M_W^{(*)2}}{E^2(1 - M_D/M_+)^2}} \tag{S.3}$$

into Eq.(S.1), which gives an E_μ for the off-shell W boson case:

$$E_\mu = \frac{E(1 - M_D/M_+)}{M_W^*}\left(1 + c_1\sqrt{1 - \frac{M_W^{*2}}{E^2(1 - M_D/M_+)^2}}\right)(M_W^*/2). \tag{S.4}$$

By substituting $M_W^{(*)} = M_+ - M_D$ for the maximum value of M_W^* into Eq.(S.1) and setting c_1 to $+1$ corresponding to the maximum in E_μ, this gives the maximum edge in muon energy,

$$E_\mu^{max} = E\frac{(1 - M_D/M_+)}{M_+ - M_D}\left(1 + \sqrt{1 - \frac{(M_+ - M_D)^2}{E^2(1 - \frac{M_D}{M_+})^2}}\right)\left(\frac{M_+ - M_D}{2}\right). \tag{S.5}$$

Simplifying this down to:

$$E_\mu^{max} = \frac{E(1 - \frac{M_D}{M+})}{2}\left(1 + \sqrt{1 - \left(\frac{M_+ - M_D}{E(1 - \frac{M_D}{M_+})}\right)^2}\right), \tag{S.6}$$

it follows that:

$$E_\mu^{max} = \frac{E(1 - \frac{M_D}{M+})}{2}(1 + \beta_+), \tag{S.7}$$

where $\beta_+ = \sqrt{1 - \left(\frac{M_+}{E}\right)^2}$.

S.2 $E_\mu^\pm$ derivations

In this section we present the derivation for the upper$(+)$ and lower$(-)$ kinks of the muon energy distribution E_μ, defined as $E_\mu^\pm$. We start with the muon energy in the laboratory frame:

$$E_\mu = \gamma_W(1 + c_1\beta_W)\left(\frac{M_W^{(*)}}{2}\right) \tag{S.8}$$

where we can substitute $\gamma_W^{(\pm)}$ and $\beta_W^{(\pm)}$ variables in terms of the upper and lower kinks of E_W, defined as:

$$\gamma_W^{(\pm)} = \frac{E_W^{(\pm)}}{M_W^{(*)}}, \tag{S.9}$$

$$\beta_W^{(\pm)} = \sqrt{1 - \left(\frac{M_W^{(*)}}{E_W^{(\pm)}}\right)^2}. \tag{S.10}$$

We substitute these into E_μ, Eq.(S.2), and set c_1 to ± 1 to give the maximum and minimum muon energy kinks $E_\mu^{(\pm)}$ in terms of $E_W^{(\pm)}$:

$$E_\mu^{(\pm)} = \frac{E_W^{(\pm)}}{M_W^{(*)}}\left(1 \pm \sqrt{1 - \left(\frac{M_W^{(*)}}{E_W^{(\pm)}}\right)^2}\right)\left(\frac{M_W^{(*)}}{2}\right). \tag{S.11}$$

After simplifying this down, this gives:

$$E_\mu^{(\pm)} = \frac{E_W^{(\pm)}}{2} \pm \frac{1}{2}\sqrt{E_W^{(\pm)2} - M_W^{(*)2}}. \tag{S.12}$$

S.3 Simultaneous equations procedure for finding M_+ and M_D

In this section we present the derivation for the DM masses M_+ and M_D, as a function of the muon energy upper and lower bounds $E_\mu^\pm$, that can be determined independent of each other. Equations (9.6) and (9.10) are used to give two simultaneous equations:

$$\frac{4E_{\mu}^{(+)2}+M_W^2}{4E_{\mu}^{(+)}} = \frac{E}{M_+}\left(\frac{M_+^2+M_W^2-M_D^2}{2M_+} + \sqrt{1-\frac{M_+^2}{E^2}}\frac{\sqrt{M_+^4+M_W^4+M_D^4-2M_+^2M_W^2-2M_+^2M_D^2-2M_W^2M_D^2}}{2M_+}\right), \tag{S.13}$$

$$\frac{4E_{\mu}^{(-)2}+M_W^2}{4E_{\mu}^{(-)}} = \frac{E}{M_+}\left(\frac{M_+^2+M_W^2-M_D^2}{2M_+} - \sqrt{1-\frac{M_+^2}{E^2}}\frac{\sqrt{M_+^4+M_W^4+M_D^4-2M_+^2M_W^2-2M_+^2M_D^2-2M_W^2M_D^2}}{2M_+}\right). \tag{S.14}$$

Performing the simultaneous equations procedure gives the equation of M_D in terms of M_+:

$$M_D^2 = M_W^2 - M_+^2\left[\frac{1}{E}\left(\frac{4E_{\mu}^{(+)2}+M_W^2}{4E_{\mu}^{(+)}}+\frac{4E_{\mu}^{(-)2}+M_W^2}{4E_{\mu}^{(-)}}\right)-1\right] \tag{S.15}$$

and substituting this onto the first simultaneous equation (S.13) results in the polynomial of M_+:

$$-M_+^4(\alpha+\beta)^2+4M_+^2E^2(\alpha\beta+M_W^2)-4M_W^2E^4=0 \tag{S.16}$$

where:

$$\alpha=\frac{4E_{\mu}^{(+)2}+M_W^2}{4E_{\mu}^{(+)}},\quad \beta=\frac{4E_{\mu}^{(-)2}+M_W^2}{4E_{\mu}^{(-)}}. \tag{S.17}$$

This gives 4 roots for M_+:

$$M_+=\pm\sqrt{2}\sqrt{\frac{-\sqrt{E^4(\alpha^2-M_W^2)(\beta^2-M_W^2)}+\alpha\beta E^2+E^2M_W^2}{(\alpha+\beta)^2}} \tag{S.18}$$

$$M_+=\pm\sqrt{2}\sqrt{\frac{\sqrt{E^4(\alpha^2-M_W^2)(\beta^2-M_W^2)}+\alpha\beta E^2+E^2M_W^2}{(\alpha+\beta)^2}}. \tag{S.19}$$

Two of these roots will be positive and the top equation will correspond to the physical mass of $D^{\pm}$. By rearranging the equation of M_D in terms of M_+ we obtain the the following equation for M_D:

$$-\left(\frac{M_W^2 - M_D^2}{\alpha + \beta - E}\right)^2 (\alpha + \beta)^2 + 4\frac{M_W^2 - M_D^2}{\alpha + \beta - E} E(\alpha\beta + M_W^2) - 4M_W^2 E^2 = 0 \tag{S.20}$$

which gives two real and two complex roots for M_D. Out of the two real roots, one is positive and gives the physical mass for D.

References

[1] O. S. Brüning, P. Collier and P. Lebrun, *LHC Design Report*. CERN Yellow Reports: Monographs. CERN, Geneva, 2004. CERN-2004-003, https://cds.cern.ch/record/782076.

[2] C. Garcia-Cely, M. Gustafsson and A. Ibarra, *Probing the inert doublet dark matter model with Cherenkov telescopes*, *Journal of Cosmology and Astroparticle Physics* **2016** (Feb, 2016) 043–043 [1512.02801].

[3] T. X. Collaboration, *The XENON1t dark matter experiment*, *The European Physical Journal C* **77** (Dec, 2017) [1708.07051].

[4] D. Akerib, C. Akerlof and D. A. et al., *The LUX-ZEPLIN (LZ) experiment*, *Nuclear Instruments and Methods in Physics Research Section A: Accelerators, Spectrometers, Detectors and Associated Equipment* **953** (Feb, 2020) 163047 [1910.09124].

[5] G. Bernardi *et. al.*, *The Future Circular Collider: a Summary for the US 2021 Snowmass Process*, 2203.06520.

[6] P. Collaboration, *Planck 2018 results*, *Astronomy and Astrophysics* **641** (Sep, 2020) A6 [1807.06209].

[7] G. Blumenthal, S. Faber, J. Primack and M. Rees, *Formation of galaxies and large-scale structure with cold dark matter*, *Nature* **313** (01, 1985). [https://doi.org/10.1038/313072a0].

[8] J. S. Bullock, T. S. Kolatt, Y. Sigad, R. S. Somerville, A. V. Kravtsov, A. A. Klypin, J. R. Primack and A. Dekel, *Profiles of dark haloes: evolution, scatter and environment*, *Monthly Notices of the Royal Astronomical Society* **321** (Mar, 2001) 559–575 [astro-ph/9908159].

[9] J. H. Oort, *The force exerted by the stellar system in the direction perpendicular to the galactic plane and some related problems*, *Bull. Astron. Inst. Netherlands* **6** (1932) 249–287. [https://cds.cern.ch/record/436532].

[10] C. L. Bennett and et. al., *Nine-year wilkinson microwave anisotropy probe wmap observations: Final maps and results*, *The Astrophysical Journal Supplement Series* **208** (Sep, 2013) 20 [1212.5225].

[11] **Planck** Collaboration, *The Scientific programme of Planck*, astro-ph/0604069.

[12] C. A. e. a. **MACHO** Collaboration, *The MACHO project: Microlensing detection efficiency*, *The Astrophysical Journal Supplement Series* **136** (Oct, 2001) 439–462 [astro-ph/0003392].

[13] T. Lasserre, *Galactic dark matter search with eros2*, *Progress in Particle and Nuclear Physics* **48** (2002), no. 1 289–290. [https://doi.org/10.1016/S0146-6410(02)00135-7].

[14] A. L. Melott, J. Einasto, E. Saar, I. Suisalu, A. A. Klypin and S. F. Shandarin, *Cluster Analysis of the Nonlinear Evolution of Large-Scale Structure in an Axion/Gravitino/Photino-Dominated Universe*, *Physical Review Letters - PHYS REV LETT* **51** (Sept., 1983) 935–938. [https://ui.adsabs.harvard.edu/abs/1983PhRvL..51..935M].

[15] S. D. M. White, C. S. Frenk and M. Davis, *Clustering in a neutrino-dominated universe*, *Journal of something* **274** (Nov., 1983) L1–L5. [https://ui.adsabs.harvard.edu/abs/1983ApJ...274L...1W].

[16] S. D. M. White, C. S. Frenk, M. Davis and G. Efstathiou, *Clusters, Filaments, and Voids in a Universe Dominated by Cold Dark Matter*, *Astrophysical Journal* **313** (Feb., 1987) 505. [https://ui.adsabs.harvard.edu/abs/1987ApJ...313..505W].

[17] D. Clowe, A. Gonzalez and M. Markevitch, *Weak-lensing mass reconstruction of the interacting cluster 1e 0657-558: Direct evidence for the existence of dark matter*, *The Astrophysical Journal* **604** (Apr, 2004) 596–603 [astro-ph/0312273].

[18] M. Markevitch, A. H. Gonzalez, D. Clowe, A. Vikhlinin, W. Forman, C. Jones, S. Murray and W. Tucker, *Direct constraints on the dark matter self-interaction cross section from the merging galaxy cluster 1e 0657-56*, *The Astrophysical Journal* **606** (May, 2004) 819–824 [astro-ph/0309303].

[19] G. A. et. al., *Observation of a new particle in the search for the standard model higgs boson with the ATLAS detector at the LHC*, *Physics Letters B* **716** (Sep, 2012) 1–29 [1207.7214].

[20] S. C. et. al., *Observation of a new boson at a mass of 125 GeV with the CMS experiment at the LHC*, *Physics Letters B* **716** (Sep, 2012) 30–61 [1207.7235].

[21] G. Jungman, M. Kamionkowski and K. Griest, *Supersymmetric dark matter*, *Phys. Rept.* **267** (1996) 195–373 [hep-ph/9506380].

[22] U. Ellwanger, C. Hugonie and A. M. Teixeira, *The Next-to-Minimal Supersymmetric Standard Model*, *Phys. Rept.* **496** (2010) 1–77 [0910.1785].

[23] G. Giudice and A. Romanino, *Split supersymmetry*, *Nucl. Phys. B* **699** (2004) 65–89 [hep-ph/0406088]. [Erratum: Nucl.Phys.B 706, 487–487 (2005)].

[24] S. Dodelson and L. M. Widrow, *Sterile-neutrinos as dark matter*, *Phys. Rev. Lett.* **72** (1994) 17–20 [hep-ph/9303287].

[25] M. Cirelli, N. Fornengo and A. Strumia, *Minimal dark matter*, *Nucl. Phys. B* **753** (2006) 178–194 [hep-ph/0512090].

[26] J. E. Kim and G. Carosi, *Axions and the Strong CP Problem*, *Rev. Mod. Phys.* **82** (2010) 557–602 [0807.3125]. [Erratum: Rev.Mod.Phys. 91, 049902 (2019)].

[27] H.-C. Cheng, J. L. Feng and K. T. Matchev, *Kaluza-Klein dark matter*, *Phys. Rev. Lett.* **89** (2002) 211301 [hep-ph/0207125].

[28] D. Hooper and S. Profumo, *Dark Matter and Collider Phenomenology of Universal Extra Dimensions*, *Phys. Rept.* **453** (2007) 29–115 [hep-ph/0701197].

[29] C. Boehm and P. Fayet, *Scalar dark matter candidates*, *Nucl. Phys. B* **683** (2004) 219–263 [hep-ph/0305261].

[30] G. Branco, P. Ferreira, L. Lavoura, M. Rebelo, M. Sher and J. P. Silva, *Theory and phenomenology of two-Higgs-doublet models*, *Phys. Rept.* **516** (2012) 1–102 [1106.0034].

[31] A. Belyaev, G. Cacciapaglia, I. P. Ivanov, F. Rojas-Abatte and M. Thomas, *Anatomy of the Inert Two Higgs Doublet Model in the light of the LHC and non-LHC Dark Matter Searches*, *Phys. Rev.* **D97** (2018), no. 3 035011 [1612.00511].

[32] N. D. Christensen, T. Han, Z. Qian, J. Sayre, J. Song and Stefanus, *Determining the Dark Matter Particle Mass through Antler Topology Processes at Lepton Colliders*, *Phys. Rev.* **D90** (2014) 114029 [1404.6258].

[33] M. Burns, K. Kong, K. T. Matchev and M. Park, *Using Subsystem MT2 for Complete Mass Determinations in Decay Chains with Missing Energy at Hadron Colliders*, *JHEP* **03** (2009) 143 [0810.5576].

[34] N. D. Christensen and D. Salmon, *New method for the spin determination of dark matter*, *Phys. Rev.* **D90** (2014), no. 1 014025 [1311.6465].

[35] A. Belyaev, L. Panizzi, A. Pukhov and M. Thomas, *Dark Matter characterization at the LHC in the Effective Field Theory approach*, *JHEP* **04** (2017) 110 [1610.07545].

[36] M. Asano, T. Saito, T. Suehara, K. Fujii, R. S. Hundi, H. Itoh, S. Matsumoto, N. Okada, Y. Takubo and H. Yamamoto, *Discrimination of New Physics Models with the International Linear Collider*, *Phys. Rev.* **D84** (2011) 115003 [1106.1932].

[37] **ATLAS** Collaboration, G. Aad *et. al.*, *Search for squarks and gluinos in final states with one isolated lepton, jets, and missing transverse momentum at* $\sqrt{s} = 13$ *with the ATLAS detector*, *Eur. Phys. J. C* **81** (2021), no. 7 600 [2101.01629]. [Erratum: Eur.Phys.J.C 81, 956 (2021)].

[38] **ATLAS** Collaboration, G. Aad *et. al.*, *Searches for electroweak production of supersymmetric particles with compressed mass spectra in $\sqrt{s} = 13$ TeV pp collisions with the ATLAS detector*, *Phys. Rev. D* **101** (2020), no. 5 052005 [1911.12606].

[39] **CMS** Collaboration, A. M. Sirunyan *et. al.*, *Search for a heavy vector resonance decaying to a Z boson and a Higgs boson in proton-proton collisions at $\sqrt{s} = 13$ TeV*, *Eur. Phys. J. C* **81** (2021), no. 8 688 [2102.08198].

[40] G. A. et. al., *Measurements of the production cross-section for a z boson in association with b-jets in proton-proton collisions at $\sqrt{s} = 13$ TeV with the ATLAS detector*, *Journal of High Energy Physics* **2020** (Jul, 2020) [2003.11960].

[41] A. Belyaev, G. Cacciapaglia, D. Locke and A. Pukhov, *Minimal consistent dark matter models for systematic experimental characterisation: Fermion dark matter*, 2203.03660.

[42] **ATLAS** Collaboration, *Cross-section measurements for the production of a Z boson in association with high-transverse-momentum jets in pp collisions at $\sqrt{s} = 13$ TeV with the ATLAS detector*, 2205.02597.

[43] **ATLAS** Collaboration, *$Z+$ heavy flavours at 13 TeV internal note*, . [https://gitlab.cern.ch/atlas-physics-office/STDM/ANA-STDM-2018-43/ANA-STDM-2018-43-INT1].

[44] A. Belyaev, U. Blumenschein, A. Freegard, S. Moretti and D. Sengupta, *Multilepton Signatures from Dark Matter at the LHC*, *Journal of High Energy Physics* **2022** (4, 2022) [2204.06411].

[45] A. Belyaev, A. Freegard, I. F. Ginzburg, D. Locke and A. Pukhov, *Decoding dark matter at future e+e- colliders*, *Phys. Rev. D* **106** (2022), no. 1 015016 [2112.15090].

[46] M. E. Peskin and D. V. Schroeder, *An Introduction to quantum field theory*. Addison-Wesley, Reading, USA, 1995.

[47] G. Altarelli, *The Standard model of particle physics*, hep-ph/0510281.

[48] T. Nakano and K. Nishijima, *Charge Independence for V-particles*, . [https://doi.org/10.1143/PTP.10.581].

[49] F. Cachazo, S. He and E. Y. Yuan, *Scattering of massless particles in arbitrary dimensions*, *Physical Review Letters* **113** (Oct, 2014) [1307.2199].

[50] P. A. M. Dirac and N. H. D. Bohr, *The quantum theory of the emission and absorption of radiation*, *Proceedings of the Royal Society of London. Series A, Containing Papers of a Mathematical and Physical Character* **114** (1927), no. 767 243–265. [https://doi.org/10.1098/rspa.1927.0039].

[51] E. Fermi, *Nuclear physics*. The University of Chicago Press, 1950.

[52] C. Quigg, *Spontaneous Symmetry Breaking as a Basis of Particle Mass*, *Rept. Prog. Phys.* **70** (2007) 1019–1054 [0704.2232].

[53] Özdal Özer, *The Higgs boson and right-handed neutrinos in supersymmetric models*. PhD thesis, Jul, 2016. [http://dx.doi.org/10.13140/RG.2.2.18314.52165].

[54] J. Goldstone, A. Salam and S. Weinberg, *Broken Symmetries*, *Physical Review* **127** (Aug., 1962) 965–970. [https://ui.adsabs.harvard.edu/abs/1962PhRv..127..965G].

[55] **ATLAS** Collaboration, G. Aad *et. al.*, *Observation of a new particle in the search for the Standard Model Higgs boson with the ATLAS detector at the LHC*, *Phys. Lett. B* **716** (2012) 1–29 [1207.7214].

[56] **CMS** Collaboration, S. Chatrchyan *et. al.*, *Observation of a New Boson at a Mass of 125 GeV with the CMS Experiment at the LHC*, *Phys. Lett. B* **716** (2012) 30–61 [1207.7235].

[57] W. Herr and B. Muratori, *Concept of luminosity*, . [https://cds.cern.ch/record/941318].

[58] **LHCb** Collaboration, R. Aaij *et. al.*, *Measurement of the semileptonic CP asymmetry in $B^0 - \overline{B}^0$ mixing*, *Phys. Rev. Lett.* **114** (2015) 041601 [1409.8586].

[59] A. D. Dolgov, *CP violation in cosmology*, in *163rd Course of International School of Physics 'Enrico Fermi': CP Violation: From Quarks to Leptons*, pp. 407–438, 11, 2005. hep-ph/0511213.

[60] T. Hambye, *CP violation and the matter–antimatter asymmetry of the universe*, *Comptes Rendus Physique* **13** (2012), no. 2 193 – 203. [https://doi.org/10.1016/j.crhy.2011.09.007].

[61] H. Lehmann, K. Symanzik and W. Zimmermann, *Zur Formulierung quantisierter Feldtheorien*, *Nuovo Cimento* **1** (1955) 205–25. [https://doi.org/10.1007/BF02731765].

[62] M. Broido, *Green functions in particle physics*, *Reports on Progress in Physics* **32** (08, 2002) 493. [https://dx.doi.org/10.1088/0034-4885/32/2/302].

[63] G. C. Wick, *The evaluation of the collision matrix*, *Phys. Rev.* **80** (Oct, 1950) 268–272. [https://doi.org/10.1103/PhysRev.80.268].

[64] F. A. Barone, H. Boschi-Filho and C. Farina, *Three methods for calculating the feynman propagator*, *American Journal of Physics* **71** (May, 2003) 483–491 [quant-ph/0205085].

[65] M. Veltman, *Diagrammatica: The Path to Feynman rules*, vol. 4. Cambridge University Press, 5, 2012.

[66] C.-K. Qiao, J.-W. Wei and L. Chen, *An overview of the compton scattering calculation*, 2103.04634.

[67] E. Daw, *Lecture 7 - rapidity and pseudorapidity*, . [https://www.hep.shef.ac.uk/edaw/PHY206/Site/2012_course_files/phy206rlec7.pdf].

[68] A. Belyaev and D. A. Ross, *The basics of nuclear and particle physics*. Springer, 2021. [https://doi.org/10.1007/978-3-030-80116-8].

[69] C. P. et al. (Particle Data Group), *Particle data group (pdg) 2016 review*, *Chin. Phys. C* **40** (2016) 100001. [https://pdg.lbl.gov/2016/reviews/contents_sports.html].

[70] X. Artru, *Classical string phenomenology. how strings work*, *Physics Reports* **97** (1983), no. 2 147 – 171. [https://doi.org/10.1016/0370-1573(83)90081-9].

[71] J. Alwall, M. Herquet, F. Maltoni, O. Mattelaer and T. Stelzer, *MadGraph 5 : Going Beyond*, *JHEP* **06** (2011) 128 [1106.0522].

[72] T. Han, *Collider phenomenology: Basic knowledge and techniques*, in *Physics in D ¿= 4. Proceedings, Theoretical Advanced Study Institute in elementary particle physics, TASI 2004, Boulder, USA, June 6-July 2, 2004*, pp. 407–454, 2005. hep-ph/0508097.

[73] U. Blumenschein, *Search for associated chargino-neutralino production in proton-antiproton collisions at 1.96 tev*, . [https://doi.org/10.2172/875533].

[74] G. F. Sterman, *Partons, factorization and resummation, TASI 95*, in *Theoretical Advanced Study Institute in Elementary Particle Physics (TASI 95): QCD and Beyond*, pp. 327–408, 6, 1995. hep-ph/9606312.

[75] P. Bartalini and J. R. Gaunt, *Multiple parton interactions at the LHC*, 1111.0469.

[76] T. Sjostrand, S. Mrenna and P. Z. Skands, *PYTHIA 6.4 Physics and Manual*, *JHEP* **05** (2006) 026 [hep-ph/0603175].

[77] Z. Was, *Radiative corrections*, in *1993 European School of High-energy Physics*, pp. 307–338, 1, 1994. [https://cds.cern.ch/record/258038/].

[78] T. Sjostrand, *Monte Carlo Generators*, in *2006 European School of High-Energy Physics*, pp. 51–74, 11, 2006. hep-ph/0611247.

[79] S. Höche, *Introduction to parton-shower event generators*, in *Theoretical Advanced Study Institute in Elementary Particle Physics: Journeys Through the Precision Frontier: Amplitudes for Colliders*, pp. 235–295, 2015. 1411.4085.

[80] M. Bengtsson and T. Sjöstrand, *A comparative study of coherent and non-coherent parton shower evolution*, *Nuclear Physics B* **289** (1987) 810–846. [https://doi.org/10.1016/0550-3213(87)90407-X].

[81] T. Sjostrand and P. Z. Skands, *Multiple interactions and the structure of beam remnants*, *JHEP* **03** (2004) 053 [hep-ph/0402078].

[82] R. D. Field, *The underlying event in hard scattering processes*, hep-ph/0201192.

[83] P. L. S. Connor, *Inclusive b Jet Production in Proton-Proton Collisions*, . 2019, [https://doi.org/10.1007/978-3-030-34383-5].

[84] J. Bellm *et. al.*, *Herwig 7.0/Herwig++ 3.0 release note*, *Eur. Phys. J. C* **76** (2016), no. 4 196 [1512.01178].

[85] M. L. Mangano and T. J. Stelzer, *Tools for the simulation of hard hadronic collisions*, *Annual Review of Nuclear and Particle Science* **55** (2005), no. 1 555–588 [https://doi.org/10.1146/annurev.nucl.55.090704.151505].

[86] R. K. et al., *Jet substructure at the large hadron collider*, *Reviews of Modern Physics* **91** (Dec, 2019) [1803.06991].

[87] G. P. Salam, *Towards jetography*, *The European Physical Journal C* **67** (May, 2010) 637–686 [0906.1833].

[88] M. Cacciari, G. P. Salam and G. Soyez, *The anti-k_t jet clustering algorithm*, *JHEP* **04** (2008) 063 [0802.1189].

[89] G. Choudalakis, *Unfolding in atlas*, 1104.2962.

[90] **ATLAS** Collaboration, S. Biondi, *Experience with using unfolding procedures in ATLAS*, tech. rep., CERN, Geneva, Nov, 2016. [https://cds.cern.ch/record/2229001].

[91] K. Reygers, *Statistical methods in particle physics WS, 9. Unfolding*, . 2018, [https://www.physi.uni-heidelberg.de/ reygers/lectures/2017/smipp/stat_methods_ss2017_09_unfolding.pdf].

[92] U. Amaldi, W. de Boer and H. Furstenau, *Comparison of grand unified theories with electroweak and strong coupling constants measured at LEP*, *Phys. Lett. B* **260** (1991) 447–455. [https://doi.org/10.1016/0370-2693(91)91641-8].

[93] A. Deur, S. J. Brodsky and G. F. de Téramond, *The QCD running coupling*, *Progress in Particle and Nuclear Physics* **90** (Sep, 2016) 1–74 [1604.08082].

[94] H. D. Politzer, *Reliable Perturbative Results for Strong Interactions?*, *Phys. Rev. Lett.* **30** (1973) 1346–1349. [https://link.aps.org/doi/10.1103/PhysRevLett.30.1346].

[95] D. J. Gross and F. Wilczek, *Asymptotically Free Gauge Theories - I*, *Phys. Rev.* **D8** (1973) 3633–3652. [https://link.aps.org/doi/10.1103/PhysRevD.8.3633].

[96] G. Altarelli, R. Ellis and G. Martinelli, *Large perturbative corrections to the drell-yan process in qcd*, *Nuclear Physics B* **157** (1979), no. 3 461–497. [https://doi.org/10.1016/0550-3213(79)90116-0].

[97] J. Kubar-Andre and F. E. Paige, *Gluon corrections to the drell-yan model*, *Phys. Rev. D* **19** (Jan, 1979) 221–229. [https://link.aps.org/doi/10.1103/PhysRevD.19.221].

[98] R. Hamberg, W. L. van Neerven and T. Matsuura, *A complete calculation of the order $\alpha - s^2$ correction to the Drell-Yan K factor*, *Nucl. Phys. B* **359** (1991) 343–405. [https://doi.org/10.1016/0550-3213(91)90064-5].

[99] I. W. Stewart, F. J. Tackmann and W. J. Waalewijn, *N-Jettiness: An Inclusive Event Shape to Veto Jets*, *Phys. Rev. Lett.* **105** (2010) 092002 [1004.2489].

[100] W. Giele, E. Glover and D. A. Kosower, *Higher-order corrections to jet cross sections in hadron colliders*, *Nuclear Physics B* **403** (1993), no. 3 633 – 667 [hep-ph/9302225].

[101] W. T. Giele and E. W. N. Glover, *Higher-order corrections to jet cross sections in e^+e^- annihilation*, *Phys. Rev. D* **46** (Sep, 1992) 1980–2010. [https://link.aps.org/doi/10.1103/PhysRevD.46.1980].

[102] A. G.-D. Ridder, T. Gehrmann and E. N. Glover, *Antenna subtraction at NNLO*, *Journal of High Energy Physics* **2005** (Sep, 2005) 056–056 [hep-ph/0505111].

[103] A. Daleo, T. Gehrmann and D. Maitre, *Antenna subtraction with hadronic initial states*, *JHEP* **04** (2007) 016 [hep-ph/0612257].

[104] S. Catani and M. Seymour, *The Dipole formalism for the calculation of QCD jet cross-sections at next-to-leading order*, *Phys. Lett. B* **378** (1996) 287–301 [hep-ph/9602277].

[105] G. F. Smoot, *COBE observations and results*, astro-ph/9902027.

[106] J. R. Brownstein and J. W. Moffat, *The bullet cluster 1e0657-558 evidence shows modified gravity in the absence of dark matter*, *Monthly Notices of the Royal Astronomical Society* **382** (Nov, 2007) 29–47 [astro-ph/0702146].

[107] L. J. Hall, K. Jedamzik, J. March-Russell and S. M. West, *Freeze-In Production of FIMP Dark Matter*, *JHEP* **03** (2010) 080 [0911.1120].

[108] Aalbers *et. al.*, *First dark matter search results from the lux-zeplin (lz) experiment*, 2207.03764.

[109] F. Bishara, J. Brod, B. Grinstein and J. Zupan, *From quarks to nucleons in dark matter direct detection*, *Journal of High Energy Physics* **2017** (Nov, 2017) [1707.06998].

[110] **Particle Data Group** Collaboration, R. L. Workman and Others, *Review of Particle Physics*, *PTEP* **2022** (2022) 083C01. [https://doi.org/10.1093/ptep/ptac097].

[111] F. Kahlhoefer, *Review of LHC dark matter searches*, *International Journal of Modern Physics A* **32** (May, 2017) 1730006 [1702.02430].

[112] J. F. Gunion and H. E. Haber, *The CP conserving two Higgs doublet model: The Approach to the decoupling limit*, *Phys. Rev. D* **67** (2003) 075019 [hep-ph/0207010].

[113] D. Eriksson, J. Rathsman and O. Stal, *2HDMC: Two-Higgs-Doublet Model Calculator Physics and Manual*, *Comput. Phys. Commun.* **181** (2010) 189–205 [0902.0851].

[114] A. Goudelis, B. Herrmann and O. Stal, *Dark matter in the Inert Doublet Model after the discovery of a Higgs-like boson at the LHC*, *JHEP* **1309** (2013) 106 [1303.3010].

[115] A. Belyaev, T. R. Fernandez Perez Tomei, P. G. Mercadante, C. S. Moon, S. Moretti, S. F. Novaes, L. Panizzi, F. Rojas and M. Thomas, *Advancing LHC Probes of Dark Matter from the Inert 2-Higgs Doublet Model with the Mono-jet Signal*, 1809.00933.

[116] M. E. Peskin and T. Takeuchi, *Estimation of oblique electroweak corrections*, *Phys. Rev. D* **46** (1992) 381–409. [https://link.aps.org/doi/10.1103/PhysRevD.46.381].

[117] R. Barbieri, L. J. Hall and V. S. Rychkov, *Improved naturalness with a heavy higgs boson: An alternative road to CERN LHC physics*, *Physical Review D* **74** (Jul, 2006) [hep-ph/0603188].

[118] A. Arhrib, R. Benbrik and N. Gaur, $H \to \gamma\gamma$ *in Inert Higgs Doublet Model*, *Phys. Rev. D* **85** (2012) 095021 [1201.2644].

[119] **ATLAS** Collaboration, G. Aad *et. al.*, *The ATLAS Experiment at the CERN Large Hadron Collider*, *JINST* **3** (2008) S08003. 437 p. Also published by CERN Geneva in 2010.

[120] CERN, *CERN Rapport annuel 2021*, tech. rep., CERN, Geneva, 2022. [https://cds.cern.ch/record/2807620].

[121] **ATLAS** Collaboration, *Public results - luminosity*, . [https://twiki.cern.ch/twiki/bin/view/AtlasPublic/LuminosityPublicResults].

[122] I. Bejar Alonso and L. Rossi, *HiLumi LHC Technical Design Report*, tech. rep., CERN, 2015. [http://cds.cern.ch/record/2069130].

[123] C. Lefèvre, *The CERN accelerator complex. Complexe des accélérateurs du CERN*, . [https://cds.cern.ch/record/1260465].

[124] CERN, *ATLAS: Letter of intent for a general purpose p p experiment at the large hadron collider at CERN*, tech. rep., CERN, 1992. [http://cds.cern.ch/record/291061].

[125] **CMS Collaboration** Collaboration, M. Della Negra *et. al.*, *CMS: letter of intent by the CMS Collaboration for a general purpose detector at LHC*, Tech. Rep. CERN-LHCC-92-003. LHCC-I-1, CERN, Geneva, 1992. [https://cds.cern.ch/record/290808].

[126] H. Dijkstra, H. J. Hilke, T. Nakada *et. al.*, *LHCb Letter of Intent, LHCb Collaboration*, tech. rep., CERN, 1995. [http://cds.cern.ch/record/691698].

[127] **ALICE Collaboration** Collaboration, T. A. Collaboration, *Letter of Intent for A Large Ion Collider Experiment [ALICE]*, Tech. Rep. CERN-LHCC-93-016. LHCC-I-4, CERN, Geneva, 1993. [https://cds.cern.ch/record/290825].

[128] G. Giacomelli, A. A. Faust and J. L. Pinfold, *A search for highly ionizing particles and slow exotic decays at the LHC using the MOEDAL detectors: letter of intent*, Tech. Rep. CERN-LHCC-98-05. LHCC-I-19, CERN, Geneva, Feb, 1998. [https://cds.cern.ch/record/347906].

[129] **TOTEM** Collaboration, W. Kienzle, *et. al.*, *Total cross section: elastic scattering and diffraction dissociation at the LHC*, tech. rep., CERN, Geneva, 1997. [http://cds.cern.ch/record/335255].

[130] O. Adriani, *LHCf Letter of Intent for a p-Pb run. A precise study of forward physics in $\sqrt{s_{NN}}$= 4.4 TeV proton-Lead ion collisions with LHCf at the LHC*, Tech. Rep. CERN-LHCC-2011-015. LHCC-I-021, CERN, Geneva, Dec, 2011. [https://cds.cern.ch/record/1404163].

[131] J. Pequenao, *Computer generated image of the whole ATLAS detector*, . 2008, [https://cds.cern.ch/record/1095924].

[132] J. T. Boyd, *LHC Run-2 and future prospects*, 2001.04370.

[133] Fartoukh *et. al.*, *LHC Configuration and Operational Scenario for Run 3*, tech. rep., CERN, Geneva, 2021. [https://cds.cern.ch/record/2790409].

[134] J. Boyd, *LHC Run-2 and Future Prospects*, 2001.04370.

[135] **ATLAS** Collaboration, *ATLAS: Detector and physics performance technical design report. Volume 1*, tech. rep., CERN, 1999. [https://cds.cern.ch/record/391176].

[136] **ATLAS** Collaboration, *ATLAS: Detector and physics performance technical design report. Volume 2*, tech. rep., CERN, 1999. [http://cds.cern.ch/record/391177].

[137] **ATLAS** Collaboration, H. ten Kate, *The atlas superconducting magnet system at the large hadron collider*, *Physica C: Superconductivity* **468** (2008), no. 15 2137 – 2142. [https://doi.org/10.1016/j.physc.2008.05.146].

[138] J. Pequenao, *Computer generated image of the ATLAS inner detector*, . [https://cds.cern.ch/record/1095926].

[139] **ATLAS** Collaboration, K. Grimm, S. Boutle, D. Casper and Others, *Primary vertex reconstruction at the ATLAS experiment*, tech. rep., CERN, Geneva, Feb, 2017. [https://cds.cern.ch/record/2253428].

[140] W. Abdallah, A. Hammad, A. Kasem and S. Khalil, *Long-lived B-L symmetric SSM particles at the LHC*, *Phys. Rev. D* **98** (2018), no. 9 095019 [1804.09778].

[141] **ATLAS** Collaboration, G. Aad *et. al.*, *Expected Performance of the ATLAS Experiment - Detector, Trigger and Physics*, 0901.0512.

[142] **ATLAS** Collaboration, M. A. et al., *Study of the material of the ATLAS inner detector for run 2 of the LHC*, *Journal of Instrumentation* **12** (Dec, 2017) P12009–P12009 [1707.02826].

[143] **ATLAS** Collaboration, M. Capeans, G. Darbo, K. Einsweiller *et. al.*, *ATLAS Insertable B-Layer Technical Design Report*, Tech. Rep. CERN-LHCC-2010-013. ATLAS-TDR-19, CERN, Sep, 2010. [https://cds.cern.ch/record/1291633].

[144] **ATLAS** Collaboration, *Operation and performance of the ATLAS semiconductor tracker*, *Journal of Instrumentation* **9** (Aug, 2014) P08009–P08009. [https://dx.doi.org/10.1088/1748-0221/9/08/P08009].

[145] A. Abdelouahab *et. al.*, *The barrel modules of the atlas semiconductor tracker*, . 2006, [https://doi.org/10.1016/j.nima.2006.08.036].

[146] B. Mindur, *ATLAS Transition Radiation Tracker (TRT): Straw tubes for tracking and particle identification at the Large Hadron Collider*, tech. rep., CERN, Geneva, Mar, 2016. [https://cds.cern.ch/record/2139567].

[147] **ATLAS** Collaboration, D. E. Boumediene, *ATLAS calorimeters: Run-2 performances and Phase-II upgrades*, tech. rep., CERN, Geneva, Oct, 2017. [https://cds.cern.ch/record/2288402].

[148] **ATLAS** Collaboration, *ATLAS liquid-argon calorimeter: Technical Design Report*. CERN, Geneva, 1996. [https://cds.cern.ch/record/331061].

[149] K. Anderson, A. Gupta, F. Merritt, M. Oreglia, J. Pilcher, H. Sanders, M. Shochet, F. Tang, R. Teuscher, H. Wu, G. Blanchot, M. Cavalli-Sforza and I. Korolkov, *Design of the front-end analog electronics for the atlas tile calorimeter*, *Nuclear Instruments and Methods in Physics Research Section A: Accelerators, Spectrometers, Detectors and Associated Equipment* **551** (10, 2005) 469–476. [https://doi.org/10.1016/j.nima.2005.06.048].

[150] D. Kar, *Experimental Particle Physics*. 2053-2563. IOP Publishing, 2019. [https://dx.doi.org/10.1088/2053-2563/ab1be6].

[151] J. Pequenao, *Computer Generated image of the ATLAS calorimeter*, . [https://cds.cern.ch/record/1095927].

[152] M. Aleksa and M. Diemoz, *Discussion on the electromagnetic calorimeters of ATLAS and CMS*, tech. rep., CERN, Geneva, May, 2013. [https://cds.cern.ch/record/1547314].

[153] F. Gianotti, M. Leltchouk, B. Lund-Jensen, B. Mansoulié, M. Nessi, G. Parrour, P. Petroff, J. Schwindling, M. Seman and V. Tisserand, *Simulation and optimization of the ATLAS electromagnetic calorimeter: energy resolution studies*, tech. rep., CERN, Geneva, Jan, 1995. [https://cds.cern.ch/record/685687].

[154] **ATLAS** Collaboration, A. Policicchio, *BSM searches in ATLAS*, tech. rep., CERN, Geneva, Mar, 2015. [https://cds.cern.ch/record/2001836].

[155] **ATLAS** Collaboration, *ATLAS muon spectrometer: Technical Design Report*. Technical design report. ATLAS. CERN, Geneva, 1997. [https://cds.cern.ch/record/331068].

[156] J. Pequenao, *Computer generated image of the ATLAS Muons subsystem*, . 2008, [https://cds.cern.ch/record/1095929].

[157] **ATLAS** Collaboration, G. Aad *et. al.*, *Performance of algorithms that reconstruct missing transverse momentum in $\sqrt{s} = 8$ TeV proton-proton collisions in the ATLAS detector*, *The European Physical Journal C* **77** (Apr, 2017). [https://doi.org/10.1140/epjc/s10052-017-4780-2].

[158] A. Hrynevich, *ATLAS jet and missing energy reconstruction, calibration and performance in LHC run-2*, *Journal of Instrumentation* **12** (Jun, 2017) C06038–C06038. [https://doi.org/10.1088/1748-0221/12/06/c06038].

[159] **ATLAS** Collaboration, *Operation of the ATLAS trigger system in run 2*, *Journal of Instrumentation* **15** (Oct, 2020) P10004–P10004 [2007.12539].

[160] **ATLAS** Collaboration, *ATLAS data quality operations and performance for 2015–2018 data-taking*, *Journal of Instrumentation* **15** (Apr, 2020) P04003–P04003 [1911.04632].

[161] Y. Pei, S. Biswas, D. S. Fussell and K. Pingali, *An elementary introduction to kalman filtering*, 1710.04055.

[162] W. Lampl, S. Laplace, D. Lelas, P. Loch, H. Ma, S. Menke, S. Rajagopalan, D. Rousseau, S. Snyder and G. Unal, *Calorimeter clustering algorithms: Description and performance*, . [http://cds.cern.ch/record/1099735].

[163] **ATLAS** Collaboration, M. Aaboud *et. al.*, *Jet reconstruction and performance using particle flow with the ATLAS Detector*, *Eur. Phys. J. C* **77** (2017), no. 7 466 [1703.10485].

[164] **ATLAS** Collaboration, G. Aad *et. al.*, *Performance of electron and photon triggers in ATLAS during LHC run 2*, *The European Physical Journal C* **80** (Jan, 2020) [1909.00761].

[165] **ATLAS** Collaboration, G. Aad *et. al.*, *Performance of the ATLAS muon triggers in run 2*, *Journal of Instrumentation* **15** (Sep, 2020) P09015–P09015 [2004.13447].

[166] **ATLAS** Collaboration, G. Aad *et. al.*, *The ATLAS inner detector trigger performance in pp collisions at 13 TeV during LHC Run 2*, *Eur. Phys. J. C* **82** (2022), no. 3 206 [2107.02485].

[167] **ATLAS** Collaboration, G. Aad *et. al.*, *Electron and photon performance measurements with the ATLAS detector using the 2015–2017 LHC proton-proton collision data*, *JINST* **14** (2019), no. 12 P12006 [1908.00005].

[168] **ATLAS** Collaboration, G. Aad *et. al.*, *Muon reconstruction performance of the ATLAS detector in proton–proton collision data at* $\sqrt{s}$ *=13 TeV*, *Eur. Phys. J. C* **76** (2016), no. 5 292 [1603.05598].

[169] **ATLAS** Collaboration, G. Aad *et. al.*, *Muon reconstruction and identification efficiency in ATLAS using the full Run 2 pp collision data set at* $\sqrt{s} = 13$ *TeV*, *Eur. Phys. J. C* **81** (2021), no. 7 578 [2012.00578].

[170] **ATLAS** Collaboration, *Cross-section measurements for the production of a z boson in association with high-transverse-momentum jets in pp collisions at* $\sqrt{s} = 13$ *[tev] with the [atlas] detector*, 2205.02597.

[171] M. Cacciari, G. P. Salam and G. Soyez, *FastJet User Manual*, *Eur. Phys. J. C* **72** (2012) 1896 [1111.6097].

[172] E. Bothmann, G. S. Chahal, S. Höche, J. Krause, F. Krauss, S. Kuttimalai, S. Liebschner, D. Napoletano, M. Schönherr, H. Schulz, S. Schumann and F. Siegert, *Event generation with sherpa 2.2*, *SciPost Physics* **7** (Sep, 2019) [1905.09127].

[173] T. Gleisberg and S. Höche, *Comix, a new matrix element generator*, *Journal of High Energy Physics* **2008** (Dec, 2008) 039–039 [0808.3674].

[174] F. Buccioni, J.-N. Lang, J. M. Lindert, P. Maierhöfer, S. Pozzorini, H. Zhang and M. F. Zoller, *OpenLoops 2*, *The European Physical Journal C* **79** (Oct, 2019) [1907.13071].

[175] F. Cascioli, P. Maierhöfer and S. Pozzorini, *Scattering amplitudes with open loops*, *Physical Review Letters* **108** (Mar, 2012) [1111.5206].

[176] A. Denner, S. Dittmaier and L. Hofer, *Collier: A fortran-based complex one-loop library in extended regularizations*, *Computer Physics Communications* **212** (Mar, 2017) 220–238 [1604.06792].

[177] S. Schumann and F. Krauss, *A parton shower algorithm based on catani-seymour dipole factorisation*, *Journal of High Energy Physics* **2008** (Mar, 2008) 038–038 [0709.1027].

[178] S. Höche, F. Krauss, M. Schönherr and F. Siegert, *A critical appraisal of NLO+PS matching methods*, *Journal of High Energy Physics* **2012** (Sep, 2012) [1111.1220].

[179] S. Höche, F. Krauss, M. Schönherr and F. Siegert, *QCD matrix elements + parton showers. the NLO case*, *Journal of High Energy Physics* **2013** (Apr, 2013) [1207.5030].

[180] S. Catani, F. Krauss, B. R. Webber and R. Kuhn, *QCD matrix elements + parton showers*, *Journal of High Energy Physics* **2001** (Nov, 2001) 063–063 [hep-ph/0109231].

[181] S. Höche, F. Krauss, S. Schumann and F. Siegert, *QCD matrix elements and truncated showers*, *Journal of High Energy Physics* **2009** (May, 2009) 053–053 [0903.1219].

[182] J. Alwall, R. Frederix, S. Frixione, V. Hirschi, F. Maltoni, O. Mattelaer, H.-S. Shao, T. Stelzer, P. Torrielli and M. Zaro, *The automated computation of tree-level and next-to-leading order differential cross sections, and their matching to parton shower simulations*, *Journal of High Energy Physics* **2014** (Jul, 2014) [1405.0301].

[183] T. Sjöstrand, S. Mrenna and P. Skands, *A brief introduction to PYTHIA 8.1*, *Computer Physics Communications* **178** (Jun, 2008) 852–867 [0710.3820].

[184] L. Lönnblad, *Correcting the colour-dipole cascade model with fixed order matrix elements*, *Journal of High Energy Physics* **2002** (May, 2002) 046–046 [hep-ph/0112284].

[185] L. Lönnblad and S. Prestel, *Matching tree-level matrix elements with interleaved showers*, *Journal of High Energy Physics* **2012** (Mar, 2012) [1109.4829].

[186] **ATLAS** Collaboration, *Modelling and computational improvements to the simulation of single vector-boson plus jet processes for the atlas experiment*, 2112.09588.

[187] S. Catani, S. Dittmaier, M. H. Seymour and Z. Trócsányi, *The dipole formalism for next-to-leading order QCD calculations with massive partons*, *Nuclear Physics B* **627** (Apr, 2002) 189–265 [hep-ph/0201036].

[188] R. D. Ball, , V. Bertone, S. Carrazza, C. S. Deans, L. D. Debbio, S. Forte, A. Guffanti, N. P. Hartland, J. I. Latorre, J. Rojo and M. Ubiali, *Parton distributions for the LHC run II*, *Journal of High Energy Physics* **2015** (Apr, 2015) [1410.8849].

[189] R. Frederix and S. Frixione, *Merging meets matching in MC@NLO*, *Journal of High Energy Physics* **2012** (Dec, 2012) [1209.6215].

[190] T. Sjöstrand, S. Ask, J. R. Christiansen, R. Corke, N. Desai, P. Ilten, S. Mrenna, S. Prestel, C. O. Rasmussen and P. Z. Skands, *An introduction to PYTHIA 8.2*, *Computer Physics Communications* **191** (Jun, 2015) 159–177 [1410.3012].

[191] **ATLAS** Collaboration, *ATLAS Pythia 8 tunes to 7 TeV data*, tech. rep., CERN, Geneva, Nov, 2014. ATL-PHYS-PUB-2014-021, [https://cds.cern.ch/record/1966419].

[192] R. D. Ball, V. Bertone, S. Carrazza, L. D. Debbio, S. Forte, A. Guffanti, N. P. Hartland and J. Rojo, *Parton distributions with QED corrections*, *Nuclear Physics B* **877** (Dec, 2013) 290–320 [1308.0598].

[193] J. Alwall, M. Herquet, F. Maltoni, O. Mattelaer and T. Stelzer, *MadGraph 5: going beyond*, *Journal of High Energy Physics* **2011** (Jun, 2011) [1106.0522].

[194] **ATLAS** Collaboration, *MadGraph+Pythia8 joboptions, 363xxx*, . [https://gitlab.cern.ch/atlas-physics/pmg/infrastructure/mc15joboptions/-/tree/master/share/DSID363xxx].

[195] A. Buckley, J. Ferrando, S. Lloyd, K. Nordström, B. Page, M. Rüfenacht, M. Schönherr and G. Watt, *LHAPDF6: parton density access in the LHC precision era*, *The European Physical Journal C* **75** (Mar, 2015) [1412.7420].

[196] **ATLAS** Collaboration, *MadGraph+Pythia8 joboptions, 363123*, . [https://gitlab.cern.ch/atlas-physics/pmg/infrastructure/mc15joboptions/-/blob/master/share/DSID363xxx/MC15.363123.MGPy8EG_N30NLO_Zmumu_Ht0_70_CVetoBVeto.py].

[197] **ATLAS** Collaboration, *MadGraph+Pythia8 joboptions, 363126*, . [https://gitlab.cern.ch/atlas-physics/pmg/infrastructure/mc15joboptions/-/blob/master/share/DSID363xxx/MC15.363126.MGPy8EG_N30NLO_Zmumu_Ht70_140_CVetoBVeto.py].

[198] **ATLAS** Collaboration, *MadGraph+Pythia8 joboptions, 363129*, . [https://gitlab.cern.ch/atlas-physics/pmg/infrastructure/mc15joboptions/-/blob/master/share/DSID363xxx/MC15.363129.MGPy8EG_N30NLO_Zmumu_Ht140_280_CVetoBVeto.py].

[199] **ATLAS** Collaboration, *MadGraph+Pythia8 joboptions, 363132*, . [https://gitlab.cern.ch/atlas-physics/pmg/infrastructure/mc15joboptions/-/blob/master/share/DSID363xxx/MC15.363132.MGPy8EG_N30NLO_Zmumu_Ht280_500_CVetoBVeto.py].

[200] **ATLAS** Collaboration, *MadGraph+Pythia8 joboptions, 363135*, . [https://gitlab.cern.ch/atlas-physics/pmg/infrastructure/mc15joboptions/-/blob/master/share/DSID363xxx/MC15.363135.MGPy8EG_N30NLO_Zmumu_Ht500_700_CVetoBVeto.py].

[201] **ATLAS** Collaboration, *MadGraph+Pythia8 joboptions, 363138*, .
[https://gitlab.cern.ch/atlas-physics/pmg/infrastructure/mc15joboptions/-/blob/master/share/DSID363xxx/MC15.363138.MGPy8EG_N30NLO_Zmumu_Ht700_1000_CVetoBVeto.py].

[202] **ATLAS** Collaboration, *MadGraph+Pythia8 joboptions, 363141*, .
[https://gitlab.cern.ch/atlas-physics/pmg/infrastructure/mc15joboptions/-/blob/master/share/DSID363xxx/MC15.363141.MGPy8EG_N30NLO_Zmumu_Ht1000_2000_CVetoBVeto.py].

[203] **ATLAS** Collaboration, *MadGraph+Pythia8 joboptions, 363144*, .
[https://gitlab.cern.ch/atlas-physics/pmg/infrastructure/mc15joboptions/-/blob/master/share/DSID363xxx/MC15.363144.MGPy8EG_N30NLO_Zmumu_Ht2000_E_CMS_CVetoBVeto.py].

[204] **ATLAS** Collaboration, *MadGraph+Pythia8 joboptions, 363124*, .
[https://gitlab.cern.ch/atlas-physics/pmg/infrastructure/mc15joboptions/-/blob/master/share/DSID363xxx/MC15.363124.MGPy8EG_N30NLO_Zmumu_Ht0_70_CFilterBVeto.py].

[205] **ATLAS** Collaboration, *MadGraph+Pythia8 joboptions, 363125*, .
[https://gitlab.cern.ch/atlas-physics/pmg/infrastructure/mc15joboptions/-/blob/master/share/DSID363xxx/MC15.363125.MGPy8EG_N30NLO_Zmumu_Ht0_70_BFilter.py].

[206] **ATLAS** Collaboration, *MadGraph FxFx+Pythia8 H_T sliced joboptions, 364995*, .
[https://gitlab.cern.ch/atlas-physics/pmg/infrastructure/mc15joboptions/-/blob/master/share/DSID364xxx/MC15.364995.aMcAtNloPy8EG_MEN31NNLO_A14N23LO_Zmumu_FxFx_200HT500.py].

[207] **ATLAS** Collaboration, *MadGraph FxFx+Pythia8 H_T sliced joboptions, 364996*, .
[https://gitlab.cern.ch/atlas-physics/pmg/infrastructure/mc15joboptions/-/blob/master/share/DSID364xxx/MC15.364996.aMcAtNloPy8EG_MEN31NNLO_A14N23LO_Zmumu_FxFx_500HT800.py].

[208] **ATLAS** Collaboration, *MadGraph FxFx+Pythia8 H_T sliced joboptions, 364997*, .
[https://gitlab.cern.ch/atlas-physics/pmg/infrastructure/mc15joboptions/-/blob/master/share/DSID364xxx/MC15.364997.aMcAtNloPy8EG_MEN31NNLO_A14N23LO_Zmumu_FxFx_800HT1500.py].

[209] **ATLAS** Collaboration, *MadGraph FxFx+Pythia8 H_T sliced joboptions, 364998*, .
[https://gitlab.cern.ch/atlas-physics/pmg/infrastructure/mc15joboptions/-/blob/master/share/DSID364xxx/MC15.364998.aMcAtNloPy8EG_MEN31NNLO_A14N23LO_Zmumu_FxFx_1500HT13000.py].

[210] **ATLAS** Collaboration, *MadGraph FxFx+Pythia8 H_T-biased inclusive joboptions, 950063*, . [https://gitlab.cern.ch/atlas-physics/pmg/mcjoboptions/-/blob/master/950xxx/950063/mc.MGPy8EG_A14NNPDF23LO_Zee_3jets_FxFx_valid.py].

[211] J. C. Collins, *Sudakov form-factors*, *Adv. Ser. Direct. High Energy Phys.* **5** (1989) 573–614 [hep-ph/0312336].

[212] S. Hoeche, F. Krauss, N. Lavesson, L. Lonnblad, M. Mangano, A. Schalicke and S. Schumann, *Matching parton showers and matrix elements*, hep-ph/0602031.

[213] F. Krauss, R. Kuhn and G. Soff, *AMEGIC++ 1.0, a matrix element generator in c++*, *Journal of High Energy Physics* **2002** (Feb, 2002) 044–044 [hep-ph/0109036].

[214] E. Bothmann, S. Hoeche, F. Krauss, M. Schoenherr, S. Schumann, F. Siegert and K. Zapp, *Sherpa Manual Version 2.2.11*, . [https://sherpa.hepforge.org/doc/SHERPA-MC-2.2.11.html].

[215] **ATLAS** Collaboration, S. Gargiulo *et. al.*, *Modeling of top quark and vector boson production as backgrounds to Higgs boson decays to b-quarks*, . [https://cds.cern.ch/record/2684592].

[216] **ATLAS** Collaboration, *Modelling and computational improvements to the simulation of single vector-boson plus jet processes for the ATLAS experiment*, 2112.09588.

[217] C. Duhr, F. Dulat, V. Hirschi *et. al.*, *Higgs production in bottom quark fusion: matching the 4- and 5-flavour schemes to third order in the strong coupling.*, 2004.04752.

[218] C. Bierlich, A. Buckley, J. Butterworth, C. H. Christensen, L. Corpe, D. Grellscheid, J. F. Grosse-Oetringhaus, C. Gutschow, P. Karczmarczyk, J. Klein, L. Lönnblad, C. S. Pollard, P. Richardson, H. Schulz and F. Siegert, *Robust independent validation of experiment and theory: Rivet version 3*, *SciPost Physics* **8** (Feb, 2020) [1912.05451].

[219] G. Hesketh, *Rivet analysis code for ATLAS_2017_I1514251, Z plus jets at 13 TeV.*, . [https://rivet.hepforge.org/analyses/ATLAS_2017_I1514251.html].

[220] M. Aaboud *et. al.*, *Measurements of the production cross section of a Z boson in association with jets in pp collisions at $\sqrt{s} = 13$ TeV with the ATLAS detector*, *The European Physical Journal C* **77** (May, 2017) [1702.05725].

[221] C. Duhr, S. Höche and F. Maltoni, *Color-dressed recursive relations for multi-parton amplitudes*, *Journal of High Energy Physics* **2006** (Aug, 2006) 062–062 [hep-ph/0607057].

[222] F. Siegert and C. Gutschow, *Official rivet analysis MC_ZJETS*, . [https://rivet.hepforge.org/analyses/MC_ZJETS.html].

[223] **ATLAS** Collaboration, *Rivet analysis code for ANA-STDM-2018-49, collinear Z plus jets at 13 TeV.*, . [https://gitlab.cern.ch/alaurier/collinear-zjets-rivet].

[224] **ATLAS** Collaboration, G. Aad *et. al.*, *Measurement of the energy response of the ATLAS calorimeter to charged pions from $W^{\pm} \to \tau^{\pm}(\to \pi^{\pm}\nu_{\tau})\nu_{\tau}$ events in Run 2 data*, *Eur. Phys. J. C* **82** (2022), no. 3 223 [2108.09043].

[225] E. Ritsch, *Fast Calorimeter Punch-Through Simulation for the ATLAS Experiment*, 2011. [https://cds.cern.ch/record/1388275].

[226] **ATLAS** Collaboration, M. Aaboud *et. al.*, *Jet energy scale measurements and their systematic uncertainties in proton-proton collisions at $\sqrt{s} = 13$ TeV with the ATLAS detector*, *Phys. Rev. D* **96** (2017), no. 7 072002 [1703.09665].

[227] **ATLAS** Collaboration, G. Aad *et. al.*, *Jet energy resolution in proton-proton collisions at $\sqrt{s} = 7$ TeV recorded in 2010 with the ATLAS detector*, *Eur. Phys. J. C* **73** (2013), no. 3 2306 [1210.6210].

[228] **ATLAS** Collaboration, M. Aaboud *et. al.*, *Electron reconstruction and identification in the ATLAS experiment using the 2015 and 2016 LHC proton-proton collision data at $\sqrt{s}$ = 13 TeV*, *Eur. Phys. J. C* **79** (2019), no. 8 639 [1902.04655].

[229] **ATLAS** Collaboration, *Luminosity determination in pp collisions at $\sqrt{s} = 13$ TeV using the ATLAS detector at the LHC*, 2212.09379.

[230] J. Butterworth, S. Carrazza, A. Cooper-Sarkar, A. D. Roeck, J. Feltesse, S. Forte, J. Gao, S. Glazov, J. Huston, Z. Kassabov, R. McNulty, A. Morsch, P. Nadolsky, V. Radescu, J. Rojo and R. Thorne, *PDF4LHC recommendations for LHC run II*, *Journal of Physics G: Nuclear and Particle Physics* **43** (Jan, 2016) 023001 [1510.03865].

[231] **ATLAS** Collaboration, *Measurement of ZZ production in the $\ell\ell\nu\nu$ final state with the ATLAS detector in pp collisions at $\sqrt{s} = 13$ TeV*, *JHEP* **1910** (May, 2019) 127. 48 p [1905.07163].

[232] **ATLAS** Collaboration, *Measurement of fiducial and differential W^+W^- production cross-sections at $\sqrt{s}$ =13 TeV with the ATLAS detector*, *Eur. Phys. J. C* **79** (May, 2019) 884. 48 p [1905.04242].

[233] **ATLAS** Collaboration, *Measurement of $W^{\pm}Z$ production cross sections and gauge boson polarisation in pp collisions at $\sqrt{s} = 13$ TeV with the ATLAS detector*, *Eur. Phys. J. C* **79** (Feb, 2019) 535. 51 p [1902.05759].

[234] **ATLAS** Collaboration, M. Aaboud *et. al.*, *$ZZ \to \ell^+\ell^-\ell'^+\ell'^-$ cross-section measurements and search for anomalous triple gauge couplings in 13 TeV pp collisions with the ATLAS detector*, *Phys. Rev. D* **97** (2018), no. 3 032005 [1709.07703].

[235] **ATLAS** Collaboration, M. Aaboud *et. al.*, *Measurement of $WW/WZ \to \ell\nu qq'$ production with the hadronically decaying boson reconstructed as one or two jets in pp collisions at $\sqrt{s} = 8$ TeV with ATLAS, and constraints on anomalous gauge couplings*, *Eur. Phys. J. C* **77** (2017), no. 8 563 [1706.01702].

[236] C. Oleari, *The POWHEG BOX*, *Nuclear Physics B - Proceedings Supplements* **205-206** (Aug, 2010) 36–41 [1007.3893].

[237] S. Frixione, G. Ridolfi and P. Nason, *A positive-weight next-to-leading-order monte carlo for heavy flavour hadroproduction*, *Journal of High Energy Physics* **2007** (Sep, 2007) 126–126 [0707.3088].

[238] P. Nason, *A new method for combining NLO QCD with shower monte carlo algorithms*, *Journal of High Energy Physics* **2004** (Nov, 2004) 040–040 [hep-ph/0409146].

[239] S. Frixione, P. Nason and C. Oleari, *Matching NLO QCD computations with parton shower simulations: the POWHEG method*, *Journal of High Energy Physics* **2007** (Nov, 2007) 070–070 [0709.2092].

[240] S. Alioli, P. Nason, C. Oleari and E. Re, *A general framework for implementing NLO calculations in shower monte carlo programs: the POWHEG BOX*, *Journal of High Energy Physics* **2010** (Jun, 2010) [1002.2581].

[241] **ATLAS** Collaboration, *Studies on top-quark Monte Carlo modelling with Sherpa and MG5_aMCatNLO*, . [https://cds.cern.ch/record/2261938].

[242] G. D'Agostini, *A multidimensional unfolding method based on Bayes' Theorem*, tech. rep., DESY, Hamburg, Jun, 1994. [http://cds.cern.ch/record/265717].

[243] T. Adye *et. al.*, *The RooUnfold package and documentation are available from*, . [http://hepunx.rl.ac.uk/ adye/software/unfold/RooUnfold.html].

[244] A. G.-D. Ridder, T. Gehrmann, E. Glover, A. Huss and T. Morgan, *Precise QCD predictions for the production of a Z boson in association with a hadronic jet*, *Physical Review Letters* **117** (Jul, 2016) [1507.02850].

[245] A. G.-D. Ridder, T. Gehrmann, E. W. N. Glover, A. Huss and T. A. Morgan, *The NNLO QCD corrections to Z boson production at large transverse momentum*, 1605.04295.

[246] F. Maltoni, G. Ridolfi and M. Ubiali, *b-initiated processes at the LHC: a reappraisal*, *Journal of High Energy Physics* **2012** (Jul, 2012) [1203.6393].

[247] H. Nikolic, *Relativistic quantum mechanics and quantum field theory*, 1205.1992.

[248] S. J. Brodsky, C. Peterson and N. Sakai, *Intrinsic heavy-quark states*, *Phys. Rev. D* **23** (Jun, 1981) 2745–2757. [https://link.aps.org/doi/10.1103/PhysRevD.23.2745].

[249] S. J. Brodsky, P. Hoyer, C. Peterson and N. Sakai, *The Intrinsic Charm of the Proton*, *Phys. Lett. B* **93** (1980) 451–455. [https://doi.org/10.1016/0370-2693(80)90364-0].

[250] P.-H. Beauchemin, V. Bednyakov, G. Lykasov and Y. Stepanenko, *Search for intrinsic charm in vector boson production accompanied by heavy-flavor jets*, *Physical Review D* **92** (Aug, 2015) [1410.2616].

[251] V. Bednyakov, M. Demichev, G. Lykasov, T. Stavreva and M. Stockton, *Searching for intrinsic charm in the proton at the LHC*, *Physics Letters B* **728** (2014) 602–606 [1305.3548].

[252] **ATLAS** Collaboration, *Identification of Jets Containing b-Hadrons with Recurrent Neural Networks at the ATLAS Experiment*, tech. rep., CERN, Geneva, Mar, 2017. [https://cds.cern.ch/record/2255226].

[253] K. Gautam, *Jet-flavour tagging at fcc-ee*, 2210.10322.

[254] F. Blekman, F. Canelli, K. Gautam and E. Plörer, *Jet flavour assignment and ghost matching*, 2022. [https://indico.cern.ch/event/1137848/contributions/4773957/attachments/2407343/4118450/GM_FCCPhysicsPerformanceMeeting.pdf].

[255] **ATLAS** Collaboration, A. Freegard, *Z+HF Rivet analysis*, Sep, 2022. [https://gitlab.cern.ch/afreegar/zbb_analysis].

[256] ATLAS Collaboration, "Measurements of the production cross-section for a Z boson in association with b-jets in proton-proton collisions at $\sqrt{s} = 13$ TeV with the ATLAS detector." HEPData (collection), 2021. [https://doi.org/10.17182/hepdata.94219].

[257] **ATLAS** Collaboration, G. Aad *et. al.*, *ATLAS b-jet identification performance and efficiency measurement with $t\bar{t}$ events in pp collisions at $\sqrt{s} = 13$ TeV*, *Eur. Phys. J. C* **79** (2019), no. 11 970 [1907.05120].

[258] **ATLAS** Collaboration, *Monte Carlo to Monte Carlo scale factors for flavour tagging efficiency calibration*, tech. rep., CERN, Geneva, May, 2020. [https://cds.cern.ch/record/2718610].

[259] **ATLAS** Collaboration, C. Debenedetti, V. Cairo, K. Hildebrand, J. L. La Rosa Navarro, M. A. L. Leite, E. Meoni, J. M. Pasner, D. Schaefer, F. Sforza, S. Turchikhin, C. Vittori, J. Mcfayden, V. Dao, L. Fabbri, B. Giacobbe, G. Lykasov, V. Jain, S. P. Swift, M. Oreglia and F. Giuli, *Measurement of a Z boson produced in association with heavy flavour jets in 36 fb^{-1} collected by the ATLAS experiment at $\sqrt{(s)} = 13$ TeV*, tech. rep., CERN, Geneva, 2017. [https://cds.cern.ch/record/2293067].

[260] A. Belyaev, N. D. Christensen and A. Pukhov, *CalcHEP 3.4 for collider physics within and beyond the Standard Model*, *Comput. Phys. Commun.* **184** (2013) 1729–1769 [1207.6082].

[261] M. Bondarenko, A. Belyaev, L. Basso, E. Boos, V. Bunichev *et. al.*, *High Energy Physics Model Database : Towards decoding of the underlying theory (within Les Houches 2011: Physics at TeV Colliders New Physics Working Group Report)*, 1203.1488.

[262] A. Buckley, J. Ferrando, S. Lloyd, K. Nordström, B. Page, M. Rüfenacht, M. Schönherr and G. Watt, *LHAPDF6: parton density access in the LHC precision era*, *Eur. Phys. J. C* **75** (2015) 132 [1412.7420].

[263] **DELPHES 3** Collaboration, J. de Favereau *et. al.*, *DELPHES 3, A modular framework for fast simulation of a generic collider experiment*, *JHEP* **1402** (2014) 057 [1307.6346].

[264] G. Belanger, B. Dumont, A. Goudelis, B. Herrmann, S. Kraml and D. Sengupta, *Dilepton constraints in the Inert Doublet Model from Run 1 of the LHC*, *Phys. Rev.* **D91** (2015), no. 11 115011 [1503.07367].

[265] E. Conte, B. Fuks and G. Serret, *Madanalysis 5, a user-friendly framework for collider phenomenology*, *Computer Physics Communications* **184** (Jan, 2013) 222–256 [1206.1599].

[266] B. Fuks *et. al.*, *Proceedings of the second MadAnalysis 5 workshop on LHC recasting in Korea*, *Mod. Phys. Lett. A* **36** (2021), no. 01 2102001 [2101.02245].

[267] D. Dercks, N. Desai, J. S. Kim, K. Rolbiecki, J. Tattersall and T. Weber, *CheckMATE 2: From the model to the limit*, *Comput. Phys. Commun.* **221** (2017) 383–418 [1611.09856].

[268] A. Freegard, *CheckMATE code for analysis ATLAS_1403_5294.*, . [https://github.com/agagsgroove/checkmate2/blob/LLP-master/tools/analysis/src/analyses/ATLAS_8TeV/atlas_1403_5294.cc].

[269] A. Freegard, *CheckMATE code for analysis ATLAS_HIGG_2013_03.*, . [https://github.com/agagsgroove/checkmate2/blob/LLP-master/tools/analysis/src/analyses/ATLAS_8TeV/atlas_higg_2013_03.cc].

[270] **ATLAS** Collaboration, M. Aaboud, G. Aad, B. Abbott, J. Abdallah, O. Abdinov, B. Abeloos, R. Aben, O. S. AbouZeid, N. L. Abraham and et al., *Measurement of the $t\bar{t}Z$ and $t\bar{t}W$ production cross sections in multilepton final states using 3.2 fb^{-1} of pp collisions at $\sqrt{s}$ = 13 TeV with the ATLAS detector*, *The European Physical Journal C* **77** (Jan, 2017) [1609.01599].

[271] **ATLAS** Collaboration, *Search for direct top squark pair production and dark matter production in final states with two leptons in $\sqrt{s} = 13$ TeV pp collisions using 13.3 fb^{-1} of ATLAS data*, tech. rep., CERN, Geneva, Aug, 2016. [http://cds.cern.ch/record/2206249].

[272] **ATLAS** Collaboration, *Search for supersymmetry with two and three leptons and missing transverse momentum in the final state at $\sqrt{s} = 13$ TeV with the ATLAS detector*, tech. rep., CERN, Geneva, Sep, 2016. [https://cds.cern.ch/record/2212162].

[273] **ATLAS** Collaboration, M. Aaboud *et. al.*, *Search for electroweak production of supersymmetric states in scenarios with compressed mass spectra at $\sqrt{s} = 13$ TeV with the ATLAS detector*, *Phys. Rev. D* **97** (2018), no. 5 052010 [1712.08119].

[274] A. M. Sirunyan, A. Tumasyan, W. Adam, F. Ambrogi, E. Asilar, T. Bergauer, J. Brandstetter, E. Brondolin, M. Dragicevic and et al., *Search for electroweak production of charginos and neutralinos in multilepton final states in proton-proton collisions at $\sqrt{s} = 13$ tev*, *Journal of High Energy Physics* **2018** (Mar, 2018) [1709.05406].

[275] **CMS** Collaboration, *Search for new physics in the compressed mass spectra scenario using events with two soft opposite-sign leptons and missing transverse momentum at $\sqrt{s} = 13$ TeV*, tech. rep., CERN, Geneva, 2016. [http://cds.cern.ch/record/2205866].

[276] **CMS** Collaboration, *Search for new physics in events with two low momentum opposite-sign leptons and missing transverse energy at $\sqrt{s} = 13$ TeV*, tech. rep., CERN, Geneva, 2017. [https://cds.cern.ch/record/2256640].

[277] G. Aad, T. Abajyan, B. Abbott, J. Abdallah, S. Abdel Khalek, A. A. Abdelalim, O. Abdinov, R. Aben, B. Abi and et al., *Improved luminosity determination in pp collisions at $\sqrt{s} = 7$ TeV using the atlas detector at the lhc*, *The European Physical Journal C* **73** (Aug, 2013) [1302.4393].

[278] E. Lundström, M. Gustafsson and J. Edsjö, *Inert doublet model and LEP II limits*, *Physical Review D* **79** (Feb, 2009) [0810.3924].

[279] A. Pierce and J. Thaler, *Natural dark matter from an unnatural Higgs boson and new colored particles at the TeV scale*, *Journal of High Energy Physics* **2007** (Aug, 2007) 026–026 [hep-ph/0703056].

[280] **CMS** Collaboration, A. Sirunyan, A. Tumasyan, W. Adam, F. Ambrogi, E. Asilar, T. Bergauer, J. Brandstetter, M. Dragicevic, J. Erö, A. Escalante Del Valle and et al., *Search for invisible decays of a higgs boson produced through vector boson fusion in proton-proton collisions at $\sqrt{s} = 13$TeV*, *Physics Letters B* **793** (Jun, 2019) 520–551 [1809.05937].

[281] N. Aghanim *et. al.*, *Planck 2018 results. VI. cosmological parameters*, *Astron. Astrophys.* **641** (2020) A6 [1807.06209].

[282] G. Bélanger, F. Boudjema, A. Goudelis, A. Pukhov and B. Zaldivar, *micrOMEGAs5.0 : Freeze-in*, *Comput. Phys. Commun.* **231** (2018) 173–186 [1801.03509].

[283] **XENON1T** Collaboration, E. Aprile *et. al.*, *Dark matter search results from a one ton-year exposure of XENON1T*, *Physical Review Letters* **121** (Sep, 2018) [1805.12562].

[284] D. Scott and G. Smoot, *Cosmic microwave background mini-review*, 1005.0555.

[285] D. P. Finkbeiner, S. Galli, T. Lin and T. R. Slatyer, *Searching for dark matter in the CMB: A compact parametrization of energy injection from new physics*, *Phys. Rev. D* **85** (Feb, 2012) 043522 [1109.6322].

[286] A. Belyaev, E. Bertuzzo, C. C. Barros, O. Eboli, G. G. di Cortona, F. Iocco and A. Pukhov, *Interplay of the LHC and non-LHC dark matter searches in the effective field theory approach*, *Physical Review D* **99** (Jan, 2019) [1807.03817].

[287] T. R. Slatyer, *Indirect dark matter signatures in the cosmic dark ages. I. generalizing the bound on s-wave dark matter annihilation from planck results*, *Phys. Rev. D* **93** (Jan, 2016) 023527 [1506.03811].

[288] **CTA Consortium** Collaboration, D. Mazin, *The Cherenkov Telescope Array*, *PoS* **ICRC2019** (2020) 741 [1907.08530].

[289] **CTA Consortium** Collaboration, C. Eckner *et. al.*, *Sensitivity of the cherenkov telescope array to a dark matter signal from the galactic centre*, in *Proceedings of 37th International Cosmic Ray Conference — PoS(ICRC2021)*, Sissa Medialab, Jul, 2021. 2007.16129.

[290] C. Duangchan, C. Pongkitivanichkul, P. Uttayarat, A. Jardin-Blicq, M. Wechakama, T. Klangburam, W. Treesukrat, D. Samart, U. Sawangwit, A. Aguirre-Santaella and M. Sá nchez-Conde, *CTA sensitivity on TeV scale dark matter models with complementary limits from direct detection*, *Journal of Cosmology and Astroparticle Physics* **2022** (May, 2022) 038 [2202.07321].

[291] J. V. Jelley, *Cherenkov Radiation: Its Properties, Occurrence, and Uses*, pp. 275–318. Springer US, Boston, MA, 1983. [https://doi.org/10.1007/978-1-4684-4505-3_6].

[292] **CTA Consortium** Collaboration, B. Acharya *et. al.*, *Science with the cherenkov telescope array*, 1709.07997.

[293] H. Silverwood, C. Weniger, P. Scott and G. Bertone, *A realistic assessment of the CTA sensitivity to dark matter annihilation*, *Journal of Cosmology and Astroparticle Physics* **2015** (Mar, 2015) 055–055 [1408.4131].

[294] **XENON** Collaboration, E. Aprile *et. al.*, *Dark Matter Search Results from a One Ton-Year Exposure of XENON1T*, *Phys. Rev. Lett.* **121** (2018), no. 11 111302 [1805.12562].

[295] P. Bambade *et. al.*, *The international linear collider: A global project*, 1903.01629.

[296] **GAMBIT** Collaboration, P. Athron *et. al.*, *Combined collider constraints on neutralinos and charginos*, *Eur. Phys. J. C* **79** (2019), no. 5 395 [1809.02097].

[297] H. Baer, T. Barklow, K. Fujii, Y. Gao, A. Hoang, S. Kanemura, J. List, H. E. Logan, A. Nomerotski, M. Perelstein, M. E. Peskin, R. Pöschl, J. Reuter, S. Riemann, A. Savoy-Navarro, G. Servant, T. M. P. Tait and J. Yu, *The international linear collider technical design report - volume 2: Physics*, 1306.6352.

[298] Y. Li and A. Nomerotski, *Chargino and Neutralino Masses at ILC*, in *International Linear Collider Workshop*, 7, 2010. 1007.0698.

[299] M. Espírito-Santo, K. Hultqvist, P. Johansson and A. Lipniacka, *Search for neutralino pair production at $\sqrt{s}$ from 192 to 208 GeV*, . [http://delphiwww.cern.ch/pubxx/delnote/dn2003.html].

[300] M. Aoki, S. Kanemura and H. Yokoya, *Reconstruction of inert doublet scalars at the international linear collider*, *Physics Letters B* **725** (2013), no. 4 302–309 [1303.6191].

[301] M. Skrzypek and S. Jadach, *Exact and approximate solutions for the electron nonsinglet structure function in QED*, *Z. Phys. C* **49** (1991) 577–584. [https://doi.org/10.1007/BF01483573].

[302] P. Chen, *Differential luminosity under multi - photon beamstrahlung*, *Phys. Rev. D* **46** (1992) 1186–1191. [https://link.aps.org/doi/10.1103/PhysRevD.46.1186].

[303] G. Heber, A. Jelenak *et. al.*, *The HDF group*, . [https://www.hdfgroup.org/].

[304] S. Höche, S. Prestel and H. Schulz, *Simulation of Vector Boson Plus Many Jet Final States at the High Luminosity LHC*, *Phys. Rev. D* **100** (2019), no. 1 014024 [1905.05120].

[305] J. Alwall, A. Ballestrero, P. Bartalini, S. Belov, E. Boos, A. Buckley, J. Butterworth, L. Dudko, S. Frixione, L. Garren and et al., *A standard format for les houches event files*, *Computer Physics Communications* **176** (Feb, 2007) 300–304 [hep-ph/0609017].

[306] E. Boos, M. Dobbs, W. Giele, I. Hinchliffe, J. Huston, V. Ilyin, J. Kanzaki, K. Kato, Y. Kurihara, L. Lonnblad, M. Mangano, S. Mrenna, F. Paige, E. Richter-Was, M. Seymour, T. Sjostrand, B. Webber and D. Zeppenfeld, *Generic user process interface for event generators*, hep-ph/0109068.

[307] Fermilab, *CDF/D0 monte carlo tutorial*, . [https://home.fnal.gov/~mrenna/041207_pythia_tutorial/07_041207_pythia_tutorial_TS_2_leshouches2.pdf].

[308] A. J. Larkoski, D. Neill and J. Thaler, *Jet shapes with the broadening axis*, *Journal of High Energy Physics* **2014** (Apr, 2014) [1401.2158].

[309] D. Bertolini, T. Chan and J. Thaler, *Jet observables without jet algorithms*, *Journal of High Energy Physics* **2014** (Apr, 2014) [1310.7584].

[310] H. Schulz, S. Hoeche and S. Prestel, *Wplus + up to 9 jets parton level events at 14 TeV in HDF5*, May, 2019. [https://doi.org/10.5281/zenodo.2678055].

[311] B. Dumont, *Implementation of a search for electroweakinos in the di-lepton + missing energy channel (20.3 fb-1; 8 TeV; ATLAS-SUSY-2013-11)*, 2021. [https://doi.org/10.14428/DVN/MPMPNN].

[312] **ATLAS** Collaboration, G. Aad, B. Abbott, J. Abdallah, S. A. Khalek, O. Abdinov, R. Aben, B. Abi, M. Abolins, O. S. AbouZeid *et. al.*, *Search for direct production of charginos, neutralinos and sleptons in final states with two leptons and missing transverse momentum in pp collisions at $\sqrt{s}$ = 8tev with the atlas detector*, *Journal of High Energy Physics* **2014** (May, 2014) [1403.5294].

[313] B. Dumont, *Implementation of an invisibly decaying Higgs boson from ZH production, in the di-lepton channel (20.3 fb-1; 13 TeV; ATLAS-HIGG-2013-03)*, 2021. [https://doi.org/10.14428/DVN/GTTIHS].

[314] **ATLAS** Collaboration, G. Aad *et. al.*, *Search for direct production of charginos, neutralinos and sleptons in final states with two leptons and missing transverse momentum in pp collisions at $\sqrt{s} = 8$ TeV with the ATLAS detector*, *JHEP* **05** (2014) 071 [1403.5294].

[315] A. Freegard, *validation notes for CheckMATE analysis ATLAS 1403 5294*, . [https://checkmate.hepforge.org/validationNotes/atlas_1403_5294.pdf].

[316] A. Freegard, *validation notes for CheckMATE analysis HIGG 2013 03*, 2021. [https://checkmate.hepforge.org/validationNotes/atlas_higg_2013_03.pdf].

[317] R. Barbieri, A. Pomarol, R. Rattazzi and A. Strumia, *Electroweak symmetry breaking after LEP-1 and LEP-2*, *Nucl. Phys. B* **703** (2004) 127–146 [hep-ph/0405040].

[318] G. Cynolter and E. Lendvai, *Electroweak Precision Constraints on Vector-like Fermions*, *Eur. Phys. J. C* **58** (2008) 463–469 [0804.4080].

[319] I. F. Ginzburg, *Simple and robust method for search Dark Matter particles and measuring their properties at ILC in various models of DM*, *PoS* **QFTHEP2010** (2010) 028 [1010.5579].